PARIS 13 UNIVERSITY

Laboratoire de Traitement et Transport de l'Information

THÈSE

pour obtenir le titre de

DOCTEUR DE L'UNIVERSITÉ PARIS 13

Spécialité: Signaux et Images

Quang Tung THIEU

Segmentation by Convex Active Contour Models - Application to Skin Lesion and Medical Images

Thèse dirigée par

Assoc. Prof. Marie LUONG and Prof. Emmanuel VIENNET

Soutenue le 24 Juin 2013

JURY

Rapporteurs:	
Mme. Nicole VINCENT	- PR, Université Paris Descartes, France
Mme. Su RUAN	- PR, Université de Rouen, France
Examinateurs:	
Dr. Jean-Marie ROCCHISANI	- Docteur en médecine nucléaire, Hôpital Avicenne, CHU Bobigny, UP13, France
Dr. Nikolay Metodiev SIRAKOV	- Associate Professor, Texas A&M University Commerce, USA
Mme. Françoise DIBOS	- PR, Université Paris 13, France
Mme. Christine CAVARO-MEDARD	- MCF, Université d'Angers, France
Directeurs et Co-encadrant:	
M. Emmanuel VIENNET	- PR, Université Paris 13, France (Directeur de thèse)
Mme. Marie LUONG	- MCF, Université Paris 13, France (Co-encadrant de thèse)

Acknowledgment

I have achieved my thesis from October 2009 to now under the guidance and support of my PhD supervisors, Associate Professor Marie Luong and Professor Emmanuel Viennet. First, I would like to express my sincere thankfulness to Dr Marie Luong for her guidance during my research and especially when I was starting my thesis. One of the most important orientations that she gave me is the idea to begin with the Chan-Vese model which is very suitable with my knowledge. From her instructions, I could discover the new ideas during my thesis. Moreover, when I have a new result, she has always verified, raised questions for a better result. Moreover, she has also helped me by her good advices about the life in France as well as the research life in the laboratory.

I am thankful to Professor Emmanuel Viennet, my supervisor, along with my co-supervisor Associate Professor Marie Luong, for their guidance. They always created the best conditions for my research as well as for the conferences that I participated.

I would like to thank Dr. Jean-Marie Rocchisani, M.D. of the Centre Hospitalier Universitaire Avicenne (Bobigny) for the volumetric medical images, software and helpful discussions. His comments and expertise are very important to valid our result on the medical images.

I would like to thank to Dr. Nikolay Metodiev Sirakov, Associate Professor of the Texas A&M University-Commerce, USA. Our collaborations in relation with the application of the proposed models to skin lesion images are fruitful. He has also advised me and shared with me his experiences in research and in the life. He is very kind and nice person that I have the chance to know. I would also like to thank Dr Richard Selvaggi, M.D., who is colleague of Nikolay Metodiev Sirakov and also an expert in skin lesion images. The accuracy of detection on these images is validated by him. Many thanks to Nikolay Metodiev Sirakov and Richard Selvaggi for the helpful skin lesion images and fruitful discussions.

I would also like to thank Professor Françoise DIBOS, head of the multidisciplinary BQR (Bonus Qualité Recherche) project (2011/2012), for “Automatic and adaptive segmentation methods for the detection and monitoring of pathology by medical imaging analysis” that I have participated during my thesis.

I also thank all members of the L2TI laboratory, Paris 13 University during the time that I worked here. Everyone always helped me with the communication in French and about the culture of France.

I especially thank my family, my friends, cPhuong - aLoc, cDung, aTrung, aChinh,

aNghia, Ha, Dam, Bau, Dunglun, Hinh, Ngà, aBang, aBao, Quang, Nguyen, Lan, Keen... and my honey Dungyeu who always encouraged me when I had troubles and hard time.

Finally, I would like to express my gratitude to the reviewers of my thesis for their helpful comments, suggestions and questions which helped me to significantly improve the quality of my thesis. I also thank the jury of my PhD defense for their instructive questions to valid my results.

Quang Tung THIEU

Contents

CHAPTER 1

Introduction

Contents

1.1 Image Segmentation and Medical Images

Segmentation is a fundamental step for image pattern recognition. It involves detecting and extracting different objects of interest from image. Essentially, it aims at partitioning pixels of the image into meaningful regions (objects), according to image properties for a specific task. These properties may be intensity, color, textures, intensity gradient and may be characterized statistically by the probability distribution function (pdf) or parameters such as means and variance. Segmentation is a basic step in image analysis or interpretation for many domains such as motion tracking and video surveillance where segmentation allows detecting and identifying objects or persons in movement [6, 7].

In medical imaging, segmentation plays a crucial role for the diagnosis [8], monitoring and treatment of diseases [9], as well as intro-operative navigation [10, 11, 12, 13, 14, 15]. Its role is to assist medical imaging experts in their task of identifying, analyzing and interpreting the useful information available in an image. More precisely, segmentation algorithms are used to identify anatomical structures, tissues or lesions within one or more medical images, providing measurements for the location, shape and volume of desired objects to detect. These algorithms are also used to determine the stage of the disease and monitor treatment response. In this crucial respect, information extracted from medical images must be accurate and repeatable for the benefits of the quality in diagnosis, radiotherapy and surgery. While classical segmentation approaches to general images are significant, the special nature of medical images requires specific and high-level treatments. This specificity stems from their methods of acquisition depending on the imaging modality. An imaging modality refers to an imaging system which uses a particular technique to produce images. Medical imaging includes techniques that provide information of anatomy or tissues below the skin.

Nowadays, with the advance in digital medical imaging technologies, many medical imaging modalities exist. They can be classified into two categories depending upon radiation type used: ionizing radiation and non-ionizing one. Ionizing radiation corresponds to radiation that has sufficient energy to ionize atoms and molecules within the body. Ionizing radiation consists of X-rays and gamma-rays. It is worth noting that these radiations need to be handled prudently to avoid harmful side-effects on the human body. In the other hand, non-ionizing radiation, such as ultrasound (high-frequency sound) has very low level of risks associated with its use.

More precisely, imaging modalities obtained with ionizing radiation, i.e. from X-ray and gamma-rays are divided in:

i) X-rays-based imaging technique including:

- X-ray Projection Radiography
- Fluoroscopy (FC)

- Mammography
- Computed Tomography (CT)

ii) Gamma-rays-based imaging technique including:

- the planar scintigraphy (or planar -imaging),
- the single-photon emission computed tomography (SPECT), and
- the positron emission tomography (PET).

As to medical imaging modalities obtained with non-ionizing radiation, there are mainly:

- Ultrasound Imaging
- Magnetic Resonance Imaging (MRI).

For more details on medical imaging, we refer the readers to [16, 17, 18].

Medical images may be in the 2D (two dimensional) form such as traditional X-ray radiography, or in the 3D (three dimensional) forms in case of Computed-Tomography (CT), Magnetic Resonance (MR) imaging, 3D Ultrasound, Positron Emission Tomography (PET) or Single Photon Emission Tomography (SPECT). While X-Ray, CT or MRI images provide information about anatomy and structure of the body, PET modality gives information of the function and metabolism of the organs, by injecting radioactive substance into the body. This modality is useful for detecting and treating cancer, heart and neuropsychiatric diseases. Generally, these modalities are all helpful and may be complementary, with the same objective to provide quantitative and meaningful information to complement the qualitative judgments by experts. These images contain information about the target object of interest which may be an organ, a tissue or cancer tumors. However, these target objects of interest may not be directly obtained from these imaging modalities. Segmentation is then required for delineating the overall images issued from these modalities to generate and isolate the desired objects of interest.

1.1.1 Challenges of segmentation in medical imaging

Although tremendous works have been devoted, segmentation in medical imaging still poses high challenges due to many reasons.

First, the target objects in medical images are complex and highly variable from person to person, in the intensity, in their shape and in their textures, e.g. soft and deformable tissues such as liver, brain, lung, airways and so forth. A target object can be easily segmented when it is somewhat homogeneous and surrounded by a different and relatively homogeneous background. However, there are many cases of superimposed structures in images, i.e. when many organs or tissues overlap (e.g. X-ray image due to its projectional

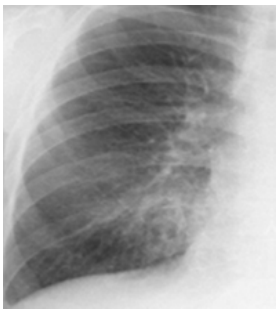

Figure 1.1. Chest X-ray with rib shadows.

nature) with the same range of intensity values. Segmenting such structures is not easy. Figure 1.1 illustrates the case of a chest X-ray with rib shadows making the segmentation of lung nodule difficult, even in-feasible without reducing rib shadows. Many occlusion problem of a 2D projection due to the presence of underlying tissue can be avoided with 3D image data. However, similar situation may arise in 3D images when an organ is in contact with other soft tissues or organs, and conventional segmentation methods cannot correctly identify each adjacent tissue.

Second, the segmentation of 3D images has to be performed on a very large number of image slices (2D images), which can be time-consuming and complex. The volumetric (3D) images are composed of a series of 2D slices for a give slice thickness. For example, Figure 1.2 shows the result of segmentation of different organs segmented by the method in [3] from a 3D image volume consisting of a thorax CT image series of resolution $257 \times 459 \times 150$ and voxel size $1.17 \times 1.17 \times 1.5\ mm^3$ (there are 150 slices of 2D images of 257×459 pixels for a 1.5 mm slice thickness). Three of the slices are presented in Figures 1.2a - 1.2c.

Another challenge in segmentation is related to the quality of medical images which is often limited by poor resolution and intrinsic noises as well as various other artifacts (For CT: see [19]).

Low-resolution adversely affects the level of detail discernible in image. As a consequence, structures of size smaller than that of the image spatial resolution would not be accurately detected. Likewise, small objects or structures that are adjacent to one another would not be correctly identified. In the other hand, noise is the inherent and major limiting factor of medical image quality. Depending upon its nature and level, noise can reduce not only the contrast but also the visibility of details or structures (Figures 1.3 and 1.4). Noises can result in edges blurred or discontinues. Thus, it would be difficult to distinguish for example tissues or tumors with poor contrast to their surroundings. Other types of artifacts can be caused by exterior factors such as the unavoidable anatomical motion of organs (e.g. cardiac motion) causing blurs, or the presence of metallic object (e.g. prosthesis) in the body causing streak artifact (appearing as intense straight lines

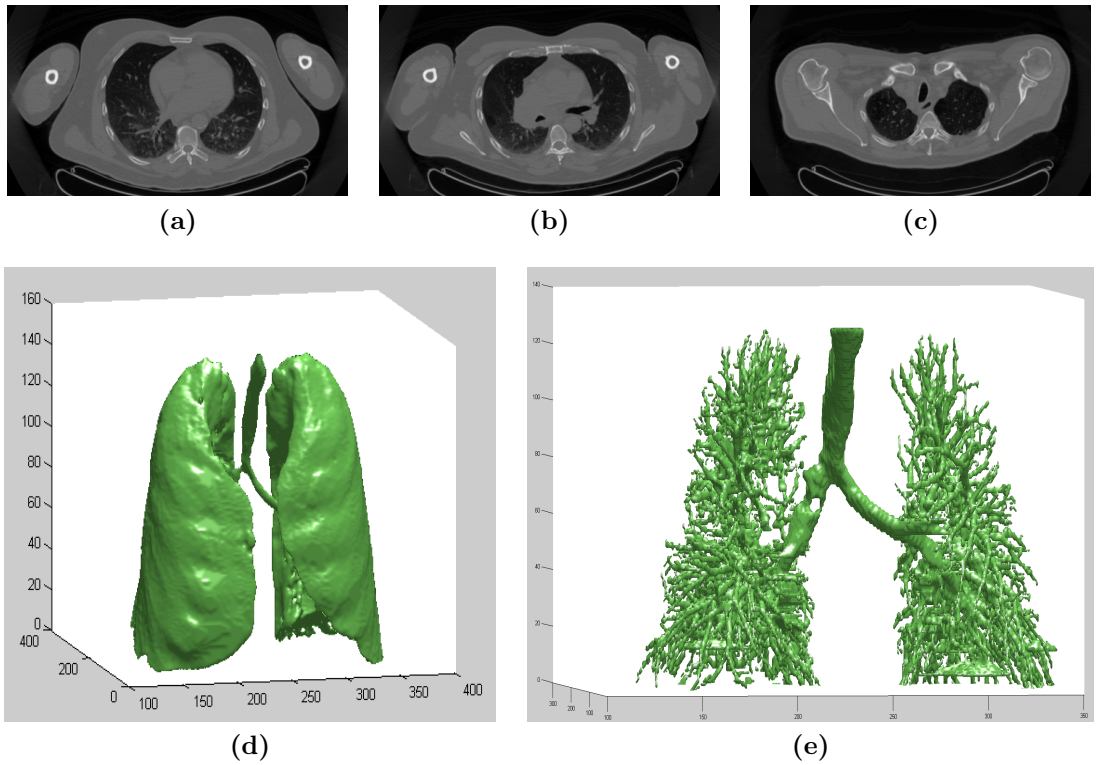

Figure 1.2. A thorax 3D image of voxels $1,17 \times 1,17 \times 1,5\ mm^3$ from 150 slices of 2D of 257×459 pixels. (a)(b)(c) Three 2D slices of a thorax 3D image (image courtesy of J.-M. Rocchisani, Avicenne-Medicine Nucleaire Hospital, Bobigny, France); (b) Obtained surface of the lung from the thorax 3D image by the C_LGR method [3]; (c) The bronchi tree inside the lung from the thorax 3D image by the C_LGR method [3].

across the image) which may cause heavy intensity gradient (see Figure 1.4).

More particularly, medical images are prone to some major artifacts induced by the data acquisition methods such as the Volume Partial Effect (VPE) and the Intensity In-Homogeneity (IIH). The VPE is caused by a poor spatial resolution of the image, resulting in blurring edges between different organ or tissue types and reducing the accuracy of data taken in the images. As to the IIH, this is another major artifact for segmentation techniques that we will focus on in the thesis and present in the next sub-section.

1.1.2 Intensity in-homogeneity (IIH)

One of the well-known artifact in medical imaging is the intensity in-homogeneity (or intensity non-uniformity or intensity bias), also referred to as shading artifact. This artifact is due to the acquisition mode and systems. Visually, it appears as local variation in intensity of the same object. This artifact can be produced by different imaging modalities,

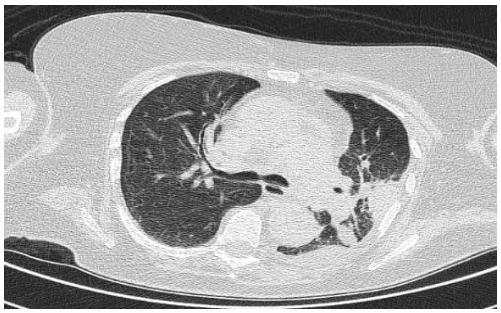

Figure 1.3. Low-dose CT image of thorax at the level of the pulmonary arteries, acquired with optimized reconstruction filter, 2mm thickness, and different parameters of tomography reconstruction. Image courtesy of J.-M. Rocchisani, Avicenne-Medicine Nucleaire Hospital, Bobigny, France.

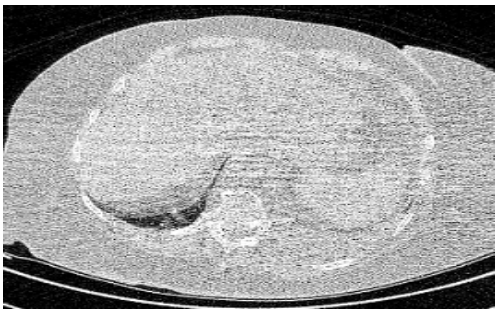

Figure 1.4. Low-dose CT image of abdomen at the liver level, affected by noise and streak artifact. Image courtesy of J.-M. Rocchisani, Avicenne-Medicine Nucleaire Hospital, Bobigny, France.

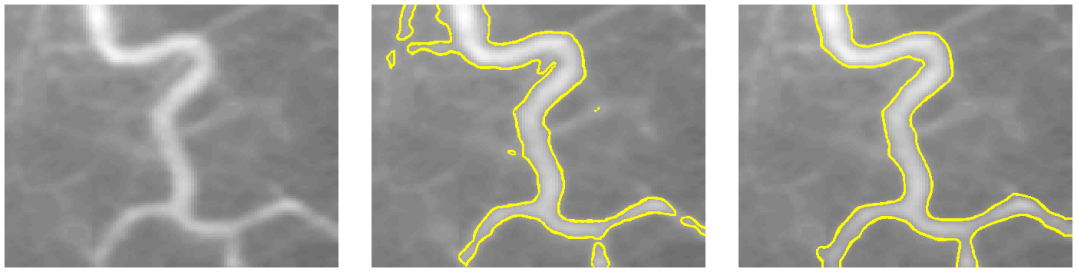

(a) **(b)** **(c)**

Figure 1.5. (a) A blood vessel X-ray with intensity in-homogeneity inside and outside the vessel to be detected (very heteregenous background) (source `http://www.unc.edu/~liwa/`); (b) Vessel is not correctly segmented due to intensity in-homogeneity by the method in [35]; (c) Vessel is well segmented by the method in [3].

such as MRI, CT, X-ray, ultrasound, etc. Figures 1.5 and 1.6 show two examples of an Blood vessel X-ray and a heart MRI images affected by this artifact. In general, this artifact is not easy to detect since gradual changes in these modalities do not appear artificial. As a consequence, this artifact may mimic pathology, and lead to misdiagnosis if it is not well detected.

In MR images, this artifact is typical and mostly due to the geometry and electromagnetic properties of the subject or object being scanned, as well as many other factors related to the acquisition system. For more details on the technology of the MRI, we refer the reader to [20, 21].

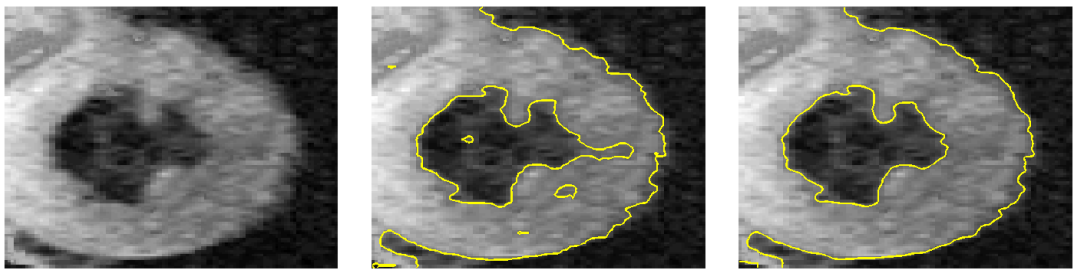

(a) (b) (c)

Figure 1.6. (a) A heart (left ventrice) MR image, with intensity in-homogeneity (source `http://www4.comp.polyu.edu.hk/~cslzhang/RD/RD.htm`); (b) Accurate boundary is not correctly detected due to intensity in-homogeneity by the method in [80]; (c) Good result of segmentation by the method in [1].

In X-ray and especially in CT imaging, shading is one of major artifacts together with streaking, rings and bands. Shading artifacts usually appear near objects of high contrast, e.g. in the soft tissue area near bony structure. In this modality, the shading artifacts are more ominous and need to be considered with high caution. These artifacts are caused by the inconsistency in the projection measurement (for 3D reconstruction), generally by a group of views that diverge (from the true measurement) and without net discontinuity in the signal. The images produced by these errors do not contain clear boundaries. Depending on the error magnitude, the artifacts may largely cover regions or an entire organ, leading to erroneous measurement [22]. It is worth noting that the IIH affects most particularly medical images but can be observed in natural images.

Thus, the shading artifacts may have impact on visual observer. More particularly, many medical image analysis methods, such as segmentation can be sensitive to the high variations of image intensities, inducing hence inaccurate segmentation results. Thereby, these artifacts may compromise the diagnosis of systems involving the segmentation such as expert systems or interpretation systems, where anatomical structures or organs derived from the segmentation method are used as prior or atlas for diagnosis purposes. Indeed, since most of these methods rely on image intensity or on the assumption of homogeneity of objects to detect, these artifacts may affect the accuracy of the segmentation results, especially for heavy intensity variation in the image. Until now, challenge still remains although this artifact has been taken into consideration by many segmentation methods. The reader may refer to some review and articles on this artifact and conventional segmentation methods dealing with this artifact in [23, 24].

In such situations and more generally, manual segmentation from human experts is primordial. However, manual segmentation is a tedious task due to the large volume of images to achieve, and tiredness may affect the quality and reliability of segmentation. For

applications which require full automation of the segmentation process, the IIH artifact would be efficiently dealt.

Basically, semi-automatic or automatic segmentation methods should:

i) handle usually large amounts of data with high performance;

ii) provide accurate and repeatable results even in case of noise and artifacts;

iii) be designed with fast algorithm, which can be expected with the increasingly high-speed computers.

1.2 Objectives

We are interested in designing a computer-aided segmentation tool to extract clinically useful information about anatomic structures or lesions through different medical imaging modalities as well as for other images such as lesion skin images. Accurate segmentation is still a challenge due to limitations of the imaging system with its artifacts such as noises, intensity in-homogeneity, partial volume effect, as well as the variability and diversity of the biological tissues. This makes the boundaries between different tissues indistinguishable. In this work, we focus on noises and more specially in intensity in-homogeneity for its high interest in the medial imaging community [77, 82, 78, 79, 83, 80].

Our objective in this work is to develop efficient segmentation methods which should be:

a) capable of dealing with IIH and providing the robustness to noises and weak edges,

b) independent of initialization, hence suitable for an automation,

c) implemented with fast algorithms to handle large volume of data.

In the scope of this thesis, we have adopted region-based active contour models in a variational framework as segmentation methods to achieve our objectives. Unlike conventional pixel (voxel)-based methods, active contours are well-known models capable of providing accurately smooth and closed curves/surface as final segmentation. In a variational framework, the active contour is obtained by minimizing an energy functional. Depending upon the choice of the energy functional, its convexity would provide a global solution, hence repeatable and reliable results. Thereby, convex energy functional-based models would be particularly suitable for an automatic segmentation system. By adopting this framework, we will address the IIH and the globally convex segmentation. In addition, we are motivated by the implementation of these methods with fast algorithms to be competitive while treating high volume of data.

In this context, these objectives have allowed my participation in the multidisciplinary BQR (Bonus Qualité Recherche) project (2011/2012), for "Automatic and adaptive segmentation methods for the detection and monitoring of pathology by medical imaging analysis" in collaboration with the LAGA laboratory (Laboratoire Analyse, Géometrie et Aplications, UMR CNRS 7539) (Professor Françoise DIBOS, head of project), the Centre Hospitalier Universitaire Avicenne (Bobigny) (Dr Jean-Marie ROCCHISANI, M.D.). On the other hand, we also collaborate with the Texas A&M University Commerce in USA (Dr. Nikolay Metodiev Sirakov and Dr. Richard Selvaggi, M.D.) for the segmentation of skin lesion images for the purpose of a computerized automated interpretation system of melanoma dots and globules. Note that medical images are not the same for skin lesion images. In such system, segmentation methods are used for accurately extracting boundary of dots typical of melanoma. This system aims at assisting experts in the screening of melanomas, improving the visual diagnosis, leading to earlier diagnosis, increasing the probability of biopsy for suspicious skin lesion and reducing the biopsy rates of benign lesions. Figure 1.7 illustrates a skin lesion image with visible melanoma dots.

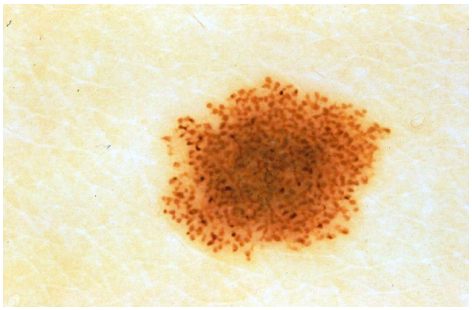

Figure 1.7. A skin lesion image with visible melanoma dots (image courtesy of Nikolay Metodiev Sirakov and Richard Selvaggi, The Texas A&M University-Commerce).

In the next sub-sections, we will present an overview of active contour model in the variational framework as well as the region-based active contour models that are known for robustness to noises and initialization, followed by problem of intensity in-homogeneity problem that can be solved by taking into account local information into a region-based active contour model. Finally, the globally convex segmentation problem is briefly described.

1.2.1 Active contour model and optimization

Many recent efficient segmentation techniques can be described by the formulation as an optimization problem, where segmentation is obtained by minimizing an appropriate criteria or an energy functional. This is the case of the variational approach and the Bayesian framework.

In Bayesian framework, segmentation techniques involve the probability density function (pdf) or the parameters to characterize the properties of images via descriptor such as intensity or textures. The distribution of image regions may be modelled by stochastic/probabilistic models and segmentation is performed by maximum *a posteriori* (MAP) or maximum likelihood (ML) estimation methods.

In variational framework, the segmentation is obtained by minimizing an energy functional. To minimize this functional, the common way is to compute the Euler-Lagrange equation. Then, an optimizer can be computed using a gradient descent method. The variational models are formulated in spatially continuous setting, thus offering well-established mathematical description. It addition, in this framework, it is easy to incorporate and impose *a priori* constraints such as geometric prior (smoothness), and other prior information accounting for the object features (intensity distribution, texture, homogeneity, motion, shape). Among the most popular variational models, Active Contour (AC) models are well-known for their accuracy and robustness in case of noise or weak boundaries.

Active contour models are also referred to as snakes or deformable models. Basically, active contours are curves (or surfaces) defined in the image that can be evolved towards the boundary or other desired features of the object of interest, according to a partial differential equation (PDE). This latter can be derived from the minimization of an energy functional. Such functional can be a criterion that accounts for image properties while satisfying the internal geometric properties of the contour. Since the publication of the paper on Snakes by Kass, Witkin, and Terzopoulos in 1988 [25], these models have become very popular in the literature, along with successful applications, particularly in analysis of medical images [26, 27, 28]. The AC can be parameterized, leading to the so called parameterized models. Such approaches convey certain advantages. Firstly, the AC is defined using an energy function that can be regularized to constrain the curve to be smooth and offer robustness to noise and gaps of boundary. Second, AC is implemented on the continuum, achieving sub-pixel segmentation accuracy, which is primordial for applications such as medical imaging. Moreover, the implementation is straightforward and rapid, using the finite difference for example. However, one of drawbacks is that by default they cannot allow change of topology of the evolving contour, implying that the segmentation of several objects or multiply-connected objects is not possible. To overcome this limitation, the Geometric AC models proposed by Caselles, Catte, Coll, and Dibos [29] have been addressed in 1993. Although these models are not derived from a variational approach, they have revolutionized the AC models, providing automatic change of topology and making possible the segmentation of complex shapes. In these models, the contour is implicitly represented by level set function and the curve evolving is defined using the evolution theory (i.e. using only geometric measures such as unit normal and curvature of the contour to study its deformation). Using always the level set representation of the contour to benefit from the automatic change of topology, another AC contour model,

namely the geodesic active model has been later proposed, but deriving from a variational framework by Caselles, Kimmel, Sapiro in 1995 [30] and successfully followed by many of its variants. We will refer to this model as the GAC model.

1.2.2 Regions-based active contour models - Robustness to noise and initialization

More recent AC models are based on regions. Recall that in variational approach, the problem is to define the energy functional/criterion to be minimized. For the classical active contour or snake, which is the edge-based (or boundary-based) active contour model, an energy functional should be composed of terms with information related to the boundary, for example the gradient information along the curve. On the other hand, in region-based variational model, an energy functional may include terms that describe the properties of regions such as its mean, variance, or histogram. Generally, region-based criteria/energy functionals depend on the statistical properties of the region. It is important to note that the region-based approaches often combine both region-based terms and boundary-based ones, mainly to reflect the characteristics of regions and add constraints on the contour by introducing a regularization term of the contour.

One of the first region-based models is the Mumford-Shad model [32] which is considered as a basic AC region-based model where a region-based criteria in the energy functional is used to penalize deviations from smoothness within region and guiding the active contours towards smooth regions. The Mumford-Shad model can represent regions by piece-smooth approximations. However, this model is computationally complex. Then, by assuming that the regions to detect are piecewise-constant, Chan and Vese proposed Mumford-Shah-based models [33, 34] which can be considered as the most popular region-based models where global intensity information of region is taken into account. This model exhibits promising and robust solutions with respect to noise and initialization. Another advantage to take into account global intensity information is the robustness of the results to detect objects with smooth or discontinuous boundaries. Likewise, in [36], the equivalence between a probabilistic formulation of the segmentation problem and the region-based functionals is established with demonstration on the advantage of the region-based segmentation models over the boundary-based models. Indeed, even though these energy functionals are non-convex and the optimization problem performed in local manner, the segmentation results have less local minima than the boundary-based models and are very robust to noise and initialization.

Hence, region-based active contour is a promising model for ensuring robustness to noise, smooth boundary and varying initialization.

1.2.3 Intensity in-homogeneity and local region-based active contour model

The intensity in-homogeneity (IIH) issue has been widely addressed in the segmentation literature using threshold-based methods [37] and clustering ones, such as the adaptive fuzzy c-means method of Pham and Prince [38], or the Expectation-Maximization methods [39, 40]. In most of the methods, the IIH correction may be considered as a necessary preprocessing step for better segmenting the image. Thus, many algorithms have been proposed to segment and correction for the IIH field simultaneously. These pixel-wise methods offer less or more good performances and many methods depend on the initial condition.

In the active contour and variational model, we propose to tackle IIH issue without estimating the IIH field. As stated above, region-based active contour models are well-known for being robust to noises and initialization. In the active contour and variational model, many models have been proposed successfully for segmenting objects by assuming homogeneity of intensity. Among them, the popular region-based Chan-Vese (Chan-Vese) model [33] is a simplified version of the Mumford-Shah function [32] by assuming that the intensities in each region inside and outside the object contour are homogeneous. However, by using only global information, such model fails to segment objects corrupted with IIH. Later, many other region-based have been proposed such as the Piecewise-Constant (PC) convex model in [41] proposed by Bresson *et al.* and the PC convex model in [42]. These models suffer the same drawback when treating images with intensity in-homogeneity. Generally, the assumption of homogeneity of feature in a region results in spatially homogeneous region models. Statistically, this refers to have the same probability density of all points in a region [33, 43], and the contour is driven by the global differences in the distributions of the intensity.

However, when the region intensity values change locally in the same object, as in the case of medical images where the target object of interest is affected by IIH, this results in a local change of intensity or non-constant regions (see Figure 1.6c). In case of heavy intensity gradient, it is not easy to accurately identify the target objects. For such cases, neither the assumption of having globally constant or smooth luminance is satisfied. Consequently, using only global region information as in the case of homogeneous region models is not sufficient to well separate image objects. However, such assumption can be valid locally, i.e. within local neighborhood. Generally, for piecewise-smooth assumption, Brox and Cremer [43] have presented a more general framework with a new interpretation of the Mumford-Shad model in the Bayesian approach and showed that the Mumford-Shad model allows the piecewise-smooth approximation of intensity within a region. Hence, while the homogeneous region statistics cannot model this, local region statistics can. They state that minimizing the full piecewise-smooth Mumford-Shad functional is equivalent to a first-order approximation of a Bayesian *a posteriori* maximization based on local region

statistics.

Therefore, in order to tackle the IIH, we propose to take into account local region information in the energy functional of a region-based model inspired from the two approaches: the Chan-Vese model (for its simplicity and efficiency) and the Bayesian formulation with full statistics to obtain more accurate segmentation. Here, we use the pixel intensity to characterize region information, and a neighborhood for each pixel is used to compute local statistics.

A state-of-the-art of the existing local region-based active contour models will be presented in Section 2.2.2 and show the performance of these methods. However, due to the non convexity of most of these models, their results are not reliable.

1.2.4 Towards globally optimal segmentation using convex energy function

The variational models proposed in the literature generally result in the minimization of a non-convex energy functional [25, 78, 68, 33, 80, 82, 83]. In this case, the minimization problem may have local minima, implying that the segmentation results may vary with the initialization. As a consequence, the obtained results may be inaccurate, hence unreliable. Some variational models are convex but do not account for IIH [35, 41, 44, 47].

Therefore, in order to get reliable segmentation, it is necessary to design segmentation models robust to varying initialization and ideally a globally convex segmentation which will allow for random initialization and hence more suitable to an automatic system. Furthermore, the energy functional should be defined with respect to IIH. Despite numerous researches, finding an efficient and globally optimal segmentation to deal with intensity in-homogeneity still remains an open problem.

1.3 Main Contributions

This thesis introduces four novel region-based active contour models to address the intensity in-homogeneity while ensuring robustness to noise and weak boundaries. In particular, three convex segmentation models are proposed to provide reliable and suitable solution for an automation. In addition, the implementation of these methods is efficiently achieved using fast algorithms.

The four proposed region-based AC models for addressing IIH are:

1. The ROBUST Local and Global Region-Based model (R_LGR)

2. The Convex Local Region-based Active Contour model (C_LR)

3. The Convex Local and Global Region-based Active Contour model (C_LGR)

4. The Convex Local and Global Fuzzy Gaussian Distribution Energy Minimization for Active Contour Model (C_LGFGD)

To define these models, we are interested in variational models such as the geometric/geodesic AC (GAC) models [29, 30], the Convex Active Contour model of Chan *el al.* [35], the Mumford-Shah-based model of Chan and Vese [33], and more general models from the probabilistic approach, to benefit from their advantages as described above.

The challenge in medical images is to obtain accurate segmentation when dealing with artifacts such as IIH. To cope with IIH, we adopt the local region-based model where local intensity is used to characterize the region. In the other words, image feature, i.e. intensity (when dealing with IIH) is considered in a neighborhood using a local window (e.g. Gaussian window). Hence each region is modelled by the intensity statistics estimated in a local neighborhood to take account for spatial varying intensity of the IIH. In the other hand, it is established that the global region-based methods provide accurate results and robustness with respect to noises, weak edges and gaps as well as varying initialization. It is hence interesting to take account for global and local intensity information in order to take advantages of the two approaches. Besides, it is possible to adaptively control the weight between these two terms.

In fact, the region-based active contour models search to characterize regions delineated by the contour using global or local features of the regions such as mean, variance and entropy. In the four models, we use the assumption that the intensity is modelled by Gaussian distribution. The first three models (Chapter 3 and Chapter 4) are characterized by local and (or) global intensity means, while the standards-deviation are fixed. In the last model (Chapter 4), we consider full statistics with means and standards-deviations.

As we adopted the region-based active contour approach, the segmentation is less sensitive to initial contour. However, challenge arises when the energy functional is not convex. Many of the AC models proposed in the literature suffer from this drawback. Non convex model may yield local minima. This implies that an accurate result requires a good position of the initial contour. This is not suitable for an automation. In contrast, a convex model guarantees the same results independently with respect to the initial contour, hence the reliability of the segmentation result. In order to cope with the dependence of result to the initialization, we have proposed to design convex energy functional to design our proposed region-based active contour models.

Although the first model, namely the ROBUST Local and Global Region-Based model (R_LGR) is not convex, it is useful to be firstly presented (in Chapter 3), for a better understating of the way how a model should be designed to deal with intensity in-homogeneity and noise. Besides, this is the first objective (objective a) in our works. Then, in the second step (in Chapter 4), we focus on the design of convex energy functional, while proposing different energy functionals capable to deal with IIH and noise.

Table 1.1. The potential applications of the proposed region-based active contour models. +: good enough, ++: good, //: fail, ?: to develop.

Model	Synthetic	X-ray	MR	CT	PET	Ultrasound	Skin lesion
R_LGR	++	+	+	//	//	+	*
C_LR	++	++	+	//	//	*	++
C_LGR	++	++	++	++	+	*	++
C_LGFGD	++	++	++	++	//	*	+

Table 1.2. Maximum of the standard deviations (that the proposed models can deal with) and corresponding parameters (see Chapter 3 and Chapter 4).

Model	Standard deviation	σ	μ	λ	λ_2
R_LGR	160	3	x	100	x
C_LR	15	25	1	x	x
C_LGR	40	1	1	0.01	1
C_LGFGD	140	1	1	0.99	x

Based on the Gaussian distribution of intensity for all the modalities of medical images or synthetic images considered in our experiences, the ability of our proposed models for addressing IIH is summarized in Table 1.1. Furthermore, the robustness of our models when dealing with noise is reported in Table 1.2. In this table, we only report one experience giving the maximum level (Gaussian) noise such that each model achieves accurate result. Other noise test also gives the same results in Section 4.6.

Our contributions are summarized as below.

1.3.1 The ROBUST Local and Global Region-Based model (R_LGR)

In Chapter 3, a novel level set region-based model is proposed to reduce the dependence to the initial contour by combining local and global intensity information in a variational level set formulation. We refer to this model as the Level Set Local and Global Region-based model (R_LGR).

More precisely, the energy functional proposed for this model consists of two components: global and local components described by the intensity using the mean as in the Chan-Vese model [33]. By introducing the local intensity information term, the images with intensity in-homogeneity can be efficiently segmented. Due to the global intensity

information, the model is expected to be robust to noises and initialization. There is no regularization term in this model, reducing hence the number of parameters. However, by using the Gaussian filtering to re-initialize the level set function to a signed distance function, and avoid classical and periodical re-initialization, this guarantees at the same time the smoothness of the level set function. Experimental results show that this model is very efficient in case of intensity in-homogeneity and provide high robustness to noises and initialization. However, this model is not convex with respect to the level set function. Therefore, we have proposed three convex models presented in Chapter 4.

1.3.2 The Convex Local Region-based Active Contour model (C_LR)

For the first convex model, we search for curves that are attracted by the true region boundaries and of minimal length using an implicit boundary-based approach, and at the same time create a partition of the image that minimize the local differences in the means by the region-based approach to handle IIH. Inspired from the convex regularization term of the Bresson's model [41], we adopted this term for its efficiency.

So, the first convex model is a local region-based active contour models which hybridizes the local region-based AC model with the regularization term resulting from the combination of the GAC model and the total variation of the level set function restricted in [0,1] (Bresson's regularization term).

Hence, our proposed model allows for taking advantages from the regularization constraint term of the Bresson's model [41] and the ability to address the IIH from the local region-based AC model. More precisely, the local region is described by the means of the intensity in a Gaussian neighborhood. The length regularization constraint is performed by coupling the total variation of the level set function constrained to lie in [0,1] as in the convex model of Chan *et al.* [35], with an edge detector function as in the GAC model, in order to find the minimal length geodesic curve. Thus, the contour is guided towards the final solution by the PDE (partial differential equation), which is derived from the joint minimization of the boundary length and the local differences in the means (local region Gaussian distribution with fixed variance) of the intensity inside and outside the contour in a local region. We refer to this model as the Convex Local Region-based AC model (C_LR).

Furthermore, instead of solving the Euler-Lagrange equation, this model is minimized in a computationally efficient way by adapting the algorithm of Bresson *et al.* [41], which is based on the algorithm of Chambolle for denoising [45]. Experimental results on synthetic and real-world images such as medical images demonstrate the effectiveness of our models. Due to the convexity of the energy functional, the results of segmentation are independent from the initial contour, hence appropriate for an automatic segmentation.

1.3.3 The Convex Local and Global Region-based Active Contour model (C_LGR)

The second convex model is an extension of the first convex model by incorporating global intensity information in addition to local information. This model takes the advantages of the local and global region-based approaches, to deal with the IIH while improving robustness to noises, and weak/blur object boundaries, without depending on initial contour. We refer to this model as the Convex Local and Global Region-based AC model (C_LGR).

More precisely, in this model, the curve is evolved by the local and global differences in the means of the intensity. The curve is regularized with the same term as for C_LR (term hybridizing the GAC model with the total variation of the level set function restricted in [0,1] or the Bresson's regularization term [41]).

The C_LGR model is more robust to noises and IIH compared with the C_LR model. Again, due to the convexity of the energy functional, the segmentation results are independent from the initialization, hence appropriate for an automation process. Likewise, instead of solving the Euler-Lagrange equation, this model is also minimized in a computationally efficient way by adapting the same algorithm of Bresson *et al.* [41], which is based on the algorithm of Chambolle for denoising [45]. Experimental results on synthetic and medical images showed the effectiveness of our models.

1.3.4 The Convex Local and Global Fuzzy Gaussian Distribution Energy Minimization for Active Contour model (C_LGFGD)

The two previously proposed convex models have proven their ability of dealing with IIH and the robustness to noises as well as weak boundaries. However, a trade-off is necessary in case of images affected with IIH and noises, limiting hence the performance of the model when compared with the case when the image is only corrupted with IIH.

In order to improve the performance when dealing with simultaneous IIH and noises, we propose lastly in this section, another convex region-based AC model which results from the hybridization of a fuzzy clustering with the region-based AC model defined in the Bayesian formulation.

In this fuzzy region-based AC model, fuzzy c-means (FCM) clustering and region-based AC are combined in the Bayesian approach and provide the local and global region information to attract the curve towards object boundaries. A length regularization term imposes smoothness constraints on the geometry of the curve, yielding accurate and stable result in case of noises. The combination of the FCM and the AC model in the Bayesian with full statistics can effectively improve the segmentation results especially in case of simultaneous noises and IIH.

In this model, the contour is driven by the local and the global differences in the distributions (using means and standard deviations). More precisely, by using the fuzzy energy, we search a partition of regions which minimize the local and global differences of the Gaussian statistics (mean and standard deviation) between the pieceswise-smooth approximation partition of regions and that of the original image, while taking into account the fact that a point in region may have partial membership inside and outside the contour. Here local information is considered in a local Gaussian neighborhood as for the two other convex models. The regularization term is performed with the total variation of the membership function (the regularization term of the convex model of Chan *et al.* [35]). Moreover, instead of using the bounded level set function, membership function is used for extracting the contour. This makes the model independent from the initial position of the contour and also suitable for an automatic segmentation. Furthermore, the energy function is minimized in a computationally efficient way by calculating the fuzzy energy alterations directly [46, 47]. Experiments are carried out to prove the performance of the proposed models over some existing methods. The obtained results confirm the efficiency of the methods.

1.4 Thesis Layout

The thesis is organized in six chapters as follows:

Chapter 1: This chapter gives a general introduction of our thesis with a brief description of image segmentation in medical images, followed by our objectives, then our main contributions and lastly the thesis layout.

Chapter 2: This chapter presents some state-of-the-art of the active contour models. In this chapter, we first review the AC models including the boundary-based models and the region-based ones. In the boundary-based model, we give an overview of the classical active contour or snake then the level set-based (or implicit) models. Then, after a description of some basic region-based AC models, we present a state-of-the-art of the models addressed for dealing with intensity in-homogeneity.

Chapter 3: In this Chapter, we introduce the ROBUST Local and Global Region-Based model (R_LGR) model, then the implemented algorithm. Then, we present the sensibility analysis of the models as well as comparison with the other methods.

Chapter 4: This chapter describes the three proposed convex AC models: The Convex Local Region-based Active Contour model (C_LR), the Convex Local and Global Region-based Active Contour model (C_LGR), and the Local and Global Fuzzy Gaussian Distribution Energy Minimization for Active Contour model (C_LGFGD). Each

model is first presented, followed by the implementation and the algorithm. Then, we present the sensibility study of parameters and the experimental results as well as comparison with the other state-of-the-art methods.

Chapter 5: This chapter presents some application of the proposed models for medical images such as skin lesion images and medical images such as lung and airways.

Chapter 6: This chapter presents the general conclusion of our thesis and our prospective works.

1.5 Publication

Journal Papers

1. **Quang Tung THIEU**, Marie LUONG, Jean-Marie ROCCHISANI, Nguyen LINH-TRUNG, Emmanuel VIENNET, "Novel Active Contour Model for Image Segmentation Based on Local Fuzzy Gaussian Distribution Fitting." Journal of Electronic Science and Technology (JEST) vol. 10, no. 2, 2012.

2. **Quang Tung THIEU**, Marie LUONG, Jean-Marie ROCCHISANI, Nikolay Metodiev SIRAKOV, Emmanuel VIENNET, "Medical Image Segmentation with an Active Contour Using Local and Global Fuzzy Gaussian Distribution." Journal of Annals of Mathematics and Artificial Intelligence (AMAI), (submitted).

3. **Quang Tung THIEU**, Marie LUONG, Richard SELVAGGI, Nikolay Metodiev SIRAKOV, Emmanuel VIENNET, "Dermoscopic Structures Extraction from Skin Lesion Images Using Region Based Convex Active Contour." Journal of ... (in preparation).

International Conference Papers

1. **Quang Tung THIEU**, Marie LUONG, Jean-Marie ROCCHISANI, Nikolay Metodiev SIRAKOV, Emmanuel VIENNET, "Segmentation by a Local and Global Fuzzy Gaussian Distribution Energy Minimization of an Active Contour Model". R.P. Barneva et al. (Eds.): IWCIA 2012, LNCS 7655, pp. 298-312. Springer, Heidelberg (2012).

2. **Quang Tung THIEU**, Marie LUONG, Jean-Marie ROCCHISANI, Nguyen LINH-TRUNG, Emmanuel VIENNET, "Novel Active Contour Model for Image Segmentation Based on Local Fuzzy Gaussian Distribution Fitting". International Conference on Signal, Image Processing and Applications ICSIA, Hong Kong 2012.

3. **Quang Tung THIEU**, Marie LUONG, Jean-Marie ROCCHISANI, Emmanuel VIENNET, Dat TRAN, "Novel Convex Active Contour Model Using Local and Global

Information". IEEE International Conference on Digital Image Computing: Techniques and Applications (DICTA), Noosa, Queensland, pp. 346-351, Digital Object Identifier: 10.1109/DICTA.2011.65, 6-8 December, Australia, 2011.

4. **Quang Tung THIEU**, Marie LUONG, Jean-Marie ROCCHISANI, Emmanuel VIENNET, "A Convex Active Contour Region-based Model for Image Segmentation". Proceeding CAIP'11, Proceedings of the 14th international conference on Computer analysis of images and patterns - Part I, LNCS 2011, Springer-Verlag Berlin, Heidelberg 2011, Volume 6854/2011, pp. 135143, 2011. (DOI: http://dx.doi.org/10.1007/978-3-642-23672-3_17).

5. **Quang Tung THIEU**, Marie LUONG, Jean-Marie ROCCHISANI, Dat TRAN, Emmanuel VIENNET, "An Efficient Local and Global Model for Image Segmentation". In 2011 International Conference on Advanced Technologies for Communications, pp. 260 263, ISBN: 978-1-4577-1206-7, Digital Object Identifier: 10.1109/ATC.2011.6027480, Da Nang, August 2-4, Vietnam, 2011.

CHAPTER 2

State of the Art

Contents

In this thesis, we consider the problems of segmentation using active contour in the variational framework to design accurate and reliable models robust to noise and artifact such as the intensity in-homogeneity. Therefore, a review of active contour models in the variational framework is necessary before introducing our proposed segmentation models in subsequent chapters.

Active contour (AC) is a curve (or surface) evolving from an initial position towards the boundary or a desired feature of the object of interest. In variational approaches, the evolving curve is a partial differential equation (PDE) derived from the minimization of the energy functional, and the final contour corresponds to the minimum of this energy. Such functional should be defined to account for image data while satisfying some internal geometric properties of the contour. The advantage of variational model to describe the image segmentation problem is to allow for *a priori* information (such as external force or shape [48]), additional features (such as color, texture, motion [49]).

There are two main families of AC models: the boundary-based active contours, and the region-based active contours. The boundary-based AC methods make use of local image properties such as intensity gradient. On the other hand, the region-based AC models tend to characterize region delineated by the contour using a descriptor.

Among boundary-based AC models, the most well-known ones are the original active contour or Snake introduced by Kass, Witki and Terzopoulos in 1987 [25], the Geometric Active contour [29] and the Geodesic Active Contour [30]. The original active contour/snake [25] is defined explicitly by a parameterized curve of points, whereas the Geometric Active contour [29] and Geodesic Active Contour [30] implicitly represent the contour with the zero-level set of the level set function. In the implicit approaches, segmentation is achieved by evolving the level set function according to a partial differential equation (PDE). Compared to the parameterized approach of the Snake model, the implicit approaches offer the advantage of allowing change in curve topology when merging and breaking occur. These implicit models have been extensively used and extended for various applications.

In this section, we address relations to prior works through a state-of-the-art of segmentation based on a variational approach. First, we review two families of the active contours: the boundary-based active contours and the region-based active contours. In the boundary-based active contour models, the traditional Snake model is first described. Then, we present the evolution theory and the level set method which allow for the implicit representation of the active contour in the Geometric active contour model and the Geodesic active contour model. The Geometric active contour model is not defined in the variational framework but it is interesting to make a brief review of this model to better understand the geodesic active contour model which was proposed later but in the variational framework. Finally, we present a state-of-the-art of the region-based models. In particular, as intensity in-homogeneity can be efficiently addressed by region-based approaches,

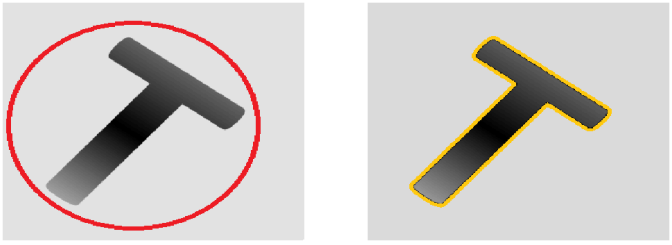

(a) (b)

Figure 2.1. An illustration for active contour: (a) The initial contour (red); (b) The final contour (yellow).

we will also present a review of those dealing with this artifact.

2.1 Boundary-based Active Contours

2.1.1 Original snake or active contour

Since the publication of the article [25] by Kass, Witki and Terzopoulos, in 1988, active contours or snakes have become popular and successfully applied in many applications.

The key idea is to identify a desired object by evolving an initial contour, like a snake, towards the boundary of the object, using an edge detector function to detect image intensity variations, i.e. which takes small values near boundaries (large image gradient) and large values in smooth image region.

Figure 2.1 shows the snake at the beginning and at the end of the evolution process.

In the variational framework, active contour is a curve C parameterized by $p \in [0,1]$ such that it minimizes a weighted energy functional F_{Snake} associated with an observed image $I \in L^1(\Omega)$ of continuous position variables $(x_1(p), x_2(p))$ defined on a domain Ω and any positive weighting parameters α, β, ω:

$$F_{Snake}(C) = F_{int}(C) + F_{ext}(C) \tag{2.1}$$

with

$$F_{int}(C) = \frac{1}{2}\left(\alpha \int_0^1 \left|\frac{\partial C(p)}{\partial p}\right|^2 dp + \beta \int_0^1 \left|\frac{\partial^2 C(p)}{\partial p^2}\right|^2 dp\right) \tag{2.2}$$

$$F_{ext}(C) = \omega \int_0^1 E_{image}(I(C(p)))dp \tag{2.3}$$

where F_{int} is the internal energy functional which imposes smoothness (tension) and rigidity constraints on the geometry of the curve, and F_{ext} is the external energy functional defined over the image domain. The first term of F_{int} discourages stretching of the snake and models this latter like an elastic membrane, while its second term discourages bending of the snake and makes it behave like a thin plate. The weighting parameters α and β control the strength of the model's tension and rigidity respectively. The external energy term, i.e. F_{ext}, depends on the data term E_{image}, defined to attracts the curve toward the object's boundaries using an edge detecting function which vanishes at infinity such as the function:

$$E_{image}(I) = -|\nabla I|^2 \quad \text{or} \quad E_{image}(I) = -|\nabla[G_\sigma * I]|^2 \tag{2.4}$$

where G_σ is a Gaussian function with standard deviation σ and ∇ is the gradient operator. By this way, the data term takes smaller values at object boundaries. Note that this second term possesses local minima at the image edges.

The variational model is then derived by finding a curve $C(p)$ which minimizes the energy functional F_{Snake}. As this function is not convex, the segmentation result is not unique. A local minimum of F_{Snake} can be reached by solving its Euler-Lagrange equation [25, 64]:

$$\frac{\partial}{\partial s}\Big(\alpha\frac{\partial C}{\partial s}\Big) - \frac{\partial^2}{\partial s^2}\Big(\beta\frac{\partial^2 C}{\partial s^2}\Big) - \nabla E_{image}(C) = 0 \tag{2.5}$$

It is worth noting that minimizing the total energy yields internal forces and external forces. Internal forces correspond to the first two terms: the first term is the elastic internal force which holds the curve together while the second term can be referred to as the rigidity internal force because it keeps the curve from over-bending. External force is defined over the image to attract the curve toward the desired object boundaries. Thus, Equation (2.5) can be seen as a force balance equation.

Now, searching a solution to Equation (2.5) can be achieved by making the curve C dynamic. Then, a local minimum of the contour can be found by applying the gradient descent algorithm. This is the same as setting the partial derivative of $C(p,t)$ w.r.t. time t equal to the left-hand side of Equation (2.5), leading to Equation (2.6), with coefficient γ such that units of the two hands are consistent:

$$\gamma\frac{\partial C}{\partial t} = \frac{\partial}{\partial s}\Big(\alpha\frac{\partial C}{\partial s}\Big) - \frac{\partial^2}{\partial s^2}\Big(\beta\frac{\partial^2 C}{\partial s^2}\Big) - \nabla E_{image}(C) \tag{2.6}$$

A solution of this problem is the one which stabilizes $C(p,t)$, i.e. when the left side vanishes. This is equivalent to placing an initial contour on the image and forcing it to deform according to Equation (2.6). Numerical implementation can be fast and efficiently performed by finite differences method in discrete formulation [25].

Although the success of this parameterized AC model, it has the main following drawbacks.

- First, the energy functional is not intrinsic because it depends on parameterization of the contour.

- Moreover, when the image force term involves the Gaussian function as in Equation (2.4), standard deviation σ must be selected to have a small value. By this way, the contour can follow the boundary accurately according to the image force term. This in turn implies that this image force can only attract the contour toward the boundary when it is initialized nearby.

  To increase the attraction range, Cohen [50] propose in the active contour model also called balloons, a pressure force defined as:

  $$E_p(C) = w_p N \tag{2.7}$$

  where N is the inward unit normal and w_p is a constant weighting parameter. The sign of w_p is chosen by the user whether to balloon or deflate the curve. Hence, this is not necessary for the initial curve to be near the desired object boundaries. The strength of the pressure force is determined by the value of w_p, maintaining the curve ballooning or deflating until it is stopped by the external force. External force defined in Equations (2.4) is guided by gradient information, which would lead to unreliable results in case of noise. Indeed, the evolving curve can be stopped at spurious or weak edges, resulting in a local solution of the energy minimizing problem. Adding the pressure force with a large enough value allows the curve to pass through spurious edges. On the other hand, this force should be smaller than the external force (derived from data as in (2.4)) at important edges in order to be stopped by the external force. Hence, the value of w_p should be correctly selected under the risk of forming loops and causing singularities during deformation. The selection is not easy, which is the weakness of this model.

- The discretization of the derivative of order four in the rigidity term (2.2) may lead to numerical instability.

- Automatic change of topology such as splitting or merging parts is not possible. This implies that object with unknown topology or complex comply can not be correctly segmented, and it is not possible to detect more than one object. This is because new parameterization must be set up when topology changes, requiring sophisticated adaptations and computations [52]. Generally, the topology of initial contour should be selected similarly with the topology of the target object.

2.1.2 Implicit approach

To overcome the limitations of the parameterized active contour models, Caselles, Catte, Coll and Dibos [29] have successfully proposed a novel active contour, namely the Geometric

Active Contour models. The idea is to evolve the curve using the curve evolution theory and the level set method [53, 54]. However, the Geometric Active Contour is not derived from a variational approach. Later, using the same representation of the contour by the level set function, Geodesic Active Contour (GAC) model has been proposed in the variational framework by Caselles, Kimmel and Sapiro [30]. These models have been widely adopted.

In what follows, we will first describe the curve evolution theory and the level set method before presenting the two Geometric and Geodesic AC models.

2.1.2.1 Curve evolution theory [55]

As stated above, the key of the Geometric AC is to be independent of parameters. Hence, it is more convenient to study the deformation of curves by geometric measures such as the unit normal and its curvature. This can be studied with the curve evolution theory. Let us denote a curve $C(p,t)$ where $p \in [0,1]$ is a parameterization and $t \in [0,\infty)$ is the time:

$$\begin{aligned} C : [a,b] \times [0,\infty] &\to \mathbb{R}^2 \\ (p,t) &\mapsto C(p,t) = x(p,t) = \begin{pmatrix} x_1(p,t) \\ x_2(p,t) \end{pmatrix} \end{aligned} \tag{2.8}$$

Then, the evolution of C can be obtained by a partial differential equation:

$$\begin{cases} \frac{\partial C(p,t)}{\partial t} & = v(p,t) \\ C(p,0) & = C_0(p) \end{cases} \tag{2.9}$$

where C_0 is the initial contour, and v is the evolution velocity (or speed) of the curve (Figure 2.2). The velocity depends on the curvature. Let us decompose the velocity v in the Frenet coordinate system associated with the curve C. Then, we obtain two components, according to the unit tangent T and the inward unit normal N to the curve, respectively (Figure 2.3). We obtain:

$$\frac{\partial C(p,t)}{\partial t} = v(p,t) = v_N(p,t)N(p,t) + v_T(p,t)T(p,t) \tag{2.10}$$

where v_N and v_T are the normal and tangential components of the evolution velocity v, respectively. Let us consider that normal component of the velocity is a geometric function of the curve, i.e. which is independent from a particular parametrization (e.g. Euclidean arc-length). Then, according to [56, 55], the geometry of the curve is only affected by this normal, while the tangential component only affects the parametrization. In other words, this normalized velocity is geometrically intrinsic to the curve. So, by assuming that the normal component of the velocity does not depend on the curve parametrization, we can

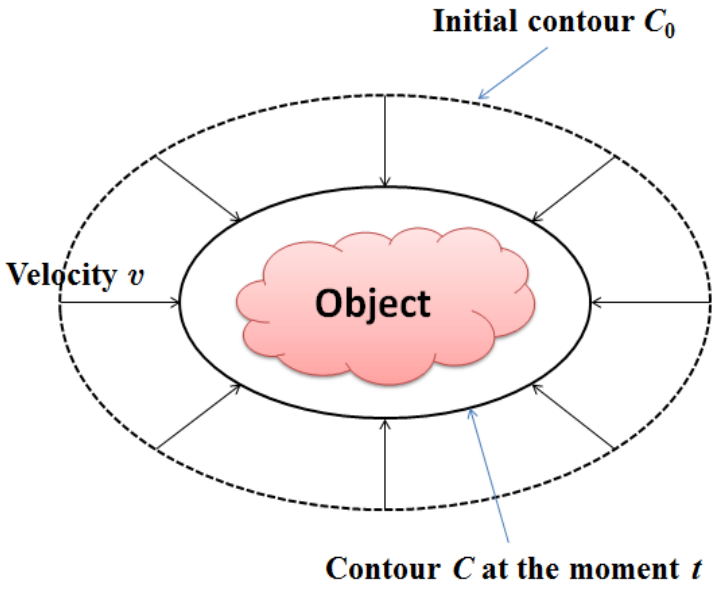

Figure 2.2. Evolution of the active contour $C(p,t)$ with the velocity v towards the the boundary of th object of interest.

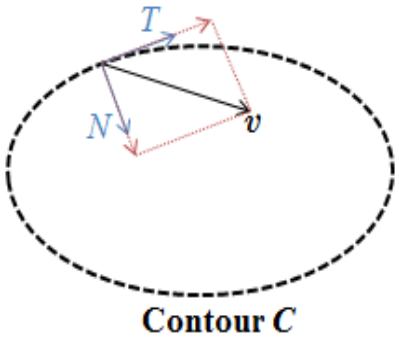

Figure 2.3. Decomposition of the velocity v according to the coordinate system asscoiated with the contour C.

consider the following pdf as the evolution of the curve along its normal direction:

$$\begin{cases} \frac{\partial C(p,t)}{\partial t} & = v(p,t) = v_N(p,t)N(p,t) \\ C(p,0) & = C_0(p) \end{cases} \tag{2.11}$$

Hence, the curves move in the normal direction with a speed function v_N. Also, a curve moving with a velocity in an arbitrary direction can always be re-parameterized to have the same form as Equation (2.11) [53].

Let us mention two common deformations: the curvature deformation and the constant deformation.

- **The curvature deformation** is defined by its speed proportional to the curvature, that is:

$$\frac{\partial C}{\partial t} = \alpha \kappa N \tag{2.12}$$

where α is a positive constant and the curvature κ is defined by

$$\kappa N = \frac{\partial^2 C}{\partial p^2} \tag{2.13}$$

where p is the arc-length parameter of the curve. The curvature deformation plays the same role as the elastic internal force in the parameterized model (2.6). Hence, the curvature deformation will smooth the curve, removing hence singularities.

- **The constant deformation** is defined by a constant speed, that is:

$$\frac{\partial C}{\partial t} = VN \tag{2.14}$$

where V is a constant. Hence, the constant deformation has the same role as the pressure force of the balloon in the parameterized model of snake. Recall that this force allows for extension of the attraction range which is useful when the initial contour is not initialized nearby [50]. Like the pressure force, the drawback of the constant deformation is the creation of singularities on the evolving curve.

As conclusion, the speed function can be designed to characterize the nature of the deformation of the curve. Thus, curvature deformation smooths the curve and corresponds to the internal smooth geometrical constraint imposed on the curve, while constant deformation increases the attraction range, corresponding hence to an external constraint. In order to stop the contour toward the desired object boundaries, the image data term is required. We will see in more details in Section 2.1.2.3 and Section 2.1.2.4 the image data term used in the geometric and the geodesic AC models.

2.1.2.2 The level set method

The level set method was proposed by Osher and Sethian [53] for implementing curve evolution. Let us recall that the level set is a set of points that have the same value. The level set method consists of representing implicitly the moving curve as a level set of a 2D scalar function, also referred to as level set function. The level set method has the main advantage of handling topological merging and splitting naturally, and can work in any number of space dimensions.

This method is used as an implicit implementation in the geometric active contour model and the geodesic active contour model [29, 30], where the contour is represented by the zero level set of a higher dimensional function. Let ϕ be the level set function which satisfies the following conditions:

1. $\phi : \mathbb{R}^2 \times \mathbb{R}^+ \longrightarrow \mathbb{R}$ is a Lipschitz function, defined on the same domain Ω as the given image.

2. $x \in C(p,t) \leftrightarrow \phi(x,t) = 0$, or we can rewrite as follows:

$$\phi(C(p,t),t) = 0, \quad \forall p \in [a,b], \forall t \geq 0 \tag{2.15}$$

3. $\phi(x)$ is the signed distance between the point x and the contour $C(p,t))$, i.e. the zero level set. The sign of $\phi(x)$ depends on the position of x inside or outside the contour which are denoted by $\Omega_{in}(t)$ and $\Omega_{out}(t)$, respectively. By convention, $\phi(x)$ is negative (positive) if x is a pixel inside (outside, respectively) the contour (see Figure 2.4). So, the function ϕ is the signed distance function if it satisfies the three following conditions:

$$\begin{cases} \phi(x,t) = 0 & \text{if } x \in C(p,t) \\ \phi(x,t) = -d(x, C(p,t)) & \text{if } x \in \Omega_{in}(t) \\ \phi(x,t) = d(x, C(p,t)) & \text{if } x \in \Omega_{out}(t) \end{cases} \tag{2.16}$$

where $d(x, C(p,t))$ denotes the Euclidean distance from the point x to the contour $C(p,t))$:

$$d(x, C(p,t)) = \min_{x_c \in C(p,t)} |x - x_c| \tag{2.17}$$

So, the signed distance function of x gives the Euclidean distance to the contour of the curve (closed curve) with a sign to indicate whether x is inside or outside of the curve.

On the other hand, if the level set function ϕ is known, we can determine the contour by finding the zero level set of ϕ. So, evolving the curve implies updating ϕ, which can be done by solving the level set equation of ϕ. This equation can be obtained as follows.

Consider the curve C evolving with the speed v_N as in Equation (2.11). By definition, C satisfies Equation (2.15). Now, taking the derivative of Equation (2.15) with respect to time t on the both sides yields the following equation:

$$\frac{\partial \phi}{\partial t} + \nabla \phi \cdot \frac{\partial C}{\partial t} = 0 \tag{2.18}$$

where $\nabla = (\frac{\partial}{\partial x_1}, \frac{\partial}{\partial x_2})$ is the gradient operator in $\mathbb{R}^2$, and $\cdot$ is the scalar product between two vector in $\mathbb{R}^2$.

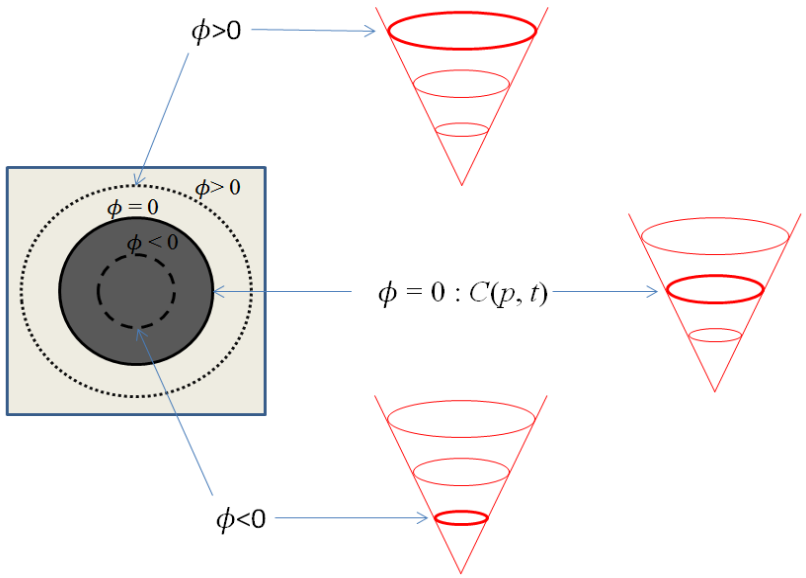

Figure 2.4. Illustration for a signed distance function ϕ.

Replacing $\frac{\partial C}{\partial t}$ in Equation (2.18) by $\frac{\partial C}{\partial t} = v_N N$ in Equation (2.11), yields the following equation:

$$\frac{\partial \phi}{\partial t} + v_N \nabla \phi \cdot N = 0 \tag{2.19}$$

Following the representation of level set function in (2.16), the inward unit normal is given by $N = -\frac{\nabla \phi}{|\nabla \phi|}$ (note that if we select $\phi(x) > 0$ for $x \in \Omega_{in}$ and $\phi(x) < 0$ for $x \in \Omega_{out}$, we have $N = \frac{\nabla \phi}{|\nabla \phi|}$). Then, the gradient flow of previous equation can be re-written as:

$$\frac{\partial \phi}{\partial t} = v_N |\nabla \phi| \tag{2.20}$$

On the other hand, the initial condition $C(p, 0) = C_0(t)$ is replaced by $\phi(x, 0) = \phi_0(x)$ which is the signed distance function to C_0. Then, PDE (2.11) is reformulated by the level set function ϕ as the following PDE (also known as level set equation):

$$\begin{cases} \frac{\partial \phi}{\partial t}(x, t) & = v_N |\nabla \phi(x, t)| \\ \phi(x, 0) & = \phi_0(x) \end{cases} \tag{2.21}$$

Equation (2.21) allows performing curve evolution using the level set method. First, an initialization step consists in building the zero level set function ($\phi(x) = 0$) using the signed distance function in (2.16). Then, the level set method evolves a curve by updating ϕ at fixed coordinates through time. This is equivalent to extend level set equation (2.21) to remain valid while the curve can change its topology. However, the solution of Equation (2.21) can become too steep or flat near the contour [57, 58]. Therefore, to recover ϕ,

a procedure called re-initialization [57, 58, 59, 60] is periodically employed to reshape ϕ to be a signed distance function during the evolution of ϕ. The fact that ϕ be a signed distance function is a desirable condition for numerical accuracy and stable evolution. There are many method for re-initialization of ϕ. In [61], Chopp proposed very time-consuming periodical re-initialization in the whole domain. Rudin and Tourin proved in [62] that the solution of $|\nabla\phi| = 1$ is itself a signed distance function. From this result, the following re-initialization equation was proposed by Sussman *et al.* in [57]:

$$\begin{cases} \frac{\partial\psi}{\partial s}(x,s) & = \text{sign}(\phi(x,t))\big(1 - |\psi(x,s)|\big) \\ \psi(x,0) & = \phi(x,t) \end{cases} \tag{2.22}$$

where s is the time variable of ψ, $\phi(x,t)$ is the solution of Equation (2.21) at time t and $\text{sign}(\phi(x,t))$ is characteristic function of the sign of $\phi(x,t)$. Then $\phi(x,t)$ will be replaced by ψ which is obtained at the steady state of Equation (2.22). Here, re-initialization is the process of replacing $\phi(x,t)$ by another function $\psi(x,t)$ that has the same zero contour as $\phi(x,t)$ but behaves better. Then, this function $\psi(x,t)$ is taken as initial data until the next re-initialization.

Generally, the re-initialization procedure by Equation (2.22) is still a difficult method and needed much time. To avoid the resolution of Equation (2.22), Li *et al.* [65] proposed a signed distance penalizing energy function:

$$P(\phi) = \frac{1}{2}\int_{\Omega} \big(|\nabla\phi(x)| - 1\big)^2 dx \tag{2.23}$$

Equation (2.23) measures the closeness between a level set function ϕ and a signed distance function in the domain $\Omega \subset \mathbb{R}^2$. By calculus of variation [63, 64], the gradient flow of $P(\phi)$ is obtained as:

$$\frac{\partial\phi}{\partial t} = -\frac{\partial P}{\partial\phi} = \nabla\cdot\left(\nabla\phi\left(1 - \frac{1}{|\nabla\phi|}\right)\right) \tag{2.24}$$

where $\nabla\cdot = \frac{\partial}{\partial x_1} + \frac{\partial}{\partial x_2}$ is the divergence operator in $\mathbb{R}^2$. Equation (2.24) is a diffusion equation with the rate $r_1(\phi) = 1 - \frac{1}{|\nabla\phi|}$. However, we can see that $r_1(\phi) \longrightarrow -\infty$ when $|\nabla\phi| \longrightarrow 0$, which may cause oscillation in the final level set function ϕ [66]. This problem is solved by applying a new diffusion rate [66] as follows:

$$r_2(\phi) = \begin{cases} \frac{\sin(2\pi|\nabla\phi|)}{2\pi|\nabla\phi|} & \text{if } |\nabla\phi| \le 1 \\ 1 - \frac{1}{|\nabla\phi|} & \text{if } |\nabla\phi| > 1 \end{cases} \tag{2.25}$$

Xie [67] also proposed a constrained level set diffusion rate as

$$r_3(\phi) = H_\epsilon(|\nabla\phi| - 1) \tag{2.26}$$

where $H_\epsilon(z) = \frac{1}{2}\left[1 + \frac{2}{\pi}\arctan\left(\frac{z}{\epsilon}\right)\right]$ and ϵ is a fixed positive parameter.

In [78], Zhang *et al.* used a convolution between ϕ with a Gaussian kernel to re-initialize ϕ without the re-initialization procedure. This way saves more execution time. In Section 3.3, we will show that this method allows us not only to obtain the signed distance function but also to ensure the smoothness of contour.

Generally, level set method offers the advantages such as:

1. The change of topology is automatic.
2. The signed distance function ϕ allows for stable and accurate numerical schemes.
3. Geometric properties (such as the normal direction, local mean curvature,..) of the contour can be easily estimated from the function ϕ. For example

$$N = -\frac{\nabla\phi}{|\nabla\phi|}, \text{ as normal direction}$$

$$\kappa = \nabla \cdot \left(\frac{\nabla\phi}{|\nabla\phi|}\right), \text{ as local mean curvature}$$

4. The formula can be easily extended to higher dimensions.

Since Osher and Sethian proposed the level set method for the evolution, the geometric AC model and the geodesic AC model [29, 30] are the first boundary-based AC models to represent the active contour with the level set method, while the model of Chan and Vese [33] is considered as the first region-based model which applied the level set function in the energy function. Many other methods using the level set function have also been proposed with promising results.

In the next sub-section, we describe the geometric AC model [29] and the geodesic AC model [30].

2.1.2.3 Geometric active contour

The geometric active contour models were proposed by Caselles, Catte, Coll, and Dibos [29]. Their works have greatly contributed to alleviate the drawbacks of parameterized active contours, by using the curve evolution theory and the level set method. Their models are independent of parameterization, and the curves (or surfaces) can be represented implicitly as a level set of a higher dimensional function.

This model is not derived from a variational framework, i.e. from an energy minimization formulation. Instead, the curve evolution is defined directly with its speed function by an equation of the form:

$$\frac{\partial C}{\partial t} = g(|\nabla I(C)|)(c + \kappa)|\nabla\phi| \tag{2.27}$$

where c is a positive constant, κ is the curvature of the contour C defined as

$$\kappa = \nabla \cdot \left(\frac{\nabla \phi}{|\nabla \phi|} \right) \tag{2.28}$$

and g is an edge detection function defined as follows:

$$g(|\nabla I|) = \frac{1}{1 + |\nabla G_\sigma * I|^p}, \quad p = 1, 2. \tag{2.29}$$

where $G_\sigma * I$ is the convolution between the image I and a Gaussian kernel G_σ:

$$G_\sigma(x) = \frac{1}{\sqrt{\sigma}} \exp^{-\frac{|x|^2}{4\sigma}}, \quad x \in \mathbb{R}^2 \tag{2.30}$$

with σ is a positive constant.

This means that each of the level set ϕ evolves according to:

$$\frac{\partial C}{\partial t} = g(|\nabla I(C)|)(c + \kappa)N \tag{2.31}$$

This model is expressed with a constant deformation (c) and a curvature deformation (κ). The curvature deformation accounts for the geometric smoothing properties, while the constant deformation has the same role as the pressure force in [50]. The curve evolution is coupled with the image data through the edge detection function in order to stop the curve towards the boundary of the target object. Depending in the sign of c, this constant deformation pushes the curve inwards or outward.

As we have just mentioned, the geometric active contour offers the important advantage which is the automatic change of the topology of objects, compared with the classic active contour proposed by Kass *et al.* [25]. However, there are two following major inconveniences of this method:

1. The constant c is fixed in advance and chosen such that $c+\kappa$ remains always positive, meanwhile the value of κ varies with the evolution of the contour. Therefore, we have to estimate the variation of κ in the evolution of the contour to select c.

2. Theoretically, the evolution of a curve governed by Equation (2.31) will stop when g is equal to zero which corresponds to an ideal contour. However, in practice, the discrete value of the gradient is bounded and generally, g is not exactly equal to zero. This is why this model may leak out (passes through the boundary) when the object boundary is weak or has gaps especially for medical images, because g cannot completely stop the curve.

In order to overcome these problems, Caselles, Kimmel and Sapiro have proposed the geodesic active contour [30, 31].

2.1.2.4 Geodesic active contour

Unlike the Geometric Active Contour model, the Geodesic Active Contour [30] is derived from an energy minimization formulation to design the speed function in the curve evolution. In [30], Caselles, Kimmel and Sapiro considered a particular case of the classic snake model (2.1)-(2.3) in [25] by selecting $\beta = 0$. They obtain the following energy function E_1:

$$E_1(C) = \alpha \int_0^1 |C'(p)|^2 dp + \lambda \int_0^1 g(|\nabla I(C(p))|) dp \tag{2.32}$$

The authors also proved that the minimization of $E_1(C)$ is equivalent with the following intrinsic energy function which is not dependent on a new curve parameterization:

$$E_{GAC}(C) = \int_0^1 g(|\nabla I(C(p))|)|C'(p)| dp = \int_0^{L(C)} g(s) ds \tag{2.33}$$

where s is the arc-length parameterization of the curve, $L(C)$ is the Euclidean length of the curve C with $L(C) = \int_0^1 |C'(p)| dp = \int_0^{L(C)} ds$. The evolving curve is a new length obtained by weighting the Euclidean element of length by the edge detection function g. The authors proved that the curve minimizing E_{GAC} is actually a geodesic or a minimal distance in a Riemannian space whose metric is defined by the image content: The boundary detection is equivalent to finding a curve of minimal weighted length. The weighting function is the edge detection function g which was proposed in the geometric active contour (2.29) [29]. This is the reason why this model is called Geodesic Active Contour and some time referred to as Geometric/Geodesic AC.

By the calculus of variations, the evolution equation of C is derived as follows:

$$\frac{\partial C}{\partial t} = \Big[g\big(|\nabla I(C)|\big)\kappa - \nabla g\big(|\nabla I(C)|\big) \cdot N \Big] N \tag{2.34}$$

where κ is the curvature of C.

By using the level set function ϕ, and taking $\frac{\partial C}{\partial t}$ from Equation (2.34) into Equation (2.18) with the inward unit normal $N = -\frac{\nabla \phi}{|\nabla \phi|}$, we obtain the following evolution equation:

$$\frac{\partial \phi}{\partial t} = g(|\nabla I|)|\nabla \phi|\kappa + \nabla g \cdot \nabla \phi \tag{2.35}$$

In [30], to detect non-convex objects and to increase the attraction of the deforming contour towards the boundary, the authors have added a constant c whose effect is as the balloon force introduced by Cohen [50] and Caselles *et al.* [29] to obtain the following evolution equation:

$$\frac{\partial \phi}{\partial t} = g(|\nabla I|)|\nabla \phi|(c + \kappa) + \nabla g \cdot \nabla \phi \tag{2.36}$$

The new force, $\nabla g \cdot \nabla \phi$ increases the attraction of the deforming contour towards the boundary, more precisely toward the "valley" of the g function and especially when gradient values of this boundary vary highly. Therefore, this model is robust to small gaps and can detect boundary with high differences of its gradient information.

2.1.2.5 Conclusion

We have presented two main implicit boundary-based active contours which are the geometric and geodesic active contours. The methods in this category utilize the local information of edge and the gradient of image to evolve the initial contour towards object boundary. Thereby, they fail to segment image with noise or weak boundary such as discontinuous or smooth edges. Furthermore, like the Snake, these models are sensitive to local minimum and the results depend on the initial contour. In order to alleviate these shortcomings, region information characteristics inside and outside the contour are exploited to make the boundary-based AC models less sensitive to noise and to varying initialization. This leads to region-based active contour models that will be described in the next subsection.

2.2 Region-based Active Contour Models and the Intensity In-homogeneity (IIH)

An effective alternative to boundary-based active contours is the region-based active contours, which uses statistical region information of the image (such as mean and variance) to evolve the contour towards the boundary of the target object. Compared with the boundary-based models, the region-based models provide better performance for their ability to segment object having weak or blur boundary and for their robustness to the initial position of the contour. Generally, the region-based AC models often combine both region-based terms and contour-based terms, mainly to model the characteristics of regions and impose regularization constraints on the contour (contour-based term). More generally, in region-based model, the problem is to determine the energy functional/criterion to be minimized. This functional describes the statistical properties of the regions. Beside, it has been proven the equivalence between the Mumford-Shah functional and the Bayesian maximum *a posteriori* (MAP) estimation [43, 68]. Here the advantage of the MAP model is that it allows a more general variational approach, and the segmentation is formulated as an optimization problem with respect to the *a posteriori* segmentation probability where the region properties need to be described by the probability density functions or statistical models, and the regularity constraints (or prior) favour a short length of the boundary.

The very popular region-based model, namely the Chan-Vese model, and many of its variants, which are based on the assumption that an image is composed of statistically homogeneous regions [33, 34, 35, 41, 47], were very successful. However, these models fail to

detect image with intensity in-homogeneity. Recall that intensity in-homogeneity behaves as gradual and local change of intensity within the object to detect. In this case, one can assume that the image consists of regions of approximately piecewise-smooth intensities. The MAP formulation has established that local statistics may account for the piecewise-smooth approximation of intensity within a region in the Mumford-Shad model [43]. So, we propose to tackle IIH issue by incorporating local information in a region-based model, inspired from two approaches: the Chan-Vese model [33] (for its simplicity and efficiency), and the Bayesian formulation to benefit fully from the statistical Gaussian distribution to get more accuracy of segmentation.

In this section, we will first present a review of the basic region-based models and then, describe some state-of-the-art region-based models proposed for dealing with the intensity in-homogeneity.

2.2.1 Basic region-based active contour models

In this section, we present two main approaches of the region-based active contours that inspired our proposed models in this thesis: the Mumford-Shah model and the Bayesian model.

The early work of D. Mumford and J. Shah made in 1985 has opened a branch, more geometric, in the field of segmentation based on regions [32]. This method is considered as the first model of the region-based active contours. However, this model is difficult to minimize in practice and has limited the application of this method. Much later, in 2001, Chan and Vese proposed the active contour without edge [33], also referred to as Chan-Vese model, based on the work of Mumford and Shah and by assuming that the regions in an image are homogeneous. This is a level set based segmentation that takes the region information into account. The success of this model is also due to the level set which simplifies representation and implementation. Since that, this model has inspired many other region-based models.

Also, the first Bayesian region-based model, namely "region competition" is introduced by Zhu *et al.* [68] in 1996. This model combines the statistical techniques of region growing and the snake/balloon model as regularization constraint and obtain the solution by minimizing a Bayes and the Minimum Description Length (MDL) criteria using the variational approach. In particular, the authors consider the pixels of the image as a realization of a random variable with Gaussian probability density. Based on the works of [70], Paragios introduce (in a purely Bayesian) geodesic active regions that unify boundary and region statistical information to find the best minimal length geodesic curve and at the same time create regions which maximize the *a posteriori* frame partition probability. This model was proposed for supervised segmentation of scalar images, and tracking of moving objects in video sequences [70, 71]. Then, Rousson and Derich [72, 73] extended the works of Paragios

to segmentation of color and textured areas that do not meet the Gaussian distribution.

Let us give more details on the two approaches in the following subsections.

2.2.1.1 The Mumford-Shah model

The goal of the Mumford-Shah (MS) approach is to find a partition of the image into distinct homogeneous regions, separated by smooth boundaries [74, 32]. This is performed by minimizing the following MS function:

$$E_{MS}(f, C) = \int_{\Omega} (f(x) - I(x))^2 dx + \lambda \int_{\Omega \backslash C} |\nabla f(x)|^2 dx + \mu \mathcal{H}^{N-1}(C) \tag{2.37}$$

where λ and μ are positive constants, I is an image defined on a domain Ω, $x \in \Omega$ is a pixel, f corresponds to a piecewise smooth approximation of the original image I, $N = 2$ or 3, C represents a curve in Ω and the length of C is given by the $(N-1)$-dimensional Hausdorff measure $\mathcal{H}^{N-1}(C)$. The first term in Equation (2.37) is a fidelity term between the given image I and the the approximative image f. The second term is a regularization term that constraints the appoximative image f not to vary much inside the regions $\Omega \backslash C$. The last term is another regularization constraints (length for $N = 2$) on the contour C.

The idea of MS approach is very interesting, but the implement is very difficult because of the properties of the energy function E_{MS}. First, the unknown C leads to the complexity when discretizing it. Second, C is a $(N-1)$-dimensional set while f is a function defined on a N-dimension space. Third, the component $\mathcal{H}^{N-1}(C)$ is not lower semi-continuous which does not allow for the calculus of variations of Equation (2.37) to obtain the Euler-Lagrange equation. Therefore, it is necessary to find a topology that ensures at the same time lower semi-continuous of E_{MS} and compactness of the minimizing sequences. To overcome this problem, an idea is to approximate the MS function E_{MS} by a sequence of regular function E_ϵ, with $\epsilon > 0$. The convergence of E_ϵ to the initial MS function E_{MS} as $\epsilon \to 0$ is understood in the Γ-convergence framework [75, 76]. These methods allow for proving the existence of a solution of the MS function, but it is very complex to find the solutions when discretizing. Finally, Chan and Vese [33] proposed to approximate the term $\mathcal{H}^{N-1}$ by using the level set method [53] in order to use directly the Euler-Lagrange equation. This will provide the model of "Active Contour Without Edges" [33].

In [33], based on the MS function E_{MS} and by assuming that the given image I includes two homogeneous regions, Chan and Vese proposed the following energy function:

$$E_2(c_1, c_2, C) = \int_{\Omega_{in}} (I(x) - c_1)^2 dx + \int_{\Omega_{out}} (I(x) - c_2)^2 dx + \mu |C| \tag{2.38}$$

where Ω_{in} and Ω_{out} are the regions inside and outside the contour C, respectively, c_1 and c_2 are two constants to approximate the intensities in Ω_{in} and Ω_{out}, respectively, μ is a positive constant, $|C|$ is the length of C.

Now, by using the level set function ϕ, we have:

$$\begin{aligned} C &= \{x \in \Omega : \phi(x) = 0\} \\ \Omega_{in} &= \{x \in \Omega : \phi(x) > 0\} \\ \Omega_{out} &= \{x \in \Omega : \phi(x) < 0\} \end{aligned}$$

Then, to represent the regions Ω_{in} and Ω_{out}, the Heaviside function H is used:

$$H(z) = \begin{cases} 1 & \text{if } z \geq 0 \\ 0 & \text{if } z < 0 \end{cases} \tag{2.39}$$

It follows that Ω_{in} is determined by the pixels x such that $H(\phi(x)) = 1$ and Ω_{out} is determined by the pixels x such that $H(\phi(x)) = 0$. Then, the energy functional (2.38) can be reformulated in terms of the level set function ϕ as follows:

$$\begin{aligned} E_{CV}(c_1, c_2, \phi) = &\int_{\Omega} (I(x) - c_1)^2 H(\phi(x)) dx \\ &+ \int_{\Omega} (I(x) - c_2)^2 (1 - H(\phi(x))) dx + \mu \int_{\Omega} |\nabla H(\phi(x))| dx \end{aligned} \tag{2.40}$$

To apply the calculus of variations method [63, 64], Heaviside function H is replaced by a smooth function H_ϵ as follows:

$$H_\epsilon(z) = \frac{1}{2}\left[1 + \frac{2}{\pi} \arctan\left(\frac{z}{\epsilon}\right)\right], \quad z \in \mathbb{R} \tag{2.41}$$

where $\epsilon > 0$ is small. Then, by calculus of variations, minimizing the energy functional E_{CV} with respect to c_1 and c_2, for fixed ϕ gives c_1 and c_2 as follows:

$$c_1 = \frac{\int_\Omega I(x) H_\epsilon(\phi(x)) dx}{\int_\Omega H_\epsilon(\phi(x)) dx} \tag{2.42}$$

$$c_2 = \frac{\int_\Omega I(x)(1 - H_\epsilon(\phi(x))) dx}{\int_\Omega (1 - H_\epsilon(\phi(x))) dx} \tag{2.43}$$

For fixed c_1 and c_2, minimizing E_{CV} with respect to ϕ gives the Euler-Lagrange equation. Then, by using artificial time t as parameter for the descent direction, $\phi = \phi(x, t)$ is a solution of the following equation:

$$\frac{\partial \phi}{\partial t} = \delta_\epsilon(\phi)\left[\mu \nabla \cdot \left(\frac{\nabla \phi}{|\nabla \phi|}\right) - (I - c_1)^2 + (I - c_2)^2\right] \tag{2.44}$$

where $\delta_\epsilon = H'_\epsilon$ and $\nabla \cdot$ is the divergence operator.

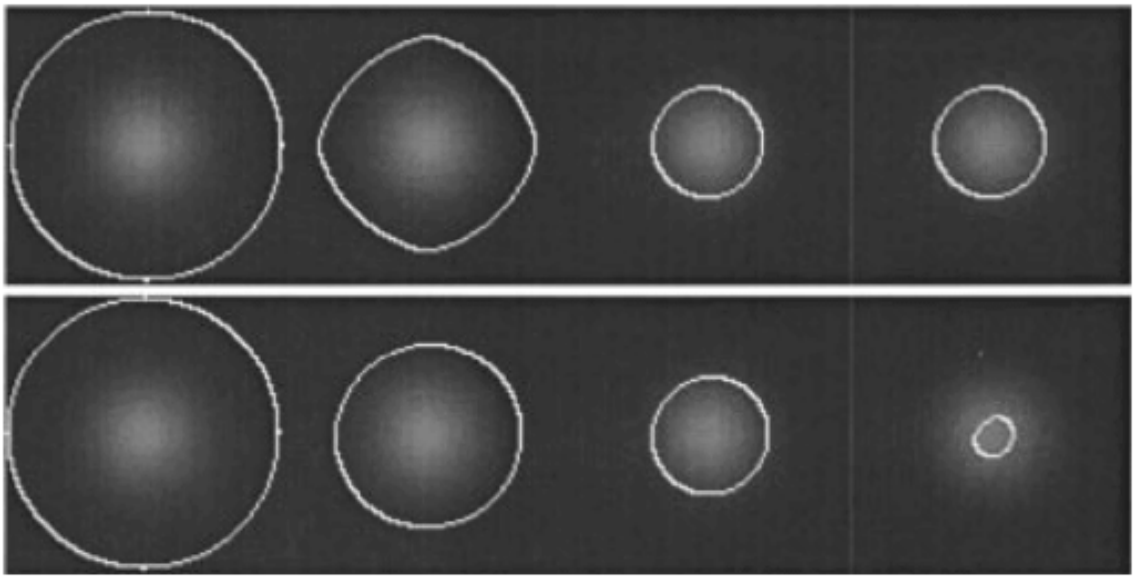

Figure 2.5. Object with smooth contour. Top: results using Chan-Vese model [33]. Bottom: results using the geometric active contour model [29].

Compared with the boundary-based active contour models, the Chan-Vese model can segment the object with smooth boundaries. Figure 2.5 shows a comparison between results of the Chan-Vese model and the geometric active contour model on an image with a smooth boundary of object. It is clear that the Chan-Vese model can extract the object boundary, which is not the case of the geometric active contour model. Another advantage of Chan-Vese model is its ability to extract objects with discontinuous boundaries and weak gradient as shown in Figure 2.6.

From Equations (2.42) and (2.43), we can see that c_1 and c_2 are the average intensities related to the global properties of the image contents inside and outside the contour, respectively. So, c_1 and c_2 represent the global information. In other words, they model the region information globally. However, these average intensities can be quite different from the original data if the intensities in either Ω_{in} or Ω_{out} are not homogeneous. Therefore, the Chan-Vese model fails to segment images with intensity in-homogeneity (see Figure 2.8 as an example). Note that, as mentioned in Section 2.1.2, the obtained solution from Equation (2.44) is re-initialized to the signed distance function to its zero-level curve. This prevents the level set function to become too flat. However, this procedure slows down the speed to obtain the solution. Another inconvenience of this model is due to the fact that the energy function is not convex. Then, it may have local minimum which could result in another segmentation than the expected result. So, for this model, the quality of the segmentation depends on the initial contour.

To overcome the dependence on the initial contour, Chan *et al.* proposed a convex

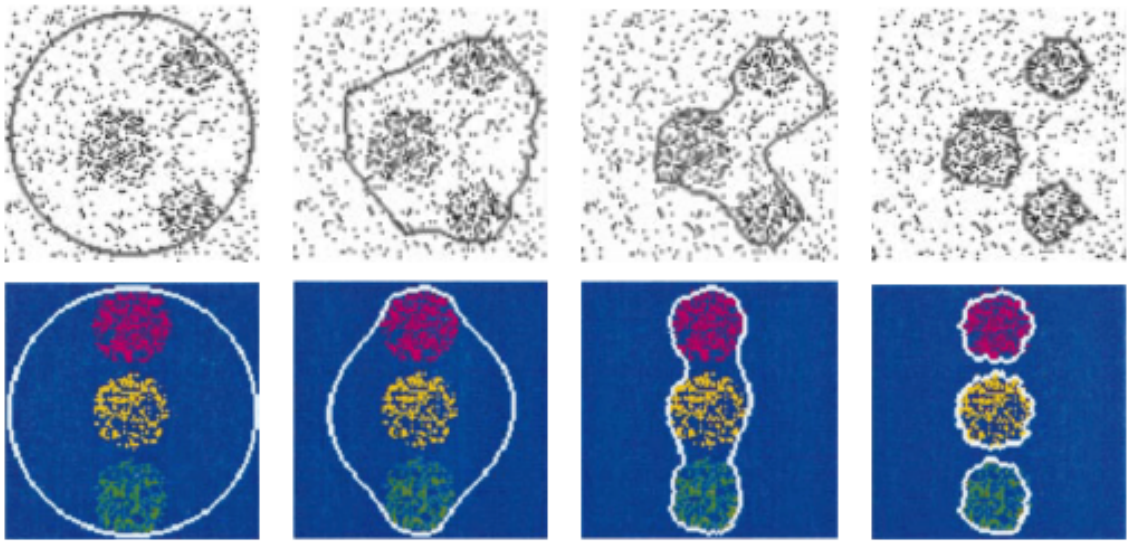

Figure 2.6. Examples for discontinuous boundaries and weak gradient: the evolution of the contour and segmentation by the Chan-Vese model [33].

model (convex Chan-Vese model) in [35] to find the global solution of the Chan-Vese model. However, this model is based also on the similar assumption as the Chan-Vese model. So, it is unable to segment images affected with intensity in-homogeneity. This method will be described in Chapter 4.

To segment more than two regions, Vese and Chan proposed a model using multiphase level set functions in [34], called piecewise-constant model. Using for example three level set function ϕ_1, ϕ_2 and ϕ_3, this model can segment 8 ($= 2^3$) regions as illustrated in Figure 2.7. Moreover, in this paper, Vese and Chan also proposed the piecewise-smooth model in order to tackle the problem of intensity in-homogeneity. This model is similar with the model proposed by Tsai *et al.* proposed in [69]. However, these models are very complex and computational expensive, limiting hence their applications. In addition, to reduce the computational cost, these methods usually require that the initial contour should be near the object boundaries.

2.2.1.2 The Bayesian approach

Let us first recall the formulation of the maximum *a posteriori* (MAP) expressed in [70, 71, 73] and its links with previous works which are also based on a Bayesian approach for image segmentation.

Let $\mathcal{A}(\Omega)$ be a partition of a given image I and $p(\mathcal{A}(\Omega)|I)$ denote the *a posteriori* segmentation probability function with respect to $\mathcal{A}(\Omega)$ given the image I. An optimal partition $\mathcal{A}(\Omega)$ is obtained if the probability $p(\mathcal{A}(\Omega)|I)$ is maximized. According to the

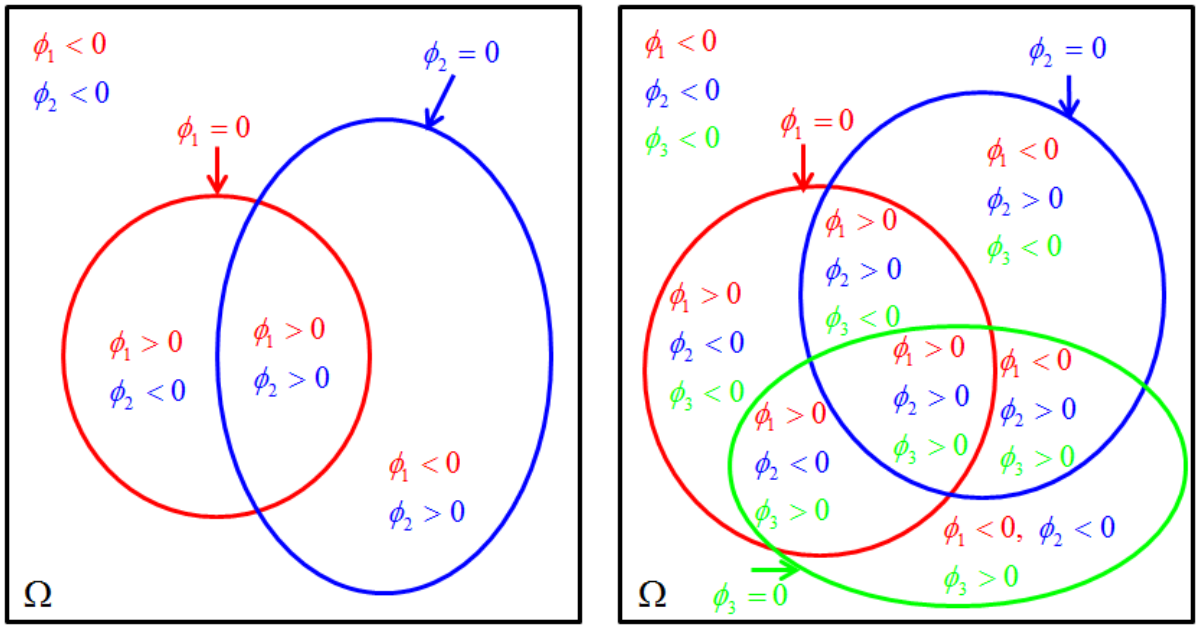

Figure 2.7. Correspondence of the level set functions and regions: (a) representation of four ($= 2^2$) regions with two level set functions, (b) representation of eight ($= 2^3$) regions with three level set functions.

Bayes' rule, we have the following formula:

$$p(\mathcal{A}(\Omega)|I) = \frac{p(I|\mathcal{A}(\Omega))}{p(I)} p(\mathcal{A}(\Omega)) \tag{2.45}$$

where $p(I)$ is the probability of the image I. $p(\mathcal{A}(\Omega))$ is the probability of the partition $\mathcal{A}(\Omega)$ of the image among all possible partitions. $p(I|\mathcal{A}(\Omega))$ is the *a posteriori* segmentation probability for the image I, given the partition $\mathcal{A}(\Omega)$. Note that, $p(I)$ is independent from $\mathcal{A}(\Omega)$. Thus, this value is considered as a constant and could be neglected. On the other hand, because of the independence between partitions, the value of $p(\mathcal{A}(\Omega))$ can be chosen as $\frac{1}{Z}$, where Z is the number of possible partitions. Therefore, Equation (2.45) becomes:

$$p(\mathcal{A}(\Omega)|I) \sim p(I|\mathcal{A}(\Omega)) \tag{2.46}$$

The calculus of $p(I|\mathcal{A}(\Omega))$ requires some assumptions as follows:

1. The regions of the optimal partition are not correlated. This assumption is reasonable by the goal of image segmentation. Then, we have:

$$p(I|\mathcal{A}(\Omega)) = p(I|(\Omega_{in}, \Omega_{out})) = p(I|\Omega_{in}) p(I|\Omega_{out}) \tag{2.47}$$

where $p(I|\Omega_{in})$ and $p(I|\Omega_{out})$ are the *a posteriori* probabilities for the image I given by the regions Ω_{in} and Ω_{out}, respectively.

2. The second assumption is that the pixels in a region must be independent. This assumption leads to:

$$p(I|\Omega_{in}) = \prod_{x \in \Omega_{in}} p(I(x)|\Omega_{in}) \tag{2.48}$$

$$p(I|\Omega_{out}) = \prod_{x \in \Omega_{out}} p(I(x)|\Omega_{out}) \tag{2.49}$$

where $p(I(x)|\Omega_{in})$ and $p(I(x)|\Omega_{out})$ are the probabilities of an intensity $I(x)$ in the regions Ω_{in} and Ω_{out}, respectively.

Taking a logarithm, the maximization can be converted to the minimization of the following energy:

$$E(\Omega_{in}, \Omega_{out}) = -\ln\big(p(\mathcal{A}(\Omega)|I)\big) \tag{2.50}$$

Replacing the expressions of Equations (2.46)-(2.49) into Equation (2.50), we obtain:

$$E(\Omega_{in}, \Omega_{out}) = -\int_{\Omega_{in}} \ln p(I(x)|\Omega_{in})dx - \int_{\Omega_{out}} \ln p(I(x)|\Omega_{out})dx \tag{2.51}$$

By introducing the length term $|C|$ of the contour C to regularize it, we obtain the following final energy function:

$$E(\Omega_{in}, \Omega_{out}, C) = -\int_{\Omega_{in}} \ln p(I(x)|\Omega_{in})dx - \int_{\Omega_{out}} \ln p(I(x)|\Omega_{out})dx + \mu|C| \tag{2.52}$$

where μ is a positive constant.

In [70, 71, 73, 68], the authors chose $p(I(x)|x \in \Omega_i)$, where $i = in, out$, to be a Gaussian distribution and permit for each region Ω_{in} and Ω_{out} not only different means c_1 and c_2, respectively, but also different standard deviation σ_1 and σ_2, respectively:

$$p(I(x)|\Omega_{in}) = \frac{1}{\sqrt{2\pi}\sigma_1} \exp^{-\frac{(I(x)-c_1)^2}{2\sigma_1^2}} \tag{2.53}$$

$$p(I(x)|\Omega_{out}) = \frac{1}{\sqrt{2\pi}\sigma_2} \exp^{-\frac{(I(x)-c_2)^2}{2\sigma_2^2}} \tag{2.54}$$

Note that, the minimization of Equation (2.51) is similar with the model proposed by Zhu *et al.* in [68]. However, the expression of the energy function is not obtained from

MAP but the technique MDL (Minimum Description Length). Hereafter, Equation (2.52) will be reformulated by the level set function ϕ as the following energy function:

$$\begin{aligned} E(c_1, c_2, \phi) =& \mu \int_\Omega |\nabla H_\epsilon(\phi(x))dx \\ & - \int_\Omega \ln\left(\frac{1}{\sqrt{2\pi}\sigma_1}\exp^{-\frac{(I(x)-c_1)^2}{2\sigma_1^2}}\right) H_\epsilon(\phi(x))dx \\ & - \int_\Omega \ln\left(\frac{1}{\sqrt{2\pi}\sigma_2}\exp^{-\frac{(I(x)-c_2)^2}{2\sigma_2^2}}\right)(1 - H_\epsilon(\phi(x)))dx \end{aligned} \tag{2.55}$$

where H_ϵ is a regularized version of the Heaviside function as mentioned in the description of the Chan-Vese model. Note that the Chan-Vese model corresponds to fixed standard deviation.

The variables c_1, c_2, σ_1 and σ_2 are calculated dynamically during the evolution of the contour. For fixed ϕ, the formulas of these parameters are obtained by calculus of variations as follows:

$$c_1 = \frac{\int_\Omega I(x)H(\phi(x))dx}{\int_\Omega H(\phi(x))dx} \tag{2.56}$$

$$c_2 = \frac{\int_\Omega I(x)(1 - H(\phi(x)))dx}{\int_\Omega (1 - H(\phi(x)))dx} \tag{2.57}$$

$$\sigma_1^2 = \frac{\int_\Omega (I(x) - c_1)^2 H(\phi(x))dx}{\int_\Omega H(\phi(x))dx} \tag{2.58}$$

$$\sigma_2^2 = \frac{\int_\Omega (I(x) - c_2)^2 (1 - H(\phi(x)))dx}{\int_\Omega (1 - H(\phi(x)))dx} \tag{2.59}$$

Meanwhile, if these variables are fixed, $\phi = \phi(x, t)$ is a solution of the following evolution equation:

$$\frac{\partial \phi}{\partial t} = \delta_\epsilon(\phi)\left[\nabla \cdot \left(\frac{\nabla \phi}{|\nabla \phi|}\right) - \frac{(I(x) - c_1)^2}{2\sigma_1^2} + \frac{(I(x) - c_2)^2}{2\sigma_2^2} + \ln\left(\frac{\sigma_1}{\sigma_2}\right)\right] \tag{2.60}$$

Note that, minimizing Equation (2.52) by using level set function requires the re-initialization procedure as in the Chan-Vese model.

By observing Equations (2.56)-(2.59), we can see that the variables c_1, c_2, σ_1 and σ_2 have the global property as the Chan-Vese model. Thus, this model fails to segment images with intensity in-homogeneity which behaves as local change of intensity in the object. A natural idea is to incorporate the local information in the energy function. Then, these variables are computed in a neighborhood to account for local region inside or outside the object.

2.2.2 Region-based active contour models and the intensity in-homogeneity

The main idea to deal with intensity in-homogeneity is to take into account the local information in the energy function such as models proposed later by Li *et al.* [77], Zhang *et al.* [78], Guo *et al.* [82] and Wang *et al.* [83].

In [77], Li *et al.* proposed the Local Binary Fitting (LBF) model to deal with intensity in-homogeneity in segmentation by taking into account local intensity information. This model adapted the Chan-Vese model for taking into account local intensity information instead of global intensity information. More precisely, instead of using the constants c_1 and c_2 in the Chan-Vese model, two varying functions $f_1(x)$ and $f_2(x)$, with $x \in \Omega$ is an image pixel, are used in the LBF model to locally approximate the image intensities inside and outside the contour in a Gaussian neighborhood. The energy function to minimize the LBF model is formulated as follows:

$$\begin{aligned} F^{LBF}(f_1, f_2, C) = \mu|C| + \lambda_1 \int_{\Omega} \left[\int_{\Omega_{in}} K_\sigma(x-y)(I(y) - f_1(x))^2 dy \right] dx \\ + \lambda_2 \int_{\Omega} \left[\int_{\Omega_{out}} K_\sigma(x-y)(I(y) - f_2(x))^2 dy \right] dx \end{aligned} \tag{2.61}$$

where λ_1 and λ_2 are two positive constants, K_σ is a Gaussian kernel with standard deviation σ. This kernel is used to account for local region. Indeed, the Gaussian kernel $K_\sigma(x-y)$ decreases drastically and approaches to zero as the point y goes away from the center point x. Therefore, the local energy at the pixel x:

$$\lambda_1 \int_{\Omega_{in}} K_\sigma(x-y)(I(y) - f_1(x))^2 dy + \lambda_2 \int_{\Omega_{out}} K_\sigma(x-y)(I(y) - f_2(x))^2 dy \tag{2.62}$$

is dominated by the intensities $I(y)$ of the points y in a neighborhood of x. This localization property plays a key role in segmenting the images with intensity in-homogeneity. For example, Figure 2.8a is an image affected by intensity in-homogeneity. One may see that the intensity of both background and foreground varies. In Figure 2.8b, final contour of the Chan-Vese model does not stop at the object boundary. In the other hand, the result of the LBF model in Figure 2.8c gives us the accurate final contour on the object boundary.

As the Chan-Vese model, the authors used the level set function ϕ and the regularized version H_ϵ of the Heaviside function H to reformulate Equation (2.61). Moreover, to eliminate the re-initialization procedure, which is the basic procedure when working with level set function to reshape the level set function as a signed distance function, the authors added the distance regularizing term published in [65] to penalize the deviation of the level set function ϕ from a signed distance function. The deviation of the level set function ϕ

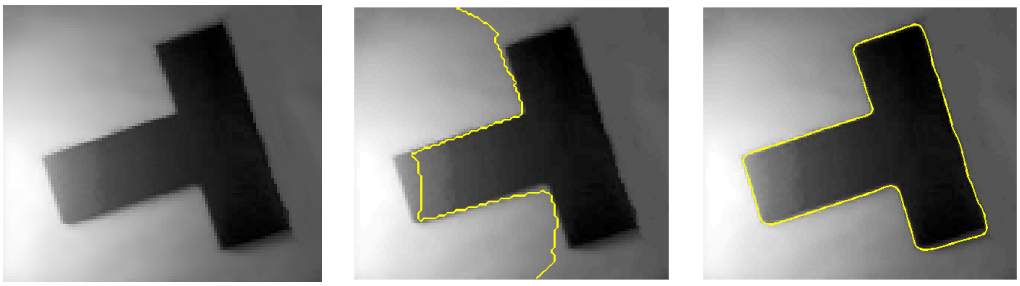

(a) **(b)** **(c)**

Figure 2.8. Result of the Chan-Vese and the LBF models on an image with intensity in-homogeneity. (a) Original contour. (b) Final contour of the Chan-Vese model. (c) Final contour of the LBF model.

from a signed distance function is characterized by the following integral as mentioned in Section 2.1.2:

$$\mathcal{P}(\phi) = \int_{\Omega} \frac{1}{2}(|\nabla\phi(x)| - 1)^2 dx \tag{2.63}$$

Then, the energy function of the LBF model is reformulated as follows:

$$\begin{aligned} F^{LBF}(f_1, f_2, \phi) =& \mu\mathcal{L}(\phi) + \nu\mathcal{P}(\phi) \\ &+ \lambda_1 \int_{\Omega} \left[\int_{\Omega} K_\sigma(x-y)(I(y) - f_1(x))^2 H_\epsilon(\phi(y)) dy \right] dx \\ &+ \lambda_2 \int_{\Omega} \left[\int_{\Omega} K_\sigma(x-y)(I(y) - f_2(x))^2 (1 - H_\epsilon(\phi(y))) dy \right] dx \end{aligned} \tag{2.64}$$

where $\mathcal{L}(\phi) = \int_\Omega |\nabla H_\epsilon(\phi(x))| dx$ is the length of the contour C.

Here we can see that each region is modeled by the mean estimated in a local Gaussian neighborhood.

The calculus of variations for F^{LBF} with respect to f_1, to f_2 for fixed ϕ allows to find the formulas of f_1, f_2 as follows:

$$f_1(x) = \frac{\int_\Omega K_\sigma(x-y) I(y) H_\epsilon(\phi(y)) dy}{\int_\Omega K_\sigma(x-y) H_\epsilon(\phi(y)) dy} \tag{2.65}$$

$$f_2(x) = \frac{\int_\Omega K_\sigma(x-y) I(y) (1 - H_\epsilon(\phi(y))) dy}{\int_\Omega K_\sigma(x-y) (1 - H_\epsilon(\phi(y))) dy} \tag{2.66}$$

and $\phi = \phi(y,t)$ is a solution of the following evolution equation when fixing f_1 and f_2:

$$\begin{aligned}\frac{\partial \phi}{\partial t} = \delta_\epsilon(\phi)\Bigg[\mu\nabla\cdot\left(\frac{\nabla\phi}{|\nabla\phi|}\right) + \nu\nabla\cdot\left(\nabla\phi\left(1-\frac{1}{|\nabla\phi|}\right)\right) \\ - \lambda_1\int_\Omega K_\sigma(x-y)(I(y)-f_1(x))^2dx \\ + \lambda_2\int_\Omega K_\sigma(x-y)(I(y)-f_2(x))^2dx\Bigg]\end{aligned} \tag{2.67}$$

where δ_ϵ is defined in Equation (2.44).

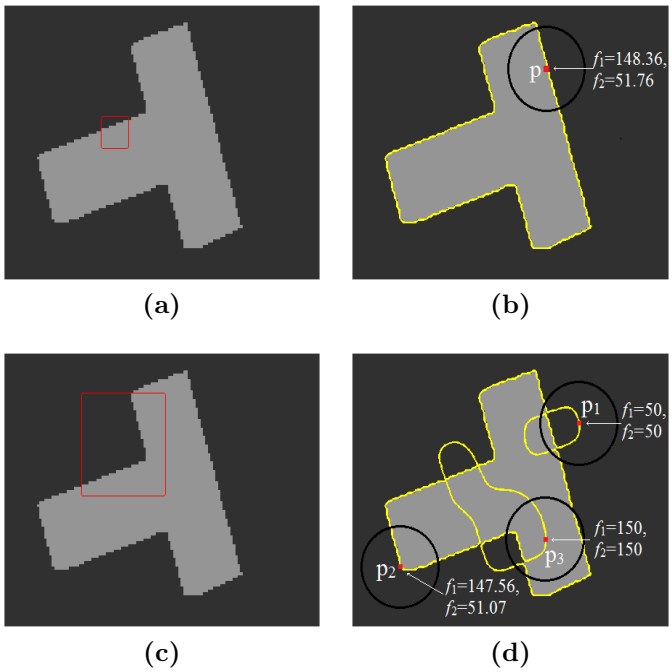

Figure 2.9. Result of the LBF model [77]. (a) (c) Original image and initial contour (red). (b) (d) Final contour (yellow) and values of f_1, f_2 for some points.

By using the local information, this model has achieved promising results for images with intensity in-homogeneity. However, because of the non-convexity property of the energy functional, its minimization may introduce local minimums. These local minimums are dependent on the initial position of the contour. Consequently, the result of segmentation is sensitive to the initial contour. The dependence on the initialization of the LBF model is shown in Figure 2.9. This figure gives us a simple experiment of the LBF model for a binary image with two initial contours Figure 2.9a and Figure 2.9c. The intensities of the background and foreground are 50 and 150, respectively. Figure 2.9b and Figure 2.9d

show the final segmentation results of the LBF model corresponding with the two different initial contours in Figure 2.9a and Figure 2.9c, respectively. One may observe that the contour in Figure 2.9b is accurate. In this case, the spatially varying fitting functions f_1 and f_2 approximate the local intensities on the two sides of the contour very well. For example, the values of f_1 and f_2 at the red point in this figure are 148.36 and 51.76 respectively, which are consistent with the local intensities. In contrast, the contour in Figure 2.9d is stuck in the middle of both background and foreground regions. This can be explained by investigating the values of f_1 and f_2 at some points. For example, the values of f_1 and f_2 at three points p_1, p_2 and p_3 are shown in Figure 2.9d. For points p_1 and p_3, the values are equal to the intensities of the background and foreground, respectively. Thus, the fitting energy F^{LBF} at the points p_1 and p_3 is minimized to zero, but the final contours in these case are incorrect. For the point p_2, the values of f_1 and f_2 approximate the local intensities on both sides of the contour very well. As a result, the local fitting energy F^{LBF} is minimized, and therefore the contour is stopped. But, the overall contour is not the accurate object boundary.

Latter, K. Zhang *et al.* [78] proposed the Local Image Fitting (LIF) model by minimizing the difference between a fitted image and the original image. The formulation is as follows:

$$F^{LIF}(\phi) = \frac{1}{2}\int_{\Omega} |I(x) - u^{LFI}(x)|^2 dx \tag{2.68}$$

where u^{LFI}, a local fitted image (LFI) formulation, is defined as follows:

$$u^{LFI} = m_1 H_\epsilon(\phi) + m_2(1 - H_\epsilon(\phi)) \tag{2.69}$$

where m_1 and m_2 are defined as follows:

$$\begin{cases} m_1 &= \text{avg}(u_0 \in (\{x \in \Omega | \phi(x) < 0\} \cap W_k(x))) \\ m_2 &= \text{avg}(u_0 \in (\{x \in \Omega | \phi(x) > 0\} \cap W_k(x))) \end{cases} \tag{2.70}$$

where $W_k(x)$ is a truncated Gaussian window $K_\sigma(x)$ with standard deviation σ and of size $(4k+1) \times (4k+1)$, where k is the greatest integer smaller than σ. This window allows for taking into account local information.

Using the calculus of variations and the steepest descent method [63, 64], the authors minimize F^{LIF} with respect to ϕ to get the corresponding gradient descent flow:

$$\frac{\partial \phi}{\partial t} = \delta_\epsilon(\phi)(I - u^{LFI})(m_1 - m_2) \tag{2.71}$$

where δ_ϵ is defined in Equation (2.44).

As the LBF model, the LIF model demonstrate promising performances for dealing with intensity in-homogeneity in images. However, the LIF has the same inconvenience as

the LBF model such as the non-convexity of its energy functional. Again, the results of the LIF model depend on the initial contour.

More recently, other models combine the local and global information in the region-based energy functional [79, 80, 81] to benefit from the advantages of the two approaches. The global information allows to cope with noises and objects with smooth or non-continuous boundaries, while the local information allows to deal with the intensity in-homogeneity. These methods give promising results.

In [79], the LGIF (Local and Global Intensity Fitting) model was recently proposed by Wang *et al.* to segment images with intensity in-homogeneity. To represent the global information, the authors make use of the constants c_1 and c_2 as in the Chan-Vese model [33], while two spatially varying fitting functions f_1 and f_2 are used to approximate the local intensities inside and outside the contour and to describe the local information. Note that this local information is inspired from the LBF model [77]. The energy functional to minimize is as follows:

$$F^{LGIF}(\phi, f_1, f_2, c_1, c_2) = (1-\omega)F^{LIF}(\phi, f_1, f_2) + \omega F^{G}(\phi, c_1, c_2) + F^{R} \tag{2.72}$$

with

$$\begin{aligned} F^{LIF} &= \alpha_1 \int_\Omega \left[\int_\Omega K_\sigma(x-y)|I(y)-f_1(x)|^2 H_\epsilon(\phi(y))dy \right] dx \\ &\quad + \alpha_2 \int_\Omega \left[\int_\Omega K_\sigma(x-y)|I(y)-f_2(x)|^2 (1-H(\phi(y)))dy \right] dx \end{aligned} \tag{2.73}$$

$$F^{G} = \alpha_1 \int_\Omega |I(x)-c_1|^2 H_\epsilon(\phi(x))dx + \alpha_2 \int_\Omega |I(x)-c_2|^2 (1-H_\epsilon(\phi(x)))dx \tag{2.74}$$

$$F^{R} = \nu \int_\Omega \frac{1}{2}(|\nabla\phi(x)|-1)^2 dx + \mu \int_\Omega |\nabla H_\epsilon(\phi(x))|dx \tag{2.75}$$

where ω is a positive constant ($0 < \omega < 1$) that controls the influence of the local and global terms. When the images are corrupted by intensity in-homogeneity, value of the parameter ω should be chosen small enough. In Equation (2.73), K_σ is a Gaussian kernel with standard deviation σ which is used to control the local property as in the LBF model. The parameters ν and μ in Equation (2.75) and α_1, α_2 in Equations (2.73) - (2.74) are positive constants. In Equation (2.75), the first term is a regular term added to describe the closeness of the level set function to a signed distance function. This term corresponds to the term $\mathcal{P}(\phi)$ in the LBF model, while the second term in (2.75) corresponds to the contour length which is the term $\mathcal{L}(\phi)$ in the LBF model. In Equations (2.73), (2.74) and (2.75), ϕ is the level set function, H_ϵ is a smooth version of the Heaviside function. The

authors use H_ϵ as in the Chan-Vese model:

$$H_\epsilon(z) = \frac{1}{2}\left[1 + \frac{2}{\pi}\arctan\left(\frac{z}{\epsilon}\right)\right], \quad z \in \mathbb{R} \tag{2.76}$$

where ϵ is a small positive constant.

Another model is the Local Chan-Vese (LCV) [80] which also combines global and local information to deal with intensity in-homogeneity. Like the LGIF model, the energy functional F^{LCV} of the LCV model has three terms, i.e., global term (F^G), local term (F^L) and regularization term (F^R) that are described as follows:

$$F^{LCV} = \alpha F^G + \beta F^L + F^R \tag{2.77}$$

where α, β are positive constants, and the regularization function F^R and the global term F^G are defined in (2.74) while the local term F^L is as follows:

$$\begin{aligned} F^L(\phi, d_1, d_2) = &\int_\Omega |g_k * I(x) - I(x) - d_1|^2 H_\epsilon(\phi(x))dx \\ &+ \int_\Omega |g_k * I(x) - I(x) - d_2|^2 (1 - H_\epsilon(\phi(x)))dx \end{aligned} \tag{2.78}$$

where g_k is an average convolution operator with a $k \times k$ size window, while d_1 and d_2 are the intensity averages of difference image $(g_k * I(x) - I(x))$ inside and outside the contour, respectively, ϕ is the level set function, and H_ϵ is determined as in (2.76).

Note that, by using the penalizing term $\mathcal{P}(\phi) = \int_\Omega \frac{1}{2}(|\nabla\phi(x)| - 1)^2 dx$ in the regularization term F^R, there is no need for the re-initialization procedure in both the LGIF and the LCV models. Experiments have demonstrated the desired performance for images affected by intensity in-homogeneity. In addition, the results of the LGIF and the LCV models also demonstrated that the dependence on the initial position of the contour is reduced compared with models using only the local information such as the LBF [77] and the LIF [78] models. However, this dependence is not reduced completely because the energy function is not convex. Therefore, there may be local minimums when segmenting the same image with varying initial contours.

In 2006, Guo *et al.* [82] used the local information to replace the global information in the model of Zhu [68] based on the Bayesian approach to obtain the following energy

functional

$$
\begin{aligned}
E(f_1,f_2,\sigma_1,\sigma_2,\phi) &= \mu \int_{\Omega} |\nabla H_\epsilon(\phi(x))dx \\
&- \int_{\Omega} \left[\int_{\Omega} \chi_{B(x,r(x))}(y) H_\epsilon(\phi(y)) \ln \left(\frac{1}{\sqrt{2\pi}\sigma_1(x)} \exp^{-\frac{(I(y)-f_1(x))^2}{2\sigma_1^2(x)}} \right) dy \right] H_\epsilon(\phi(x))dx \\
&- \int_{\Omega} \left[\int_{\Omega} \chi_{B(x,r(x))}(y)(1-H_\epsilon(\phi(y))) \ln \left(\frac{1}{\sqrt{2\pi}\sigma_2(x)} \exp^{-\frac{(I(y)-f_2(x))^2}{2\sigma_2^2(x)}} \right) dy \right] (1-H_\epsilon(\phi(x)))dx
\end{aligned}
\tag{2.79}
$$

where local region is represented by a circle $B(x, r(x))$ of center x and radius $r(x)$ which depends on x:

$$
r(x) = \frac{r_1}{1 + r_2|\nabla \tilde{I}(x)|} \tag{2.80}
$$

with $\tilde{I}$ is a smoothed version of the updating image I obtained through convolving it with a smooth kernel. r_1 is an integer chosen based on noisy level of the image I: r_1 is higher if the noisy level is high, and chosen smaller otherwise, r_2 is chosen to be small all the time to enhance boundaries while smoothing, $\chi_{B(x,r(x))}$ is the characteristic function of $B(x, r(x))$, H_ϵ is an regularized version of the Heaviside function, $f_1(x)$ and $f_2(x)$ are respectively the intensities inside and outside the contour, in the local region B, at the pixel x, $\sigma_1(x)$ and $\sigma_2(x)$ are the local standard deviations inside and outside the contour, respectively, at the pixel x.

However, to reduce the computational complexity, the author replaced the logarithm of the Gaussian kernel by a quadratic kernel such as $P(u) = \frac{3}{4}(1-u^2)\chi_{[-1,1]}(u)$, where $\chi_{[-1,1]}$ is the characteristic function of $[-1, 1]$. Note that, $I(y) - f_i(x)$, $i = 1, 2$, is assumed to be in the interval $[-1, 1]$. Thus, the following energy function is obtained:

$$
\begin{aligned}
E_{Guo}(f_1,f_2,\phi) &= \mu \int_{\Omega} |\nabla H_\epsilon(\phi(x))dx \\
&- \int_{\Omega} \left[\int_{\Omega} \chi_{B(x,r(x))}(y) H_\epsilon(\phi(y)) \frac{3}{4}\big(1 - (I(y) - f_1(x)\big)^2 dy \right] H_\epsilon(\phi(x))dx \\
&- \int_{\Omega} \left[\int_{\Omega} \chi_{B(x,r(x))}(y)(1-H_\epsilon(\phi(y))) \frac{3}{4}\big(1 - (I(y) - f_2(x)\big)^2 dy \right] (1-H_\epsilon(\phi(x)))dx
\end{aligned}
\tag{2.81}
$$

In 2009, Wang *et al.* [83] proposed the LGDF (Local Gaussian Distribution Fitting)

model which minimizes the following energy function:

$$
\begin{aligned}
E_{LGDF}(f_1, f_2, \sigma_1, \sigma_2, \phi) &= \mu\mathcal{L}(\phi) + \nu\mathcal{P}(\phi) \\
&- \int_\Omega \left[\int_\Omega K_\sigma(x-y) \ln \left(\frac{1}{\sqrt{2\pi}\sigma_1(x)} \exp^{-\frac{(I(y)-f_1(x))^2}{2\sigma_1^2(x)}} \right) H_\epsilon(\phi(y)) dy \right] dx \\
&- \int_\Omega \left[\int_\Omega K_\sigma(x-y) \ln \left(\frac{1}{\sqrt{2\pi}\sigma_2(x)} \exp^{-\frac{(I(y)-f_2(x))^2}{2\sigma_2^2(x)}} \right) (1 - H_\epsilon(\phi(y))) dy \right] dx \quad (2.82)
\end{aligned}
$$

where $\mathcal{L}, \mathcal{P}$ are defined in the energy function of the LBF model (2.64), while H_ϵ is a regularized version of the Heaviside function.

The penalized term $\mathcal{P}(\phi)$ allows the LGDF model to avoid the re-initialization procedure which is not the case of the Guo's model.

Generally, these models give good results when segmenting images with intensity in-homogeneity. However, like other models using level set function, the energy functional of these models is not convex. Thus, the quality of segmentation result depend on the position of the initial contour, which cannot provide reliable results. This is the main shortcoming of these models.

2.3 Conclusion

We have presented in this chapter a state-of-the-art of the AC models including the boundary-based models and the region-based ones with a review of those allowing for handle the intensity in-homogeneity. We also shown that the region-based models exhibit many advantages over the boundary-based ones, such as robustness to noises, to weak and smooth boundaries, to gaps as well as to varying initialization. We have also described some state-of-the-art region-based models following two groups, the Mumford-Shad model and the Bayesian one. Here we limit on works using Gaussian statistics to model a region globally or locally. While local region information allows to account for piecewise-smooth approximation as in the case of intensity in-homogeneity, the global intensity information allows for improving the robustness to noises weak boundary and gaps as well as varying initialization.

We have presented an overview of the region-based models capable of addressing the intensity in-homogeneity by using local intensity information. This study shows that the main weakness of the existing methods is the non-convexity of their energy functional, making these models dependent on the initial contour. Hence, the issue for these models is to find good initial contour. This problem can be overcome by convexification of the local information of the region-based models. This is the motivation for our works in this thesis.

CHAPTER 3

The Proposed Robust Local and Global Region-based Model (R_LGR)

Contents

3.1 Introduction

As it has been presented in Chapter 2, local information may be taken into account in the energy functional of a region-based AC model to deal with intensity in-homogeneity. The Local Binary Fitting (LBF) model proposed by Li *et al.* [77] is considered as the first model using the local image intensity to deal with IIH. Whereas the Chan-Vese model [33] describes the region using global intensity information, the LBF model extends the Chan-Vese model by incorporating local intensity information instead of the global intensity information to segment the images affected by intensity in-homogeneity. Like the Chan-Vese model [33], the active contour of the LBF model is characterized by zero level of the level set function. Another advantage of the LBF is related to the procedure changing the level set function to the signed distance function. Indeed, instead of the classical re-initialization procedure, the LBF model uses a penalty term in the energy functional, allowing automatic change of the level set function to the signed distance function in the evolution process.

Recently, Zhang *et al.* take into account the local information in a region-based AC model and propose the Local Image Fitting (LIF) model [78]. As the LBF model, Zhang *et al.* also utilize a Gaussian kernel window to calculate the local intensities for a fitting image to approximate the original image. However, the difference of the LIF model from the LBF model is that there is neither a regularization term in the LIF energy function or the penalty term to change the level set function to the signed distance function. However, to ensure that the contour is smooth and the level set function is changed to the signed distance function, the level set function in the LIF model is convoluted with a Gaussian kernel in the implementation.

For a better understanding of the contribution of the local and global information, the objective in this chapter aims at Intensity In-homogeneity without requiring that the model be convex, i.e. the independence of the model with respect to initialization, because this issue will be addressed in the Chapter 4.

So, in this chapter, a simple region-based active contour model is proposed in the variational framework in order to illustrate how combining global and local information in the energy functions can deal with IIH while providing robustness to noise, to weak edges and to initialization. This model is inspired from the Chan-Vese model [33] and the LIF model [78] but we use a constant window to compute local intensities. Hereafter, we will refer this model as ROBUST Local an Global Region-based (R_LGR).

In the next sections of this chapter, the R_LGR model will be presented firstly. Then, the numerical implementation will be presented for the minimization of the energy functional, followed by the investigation on the sensibility of model parameters as well as the experiments results to evaluate the performance of the proposed model.

3.2 The Proposed ROBUST Local and Global Region-based Model (R_LGR)

Let $\Omega \subset \mathbb{R}^2$ be an image domain and $I : \Omega \to \mathbb{R}+$ denote the image determined on Ω. Let us denote by C an active contours in Ω, and by ϕ a level set function whose values are positive (negative) inside (outside, respectively) C and vanish on C. Let us denote by $\Omega_{in} = \{x \in \Omega : \phi(x) > 0\}$ the domain inside the contour C and by $\Omega_{out} = \{x \in \Omega : \phi(x) < 0\}$ the domain outside the contour C.

We propose to associate the global and local components in the energy function to take advantages of the two terms. In the global component, a global fitting image I_G is presented to approximate the given image I, while a local fitting image I_L is introduced to approximate I in the local component. The energy function to minimize of the R_LGR model is as follows:

$$E(\phi) = \int_{\Omega} \big(I(x) - I_G(x,\phi)\big)^2 dx + \frac{\lambda}{2} \int_{\Omega} \big(I(x) - I_L(x,\phi)\big)^2 dx \tag{3.1}$$

where x is a pixel in Ω and λ is a positive constant.

For a better understanding of the model, let us illustrate first the global fitting image I_G in Section 3.2.1, then the local fitting image I_L in Section 3.2.2.

3.2.1 The global fitting image

The global fitting image I_G is determined as follows:

$$I_G(x,\phi) = c_1 H(\phi(x)) + c_2(1 - H(\phi(x))) \tag{3.2}$$

where H is the Heaviside function: $H(z)$ is 0 if $z < 0$ and is 1 else, c_1 and c_2 are two constants. Then, the best approximation of I is c_1 in Ω_{in} while the best approximation of I is c_2 in Ω_{out}.

As it can be seen in Figure 3.1, c_1 and c_2 are constants to approximate the image intensity in the brown (Ω_{in}) and white (Ω_{out}) regions, respectively.

3.2.2 The local fitting image

The local fitting image I_L is determined as follows:

$$I_L(x,\phi) = f_1(x) H(\phi(x)) + f_2(x)(1 - H(\phi(x))) \tag{3.3}$$

where $f_1(x)$ and $f_2(x)$ are two average intensities of I on a neighborhood V_x of the pixel x inside and outside the contour:

$$f_1(x) = \text{avg}(I) \text{ on } V_x \cap \{y \in \Omega : \phi(y) > 0\} \tag{3.4}$$

$$f_2(x) = \text{avg}(I) \text{ on } V_x \cap \{y \in \Omega : \phi(y) < 0\} \tag{3.5}$$

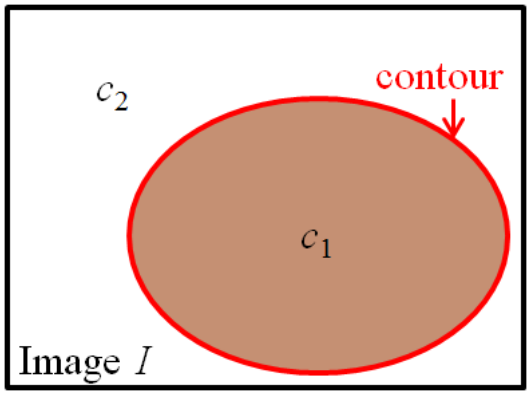

Figure 3.1. Illustration for c_1 and c_2 in our global fitting image.

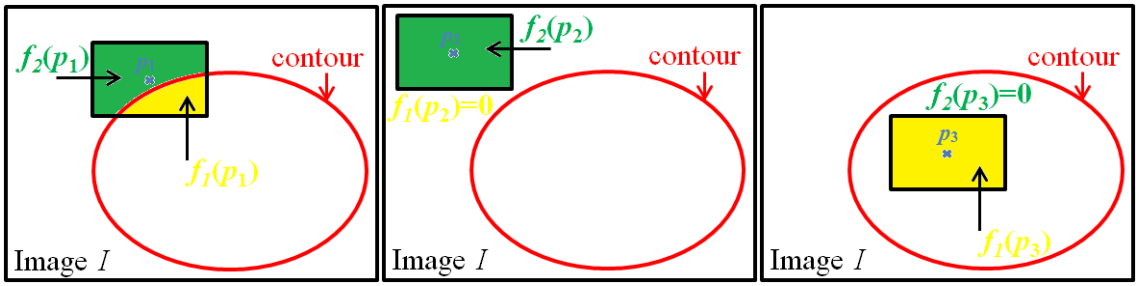

(a) **(b)** **(c)**

Figure 3.2. Illustration for f_1 and f_2 in our local fitting image.

Because $f_1(x)$ and $f_2(x)$ are calculated on a neighborhood V_x of the pixel x, they are called the local intensities. To determine the neighborhood V_x, we use a constant window K_σ with value 1 and its size is $\sigma \times \sigma$.

Figure 3.2 gives some illustrations of the local intensities f_1 and f_2 at three positions of the pixels p_1, p_2 and p_3. In Figure 3.2a, the neighborhood V_{p_1} of the pixel p_1 has two components: yellow region (inside the contour) and green region (outside the contour). The value of $f_1(p_1)$ is the average intensity of I on the yellow region, while the value of $f_2(p_1)$ is the average intensity of I on the green region. In Figure 3.2b, the neighborhood V_{p_2} of the pixel p_2 is the green region. In this case, the value of $f_1(p_2)$ is 0 while the value of $f_2(p_2)$ is the average intensity of I on the whole green region. In Figure 3.2c, the neighborhood V_{p_3} of the pixel p_3 is the yellow region. In this case, the value of $f_1(p_3)$ is the average intensity of I on the whole yellow region, while the value of $f_2(p_3)$ is 0.

Before giving solutions of the proposed R_LGR model, we will show another way to represent this energy function by Proposition 3.1. This alternative representation is useful for our calculation later (in Equation (3.9)).

Proposition 3.1. *The global component in Equation (3.1) can be represented as follows:*

$$\int_{\Omega} \big(I(x)-I_G(x,\phi)\big)^2 dx = \int_{\Omega} \big(I(x)-c_1\big)^2 H(\phi(x))dx + \int_{\Omega} \big(I(x)-c_2\big)^2 (1-H(\phi(x)))dx \quad (3.6)$$

Proof. Indeed, we will develop the left-hand side of Equation (3.6) to obtain the right-hand side of the same Equation.

$$\begin{aligned}\int_{\Omega} \big(I(x) - I_G(x,\phi)\big)^2 dx &= \int_{\Omega} \big(I(x) - c_1 H(\phi(x)) - c_2(1 - H(\phi(x)))\big)^2 dx \\ &= \int_{\Omega_{in}} \big(I(x) - c_1 H(\phi(x)) - c_2(1 - H(\phi(x)))\big)^2 dx \\ &\quad + \int_{\Omega_{out}} \big(I(x) - c_1 H(\phi(x)) - c_2(1 - H(\phi(x)))\big)^2 dx \end{aligned} \quad (3.7)$$

Note that $H(\phi(x)) = 1$ if $x \in \Omega_{in}$ and $H(\phi(x)) = 0$ if $x \in \Omega_{out}$. It follows that Equation (3.7) becomes:

$$\begin{aligned}\int_{\Omega} \big(I(x) - I_G(x,\phi)\big)^2 dx &= \int_{\Omega_{in}} \big(I(x) - c_1\big)^2 dx + \int_{\Omega_{out}} \big(I(x) - c_2\big)^2 dx \\ &= \int_{\Omega} \big(I(x) - c_1\big)^2 H(\phi(x))dx + \int_{\Omega} \big(I(x) - c_2\big)^2 (1 - H(\phi(x)))dx \end{aligned} \quad (3.8)$$

One may see that Equation (3.8) is exactly Equation (3.6). □

Remark 3.1. *One may observe that the right-hand side in Equation (3.6) is the first and second in the energy function (2.40) of the Chan-Vese model. This why we have told that the R_LGR model is inspired from the Chan-Vese model.*

By Proposition 3.1, in this chapter, we use the following energy function:

$$\begin{aligned}E(\phi) = &\int_{\Omega} \big(I(x) - c_1\big)^2 H(\phi(x))dx + \int_{\Omega} \big(I(x) - c_2\big)^2 (1 - H(\phi(x)))dx \\ &+ \frac{\lambda}{2} \int_{\Omega} \big(I(x) - I_L(x,\phi)\big)^2 dx \end{aligned} \quad (3.9)$$

3.3 Numerical Algorithm

To minimize the energy function (3.9), we use the iteration method with two steps in each of the iterations.

Step 1. In this step, the level set function is fixed. Then, by applying calculus of variation [63, 64] for (3.9) with respect to c_1 and to c_2, we obtain:

$$c_1 = \frac{\int_\Omega I(x)H(\phi(x))dx}{\int_\Omega H(\phi(x))dx} \tag{3.10}$$

$$c_2 = \frac{\int_\Omega I(x)(1-H(\phi(x)))dx}{\int_\Omega (1-H(\phi(x)))dx} \tag{3.11}$$

To calculate values of f_1 and f_2, we thank to the Heavisie function and note that K_σ is 1 on the neighborhood V and 0 otherwise, we have the formulas of f_1 and f_2 as follows:

$$f_1(x) = \frac{\int_\Omega K_\sigma(x-y)I(y)H(\phi(y))dy}{\int_\Omega K_\sigma(x-y)H(\phi(y))dy} \tag{3.12}$$

$$f_2(x) = \frac{\int_\Omega K_\sigma(x-y)I(y)(1-H(\phi(y)))dy}{\int_\Omega K_\sigma(x-y)(1-H(\phi(y)))dy} \tag{3.13}$$

Remark 3.2. *One may observe that the formulas of c_1 and c_2 are the same as in formulas of the global intensities in the Chan-Vese model presented in Section 2.2.1. This is why c_1 and c_2 are called the global intensities.*

Step 2. In this step, for fixed c_1, c_2, f_1 and f_2, we find ϕ by the calculus of variations method and the steepest descent method. Note that ϕ is considered as a variable of the Heaviside function H. However, the Heaviside function H is not continuous at 0. Therefore, to apply the calculus of variation for ϕ, we replace H by a smooth version H_ϵ as the other models using level set function mentioned in Chapter 2:

$$H_\epsilon(z) = \frac{1}{2}\left[1 + \frac{2}{\pi}\arctan\left(\frac{z}{\epsilon}\right)\right], \quad z \in \mathbb{R} \tag{3.14}$$

where ϵ is small positive. Then Equation (3.9) yields the following energy function:

$$\begin{aligned} E_\epsilon(\phi) = &\int_\Omega \big(I(x)-c_1\big)^2 H_\epsilon(\phi(x))dx + \int_\Omega \big(I(x)-c_2\big)^2(1-H_\epsilon(\phi(x)))dx \\ &+ \frac{\lambda}{2}\int_\Omega \big(I(x) - I_\epsilon^L(x,\phi)\big)^2 dx \end{aligned} \tag{3.15}$$

where $I_\epsilon^L(x,\phi) = f_1(x)H_\epsilon(\phi(x)) + f_2(x)(1-H_\epsilon(\phi(x)))$.

Theorem 3.1 and Theorem 3.2 presented as follows allow us to obtain the derivative of E_ϵ with respect to ϕ.

Theorem 3.1. *Let c_1 and c_2 be two constants, $\phi \in L^2(\Omega)$−the space of square-integrable functions on Ω. Consider the following functions:*

$$E_\epsilon^G(\phi) = \int_\Omega \big(I(x) - c_1\big)^2 H_\epsilon(\phi(x))dx + \int_\Omega \big(I(x) - c_2\big)^2 (1 - H_\epsilon(\phi(x)))dx \tag{3.16}$$

The derivative of E_ϵ^G with respect to ϕ is as follows:

$$\frac{\partial E_\epsilon^G}{\partial \phi} = \delta_\epsilon(\phi)\Big[\big(I - c_1\big)^2 - \big(I - c_2\big)^2\Big] \tag{3.17}$$

Proof. [33]. See Appendix B.1. □

Theorem 3.2. *Let f_1 and f_2 be given functions determined on Ω, $\phi \in L^2(\Omega)$−the space of square-integrable functions on Ω. Consider the following functions:*

$$E_\epsilon^L(\phi) = \frac{\lambda}{2}\int_\Omega \big(I(x) - f_1(x)H_\epsilon(\phi(x)) - f_2(x)(1 - H_\epsilon(\phi(x)))\big)^2 dx \tag{3.18}$$

The derivative of E_ϵ^L with respect to ϕ is as follows:

$$\frac{\partial E_\epsilon^L}{\partial \phi} = -\delta_\epsilon(\phi)\big[\lambda\big(I - f_1H_\epsilon(\phi) - f_2(1 - H_\epsilon(\phi))\big)\big(f_1 - f_2\big)\big] \tag{3.19}$$

Proof. [78]. See Appendix B.2. □

From Theorem 3.1 and Theorem 3.2, we obtain the derivative of E_ϵ with respect to ϕ as follows:

$$\frac{\partial E_\epsilon}{\partial \phi} = -\delta_\epsilon(\phi)\Big[\lambda\big(I - f_1H_\epsilon(\phi) - f_2(1 - H_\epsilon(\phi))\big)\big(f_1 - f_2\big) - \big(I - c_1\big)^2 + \big(I - c_2\big)^2\Big] \tag{3.20}$$

Then, by the steepest descent method [63, 64], we obtain the evolution equation of ϕ with respect to time t as follows:

$$\frac{\partial \phi}{\partial t} = -\frac{\partial E_\epsilon}{\partial \phi} = \delta_\epsilon(\phi)\Big[\lambda\big(I - f_1H_\epsilon(\phi) - f_2(1 - H_\epsilon(\phi))\big)\big(f_1 - f_2\big) - \big(I - c_1\big)^2 + \big(I - c_2\big)^2\Big] \tag{3.21}$$

Note that, in the energy function (3.15), there is not the regularization term $\mathcal{L}(\phi) = \int_\Omega |\nabla H_\epsilon(\phi(x))|dx$ as in the Chan-Vese and the LBF models. On the other hand, to re-initialize ϕ to the signed distance function, we use the convolution $\phi * G_{\sqrt{2t}}$ between the solution ϕ of Equation (3.21) and a Gaussian kernel $G_{\sqrt{2t}}$ with standard deviation $\sqrt{2t}$. Indeed, let us consider the evolution of ϕ such that the following regularization term is minimized:

$$\mathcal{L}(\phi) = \int_\Omega |\nabla H_\epsilon(\phi(x))|dx \tag{3.22}$$

which has the derivative with respect to ϕ (see Appendix B.3) as follows:

$$\frac{\partial \mathcal{L}}{\partial \phi} = -\delta_\epsilon(\phi)\nabla \cdot \left(\frac{\nabla \phi}{|\nabla \phi|}\right) \tag{3.23}$$

where $\delta_\epsilon(z) = H'_\epsilon(z)$, $z \in \mathbb{R}$, and $\nabla\cdot$ is the divergence operator.

Then, by the steepest descent method [63, 64], we obtain the evolution equation of ϕ as follows:

$$\frac{\partial \phi}{\partial t} = \delta_\epsilon(\phi)\nabla \cdot \left(\frac{\nabla \phi}{|\nabla \phi|}\right) \tag{3.24}$$

In [59] and [33], the authors shown that we can replace $\delta_\epsilon(\phi)$ by $|\nabla\phi|$ to extend the evolution to all level sets of ϕ. Then, the evolution equation of ϕ becomes:

$$\frac{\partial \phi}{\partial t} = |\nabla\phi|\nabla \cdot \left(\frac{\nabla \phi}{|\nabla \phi|}\right) \tag{3.25}$$

Now, by the re-initialization procedure to obtain $|\nabla\phi| = 1$, we have then:

$$\frac{\partial \phi}{\partial t} = \nabla \cdot (\nabla\phi) = \Delta\phi \tag{3.26}$$

with the initial condition $\phi(x, 0) = \phi_0(x)$, $x \in \Omega$. This is the heat equation which has an unique solution [63] as follows:

$$\phi = \phi_0 * G_{\sqrt{2t}} \tag{3.27}$$

where $G_{\sqrt{2t}}$ is a Gaussian kernel with standard deviation $\sqrt{2t}$.

So, if we have ϕ^k which is the solution of Equation (3.21) at the iteration k, we can use the evolution $\phi^k * G_{\sqrt{2t}}$ to re-initialize ϕ^k to the signed distance function while keeping the smoothness of the level set function. For more details, please refer to [78].

Remark 3.3. *When the Heaviside function H is replaced by the smooth function H_ϵ, the formulas* (3.10), (3.11), (3.12) *and* (3.13) *become the following equations:*

$$c_1 = \frac{\int_\Omega I(x)H_\epsilon(\phi(x))dx}{\int_\Omega H_\epsilon(\phi(x))dx} \tag{3.28}$$

$$c_2 = \frac{\int_\Omega I(x)(1 - H_\epsilon(\phi(x)))dx}{\int_\Omega (1 - H_\epsilon(\phi(x)))dx} \tag{3.29}$$

$$f_1(x) = \frac{\int_\Omega K_\sigma(x - y)I(y)H_\epsilon(\phi(y))dy}{\int_\Omega K_\sigma(x - y)H_\epsilon(\phi(y))dy} = \frac{\big(K_\sigma * (IH_\epsilon(\phi))\big)(x)}{(K_\sigma * H_\epsilon(\phi))(x)} \tag{3.30}$$

$$f_2(x) = \frac{\int_\Omega K_\sigma(x - y)I(y)(1 - H_\epsilon(\phi(y)))dy}{\int_\Omega K_\sigma(x - y)(1 - H_\epsilon(\phi(y)))dy} = \frac{\big(K_\sigma * (I(1 - H_\epsilon(\phi)))\big)(x)}{\big(K_\sigma * (1 - H_\epsilon)\big)(x)} \tag{3.31}$$

Now, to discretize Equation (3.21) in ϕ, we use an explicit scheme. We first recall the usual notation: let Δt be the time step, h be the space step, and $(x_i, y_j) = (ih, jh)$ be the grid points, for $1 \leq i \leq m_1$, $1 \leq j \leq m_2$ ($m_1 \times m_2$ is the size of the image I). Let $\phi^n_{i,j} = \phi(n\Delta t, x_i, y_j)$ be an approximation of $\phi(t, x, y)$, with $n \geq 0$, $\phi^0 = \phi_0$.

The algorithm is as follows: knowing ϕ^n, we first compute c_1^n, c_2^n, f_1^n and f_2^n using Equations (3.28), (3.29), (3.30) and (3.31). Then, we compute ϕ^{n+1} by the following discretization of Equation (3.21) in ϕ:

$$\frac{\phi^{n+1} - \phi^n}{\Delta t} = \delta_\epsilon(\phi^n)\Big[\lambda\big(I - f_1^n H_\epsilon(\phi^n) - f_2^n(1 - H_\epsilon(\phi^n))\big)\big(f_1^n - f_2^n\big) - \big(I - c_1^n\big)^2 + \big(I - c_2^n\big)^2\Big] \tag{3.32}$$

Remark 3.4. *The computational cost of f_2 in Equation* (3.31) *can be effectively done. First, we notice that f_2 in Equation* (3.31) *can be rewritten as follows:*

$$f_2(x) = \frac{\big(K_\sigma * I\big)(x) - \big(K_\sigma * (IH_\epsilon(\phi))\big)(x)}{\big(K_\sigma * \mathbf{1}\big)(x) - \big(K_\sigma * H_\epsilon(\phi)\big)(x)} \tag{3.33}$$

where $\mathbf{1}$ is the constant function with value 1. In the above expression of f_2 (3.33)*, the second terms in the numerator and the denominator as the same as the numerator and the denominator in f_1* (3.30)*, while the term $K_\sigma * I$ in the numerator and $K_\sigma * \mathbf{1}$ in the denominator do not depend on the evolution of the level set function ϕ. Therefore, the two convolutions $K_\sigma * I$ and $K_\sigma * \mathbf{1}$ can be computed only once before the iteration. So, during the iterations, only the two convolutions $K_\sigma * (IH_\epsilon(\phi))$ and $K_\sigma * H_\epsilon(\phi)$ are calculated for the evolution of ϕ.*

Remark 3.5. *By Proposition B.1 in Appendix B, Section B.3, we need the boundary condition: $\frac{\partial \phi}{\partial N} = 0$, where N is the exterior normal to the boundary $\partial\Omega$. This condition can be taken in each iteration as follows:*

$$\phi(x_i, y_1) = \phi(x_i, y_2), \quad i = 1, ..., m_1 \tag{3.34}$$

$$\phi(x_i, y_{m_2}) = \phi(x_i, y_{m_2 - 1}), \quad i = 1, ..., m_1 \tag{3.35}$$

$$\phi(x_1, y_j) = \phi(x_2, y_j), \quad j = 1, ..., m_2 \tag{3.36}$$

$$\phi(x_{m_1}, y_j) = \phi(x_{m_1 - 1}, y_j), \quad j = 1, ..., m_2 \tag{3.37}$$

where $m_1 \times m_2$ is the size of the image I.

Finally, the principal steps of the algorithm are summarized as follows:

Step 1. Initialize ϕ^0 by ϕ_0, $n = 0$.

Step 2. Compute c_1^n, c_2^n and f_1^n using Equations (3.28), (3.29) and (3.30), respectively, while f_2 is computed as Remark 3.4.

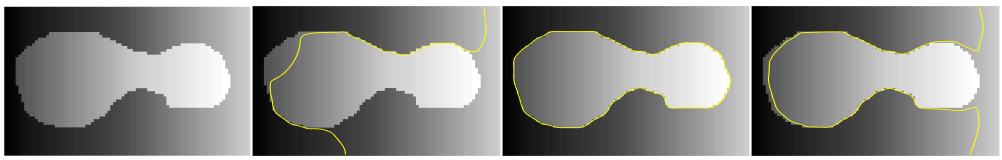

(a) Original image **(b)** $\sigma = 6$ **(c)** $\sigma = 15$ **(d)** $\sigma = 54$

Figure 3.3. Results of the R_LGR model on a non-homogeneous synthetic images with different values of σ.

Step 3. Solve the PDE (3.21) in ϕ using Equation (3.32) to obtain ϕ^{n+1}.

Step 4. Regularize the level set function by a convolution with a Gaussian kernel, i.e. $\phi^{n+1} = K_\zeta * \phi^{n+1}$, where K_ζ is a Gaussian kernel with the standard deviation ζ.

Step 5. Satisfy the boundary condition to ϕ using Remark 3.5.

Step 6. Check whether the evolution is stationary. If not, $n = n+1$ and repeat to Step 2.

3.4 Sensibility of the Parameters

In the proposed model, local average intensity is used to handle intensity in-homogeneity (IIH). As stated in Section 3.2.2, to determine this local average intensity, we use a constant window K_σ with value 1 and size is $\sigma \times \sigma$. Therefore, the main parameters chosen by the user for this method are σ and λ.

3.4.1 Parameter σ

In the proposed method, the intensity of a pixel is approximated by the average of the intensity in the neighborhood K_σ inside and outside the evolution contour. Therefore, a small value of σ may provide high sensibilities to local image information such as noise. On the contrary, if σ is large, e.g. such that the constant window K_σ may contain the whole image, the local intensity will become the global one and the model would not be able to deal with IIH.

One may observe in Figure 3.3 that we can obtain accurate result with σ bounded in an interval of values. A suitable and small enough σ (in this interval depending on the nature of image) allows for an accurate segmentation (if λ is well chosen) (see Figure 3.3b and Figure 3.3d).

For more results, please see Appendix E.

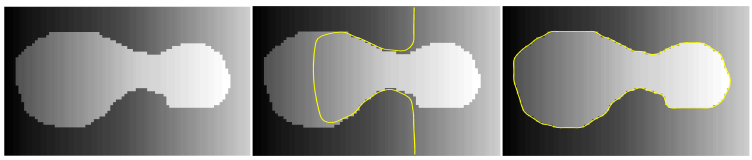

(a) Original image **(b)** $\lambda = 100$ **(c)** $\lambda = 1000$

Figure 3.4. Results of the R_LGR model on a non-homogeneous synthetic images with different values of λ.

3.4.2 Parameter λ

The parameter λ controls the sensibility of the local with respect to the global terms. If λ is large (at least superior than 2), then the sensibility of the local term is stronger than that of the global term. On the contrary, the local term is weaker than the global term, resulting in the equivalent Chan-Vese model, hence providing robustness to noise but resulting in inability to cope with IIH. Therefore, if the given image is corrupted with intensity in-homogeneity, then the value of λ should be large enough. On the other hand, if λ is small, then the model approaches the global energy function, and would not be able to deal with IIH.

Figure 3.4 validate the above argumentation by applying multiple values of λ. In Appendix E, we can find more results of the proposed model with varying values of λ.

To summarize, in order to obtain good accuracy in segmenting object with IIH, λ should be large and σ should be in an interval of values (not too large values). Indeed, a too large σ would not enable segmentation of image with IIH.

If the image is corrupted by IIH and noise, a trade-off between the values of σ and λ should be made to obtain good accuracy.

3.5 Experimental Results

To evaluate the performance of our R_LGR method, several experiments have been carried out on images with non-homogeneous regions and on noisy images with non-homogeneous regions. Examples are shown here for some synthetic, noisy ultrasound, MR and X-Ray images. A comparative evaluation has been performed to demonstrate the advantages of our R_LGR method over some state-of-the-art methods such as the Chan-Vese [33] and the LIF [78] models. The code of the LIF model can be downloaded on the page of the author (`http://www4.comp.polyu.edu.hk/~cslzhang/`).

We used the MATLAB r2008a to implement our algorithm. The program was run on a Dell (OptiPlex 360), which has Intel Core 2 Duo E7500 @ 2.93GHz and 4GB RAM. The parameters in this section are given in Table 3.1.

Results on a non-homogeneous synthetic image are reported and compared with the Chan-Vese and the LIF methods (Figure 3.5). We see that the Chan-Vese model fails to detect the object boundary, while the LIF and our R_LGR methods provide accurate segmentation of the object. This can be explained by the fact that the intensity of the tested image is non-homogeneous, while the Chan-Vese model utilizes only the global intensity information in the energy function to approximate the image. In contrast, the LIF and our R_LGR methods utilize the local intensity to better detect variation inside the object or the background.

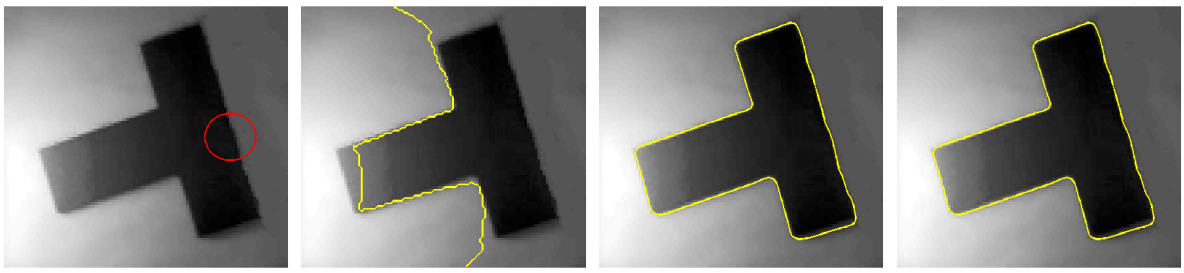

Figure 3.5. Result for a synthetic image with intensity in-homogeneity. From left to right: Original image and initial contour; result of the Chan-Vese method, the LIF method and the proposed R_LGR method.

In Figure 3.6, results of the LIF and our R_LGR methods on a real image of DNA channel are reported for comparison regarding the ability of these models to handle intensity in-homogeneity. The task is to segment object with intensity variation. In this figure, nuclei appear much brighter than the background in the DNA channel and some nuclei are very close to each other. One may observe that the LIF model ($\sigma = 3$ (see Equation (2.70)) failed to segment the nuclei boundaries, whereas our result not only satisfies the segmentation but also separates nuclei distinctly. In the case of higher values of σ (σ =11), the results of the LIF are still far from expected, even at the expense of the computational time.

In Figure 3.7, the segmentation results for three blood vessel X-Ray images with the intensity in-homogeneity are reported for comparison with the Chan-Vese and the LIF methods. It can be seen from the second and the third columns that the Chan-Vese and the LIF methods failed to segment all the three images. For the Chan-Vese method, the reason is due to the disadvantage of not using the local information, while the reason of the LIF method is due to the non-convexity of the model, the initial contours in these cases are not suitable to yield good results. We can find better results of the LIF method published in [78]. In contrast, our results presented in the third column clearly show that the boundaries were accurately segmented. Besides, it can be seen from Figure 3.8 that our R_LGR method is less sensitive to the position of initial contour while giving accurate

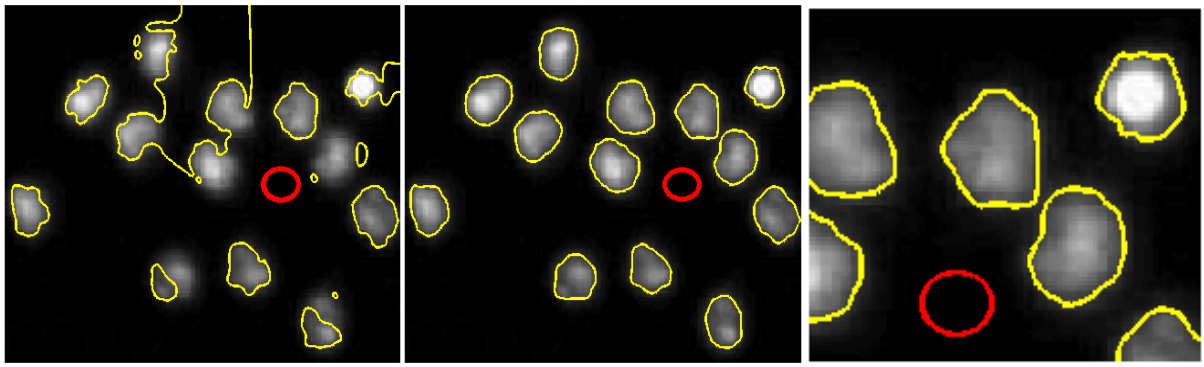

(a) (b) (c)

Figure 3.6. Results on a real image of DNA channel. Green (red) line is the initial (final) contour: (a) result of the LIF method, (b) result of the proposed R_LGR method, (c) zoom of our R_LGR method.

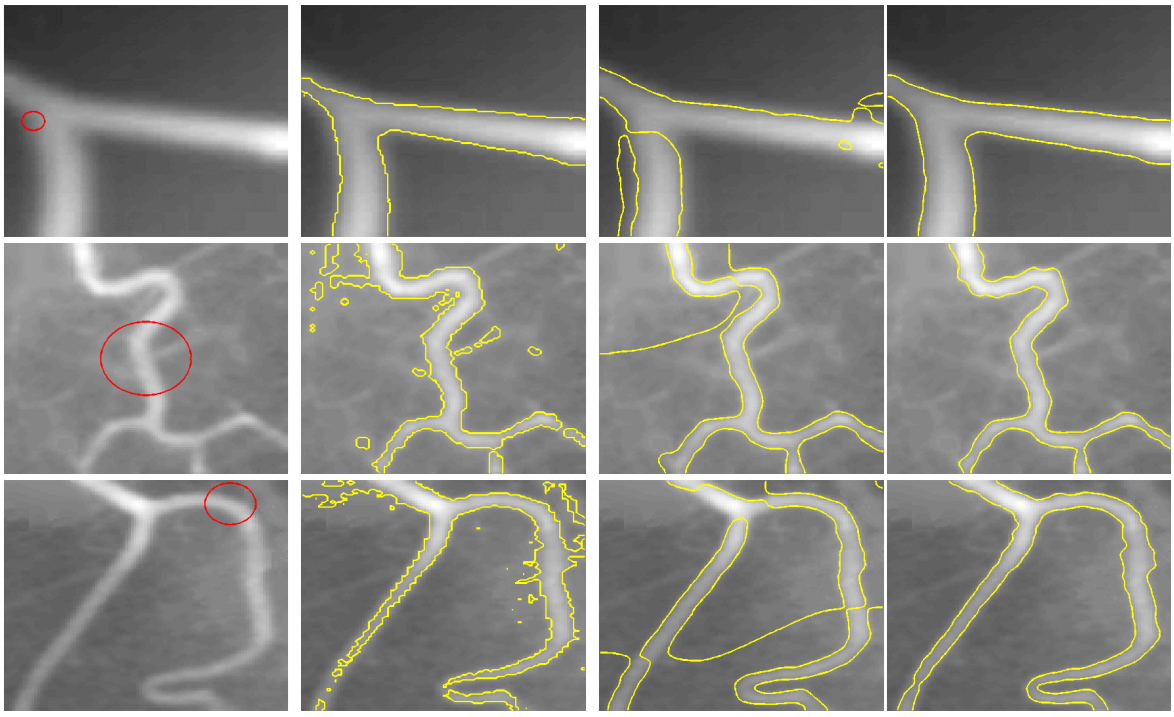

Figure 3.7. Results for blood vessel X-Ray images (source `http://www.unc.edu/~liwa/`). From left to right: original images and initial contour; results of the Chan-Vese method, the LIF method and the proposed R_LGR method.

results. However, the energy function of the proposed model is not convex which implies that the final contour of our R_LGR model still depends on the position of the initial

contour.

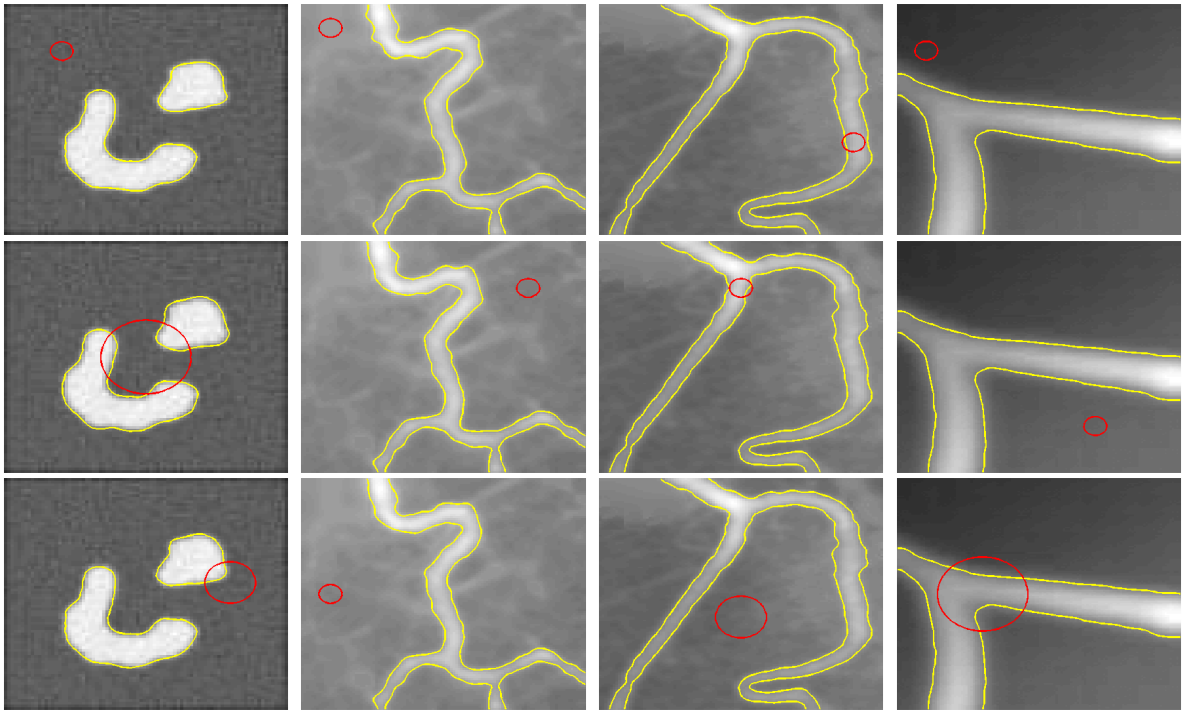

Figure 3.8. Results of the proposed R_LGR on X-Ray vessel images with different positions of initial contour. The red and yellow lines are the initial and final contours, respectively.

Lastly, we have also compared our R_LGR method with the LIF model on very noisy medical images. In Figure 3.9, the top (the bottom) row shows the results for a noisy ultrasound (MR, respectively) image. The third column shows the results of our R_LGR method, which are obviously more accurate than the results of the LIF model. These images illustrate the perfomance of the proposed model to deal with IIH, discontinuity of boundary and noise (Figure 3.9 for ultrasound image).

3.6 Conclusion

In this chapter, we have proposed a new method for segmentation image which utilizes the advantage of global and local information of image to deal with intensity in-homogeneity. Local information allows to deal with IIH, while global information provide more robustness to noise and weak or blur edges as well as gaps. Our proposed model is inspired from the Chan-Vese model [33]. Moreover, for stability of the curve and avoiding to be trapped into many local minimum in case of noise, the smoothness of the evolving curve is derived from a Gaussian filtering in the implementation as in [78]. The experimental results have shown

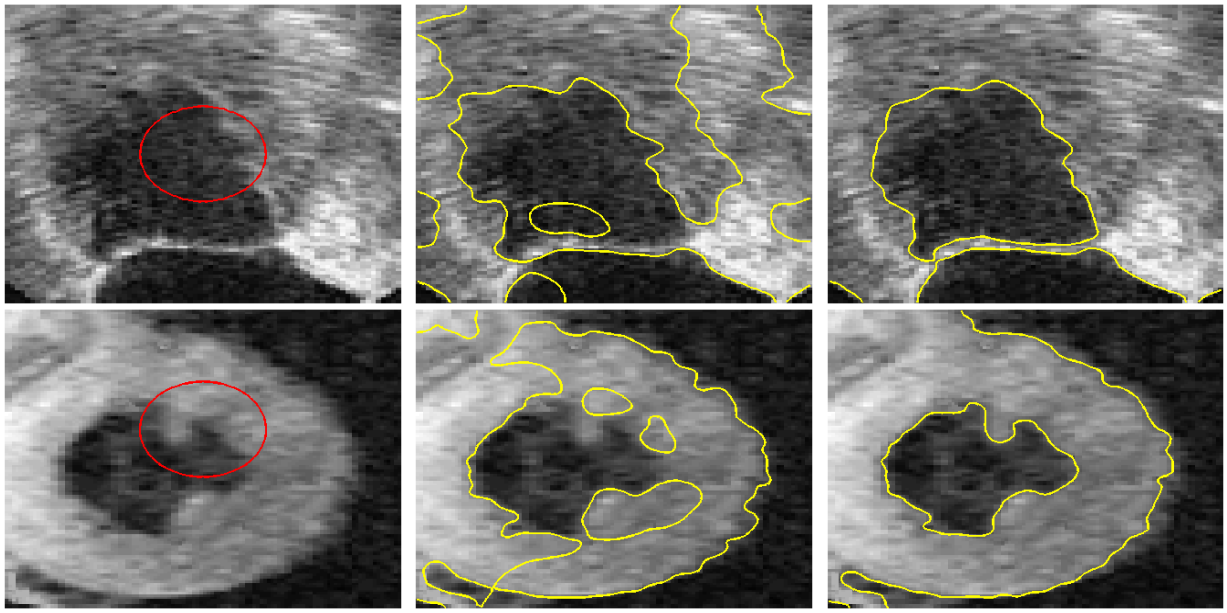

Figure 3.9. Comparison of the proposed R_LGR with the LIF method on UltraSound and MR images (sources `http://www.unc.edu/~liwa/` and `http://www4.comp.polyu.edu.hk/~cslzhang/RD/RD.htm`). Original images and initial contours are in the first column. The results of the LIF and our R_LGR methods are in the second and third columns respectively.

Table 3.1. Parameters used in Chapter 3

Figure	3.5	3.6	3.8				3.9	
			col. 1	col. 2	col. 3	col. 4	top	bottom
σ	15	5	5	11	9	11	5	7
ζ	2.5	0.5	3	1.5	1.5	0.5	2	2
ϵ	1.5	0.5	1.5	1.5	1.5	1.5	1.5	1.5
λ	99	9	9	9	9	9	9	9

the efficiency of our R_LGR method both on the non-homogeneous synthetic or real-world images, especially for the medical images.

The contribution of this model

1. The proposed R_LGR provides a better understanding of the contribution of the local and global energy functional when considering region-based Active Contour model for dealing with the intensity in-homogeneity which could affect the quality of

segmentation.

2. The proposed R_LGR parameters λ and σ have been analyzed and recommendations have been provided regarding the values that will yield high accuracy of boundary extraction to non-homogeneous regions with/or without noise and gaps.

3. From the application field point of view, the R_LGR can be used for medical images such as the X-Ray, MR and UltraSound images, as well as synthetic and other real-world images.

Weakness of the method

The resulting model provide accuracy segmentation in case of IIH and robustness to simultaneous noises and IIH. The main weakness to the proposed model is the dependence of the initial contour, which is not suitable for an automation. Therefore, it is necessary that the energy functional of the model is convex to provide reliable and accurate segmentation. This is the goal of the next Chapter.

CHAPTER 4

Convex Models

Contents

4.1 Introduction and Related Works: Region-based Convex Active Contour

In Chapter 2 and Chapter 3, we have seen the negative impact of the intensity in-homogeneity (IIH) on the accuracy of the segmentation. Also the energy functional of the active contours using traditional level set function is not convex. Therefore, the final contour is dependent on the position of the initial contour. It means that it requires a suitable and good position of the initial contour to have an accurate result of the final contour. Therefore, even though these methods have gotten achievements in handling IIH, the results are not reliable because they cannot guarantee the same results independently from initial contour. The challenge is then to cope with the non-convexity of the energy functional. This is also the objective of this chapter.

In a variational approach, the problem is to define a suitable energy functional to cope with the objective of segmentation. On the other hand, to avoid local minimum solution, i.e. the dependence with respect to the initial contour, it is necessary that the energy functional is a convex function. Efforts have been effective in this direction since the publication of the works on the convex region-based model of Chan *et al.* [35]. This is a convexification of the Chan-Vese model. We will then refer to this model as the convex Chan-Vese model. Inspired from this model, Bresson *et al.* [41] proposed another convex model by modifying the regularized term (which accounts for smoothing of the curve), into a weighted version one using gradient information of the image via an edge detection function. The similarity of these two models relies on restricting the level set in the interval [0,1]. Later, in the so called Fuzzy Energy-Based AC (FEBAC) [47], Krinidis *et al.* proposed to use the membership function, which is naturally in the interval [0,1] to obtain the independence of their model to initial condition when there is no regularization of the curve. However, all these models are based on the assumption of approximately piecewise-constant regions in image. Therefore, they fail when addressing IIH.

In our works, we assume piecewise-smooth approximation of regions in image and design convex energy functions to handle IIH. As explained in Chapter 2 and Chapter 3, we tackle IIH by using the local statistical information in a region-based active contours approach. Moreover, we incorporate global information to improve the robustness with respect to noises and weak/blur edges. In this chapter, we will focus more on dealing with convex energies.

Here, we introduce three novel convex region-based active contour models to efficiently tackle IIH while offering the globally optimal segmentation thanks to the convexity of the associated energy functionals. Thus, the proposed models are convex which implies that the accuracy and repeatability of the results are invariant with respect to the initial position of the active contour. Furthermore, the energy function of the proposed models

is minimized in a computationally efficient way using two fast algorithms: the first one (Section 4.3 and Section 4.4) uses the Chambolle method [45] proposed for denoising and adapted by Bresson *et al.* [41] for segmentation; the second (Section 4.5) is a fast numerical scheme proposed by Song *et al.* [46] and developed by Krinidis *et al.* [47].

First, we will present related works on some existing state-of-the art convex active contour models, namely the convex model of Chan *et al.* [35], the Bresson *et al.*'s model [41] and the Krinidis *et al.*'s model [47]. Particularly, these models inspired our proposed convex energy functions. Then, we present our proposed convex models which are: i) The Convex Local Region-based Active Contour model (C_LR); ii) The Convex Local and Global Region-based Active Contour model (C_LGR); iii) The Convex Local and Global Region-based with Fuzzy Gaussian Distribution for Active Contour model (C_LGFGD). The major advantage of these models is that their energy functions are convex. Therefore, the obtained minimizer of the energy function is global and invariant with respect to the initial position of the active contour.

4.2 Related Works

All the following state-of-the-art models assume that image regions are characterized by piecewise-constant intensity.

4.2.1 The convex Chan-Vese model

In [35], the so-called convex Chan-Vese model was proposed to make the region-based Chan-Vese model proposed in [33] independent from the initial condition.

Let us first recall the Chan-Vese model. The Chan-Vese model assumes that image regions are characterized by piecewise-constant intensity. The corresponding energy functional is:

$$E(c_1, c_2, C) = \int_{\Omega_{in}} (I(x) - c_1)^2 dx + \int_{\Omega_{out}} (I(x) - c_2)^2 dx + \mu |C| \tag{4.1}$$

where Ω_{in} and Ω_{out} are the regions inside and outside the contour C, respectively, constants c_1 and c_2 are the average intensities inside and outside the contour Ω_{in} and Ω_{out}, respectively, μ is a positive constant, and $|C|$ is the length of C. The length term is used to regularize the curve C, accounting for smoothing the curve.

Then, when fixing c_1 and c_2 and using a level set function ϕ as well as a smooth Heaviside function H_ϵ, the optimal curve can be obtained, by the following gradient flow:

$$\frac{\partial \phi}{\partial t} = \delta_\epsilon(\phi) \left[\mu \nabla \cdot \left(\frac{\nabla \phi}{|\nabla \phi|} \right) - (I - c_1)^2 + (I - c_2)^2 \right] \tag{4.2}$$

where $\delta'_\epsilon = H'_\epsilon$ and $\nabla\cdot$ is the divergence operator.

In order to eliminate the problem of non-convex function, Chan *et al.* [35] observed that the steady state solution of the previous equation is the same for the steady state of a simpler gradient flow which corresponds to an energy functional where the regularization term is the total variation of the level set ϕ. Due to the non-uniqueness of level set representation, Chan *et al.* demonstrated that by restricting ϕ on [0,1], the minimization problem is convex, resulting in the so-called convex Chan-Vese model:

$$\min_{\substack{c_1,c_2\\0\leq f\leq 1}} \left\{ \mu \int_\Omega |\nabla f(x)|dx + \int_\Omega f(x)(c_1 - I(x))^2 dx + \int_\Omega (1-f(x))(c_2 - I(x))^2 dx \right\} \tag{4.3}$$

where $x = (x_1, x_2) \in \Omega$ is a pixel, f is the level set function which is restricted in [0,1], $|\nabla f(x)| = \sqrt{\left(\frac{\partial f}{\partial x_1}\right)^2 + \left(\frac{\partial f}{\partial x_2}\right)^2}$. Using the calculus variation [64], these constants are calculated by calculus variation by deriving the above energy functional with respect to c_1 and c_2:

$$c_1 = \frac{\int_\Omega I(x)f(x)dx}{\int_\Omega f(x)dx}, \tag{4.4}$$

$$c_2 = \frac{\int_\Omega I(x)(1-f(x))dx}{\int_\Omega (1-f(x))dx} \tag{4.5}$$

Note that, when c_1 and c_2 are fixed, problem (4.3) is equivalent to the following problem:

$$\min_{0\leq f\leq 1} F(f) = \mu \int_\Omega |\nabla f(x)|dx + \int_\Omega f(x)e_r(x)dx \tag{4.6}$$

where $e_r(x) = (c_1 - I(x))^2 - (c_2 - I(x))^2$. Then, the constraint $0 \leq f \leq 1$ of problem (4.6) is eliminated using the unconstrained problem according to the following claim [35].

Claim 4.1. **[35]** *Let $e_r(x) \in L^\infty(\Omega)$, for $c_1, c_2 \in \mathbb{R}$, $\mu \in \mathbb{R}^+$, then the convex constrained minimization problem (4.6) has the same set of minimizers as the following convex and unconstrained minimization (UM) problem:*

$$\min_f \left\{ F^{UM}(f) = \mu \int_\Omega |\nabla f(x)|dx + \int_\Omega (f(x)e_r(x) + \alpha\psi(f(x)))dx \right\} \tag{4.7}$$

where $\psi(z) = max\{0, 2|z - \frac{1}{2}| - 1\}$ is a penalty function to enforce the constraint provided that the constant α is chosen large enough such as $\alpha > \frac{1}{2}\|e_r(x)\|_{L^\infty(\Omega)}$.

Then, the minimizer f^* of (4.7) can be determined by using the classical Euler-Lagrange equations method:

$$\frac{\partial F^{UM}}{\partial f} = 0 \tag{4.8}$$

where $\frac{\partial F^{UM}}{\partial f}$ is the partial derivative of F^{UM} with respect to f [35] as follows:

$$\frac{\partial F^{UM}}{\partial f} = -\mu\nabla \cdot \left(\frac{\nabla f}{|\nabla f|}\right) + e_r(x) + \alpha\psi'(f) \tag{4.9}$$

Then the gradient descent method is used to establish the evolution equation of the contour:

$$\frac{\partial f}{\partial t} = -\frac{\partial F^{UM}}{\partial f} \tag{4.10}$$

The authors in [35] also proved that if c_1 and c_2 are fixed, and if f^* is a solution of Equation (4.10), the set $M = \{x : f^*(x) > \alpha_{thres}\}$, $\forall\alpha_{thres} \in (0, 1)$, determines a global minimizer of the convex Chan-Vese model. In other words, the segmentation result is determined by thresholding the level set according to the set M.

4.2.2 The Bresson *et al.*'s model

Later, in [41], Bresson *et al.* modified the total variation regularization term (first term of Equation (4.3)) of the convex Chan-Vese model, by incorporating gradient information via an edge detection function to weight the total variation of the restricted level set function f. The resulting energy function of this model is as follows:

$$\min_{\substack{c_1,c_2 \\ 0\le f\le 1}} \left\{ \mu \int_\Omega g(x)|\nabla f(x)|dx + \int_\Omega f(x)(c_1 - I(x))^2 dx + \int_\Omega (1 - f(x))(c_2 - I(x))^2 dx \right\} \tag{4.11}$$

where c_1 and c_2 are mentioned in Equation (4.3) and calculated by Equations (4.4) and (4.5) for fixed f, while g is an edge indicator function so that it gets small value at object boundaries. In [41], Bresson *et al.* used $g(x) = \frac{1}{1+|\nabla I(x)|^2}$,

The weighted regularization term behaves as the GAC. This encourages segmentation where the edge detection function is minimum, resulting in more detailed segmentation while maintaining smooth contours.

For fixed c_1 and c_2, problem (4.11) is transformed to the following problem by Claim 4.1:

$$\min_f \left\{ \mu \int_\Omega g(x)|\nabla f(x)|dx + \int_\Omega (f(x)e_r(x) + \alpha\psi(f(x)))dx \right\} \tag{4.12}$$

where e_r and ψ are defined in the convex Chan-Vese model.

Remark 4.1. *For technical convenience, problem* (4.12) *above is the same as the following problem:*

$$\min_f \left\{ \int_\Omega g(x)|\nabla f(x)|dx + \int_\Omega (\frac{1}{\mu} f(x)e_r(x) + \frac{\alpha}{\mu}\psi(f(x)))dx \right\} \tag{4.13}$$

Problem (4.13) can be solved by the Euler-Lagrange equation as in the case of the convex Chan-Vese model. However, the convergence of solution is very slow because of the regularization process of the first term (the total variation norm of f). To avoid this problem, first, Bresson *et al.* [41] used a variable v to change problem (4.7) to the following dual problem:

$$\min_{f,v} F^{B-dual}(f,v) = \int_{\Omega} g(x)|\nabla f(x)|dx + \frac{1}{2\theta}\int_{\Omega}(f(x)-v(x))^2dx + \int_{\Omega}(\frac{1}{\mu}v(x)e_r(x) + \frac{\alpha}{\mu}\psi(v(x)))dx \tag{4.14}$$

where the parameter $\theta > 0$ is chosen small enough so that f be close to v. Indeed, if θ is small, $\frac{1}{2\theta}$ is large. Thus, $|f-v|$ must be small to minimize F^{B-dual}.

Remark 4.2. *Obviously, one may observe that the dual function $F^{B-dual}(f,v)$ is convex with respect to f and to v. Therefore, the global solution can be computed by separately minimizing f and v and iterate until convergence.*

Then, a fast algorithm for solving (4.14) is proposed using the fast algorithm introduced by Chambolle for denoising [45]. This algorithm consists of two following minimization problems:

1) Fixing f, v is the solution of the following problem:

$$\min_{v}\left\{\frac{1}{2\theta}\int_{\Omega}(f(x)-v(x))^2dx + \int_{\Omega}(\frac{1}{\mu}e_r(x)v(x) + \frac{\alpha}{\mu}\psi(v(x)))dx\right\} \tag{4.15}$$

2) Fixing v, f is the minimizer of the problem:

$$\min_{f}\left\{TV_g(f) + \frac{1}{2\theta}\int_{\Omega}(f(x)-v(x))^2dx\right\} \tag{4.16}$$

The above problems are solved by the following two propositions proven in [45, 41].

Proposition 4.1. [45, 41] *The solution of Equation (4.15) is given by:*

$$v(x) = \min\{\max\{f(x) - \frac{\theta}{\mu}e_r(x), 0\}, 1\}. \tag{4.17}$$

Proposition 4.2. [45, 41] *The solution of Equation (4.16) is given by:*

$$f = v - \theta \mathrm{div}p \tag{4.18}$$

where div *is the divergence operator and* $p = (p^1, p^2)$ *is given by Equation (4.19):*

$$g(x)\nabla(\theta \text{div} p - v) - |\nabla(\theta \text{div} p - v)|p = 0 \tag{4.19}$$

The previous equation can be solved by a fixed point method with the initial value $p_0 = (0, 0)$ *and iteration formula:*

$$p_{n+1} = \frac{p_n + \tau\nabla(\text{div} p_n - \frac{v}{\theta})}{1 + \frac{\tau}{g(x)}|\nabla(\text{div} p_n - \frac{v}{\theta})|} \tag{4.20}$$

where τ *is the temporal step. For more details, please refer to [45, 41].*

4.2.3 The Krinidis *et al.*'s model

The fuzziness in FEBAC [47] is inspired by the fuzzy c-means (FCM) method published by Dunn in 1973 [86] and improved by Bezdek in 1981 [87].

In [47], Krinidis *et al.* hybridize the region-base active contour model with the soft clustering technique namely the fuzzy c-means to take advantages of the two approaches. Fuzzy clustering methods provide robust data clustering, while region-based active contours are robust to noise, weak/blur edges and initialization. Generally, fuzzy c-means method is a clustering technique that searches to cluster data points by iteratively computing a fuzzy membership function and the mean value for each cluster. The fuzzy membership function gives an indication of the degree of similarity between the data value at a location and the centroid (prototype) of its cluster. Thus, a high membership value indicates that the data value at a location is near the centroid for the cluster in consideration.

More specifically, a criterion is designed to fit a problem which may be formulated as the sum-of-squared-error-criterion, to find the partition of n data points into c clusters with respect to the fuzzy membership functions and the centroids. The criterion may be a distance or a similarity measure between the centroid of a cluster and a data point in the same cluster.

The problem is equivalent to finding the fuzzy membership u_{ik} of each data point x_k ($k = 1, 2, ..., n$) to a cluster w_i ($i = 1, 2, ..., c$). A cluster k is defined by the cluster centroid which is calculated as the mean of data points in the cluster. Each data point can be a member in one or different clusters. This implies that each data point has a partial fuzzy membership in multiple clusters. Therefore, the fuzzy membership of a data point in the feature space is a continuous fuzzy membership functions.

As the fuzzy membership function is constrained to be in the interval [0, 1], and similar to the two previously presented methods, it is taken into account as a pseudo-level set function into the mixed model named Fuzzy Energy-Based Active Contour (FEBAC) for segmentation [47]. This model is formulated as the minimization of the following energy

function with respect to the curve C, constants c_1 and c_2 that approximate image intensity inside and outside the contour C respectively, and the fuzzy membership function u:

$$F(C, c_1, c_2, u) = \mu|C| + \int_{\Omega} [u(x)]^m \big(I(x) - c_1\big)^2 dx + \int_{\Omega} [1 - u(x)]^m \big(I(x) - c_2\big)^2 dx \quad (4.21)$$

where Ω is the set of pixel locations in the image domain, μ is a positive constant, $|C|$ is the length of the curve C, $m \geq 1$ is a weighting exponent on each fuzzy membership and determines the fuzziness of the fuzzy clustering. The higher m, the fuzzier the membership assignment is. Here, there are only two clusters namely, the regions inside Ω_{in} and outside Ω_{out} the contour with corresponding centroids c_1 and c_2 respectively. The fuzzy membership of an image pixel $I(x)$ at location x for cluster Ω_{in} (inside the contour C) is $u(x) \in [0, 1]$. As a consequence, the fuzzy membership of the image pixel $I(x)$ at location x for cluster Ω_{out} (outside the contour) is $(1 - u(x))$. Then, one may observe that a pixel x belongs to the cluster Ω_{in} (inside the active contour with the centroid c_1) if it attains high membership value $u(x)$. On the contrary, a pixel x belongs to the cluster Ω_{out} (outside the contour or background, with the centroid c_2) if it attains high membership value $1 - u(x)$.

Hence, problem (4.21) is to search for a minimal length of curve, while at the same time defining a partition of data into two clusters which minimize the global differences between the observed image intensity and the centroids, i.e. average intensity inside (or outside) the contour. Indeed, the first term of Equation (4.21) is the regularity term which accounts for smoothing of the curve C, while the two last terms in this equation are the fidelity terms between the image I with c_1 and c_2, respectively.

The curve C is represented by the pseudo level-set formulation which is defined similarly to the level set method [53], based on the membership values u. Hence, the curve C is represented by the Lipschitz function u by: $C = \{x \in \Omega : u(x) = 0.5\}$, $inside(C) = \{x \in \Omega : u(x) > 0.5\}$, $outside(C) = \{x \in \Omega : u(x) < 0.5\}$.

The result is given by alternate minimization.

For fixed u, minimizing the energy function $F(C, c_1, c_2, u)$ in (4.21) with respect to c_1 and c_2 by using calculus of variations method [63, 64] gives the following formulas of c_1 and c_2:

$$c_1 = \frac{\int_{\Omega} [u(x)]^m I(x) dx}{\int_{\Omega} [u(x)]^m dx} \quad (4.22)$$

$$c_2 = \frac{\int_{\Omega} [1 - u(x)]^m I(x) dx}{\int_{\Omega} [1 - u(x)]^m dx} \quad (4.23)$$

Then, for fixed c_1 and c_2, the minimization of the energy function $F(C, c_1, c_2, u)$ in (4.21) with respect to u is done by calculus of variations method [63, 64], yielding the variable u

as follows:

$$u(x) = \frac{1}{1 + \left[\frac{(I(x)-c_1)^2}{(I(x)-c_2)^2}\right]^{\frac{1}{m-1}}} \tag{4.24}$$

Note that the regularity term in (4.21) is calculated as follows:

$$|C| = \sum_{i,j} \sqrt{\left(Q_{i+1,j} - Q_{i,j}\right)^2 + \left(Q_{i,j+1} - Q_{i,j}\right)^2} \tag{4.25}$$

where $Q_{i,j} = H(u_{i,j} - 0,5)$, $u_{i,j}$ is the value of u at the (i,j) pixel and $H(\cdot)$ is the Heaviside function. Thus, the length term can be computed knowing $H(u - 0,5)$. For more details, please refer to [47].

For the sake of simplicity, without losing the generality, the above minimization (4.24) has been considered without the length term ($\mu = 0$). The authors have shown that the result is independent from the initial contour in this case, $\mu = 0$ (without regularization). Indeed, one may observe that the energy functional (4.21) is convex with respect to u when $\mu = 0$.

For $\mu \neq 0$, the contour length is calculated by Equation (4.25), then the FEBAC energy functional is not convex with respect to u. However, regularization constraint is useful to segment images affected by noise and objects with week boundaries.

In the Convex Local and Global Region-based with Fuzzy Gaussian Distribution for Active Contour model (C_LGFGD) that we propose in Section 4.5, we developed the contour length regularization term so that the C_LGFGD energy functional is convex for any μ.

The usual approach to solve a minimization of an energy function as (4.21) is to compute its Euler-Lagrange equation and use the steepest descent method, then perform an implicit iteration method. This method requires a smooth version of the Heaviside function and some conditions to ensure numerical stability constrains such as the value of time step in a PDE. To avoid these issues, the authors in [47] proposed an algorithm method for the FEBAC model as follows:

1) Give an initial partition of the image, set $u > 0.5$ for one part and $u < 0.5$ for other.

2) Compute c_1 using (4.22) and c_2 using (4.23).

3) Assume that the value of the x_0 pixel is I_0 and the corresponding fuzzy membership for this point is u_{x_0}. The fuzzy membership u_{x_0} changes to the new value u_{nx_0} by (4.24). Denote by ΔF the difference between the new and old energies calculated at the new and old fuzzy memberships of I_0. The formula of ΔF is expressed as follows (see Appendix C):

$$\Delta F = \mu \Delta l + \frac{s_1 \Delta u_m}{s_1 + \Delta u_m}\left(I_0 - c_1\right)^2 + \frac{s_2 \Delta v_m}{s_2 + \Delta v_m}\left(I_0 - c_2\right)^2 \tag{4.26}$$

where Δl is the change of the contour length, $s_1 = \sum_{x\in\Omega}[u(x)]^m$, $s_2 = \sum_{x\in\Omega}[1-u(x)]^m$, $\Delta u_m = [u_{nx_0}]^m - [u_{x_0}]^m$, $\Delta v_m = [1-u_{nx_0}]^m - [1-u_{x_0}]^m$.

If $\Delta F < 0$, then change u_{x_0} with u_{nx_0}, else keep the old (u_{x_0}) one.

4) Repeat Step 3 to compute the total energy F of the image.

5) Repeat Steps 2-4 until the total energy F remains unchanged.

The convex models of Chan *et al.* [35], Bresson *et al.* [41] and Krinidis *et al.* [47] generally give the global solution for their segmentation problem (except the Krinidis *et al.*'s model with regularization term). The results of these models published in [35, 41, 47] proved that they can be applied successfully for image with homogeneous regions, noises and weak boundaries. However, these models cannot handle the intensity in-homogeneity because the global intensities c_1 and c_2 account for the intensity homogeneity of regions. It is necessary to take into account local image information in the energy function to segment image affected by intensity in-homogeneity.

In the next sections of the chapter, we will present three proposed convex models which incorporate the local information with or without combining the global information in the energy function to tackle the intensity in-homogeneity issue.

4.3 First Proposed Convex Model: A Convex Local Region-based Active Contour Model for Image Segmentation (C_LR)

In this section, we will first describe the C_LR model, then the minimization problem, followed by the fast algorithm used to solve the minimization problem. Finally, we present the investigation on the sensibility of model parameters as well as the experiments results to evaluate the performance of the proposed convex model.

4.3.1 Description of the C_LR model

Let us introduce the basic idea of this model. The proposed model is designed to:

i) accurately segment objects affected by IIH, noises or objects with smooth, blur or discontinuous boundaries.

ii) provide the same and reliable results whatever the initialization.

In order to achieve objectives i), we adopt the region-based approach for its robustness to noises and weak/blur boundaries. To cope with IIH, we simply take into account local

intensity information into the region-based active contour models. Thus, instead of using global and constant means, we use smooth functions that approximate the local intensities inside and outside the contour.

In order to obtain accurate and stable result in case of noises, we need to regularize the evolving curve by choosing appropriate length regularized term to obtain the minimal distance while smoothing the curve to avoid the model to be trapped into local minimum. This can be handled by adopting the weighted total variation regularization term of the Bresson *et al.*'s model [41]. Indeed, this regularization term combines the accuracy of an edge detection using gradient information with the smoothness constraint by the total variation of the level set function restricted in [0,1]. By this way, this regularization function is convex with respect to this level set function and similar with the GAC model.

Hence, as final segmentation, we can expect for a smooth contour of minimal length which minimizes the fidelity (in terms of local intensity differences) between the original image intensity and the associated piecewise-smooth approximation of the original image.

We will now give more details on the method.

Let $\Omega \subset \mathbb{R}^2$ be a bounded image domain and $I : \Omega \to \mathbb{R}^+$ be a given image on this domain.

As the model takes into account local information, local intensity mean is used as descriptor and computed on a neighborhood using a non-negative kernel function $K : \mathbb{R}^2 \to [0, +\infty)$ with the following properties:

1. $K(-u) = K(u)$,
2. $K(u) \geq K(v)$ if $|u| \leq |v|$,
3. $\int_{\mathbb{R}^2} K(x)dx = c$, where $c > 0$.

It follows from property 3) that $\lim_{|u|\to\infty} K(u) = 0$. To comply with the above conditions, the following Gaussian function is selected as a kernel:

$$K_\sigma(u) = \frac{1}{\sqrt{2\pi}\sigma} \exp\left(\frac{-|u|^2}{2\sigma^2}\right) \tag{4.27}$$

where σ is the standard deviation.

As explained above, to cope with the requirements i) and ii), the convex local region-based active contour model is formulated as follows:

$$\min_{\substack{u_1,u_2 \\ 0\leq f\leq 1}} \left\{ E(u_1, u_2, f) = \mu TV_g(f) + \int_\Omega f(x)e_{in}(x, u_1)dx + \int_\Omega (1 - f(x))e_{out}(x, u_2)dx \right\} \tag{4.28}$$

where x is a pixel in Ω, u_1 (and u_2) is the smooth function that approximates local intensity inside (outside, respectively) the contour, μ denotes a positive constant, f is a bounded

level set function in $[0, 1]$. An illustration for u_1 and u_2 is presented in Figure 4.1 where u_1 is the average intensity of $I(x)$ on the yellow region and u_2 is the average intensity of $I(x)$ on the green region.

The energy function (4.28) contains three terms. The first one is the weighted total variation regularization term, with $TV_g(f)$ defined as:

$$TV_g(f) = \int_\Omega g(x)|\nabla f(x)|dx. \tag{4.29}$$

where $|\nabla f(x)| = \sqrt{\left(\frac{\partial f}{\partial x_1}\right)^2 + \left(\frac{\partial f}{\partial x_2}\right)^2}$ and g is the edge detection function: $g(x) = \frac{1}{1+|\nabla I(x)|^2}$.

The second and third terms are the data fidelity terms. Here, e_{in} (e_{out}) represents the local differences in intensity between the average intensity u_1 (u_2, respectively) and the image I. These data fidelity terms are computed within the local Gaussian K_σ window :

$$e_{in}(x, u_1) = \frac{\int_\Omega K_\sigma(x-y)(I(x)-u_1(y))^2 dy}{\int_\Omega K_\sigma(x-y)dy} \tag{4.30}$$

$$e_{out}(x, u_2) = \frac{\int_\Omega K_\sigma(x-y)(I(x)-u_2(y))^2 dy}{\int_\Omega K_\sigma(x-y)dy} \tag{4.31}$$

where x and y are pixels. We can also see that these fidelity terms are the local variances of image in this local Gaussian window.

Note that, if the pixel y is far from the pixel x, the Gaussian kernel $K_\sigma(x-y)$ approaches zero. In particular, the values of this kernel are effectively zeros when $|x-y| > 3\sigma$ [77]. Therefore, the energy:

$$E^x(u_1, u_2, f) = f(x)e_{in}(x, u_1) + (1-f(x))e_{out}(x, u_2) \tag{4.32}$$

is dominated by only the pixels in the neighborhood $\{y : |x-y| \leq 3\sigma\}$, and we can consider E^x in a ball with a center x and radius 3σ.

Remark 4.3. *Note that formulas* (4.30) *and* (4.31) *are not the same as the formulas of local intensity fitting functions in the Local Binary Fitting (LBF) model [77]: First, the local energy functions defined by $e_{in}(x)$ and $e_{out}(x)$ are computed with the contribution of $u_1(y)$ and $u_2(y)$ and evaluated for y varying over a neighborhood of a point x (integral with respect to y which is the variable of u_1 and u_2), while the local fitting energy of the LBF model is evaluated with the contribution of original image $I(y)$ (integral with respect to y which is the variable of I). Furthermore, we divide the weight function $K_\sigma(x-y)$ by $\int_\Omega K_\sigma(x-y)dy$, which can be considered as the area of the neighborhood of x.*

To determine the finite values of e_{in} and e_{out}, we assume that u_1 and u_2 belong to the space $L^2(\Omega)$ which is a space of square-integrable functions on Ω.

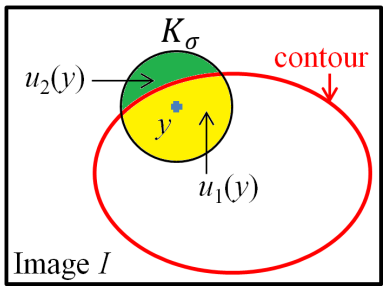

Figure 4.1. An illustration of u_1 and u_2.

As for the convex Chan-Vese model [35] and the Bresson *et al.*'s model [41], function f in our proposed model, is a restricted level set function in [0,1] and plays the same role as the level set function. However, comparing with the conventional level set method where the contour is determined by the zero-level set, the contour in our C_LR method is determined by a threshold α_{thres}, where $\alpha_{thres} \in (0, 1)$. Theorem 4.1, formulated in Section 4.3.3, allows us to select the above threshold as an arbitrary value from (0,1).

4.3.2 Convexity and Fast Minimization

First, we can see that our energy functional E in (4.28) is convex with respect to each variable f, u_1 and u_2. This is an important property of the model used to obtain its globally optimal solution. For more details, a proof is provided in Appendix D.

Since energy function E in (4.28) is convex, any minimizer of E is a global minimizer. Here, minimization of the energy functional in (4.28) is performed in two steps by iteration to find a globally optimal solution of the segmentation model. In the first step, for fixed f, using the calculus of variation, u_1 and u_2 are computed using calculus of variation. In the second step, for fixed u_1 and u_2, we adopt the Fast minimization method based on a Dual Formulation of the Total Variation Norm in [45, 41] to find f. The details of these steps are as follows.

Step 1: For fixed f, using variation calculus method [63, 64] for problem (4.28) with respect to u_1 and to u_2, we obtain:

$$u_1(y) = \frac{\int_\Omega K_\sigma(x-y)I(x)f(x)dx}{\int_\Omega K_\sigma(x-y)f(x)dx} \tag{4.33}$$

$$u_2(y) = \frac{\int_\Omega K_\sigma(x-y)I(x)(1-f(x))dx}{\int_\Omega K_\sigma(x-y)(1-f(x))dx} \tag{4.34}$$

Step 2: For fixed u_1 and u_2, Equation (4.28) is equivalent to the following problem:

$$\min_{0\le f\le 1}\left\{E(f) = \mu TV_g(f) + \int_\Omega f(x)e_r^{CLR}(x, u_1, u_2)dx\right\} \tag{4.35}$$

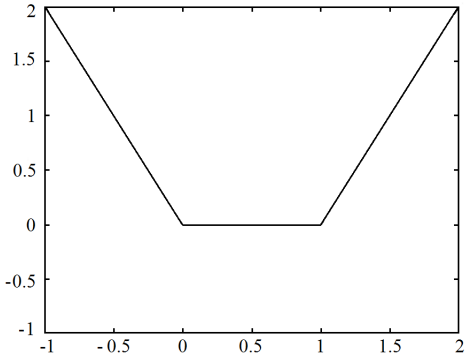

Figure 4.2. Graph of the function $\psi(z) = max\{0, 2|z - \frac{1}{2}| - 1\}$.

where $e_r^{CLR}(x, u_1, u_2) = e_{in}(x, u_1) - e_{out}(x, u_2)$, $x \in \Omega$.

Then, we consider the following claim proposed by Chan *et al.* [35] to change the constrained minimization problem (4.35) to an unconstrained minimization problem.

Claim 4.2. [35] *Let $e_r^{CLR}(x) \in L^\infty(\Omega)$, for $u_1, u_2 \in \mathbb{R}$, $\mu \in \mathbb{R}^+$, then the convex constrained minimization problem (4.35) has the same set of minimizers as the following convex and unconstrained minimization problem:*

$$\min_f \left\{ F(f) = \mu TV_g(f) + \int_\Omega (f(x)e_r^{CLR}(x) + \alpha\psi(f(x)))dx \right\} \tag{4.36}$$

where $\psi(z) = max\{0, 2|z - \frac{1}{2}| - 1\}$ is a penalty function provided that the constant α is chosen large enough such that $\alpha > \frac{1}{2}\|e_r^{CLR}(x)\|_{L^\infty(\Omega)}$.

Note that, one can solve the minimization problem (4.36) by two different approaches. In the first approach, one can use the PDE method as in Chan *et al.* [35] to solve the problem by deriving its Euler-Lagrange equation and the gradient descent based method. For that, its Euler-Lagrange equation is obtained with:

$$\frac{\partial F}{\partial f} = 0 \tag{4.37}$$

where

$$\frac{\partial F}{\partial f} = -\mu\nabla \cdot \left(g\frac{\nabla f}{|\nabla f|} \right) + e_r^{CLR}(x) + \alpha\psi'(f) \tag{4.38}$$

Then, the gradient descent method is used to obtain the following evolution equation of the contour:

$$\frac{\partial f}{\partial t} = -\frac{\partial F}{\partial f} \tag{4.39}$$

For numerical implementation, an approximation of the term $|\nabla f|$ in Equation (4.38) is required by $\sqrt{|\nabla f|^2 + \epsilon}$, where ϵ is a small positive constant. This approximation is necessary because $|\nabla f|$ in the term $TV_g(f)$ is not differentiable with respect to f if $|\nabla f| \equiv (0, 0)$. However, the iteration process depends on ϵ which slows down the speed to obtain the steady-state solution. On the other hand, if ϵ is not small enough, the obtained solution does not belong to $[0, 1]$.

Unlike the first approach for solving the problem (4.36), the second approach uses a convex regularization by a dual formulation of the Total Variation Norm algorithm which is proposed by Chambolle [45] for denoising, and adapted by Bresson *et al.* [41] for segmentation. Since the second method is computationally cheaper, we select this one to solve our minimization problem (4.36).

Fast minimization for Dual Formulation

For technical convenience, we change Problem (4.36) to the following equivalent problem:

$$\min_f \left\{ F(f) = TV_g(f) + \int_\Omega (\frac{1}{\mu} f(x) e_r^{CLR}(x) + \frac{\alpha}{\mu}\psi(f(x)))dx \right\} \tag{4.40}$$

The dual problem of (4.40) is formulated by incorporating a variable v as follows:

$$\min_{f,v} \left\{ F^{dual}(f, v) = TV_g(f) + \frac{1}{2\theta}\int_\Omega (f - v)^2 dx + \int_\Omega (\frac{1}{\mu} e_r^{CLR}(x, u_1, u_2)v(x) + \frac{\alpha}{\mu}\psi(v(x)))dx \right\} \tag{4.41}$$

where $\theta > 0$ must be chosen sufficiently small to force $|f - v|$ to be close to 0. Indeed, if θ is small, $\frac{1}{2\theta}$ is large. Thus, $|f - v|$ must be small to minimize F^{dual}.

Remark 4.4. *We can see that the energy function $F^{dual}(f, v)$ in* (4.41) *is the same as the energy function $F^{B-dual}(f, v)$ in* (4.14) *(in the convex model of Bresson et al. [41]). Thus, energy functional* (4.41) *is convex with respect to f and to v. It follows that we can use the iteration method to find the value of each of the variables f and v to minimize $F^{dual}(f, v)$.*

Therefore, the two following minimization problems are considered to solve the minimization problem (4.41).

1) For fixed f, we determine v as a solution of:

$$\min_v \left\{ \frac{1}{2\theta}\int_\Omega (f(x) - v(x))^2 dx + \int_\Omega (\frac{1}{\mu} e_r^{CLR}(x, u_1, u_2)v(x) + \frac{\alpha}{\mu}\psi(v(x)))dx \right\} \tag{4.42}$$

2) For fixed v, we search for f as a solution minimizing:

$$\min_f \left\{ TV_g(f) + \frac{1}{2\theta} \int_\Omega (f(x) - v(x))^2 dx \right\} \tag{4.43}$$

The Equations (4.42) and (4.43) allow us to apply the following two propositions proven in [45, 41].

Proposition 4.3. *The solution of Equation (4.42) is given by:*

$$v(x) = \min\{\max\{f(x) - \frac{\theta}{\mu} e_r^{CLR}(x, u_1, u_2), 0\}, 1\}. \tag{4.44}$$

Proposition 4.4. *The solution of Equation (4.43) is given by:*

$$f = v - \theta \text{div} p \tag{4.45}$$

where div *is the divergence operator and* $p = (p^1, p^2)$ *is given by the approximate solution of Equation (4.46):*

$$g(x)\nabla(\theta \text{div} p - v) - |\nabla(\theta \text{div} p - v)|p = 0 \tag{4.46}$$

The previous equation can be solved by a fixed point method with the initial value $p_0 = (0, 0)$ *and iteration formula:*

$$p_{n+1} = \frac{p_n + \tau\nabla(\text{div} p_n - \frac{v}{\theta})}{1 + \frac{\tau}{g(x)}|\nabla(\text{div} p_n - \frac{v}{\theta})|} \tag{4.47}$$

where τ *is the temporal step.*

4.3.3 Algorithm for segmentation by the C_LR model

To find the final segmentation with this model, an iterative approach is used with two steps for each iteration. In the first one, we fix f and calculate the local intensities u_1 and u_2 by using variation calculus method [64]. In the second step, we fix u_1, u_2, and determine f by applying the algorithm of Chambolle [45] for denoising adapted by Bresson *et al.* [41] for segmentation.

1) In the first step, by fixing f and using variation calculus, we obtain the following formulas:

$$u_1(y) = \frac{\int_\Omega K_\sigma(x - y) I(x) f(x) dx}{\int_\Omega K_\sigma(x - y) f(x) dx} \tag{4.48}$$

$$u_2(y) = \frac{\int_\Omega K_\sigma(x - y) I(x)(1 - f(x)) dx}{\int_\Omega K_\sigma(x - y)(1 - f(x)) dx} \tag{4.49}$$

It is easy to see that local intensities $u_1(y)$ and $u_2(y)$ are calculated by the integral on the Gussian K_σ window, but expressed here by the integral on Ω. Indeed, since $K_\sigma(x-y)$ is small enough if $|x-y| \geq 3\sigma$. So the functions under the integrals are small (as we mentioned in section 4.3.1). It follows that the values of these integrals could be approximated with the integrals on the neighborhood $\{x : |x-y| \leq 3\sigma\}$ of the pixel y, providing $u_1(y)$ and $u_2(y)$ in this neighborhood of y. This is the reason why they are called local intensities.

Remark 4.5. *We can rewrite the formulas* (4.48) *and* (4.49) *under the convolution formulas as follows:*

$$u_1(y) = \frac{\int_\Omega K_\sigma(x-y)I(x)f(x)dx}{\int_\Omega K_\sigma(x-y)f(x)dx} = \frac{\big(K_\sigma * (If)\big)(y)}{(K_\sigma * f)(y)} \tag{4.50}$$

$$u_2(y) = \frac{\int_\Omega K_\sigma(x-y)I(x)(1-f(x))dx}{\int_\Omega K_\sigma(x-y)(1-f(x))dx} = \frac{\big(K_\sigma * (I(1-f))\big)(y)}{\big(K_\sigma * (1-f)\big)(y)} \tag{4.51}$$

Computational cost for computing u_2 in Equation (4.51) *is saved as follows. First, we notice that u_2 in Equation* (4.51) *can be rewritten as follows:*

$$u_2(y) = \frac{\big(K_\sigma * I\big)(y) - \big(K_\sigma * (If)\big)(y)}{\big(K_\sigma * \mathbf{1}\big)(y) - \big(K_\sigma * f\big)(y)} \tag{4.52}$$

where $\mathbf{1}$ is the constant function with value 1. In the above expression of u_2 (4.52)*, the second terms in the numerator and the denominator as the same as the numerator and the denominator in u_1* (4.50)*, while the term $K_\sigma * I$ in the numerator and $K_\sigma * \mathbf{1}$ in the denominator do not depend on the evolution of the function f. Therefore, the two convolutions $K_\sigma * I$ and $K_\sigma * \mathbf{1}$ can be computed only once before the iteration. During the iterations, only the two convolutions $K_\sigma * (If)$ and $K_\sigma * f$ are calculated for the evolution of f.*

2) In the second step, we fix u_1 and u_2, then the minimizer f is found as the solution of the minimization problem (4.35) by applying Propositions 4.3 and 4.4.

Then, the global solution of our model is given by a threshold value $\alpha_{thres} \in (0,1)$ determined by the following theorem proven in [35]:

Theorem 4.1. [35] *If $g(x) \in [0,1]$ for $\forall x \in \Omega$, and for fixed u_1 and u_2, and if f is a minimizer of $E(u_1, u_2, \cdot)$ in problem (4.28), then the function*

$$1_{\{x:f(x)\geq\alpha_{thres}\}}(x), \quad x \in \Omega \tag{4.53}$$

is a global minimizer of $E(u_1, u_2, \cdot)$ for all $\alpha_{thres} \in (0,1)$, where $1_{\{x:f(x)\geq\alpha_{thres}\}}(x)$ is the characteristic function of the set $\{x : f(x) \geq \alpha_{thres}\}$. Its value is 0 if $f(x) < \alpha_{thres}$, and is 1 if $f(x) \geq \alpha_{thres}$.

Following the above theory, the fast segmentation algorithm for solving our C_LR model is summarized below.

Algorithm 4.1

Input $I, g, \theta, , \tau, \sigma, \mu, f$ and α_{thres}

Repeat (*)

Calculate u_1, u_2 by (4.50) and (4.52)

Calculate e_{in}, e_{out} by (4.30)-(4.31)

Calculate e_r^{CLR} as in (4.35)

$v = \min\{\max\{f - \frac{\theta}{\mu} e_r^{CLR}, 0\}, 1\}$

$p_0 := (0, 0)$

Repeat (**)

$$p_{n+1} = \frac{p_n + \tau\nabla\left(\text{div}(p_n) - \frac{v}{\theta}\right)}{1 + \frac{\tau}{g}|\nabla\left(\text{div}(p_n) - \frac{v}{\theta}\right)|}$$

To $p_{n+1} \approx p_n$

$f := v - \theta\text{div}(p_{n+1})$

To convergence

$f(x) = 0$ if $f(x) < \alpha_{thres}$

$f(x) = 1$ if $f(x) \geq \alpha_{thres}$

Output f

Paper [45] states that the convergence of p_n is guaranteed for $\tau \leq \frac{1}{8}$. The stopping criteria is $\max(|f_{k+1} - f_k|, |v_{k+1} - v_k|) \leq \epsilon$, where f_j and v_j are values of f and v at the j^{th} iteration, $j = k, k + 1$, and ϵ is a given positive constant.

4.3.4 Sensibility of the parameters of the C_LR model

The goal of this study is to investigate the effects of the parameters of the model on the segmentation.

There are two main parameters which control the results of the C_LR model: the regularization parameter μ (in (4.28)) and the standard deviation σ of local Gaussian window (in (4.27)).

4.3.4.1 Regularization parameter μ

Parameter μ is a positive constant to control the contour length or the scale of segmentation. Large μ allows for detection of as many objects as possible at the finest level. Decreasing μ tends to augment the length of the contour, resulting in segmentation of coarser level by grouping of objects together.

On the other hand, the regularization term $TV_g(f)$ (first term in (4.28)) also includes edge detector g which depends on the gradient of the image information. Thus, the edge

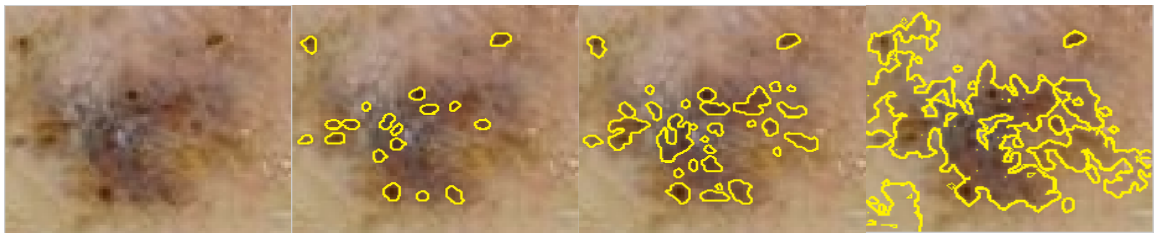

(a) (b) (c) (d)

Figure 4.3. An application of the new region based convex active contour C_LR on a skin lesion image (image courtesy of Nikolay Metodiev Sirakov and Richard Selvaggi, The Texas A&M University-Commerce). (a) Original image. (b)-(d) Results with $\mu = \frac{1}{3}.10^4$, 10^3 and 1, respectively. ($\theta = \tau = 0.1$ and $\sigma = 3$).

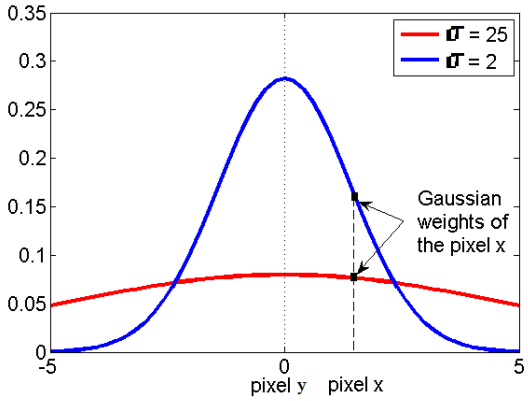

Figure 4.4. Graph of Gaussian kernel.

detector allows for the segmentation of narrow details and fine scale while maintaining smooth curves.

The effect of μ on the scale of the segmentation can be observed in Figure 4.3 which is used for the detection of small objects such as lesion dots. For large values of μ it can be seen as in Figure 4.3b that the C_LR recognizes multiple small objects (lesion dots) with sharp contour. In contrast, smaller value of μ leads to the segmentation of objects at coarser level, grouping many objects into one larger region with smoothly changing contour, as it is shown in Figures 4.3c and 4.3d. Since the dots are small objects, we need to give a high weight for the regularization term. Hence, μ should be large.

4.3.4.2 Standard deviation σ of the local Gaussian window K_σ

In what concerns the parameter σ, the size of the Gaussian kernel window K_σ is defined by $(4\sigma+1)\times(4\sigma+1)$. The local intensities u_1 and u_2 are calculated by the average intensities

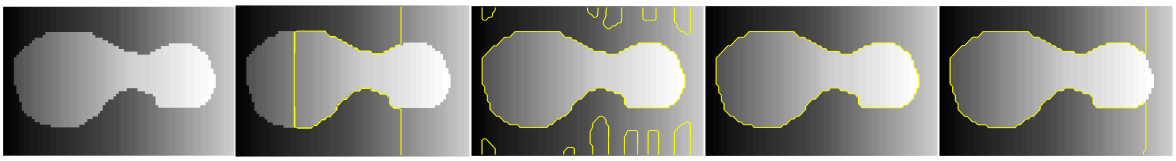

(a) Original image **(b)** convex Chan-Vese **(c)** $\sigma = 2$ **(d)** $\sigma = 7$ **(e)** $\sigma = 13$

Figure 4.5. Results of the C_LR model (c)-(e) on a non-homogeneous synthetic image with different values of σ.

in the neighborhood inside and outside the evolution contour with weights provided from the Gaussian kernel K_σ. Figure 4.4 shows how the graph of the Gaussian changes when σ varies. One may observe that if σ is small (blue line), the value of $K_\sigma(x-y)$ at pixel x closed to y is different from its value at pixel x further from y. This makes the model sensitive to noise. On the contrary, if σ is large (red line), the value of $K_\sigma(x-y)$ at a pixel x closed to y is similar with its value at a pixel x farther from y. If the value of σ is large enough such that the Gaussian window contains the whole image, the local information will become the global information. We may observe the sensibility of σ for dealing with intensity in-homogeneity in Figure 4.5. If σ is small (Figure 4.5c), the window used for the kernel is small. Thus a lot of local information is missed and artifacts are captured. For large σ (Figure 4.5e), the local information is used as global information and the result is rather similar to the one from the convex Chan-Vese [35] (in Figure 4.5b) which uses only global information. On the other hand, the result in Figure 4.5d is accurate with a suitable value of σ.

To summarize, small value of σ makes the model sensitive to noise, while a high value of σ makes the model more robust to noise but this could not handle IIH. Therefore, to deal with IIH and the robustness to noise, σ should be in a bounded interval of values (neither too large or too small).

More results of the C_LR model with varying values of σ can be found in Appendix E.

4.3.5 Experimental results and performance evaluation

To evaluate the performance of our C_LR method, several experiments have been carried out on images with intensity in-homogeneity. Examples are shown here for some synthetic and MR as well as X-Ray images. A comparative evaluation has been performed to demonstrate the advantages our convex region-based model over some existing state-of-the-art convex models such as the convex Chan-Vese [35] and the LBF [77] models. Note that the LBF model is the region-based model which only uses local intensity information in the energy function as our proposed model C_LR, while the convex Chan-Vese only uses global intensity information. The code of the LBF model can be downloaded on the page of the

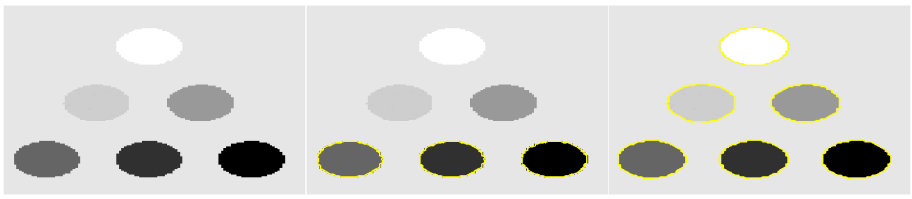

(a) (b) (c)

Figure 4.6. Test on a homogeneous synthetic image: (a) Original image; (b) Result of the convex Chan-Vese model; (c) Result of the C_LR model.

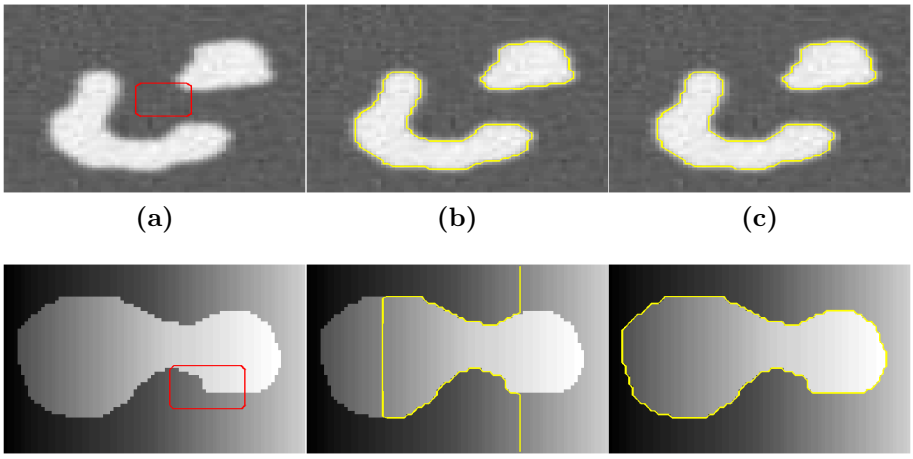

(a) (b) (c)

(d) (e) (f)

Figure 4.7. Test on two synthetic image: First column: Initial contour; Second column: Result of the convex Chan-Vese model; Third column: Result of the C_LR model.

author (http://www. engr.uconn.edu/∼cmli/)

We use the MATLAB r2008a to implement our algorithm. The program was run on a Dell (OptiPlex 360), which has Intel Core 2 Duo E7500 @ 2.93GHz and 4GB RAM. In our numerical experiments, we use the following values of parameters: $\tau = 0.01, \alpha_{thres} = 0.5$. The other parameters are specified in Table 4.3.

Local intensity information versus local intensity information for the intensity in-homogeneity

The goal of this test is to show the advantage of using local information instead of global information to accurately segment image with IIH.

First, we compare the C_LR and the convex Chan-Vese models on a synthetic image which has some homogeneous objects with different intensities in Figure 4.6. One may see that the convex Chan-Vese model detects only three objects with intensities (Figure 4.6b)

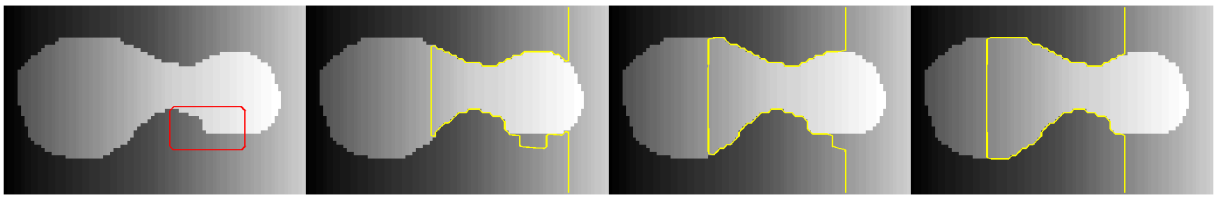

(a) initial contour **(b)** 3^{rd} iteration **(c)** 6^{th} iteration **(d)** 23^{rd} iteration

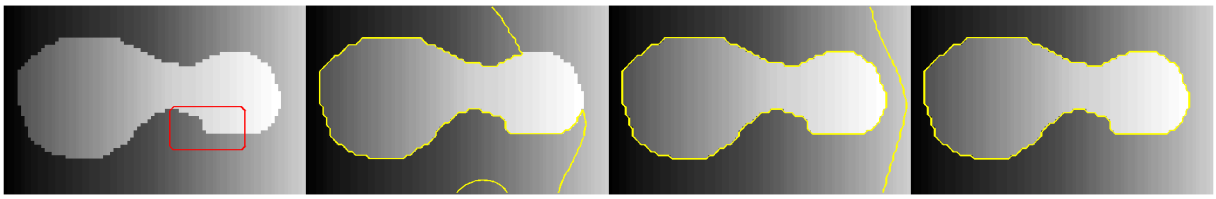

(e) initial contour **(f)** 3^{rd} iteration **(g)** 6^{th} iteration **(h)** 23^{rd} iteration

Figure 4.8. The evolution of the evolving curve by the convex Chan-Vese model (first row) and the C_LR model (second row) for Figure 4.7d.

very different from intensity of background. The three other objects are missed because they have quite similar intensities with the background. This is due to the fact that the convex Chan-Vese model approximates the original image by a piecewise-constant version given by only two global intensities c_1 and c_2 in the energy function. Thus, in this case, the missed objects are considered as background in the result of the convex Chan-Vese model because of their similar intensities with the true background, while the other objects are considered as objects by this model because of the clear difference of their intensities with the background. Contrary to the convex Chan-Vese model, the C_LR recognizes all the objects by using the local intensities instead of global intensities (Figure 4.6c). Indeed, all the objects are considered as "one" object with non-constant intensities. However, since the edge detector in the regularization term helps enhancing the detection at fine scale with an appropriate value of μ, this allows the detection of all these objects.

Figure 4.7 reports the results of the C_LR and the convex Chan-Vese models on two synthetic images where one of them (Figure 4.7a) has two homogeneous objects with similar intensities, while Figure 4.7d is an image with non-homogeneous object and background. As it can be seen in Figure (4.7b) and Figure (4.7c), the final contours of the C_LR and the convex Chan-Vese stop at object boundaries. However, for the image with intensity in-homogeneity in Figure (4.7d), the convex Chan-Vese model cannot evolve the initial contour to the true object boundary, while the C_LR gives the accurate result. We also present the evolution of the contour of this test image (Figure (4.7d)) versus the number of iterations in Figure 4.8.

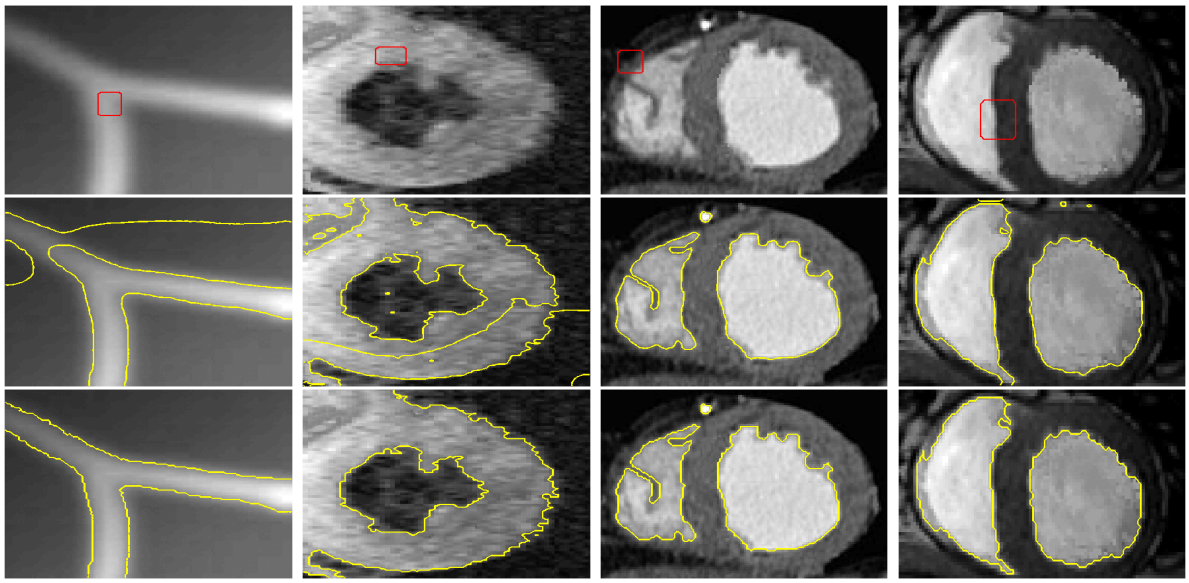

Figure 4.9. Test of the C_LR and the LBF models on blood X-ray (source `http://www.unc.edu/~liwa/`) and heart MR images (sources `http://www4.comp.polyu.edu.hk/~cslzhang/RD/RD.htm` and `http://www.unc.edu/~liwa/`). First row: Initial contour; Second row: Result of the LBF model; Third row: Result of the C_LR model.

Convexity versus Non-Convexity

The objective of this study is to compare the performance of our convex model, namely the C_LR with the non-convex model, namely the LBF, both of them are local region-based AC model.

We achieve the comparison of these models on a blood X-Ray image and three heart MR images in Figure 4.9. These medical images are affected by in-homogeneity. Since, both of the two models use the local information in the energy function, they can efficiently apply to non-homogeneous images. However, while all the results of the C_LR are quite accurate, those of the LBF are only quite good for two heart MR images (3^{rd} and 4^{th} columns). The reason why the LBF failed may be due to the unsuitability of the position of the initial contour. In Figure 4.10, we report the results of the C_LR and the LBF models for some positions of the initial contour. We can see that certain initial contours lead to the accurate result by the LBF model but not for all of the initial contours. On the contrary, the C_LR model gives the same and accurate results for all of the initial contours (position and size and so forth). Moreover, we show in Figure 4.11 the results of the C_LR model for other images with different positions of the initial contour to see that the C_LR model is not dependent on the initial contour since the energy function of the model is convex.

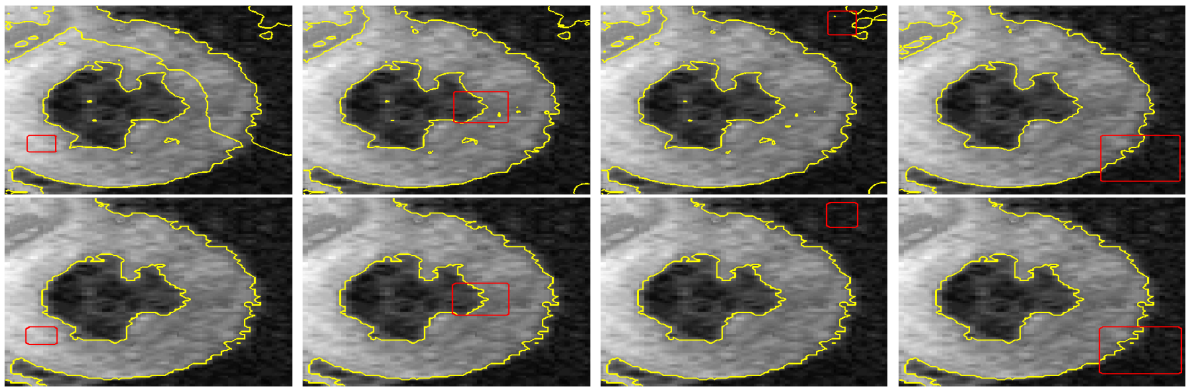

Figure 4.10. Comparison of the C_LR and the LBF models for different initial contours on a heart MR image (source `http://www4.comp.polyu.edu.hk/~cslzhang/RD/RD.htm`). First row: Result of the LBF model; Second row: Result of the C_LR model. Red line: Initial contour; Yellow line: Final contour.

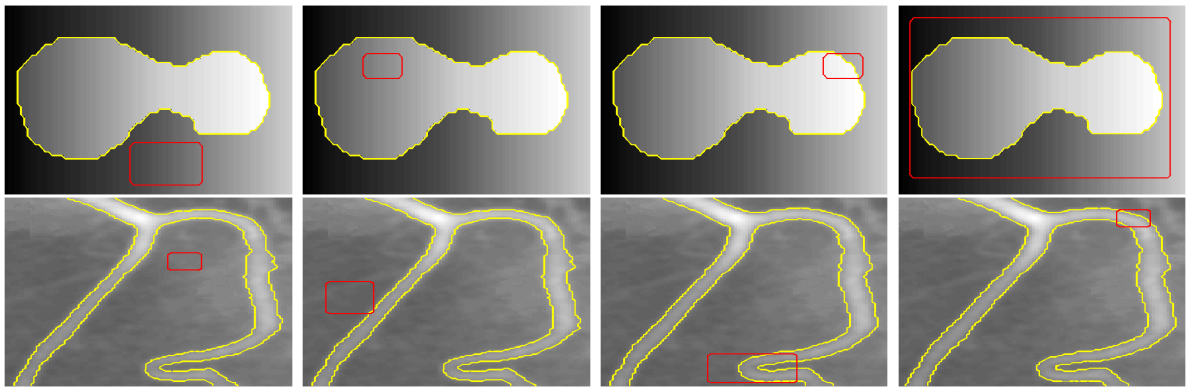

Figure 4.11. Result of the C_LR model for different initial contours on a synthetic image and a blood vessel X-ray image. Red line: Initial contour; Yellow line: Final contour.

Robustness to weak/ blur edges of the C_LR model

Thanks to the regularization term and local information, the proposed C_LR model success in segmenting not only objects with intensity in-homogeneity (see above) but also objects with smooth and blur boundaries. This can be observed in the Blood vessel X-ray images in Figure 4.9 and Figure 4.11 where vessel boundaries are very blur or in some parts of the heart image in Figure 4.12.

Accuracy of the C_LR model

To evaluate quantitatively the accuracy of the proposed model, results of this model are compared with the ground truth established by our expert. In Figure 4.12, an example is reported for the heart MR images. One may observe that the ventricle boundaries of the

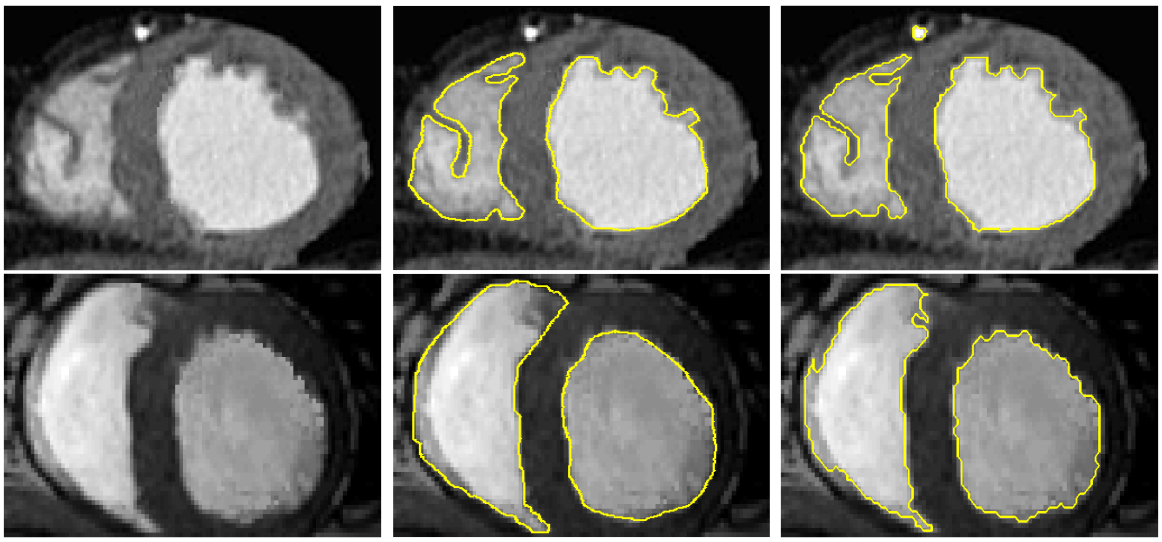

Figure 4.12. Comparison of the result of the C_LR model with the ground truth on two heart MR images (sources `http://www4.comp.polyu.edu.hk/~cslzhang/RD/RD.htm` and `http://www.unc.edu/~liwa/`). First column: Original image; Second column: Ground truth; Third column: Result of the C_LR model.

Table 4.1. DSC values for third column of Figure 4.12

		Row 1	Row 2
DSC	left part	0.93	0.93
	right part	0.98	0.97

heart are accurately extracted, as compared with the contour segmented by our expert. Moreover, to quantitatively evaluate the accuracy of our results, we use Dice Similarity Coefficient (DSC) [88], which is defined as:

$$DSC = \frac{2N(S_1 \cap S_2)}{N(S_1) + N(S_2)} \tag{4.54}$$

where S_1 and S_2 represent the obtained segmentation and the ground truth, respectively, $N(\cdot)$ indicates the numbers of pixels in the enclosed set. The closer the DSC value is to 1, the better the segmentation is. Table 4.1 shows the DSC values of our C_LR method. From this table, our results are very close to the ground truth established by expert, since the DSC values are very close to 1.

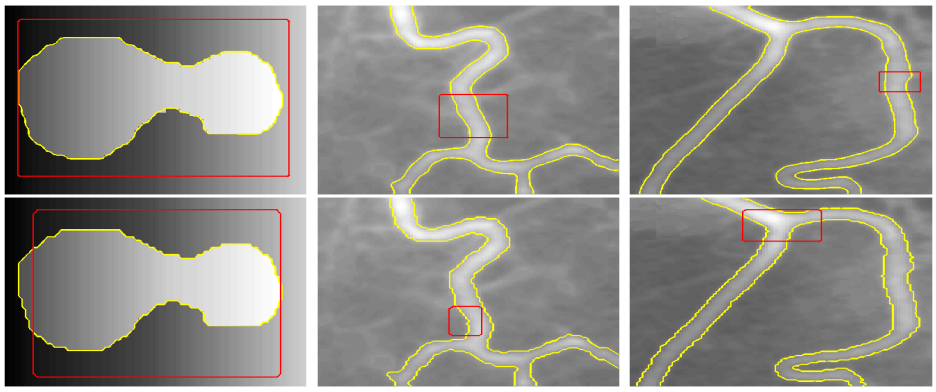

Figure 4.13. The accurate segmentation results of the LBF (top) and the C_LR models (bottom). Red line: Initial contour; Yellow line: Final contour.

Table 4.2. Comparison of the CPU time (in second) and the number of iterations (NoI) between the C_LR and the LBF model for Figure 4.13

	Column 1		Column 2		Column 3	
	Time(s)	NoI	Time(s)	NoI	Time(s)	NoI
The LBF model	0.21	18	1.03	160	2.84	160
The C_LR model	0.12	8	0.20	18	0.58	15

Table 4.3. Parameters of the C_LR model in Section 4.3.5

Figure	4.6	4.7		4.9			
		Row 1	Row 2	Column 1	Column 2	Column 3	Column 4
μ	1	1	1	1	10	10	1
θ	0.01	0.01	0.01	0.01	0.1	0.1	0.01
σ	3	7	7	5	13	13	7

Performance in terms of computational time

Finally, we have made a comparative study for the CPU time between the C_LR and the LBF model using the same images and segmented results. As shown in Figure 4.13 and Table 4.2, the C_LR method not only is faster but also takes less numbers of iterations than the LBF model.

4.3.6 Conclusion

In this section, we have proposed a novel region-based convex active contour model (CLR-GAC) using local intensity information to cope with the intensity in-homogeneity. Unlike existing state-of-the-art local region-based active contour models designed for addressing the intensity in-homogeneity, such as the LBF, we use the bounded level set function instead of the classical level set function to represent the contour and make the energy function convex.

More precisely, to design a convex energy functional, we hybridize the regularization term as in the Bresson *et al.*'s model with the local intensity information from a region-based active contour model. The mean of intensity is used to characterize the region, while the regularization term is the weighted total variation of a bounded level set function (in [0,1]). By restricting the level function in [0,1] and using the total variation regularization, the model is convex, i.e. the segmentation results are the same even if the initial contour starts from different image positions. This makes the accuracy of segmentation invariant with respect to the position of the active contour. It means that every time we apply the C_LR method anywhere on one image, the C_LR model produces the same result and accuracy. These features make the C_LR model reliable and user friendly and suitable for automation. Furthermore, the implementation of our model is performed using the dual formulation and the fast iterative algorithm of Chambolle [45] for denoising and developed by Bresson *et al.* [41] for segmentation.

The list of the main contribution of Section 4.3 is as follows:

1. We have developed a novel local region-based convex energy functional (4.28) with respect to the bounded level set function f used to determine the active contour;

2. The combination of local intensity image information with the convex regularization term allows for addressing the intensity in-homogeneity while guaranteeing accurate and reliable results independently from the initial contours;

3. The region-based active contour using local information allows for robustness with respect to noises, weak/blur edges and gaps.

4. The C_LR parameters μ and σ have been studied and recommendations have been given regarding the values that will provide high accuracy of boundary extraction to non-homogeneous regions with/or without noise.

The advantages of our paper versus the other convex methods and active contours [35, 41, 77] are as follows:

a) Higher accuracy of extraction of multiple non-homogeneous regions;

b) The obtained results are invariant with respect to the position of the initial curve which is guaranteed by the convexity of the model;

c) Computationally fast numerical implementation.

d) From the application field point of view, the C_LGR can be used for medical images such as the X-Ray and the MR images, as well as synthetic and natural images such as those used for dots of skin lesion detection.

4.4 Second Proposed Convex Model: A Convex Local and Global Region-based Geodesic Active Contour for Image Segmentation (C_LGR)

The C_LR model proposed previously is a convex model that takes into account local intensity information into a region-based active contour model to deal with IIH. In this section, we propose to extend the C_LR model by incorporating global intensity energies in addition to the local intensity energies, in order to benefit from the advantages offered by the two local and global energies: the model can efficiently deal with the intensity in-homogeneity, while offering improved performance in terms of robustness when segmenting noisy images or objects with weak/blur boundaries. Furthermore, since the energy functional is convex, it offers reliable segmentation results. Hereafter, we will refer to the proposed model in this section as the C_LGR (convex local and global region-based geodesic active contour). Like the other approaches, such as the LGIF [79] and the LCV [80] models (please see Section 2.2.2) which combine global and local information for dealing with IIH, the robustness of segmentation to noises and initialization is improved compared to the region-based model which only takes into account local information. However, these models are not convex. Thus, they cannot provide reliable results.

First, we will describe the C_LGR model, then present the convex minimization by dual minimization problem, followed by the algorithm used to solve the C_LGR problem. Afterwards, we will present the study on the sensibility of model parameters as well as the experiments results to evaluate the performance of the proposed convex model.

4.4.1 Description of the C_LGR model

Let $\Omega \subset \mathbb{R}^2$ be a bounded image domain and $I : \Omega \to \mathbb{R}^+$ be a given image on this domain.

The objective is always to cope with IIH but the model should offers better robustness to noises and weak/blur edges, while being independent of the initialization.

The region-based contour model is considered. In order to improve the robustness to noises and weak/blur object boundaries, we take into account not only the local intensity

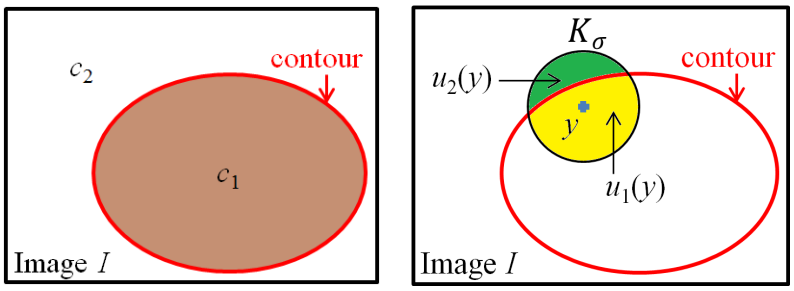

Figure 4.14. Illustration for c_1, c_2, u_1 and u_2 of the C_LGR model.

information for dealing with IIH but also the global intensity information in the region-based approach for its robustness to noises and weak object boundaries. Here, the regions are described locally or globally by the intensity means. So, to take into account the global intensity information, we assume that the image I consists of two regions inside (object) and outside (background) the contour of approximately piecewise-constant intensities of distinct values c_1 and c_2. On the other hand, local intensity information is taken into account by smooth functions that approximate the intensities inside and outside the contour on a local neighborhood using a window. This results in a piecewise-smooth approximation of the image I.

In addition, to obtain a convex model, we adopt the smoothness regularization of the Bresson *et al.*'s model [41] as in the proposed C_LR model (see Section 4.3).

The energy function of the C_LGR model is formulated as follows:

$$\min_{\substack{u_1,u_2,c_1,c_2 \\ 0\le f\le 1}} E(u_1,u_2,c_1,c_2,f) = \mu \int_\Omega g(x)|\nabla f(x)|dx + \lambda E_L(u_1,u_2,f) + \lambda_2 E_G(c_1,c_2,f) \tag{4.55}$$

where x is a pixel in Ω, c_1 and c_2 are constants to approximate global intensities inside and outside the contour respectively, while u_1 and u_2 are smooth functions that approximate the local intensities inside and outside the contour respectively in a local neighborhood which is the Gaussian kernel K_σ window as in the C_LR (Section 4.3), parameters μ, λ, λ_2 are positive constants, f is a bounded level set function in [0, 1], and the function g is the edge detection function: $g(x) = \frac{1}{1+|\nabla I(x)|^2}$. In Figure 4.14, an illustration for c_1, c_2, u_1 and u_2 is presented. In Figure 4.14a, c_1 and c_2 are the average intensities of $I(x)$ on the brown and white regions, respectively, while u_1 and u_2 are the average intensities of $I(x)$ respectively on the yellow and green regions in Figure 4.14b.

The energy function (4.55) contains three terms. The first one is the weighed total variation regularization term, with $TV_g(f)$ defined in (4.28). The second and third terms are the local (E_L) and global (E_G) data fidelity terms respectively.

E_L is the local energy function which depends on the local intensities u_1, u_2, and the function f. Correspondingly, E_G is the global energy function which depends on the global intensities c_1, c_2, and f. These local and global energy functions are defined as follows:

$$E_L = \int_\Omega f(x)e_{in}(x,u_1)dx + \int_\Omega (1-f(x))e_{out}(x,u_2)dx \tag{4.56}$$

$$E_G = \int_\Omega f(x)(I(x)-c_1)^2dx + \int_\Omega (1-f(x))(I(x)-c_2)^2dx \tag{4.57}$$

where e_{in} (e_{out}) represents the fidelity term between u_1 (u_2, respectively) and the image I:

$$e_{in}(x,u_1) = \frac{\int_\Omega K_\sigma(x-y)(I(x)-u_1(y))^2dy}{\int_\Omega K_\sigma(x-y)dy} \tag{4.58}$$

$$e_{out}(x,u_2) = \frac{\int_\Omega K_\sigma(x-y)(I(x)-u_2(y))^2dy}{\int_\Omega K_\sigma(x-y)dy} \tag{4.59}$$

where y is a pixel in Ω, K_σ is a Gaussian kernel with a standard deviation σ.

Hence, as final segmentation, we expect for a smooth contour of minimal length which minimizes the fidelity in terms of local (and global) intensity differences between the original image intensity and the associated piecewise-smooth (piecewise-constant respectively) approximation of the original image.

Remark 4.6. *One may observe that E_L and E_G are the fidelity components of the C_LR and the convex Chan-Vese models, respectively. Therefore, the C_LGR model is a combination between the C_LR and the convex Chan-Vese models. Moreover, because μ, λ and λ_2 are positive and because of the convexity of the C_LR and the convex Chan-Vese models, the energy function of the C_LGR model is convex with respect to each variable f, c_1, c_2, u_1 and u_2.*

4.4.2 Convex minimization problem

As it has been stated in Remark 4.6, the energy functional $E(u_1, u_2, c_1, c_2, f)$ in (4.55) is convex with respect to u_1, u_2, c_1, c_2 and f. This implies that we can minimize the energy function (4.55) with respect to f, to u_1, to u_2, to c_1 and to c_2, separately.

The minimums with respect to u_1, u_2, c_1 and c_2 are calculated by the calculus of variations [64], while the minimum f is found by minimizing a dual minimization problem as presented in the next section.

4.4.2.1 Minimization

As the energy function is convex, we can perform minimization of the model (4.55) in two steps and iterate to obtain the globally optimal final curve.

Step 1: For fixed f, by using variation calculus [64] for problem (4.55) with respect to c_1, to c_2, to u_1 and to u_2, we obtain:

$$c_1 = \frac{\int_\Omega f(x)I(x)dx}{\int_\Omega f(x)dx} \tag{4.60}$$

$$c_2 = \frac{\int_\Omega (1-f(x))I(x)dx}{\int_\Omega (1-f(x))dx} \tag{4.61}$$

$$u_1(y) = \frac{\int_\Omega K_\sigma(x-y)I(x)f(x)dx}{\int_\Omega K_\sigma(x-y)f(x)dx} \tag{4.62}$$

$$u_2(y) = \frac{\int_\Omega K_\sigma(x-y)I(x)(1-f(x))dx}{\int_\Omega K_\sigma(x-y)(1-f(x))dx} \tag{4.63}$$

When u_1 and u_2 are fixed, Equation (4.55) is equivalent to the following problem:

$$\min_{0\le f\le 1}\left\{E(f) = \mu TV_g(f) + \int_\Omega f(x)e_r^{CLGR}(x)dx\right\} \tag{4.64}$$

where

$$\begin{aligned} e_r^{CLGR}(x) &= \lambda e_r^1(x) + \lambda_2 e_r^2(x), \\ e_r^1(x) &= e_{in}(x,u_1) - e_{out}(x,u_2), \\ e_r^2(x) &= (I(x)-c_1)^2 - (I(x)-c_2)^2, \quad x\in\Omega \end{aligned} \tag{4.65}$$

Like the C_LR, we consider the following claim proposed by Chan *et al.* [35] to change the constrained minimization problem (4.64) to unconstrained minimization problem.

Claim 4.3. *Let $e_r^{CLGR}(x) \in L^\infty(\Omega)$, for $u_1, u_2 \in \mathbb{R}$, $\mu \in \mathbb{R}^+$, then the convex constrained minimization problem (4.64) has the same set of minimizers as the following convex and unconstrained minimization problem:*

$$\min_f\left\{F(f) = \mu TV_g(f) + \int_\Omega (f(x)e_r^{CLGR}(x) + \alpha\psi(f(x)))dx\right\} \tag{4.66}$$

where $\psi(z) = max\{0, 2|z-\frac{1}{2}|-1\}$ is a penalty function provided that the constant α is chosen large enough such that $\alpha > \frac{1}{2}\|e_r^{CLGR}(x)\|_{L^\infty(\Omega)}$.

One can observe that Equation (4.66) is similar to Equation (4.36) (in the C_LR model). Using the PDE method to solve (4.66) has the same inconvenience as we mentioned in Section 4.3.2. That is why we apply the algorithm proposed by Chambolle [45] for denoising, and adapted by Bresson *et al.* [41] for segmentation to solve (4.66) since its computationally cheaper.

4.4.2.2 Dual problem

For technical convenience, Problem (4.66) is rewritten as the following equivalent problem:

$$\min_{f}\left\{F(f)=TV_g(f)+\int_{\Omega}(\frac{1}{\mu}f(x)e_r^{CLGR}(x)+\frac{\alpha}{\mu}\psi(f(x)))dx\right\} \tag{4.67}$$

The dual problem of (4.67) is obtained by incorporating a variable v as follows:

$$\min_{f,v}\left\{F^{dual}(f,v)=TV_g(f)+\frac{1}{2\theta}\int_{\Omega}(f-v)^2dx+\int_{\Omega}(\frac{1}{\mu}e_r^{CLGR}(x)v(x)+\frac{\alpha}{\mu}\psi(v(x)))dx\right\} \tag{4.68}$$

where $\theta>0$ must be chosen sufficiently small to force $|f-v|$ to be close to 0.

Like the dual problem (4.41) of the C_LR model, Equation (4.68) is convex with respect to f and to v which implies that we can use an iteration method to find the value of each of the variables f and v to minimize the dual function. Therefore, the following minimization problems are considered:

1) For fixed f, v is a solution of:

$$\min_{v}\left\{\frac{1}{2\theta}\int_{\Omega}(f(x)-v(x))^2dx+\int_{\Omega}(\frac{1}{\mu}e_r^{CLGR}(x)v(x)+\frac{\alpha}{\mu}\psi(v(x)))dx\right\} \tag{4.69}$$

2) For fixed v, we search for f as a solution minimizing:

$$\min_{f}\left\{TV_g(f)+\frac{1}{2\theta}\int_{\Omega}(f(x)-v(x))^2dx\right\} \tag{4.70}$$

The Equations (4.69) and (4.70) allow for applying the following two propositions proven in [45, 41].

Proposition 4.5. *The solution of Equation (4.69) is given by:*

$$v(x)=\min\{\max\{f(x)-\frac{\theta}{\mu}e_r^{CLGR}(x),0\},1\}. \tag{4.71}$$

Proposition 4.6. *The solution of Equation (4.70) is given by:*

$$f=v-\theta\mathrm{div}p \tag{4.72}$$

where div *is the divergence operator and* $p=(p^1,p^2)$ *is given by the approximate solution of Equation (4.73):*

$$g(x)\nabla(\theta\mathrm{div}p-v)-|\nabla(\theta\mathrm{div}p-v)|p=0 \tag{4.73}$$

The previous equation can be solved by a fixed point method with the initial value $p_0 = (0, 0)$ *and iteration formula:*

$$p_{n+1} = \frac{p_n + \tau\nabla(\text{div}p_n - \frac{v}{\theta})}{1 + \frac{\tau}{g(x)}|\nabla(\text{div}p_n - \frac{v}{\theta})|} \tag{4.74}$$

where τ *is the temporal step.*

4.4.3 Algorithm of segmentation by the C_LGR model

To solve the C_LGR model, an iterative approach is used with two steps for each iteration. In the first one, we fix f and calculate u_1, u_2, c_1 and c_2 by using variation calculus method [64]. In the second step, we fix u_1, u_2, c_1, c_2 and determine f by applying the algorithm of Chambolle [45] for denoising adapted by Bresson *et al.* [41] for segmentation.

1) In the first step, by fixing f and using variation calculus, we obtain the following formulas:

$$c_1 = \frac{\int_\Omega f(x)I(x)dx}{\int_\Omega f(x)dx} \tag{4.75}$$

$$c_2 = \frac{\int_\Omega (1 - f(x))I(x)dx}{\int_\Omega (1 - f(x))dx} \tag{4.76}$$

$$u_1(y) = \frac{\int_\Omega K_\sigma(x - y)I(x)f(x)dx}{\int_\Omega K_\sigma(x - y)f(x)dx} \tag{4.77}$$

$$u_2(y) = \frac{\int_\Omega K_\sigma(x - y)I(x)(1 - f(x))dx}{\int_\Omega K_\sigma(x - y)(1 - f(x))dx} \tag{4.78}$$

As mentioned above, the value of $K_\sigma(x - y)$ is close to 0 if x is far from y. Therefore, the values of local intensities $u_1(y)$ and $u_2(y)$ are dominated by the values $I(x)$ and $f(x)$ when the pixels x are near the pixel y, e.g., when the pixels x are within the neighborhood of the pixel y determined by K_σ. Unlike u_1 and u_2, c_1 and c_2 are calculated without any special point. Thus, c_1 and c_2 are called by global intensities.

Remark 4.7. *As in Remark 4.5 in Section 4.3.3 for the C_LR model, we can rewrite the formulas of* u_1 *and* u_2 *in* (4.77) *and* (4.78) *respectively and under the same convolution formulas and save computation time for* u_2*.*

2) In the second step, we fix u_1 and u_2, then the minimizer f is found as the solution of the minimization problem (4.64) applying Propositions 4.5 and 4.6.

Then, the global solution of the C_LGR model is given by a threshold value $\alpha_{thres} \in (0, 1)$ determined by the Theorem 4.1 in Section 4.3.3.

Therefore, the fast segmentation algorithm for solving the C_LGR model is summarized below.

Algorithm 4.2

Input $I, g, \theta, \mu, \lambda, \lambda_2, \tau, \sigma, f$ and α_{thres}

Repeat (*)

Calculate c_1, c_2, u_1 and u_2 by (4.75) (4.76) (4.77) and (4.78)

Calculate e_{in}, e_{out} by (4.58)-(4.59)

Calculate e_r^1, e_r^2, e_r^{CLGR} as in (4.64)

$v = \min\{\max\{f - \frac{\theta}{\mu} e_r^{CLGR}, 0\}, 1\}$

$p_0 := (0, 0)$

Repeat (**)

$$p_{n+1} = \frac{p_n + \tau\nabla\left(\mathrm{div}(p_n) - \frac{v}{\theta}\right)}{1 + \frac{\tau}{g}\left|\nabla\left(\mathrm{div}(p_n) - \frac{v}{\theta}\right)\right|}$$

To $p_{n+1} \approx p_n$

$f := v - \theta \mathrm{div}(p_{n+1})$

To convergence

$f(x) = 0$ if $f(x) < \alpha_{thres}$

$f(x) = 1$ if $f(x) \geq \alpha_{thres}$

Output f

Paper [45] states that the convergence of p_n is guaranteed for $\tau \leq \frac{1}{8}$. The stopping criteria is $\max(|f_{k+1} - f_k|, |v_{k+1} - v_k|) \leq \epsilon$, where f_j and v_j are values of f and v at the j^{th} iteration, $j = k, k+1$, and ϵ is a given positive constant.

4.4.4 Sensibility of the parameters of the C_LGR

The objective of this study is to investigate the effects of the parameters of the model on the segmentation results. There are four parameters in our C_LGR method: λ (local coefficient), λ_2 (global coefficient), μ (regularization coefficient) and σ.

4.4.4.1 Local and Global trade-off via λ and λ_2 to account for intensity in-homogeneity

The couple of parameters λ and λ_2 control the trade-off between the local term and the global term. When the intensity in-homogeneity is evident, the local component should be dominant to accurately locate object boundaries and the value of λ should be greater than that of λ_2. Generally, we fix $\lambda = 1$ and adapt the value of λ_2 accordingly. In Figure 4.15, we test the C_LGR model on a synthetic image with intensity in-homogeneity, for variable values of λ_2 being 0.01, 1 and 10. We fix $\mu = 1$ and $\lambda = 1$. We can see that when λ_2 increases (Figure 4.15c and Figure 4.15d), the global term is more dominant, and the object is not well detected.

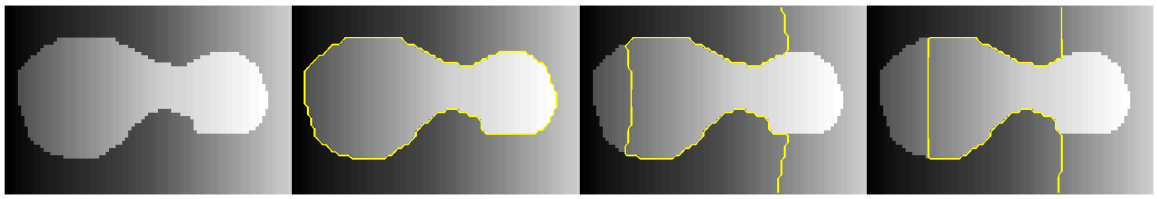

(a) (b) (c) (d)

Figure 4.15. Result of the C_LGR model on a non-homogeneous synthetic image with some different values of λ_2. (a) Original image. (b)-(d) Results with $\lambda_2 = 0.01$, 1 and 10, respectively.

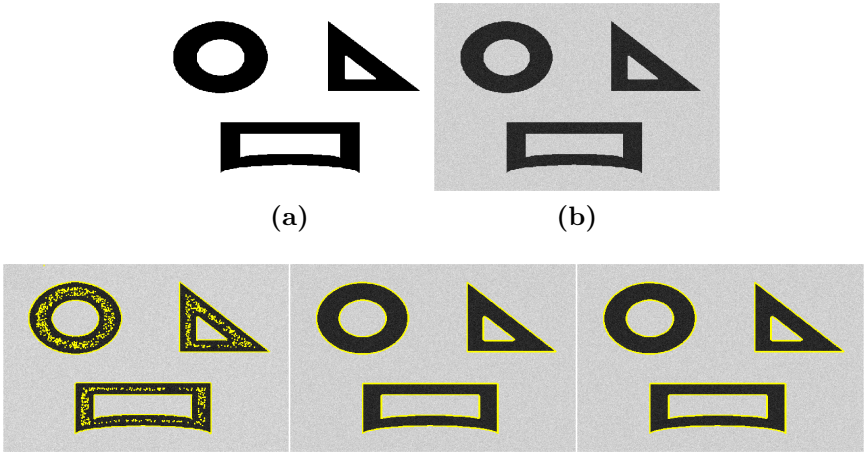

(a) (b) (c) (d) (e)

Figure 4.16. Experiment for a synthetic image. (a) Original image. (b) Version noise of (a). (c) Result of the C_LGR for noisy image (b) with $\sigma = 3$ and $\lambda_2 = 0.01$. (d) Result of the C_LGR for noisy image (b) with $\sigma = 9$ and $\lambda_2 = 0.01$, (e) Result of the C_LGR for noisy image (b) with $\sigma = 3$ and $\lambda_2 = 10$.

4.4.4.2 Regularization parameter μ

The parameter μ controls the effect of contour length or the scale of segmentation. The role of this parameter is the same as μ in the C_LR model: the larger μ, the higher the weight is, resulting in smaller length of the contour or detection of as many objects as possible at the finer level of the segmentation. Conversely, small μ allows for segmentation of a coarse level by grouping of objects together.

4.4.4.3 Standard deviation σ of the local Gaussian window K_σ

Parameter σ has the role as for the as for the C_LR model analyzed in Section 4.3.4.2, since it is also used to define local windows in which the smooth intensities u_1 and u_2 are estimated. Hence, a too small value of σ may result in missed local information and hence fail to deal with IIH, while a too high value of σ tends to approximate local intensity to global intensity.

Moreover, σ has also the influence on noises. Thus, in the C_LGR model, this parameter is particularly useful when segmenting image with high noise. Small value of σ makes the model sensitive to noise, while a high value of σ makes the model more robust to noise. Therefore, to deal with IIH and the robustness to noise, σ should be neither too large or too small.

In the other hand, as previously mentioned, noise influence can be reduced by the global term (third term of Equation (4.55)) in the C_LGR model by selecting high value of λ_2 with respect to λ. However, in case of severe noisy image with intensity in-homogeneity, normally parameter λ_2 should be small with respect to λ to segment objects with intensity in-homogeneity. This in turn leads to reducing the influence of the global term, thus making the effect of noise visible. In this case, a reasonably large value of σ should be chosen to reduce the noise influence. We can see that a trade-off on the value of σ should be made to deal with the robustness to noise (high σ) and IIH (σ should not be too high or too small). This means that without IIH, the model can allows better robustness to noise (high σ).

To summarize, in case of severe image noise, dealing with IIH can be achieved by choosing λ_2 smaller than λ and σ should be in a bounded interval of values.

We can see in Figure 4.16 that the result of segmentation in case of noise is better in the case of high value of σ ($\sigma = 9$) and $\lambda_2 = 0.01$ (see Figure 4.16d) compared with the case of smaller σ and the same global coefficient $\lambda_2 = 0.01$ (see Figure 4.16c) where some contours which are not boundaries of objects are detected, due to the effect of noise. On the other hand, if we augment the value of λ_2 ($\lambda_2 = 10$) to have dominant the global term, the accurate result in case of noise is also obtained although σ is small ($\sigma = 3$, see Figure 4.16e). Note that $\mu = 1$ and $\lambda = 1$ are used for all experiments in this figure.

More experiments for a comparison study of the results with those of the C_LR model with respect to varying values of σ can be found in Appendix E.

4.4.5 Experimental results

In this section, to evaluate the performance of proposed model for images with intensity in-homogeneity, we present the comparison between the C_LGR model with the LGIF [79] and the LCV [80] models as well as with the ground truth given by our expert. Note

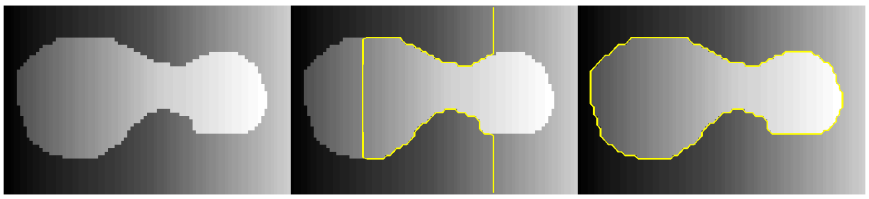

(a) **(b)** **(c)** Original image

Figure 4.17. Results of the C_LGR (c) and the Bresson *et al.*'s (b) models [41] on a non-homogeneous image (a).

that the LGIF and the LCV model also use the global and local information in the energy function. The code of the LGIF model is implemented by incorporating the well-known global component of Chan-Vese model [33] in the LBF code [77] which is downloaded from the page of the author [77], while the code of the LCV model is obtained by email, courtesy of the authors [80].

We use the MATLAB r2008a to implement our algorithm. The program was run on a Dell (OptiPlex 360), which has Intel Core 2 Duo E7500 @ 2.93GHz and 4GB RAM. Here, unless otherwise specified, we use the following parameters $\tau = 0.1$, $\theta = 0.01$, $\alpha_{thres} = 0.5$ and $\lambda = 1$ for all the experiments in this section. The other parameters are reported in Table 4.6.

Ability in dealing with the intensity in-homogeneity - Independence from initialization - Accuracy

First, we demonstrate that the C_LGR can deal with intensity in-homogeneity by comparing with the convex model of Bresson [41, 85]. In [85], Goldstein *et al.* show that the convex model published in [41] can deal with intensity in-homogeneity. However, this is not always true, depending on the content of the image. Figure 4.17 presents results of the C_LGR and the Bresson *et al.*'s models for a synthetic image where the intensities of both object and background vary strongly. One may observe that the convex model of Bresson *et al.* does not give the accurate result which is not the case of the C_LGR model.

Then, we compare with the LGIF model on a synthetic homogeneous image. We will show that that values of variables in our model behave better when minimizing the energy function. This is shown via an example in Figure 4.18. At the point p in Figure 4.18b and Figure 4.18c, the value of u_1 of our model is 149.85, which is more consistent with the intensity of the object (150) than the value f_1 of the LGIF model (148.36). Likewise, the value u_2 of our model is 50.04, which matches more with the intensity of background (50) than the value f_2 of the LGIF model (51.76). Similar observations can be made for the point p_2 in Figure 4.18e and Figure 4.18f. Moreover, at the points p_1 and p_3, our model

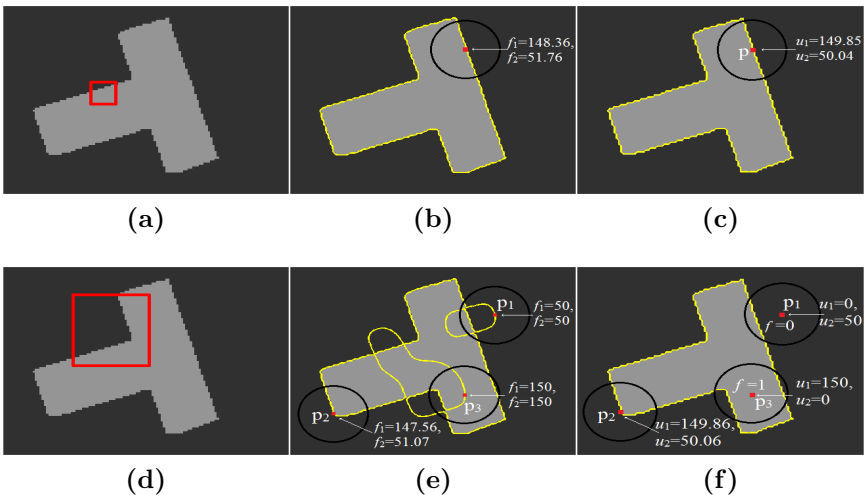

Figure 4.18. Experiment on a synthetic image of the LGIF and our C_LGR models. (a)(d) Original image and intitial contour. (b)(e) Results of the LGIF model. (c)(f) Results of the C_LGR model.

gives the accurate results while the LGIF model failed. Indeed, we can see in Figure 4.18f that $f = 0$ for p_1. As stated in Algorithm 4.2, it means that p_1 is a pixel outside the contour. Likewise, as $f(p_3) = 1$, p_3 is detected as pixel inside the contour. Figure 4.18 allows to show that the result of the LGIF model depends on the initial contour.

In Figure 4.19, we demonstrate the performance of our C_LGR model for addressing the intensity in-homogeneity by comparing with the LGIF and the LCV models for typical images such as blood vessel X-ray and heart MR images. Obviously, our C_LGR method successfully achieves the segmentation of the interested objects for all tested cases while the other models fail all of cases. We can find better results for these images by the LGIF and the LCV models in their papers, or in the Figure 4.23. In fact, the initial contours that we use in Figure 4.19 are not suitable to obtain the good results, because the energy functions of these models are not convex, making the segmentation results dependent on the initial contours.

In Figure 4.20, we compare our C_LGR model with the LGIF and the LCV models on four thorax CT images. We see that only results of our model are satisfactory which is not the case of the results of the LGIF and the LCV models. Moreover, to demonstrate the accuracy of our results, we also present validation results with real expert-segmented thorax CT images. As can be seen in Figure 4.21, the interior boundaries of the thorax are accurately extracted, as compared with the contour segmented by our expert. Furthermore, we can quantitatively evaluate the accuracy of our results with a metric, namely, the Dice

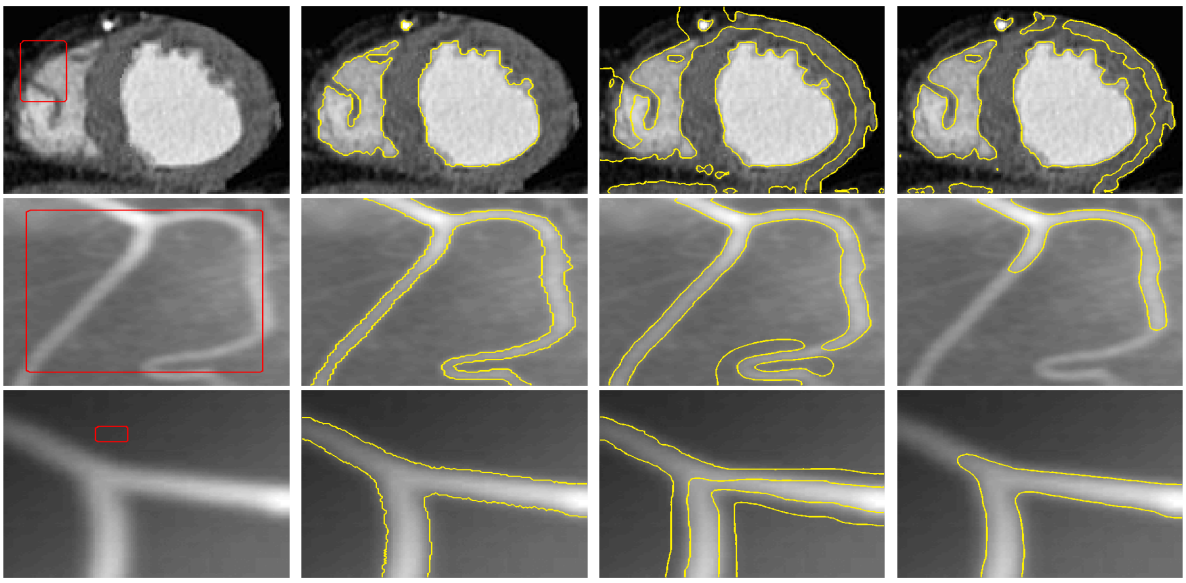

Figure 4.19. Comparison of our C_LGR method with the LGIF and the LCV models for a heart MR and two blood vessel X-ray images (sources `http://www4.comp.polyu.edu.hk/~cslzhang/RD/RD.htm` and `http://www.unc.edu/~liwa/`). Column 1: Original image and initial contour. Columns 2 - 4: Result of the C_LGR, the LGIF and the LCV models, respectively.

Table 4.4. DSC values for third column of Figure 4.21

		row 1	row 2	row 3	row 4
DSC	left thorax	0.94	0.96	0.98	0.97
	right thorax	0.97	0.99	0.99	0.96

Similarity Coefficient (DSC) [88], which is defined as

$$DSC = \frac{2N(S_1 \bigcap S_2)}{N(S_1) + N(S_2)} \tag{4.79}$$

where S_1 and S_2 represent the obtained segmentation and the ground truth, respectively, and $N(\cdot)$ indicates the numbers of pixels in the enclosed set. The closer the DSC value is to 1, the better the segmentation is. Table 4.4 shows the DSC values of the C_LGR method. From this table, we can see that our results are very close to the ground truth established by expert, since the DSC values C_LGR are very close to 1.

To demonstrate the independence from the initial contour of our C_LGR method, we tested on blood vessel and hand X-ray images and a thorax CT image with some different positions of initial contour. The results are shown in Figure 4.22. We can see that, on the each image, the results with the different initial contours are very similar.

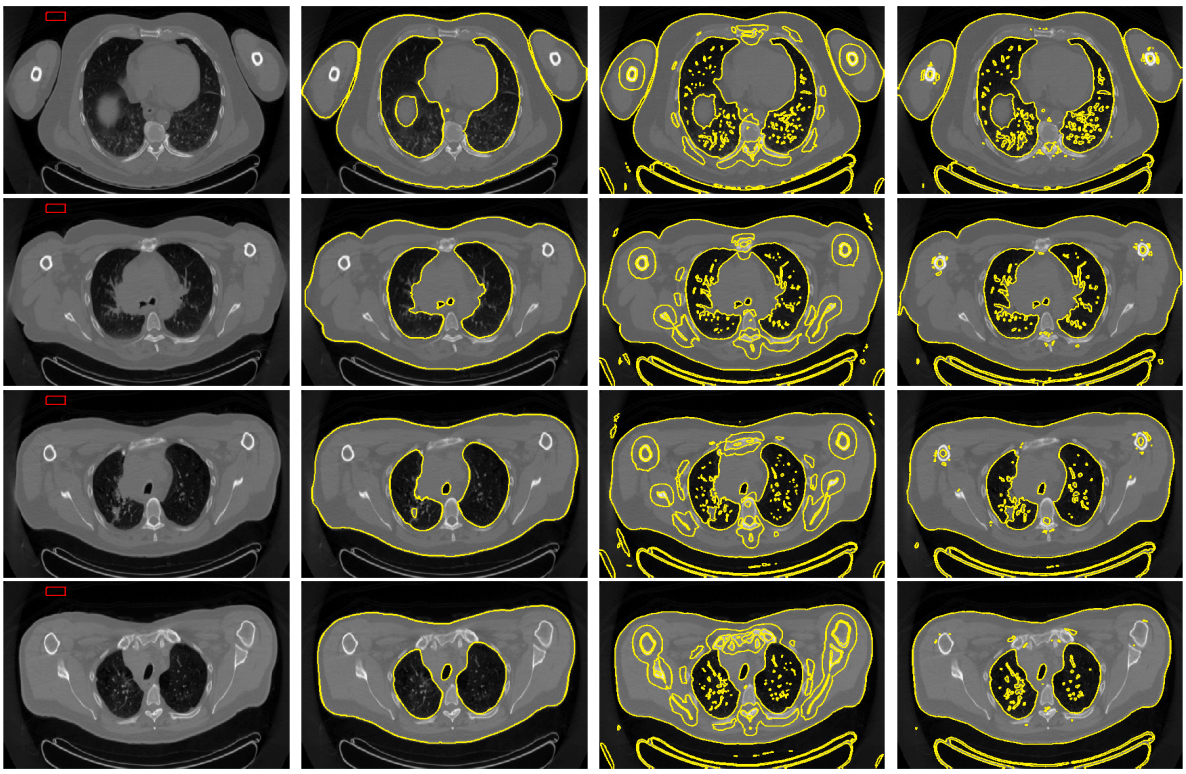

Figure 4.20. Comparison of our C_LGR method with the LGIF and the LCV models for thorax CT images (images courtesy of J.-M. Rocchisani, Avicenne-Medicine Nucleaire Hospital, Bobigny, France). Column 1: original images and initial contour (red). Column 2: results of the C_LGR method (yellow). Column 3: results of the LGIF model (yellow). Column 4: results of the LCV model (yellow).

Table 4.5. Comparing CPU time (in second) and number of the iteration (NoI) between our C_LGR model with the LGIF and the LCV models in Figure 4.23.

	Column 1		Column 2		Column 3	
	Time(s)	NoI	Time(s)	NoI	Time(s)	NoI
The LGIF model	6.44	240	11.58	400	37.88	800
The LCV model	0.39	100	0.68	160	0.36	50
The C_LGR model	2.26	8	2.31	9	2.17	10

Performance in computation time

The last comparison concerns the CPU time, as well as the number of iteration between our model with the LGIF and the LCV models. Accordingly, we found the positions of initial contour such that the results of these models are accurate. To find these positions,

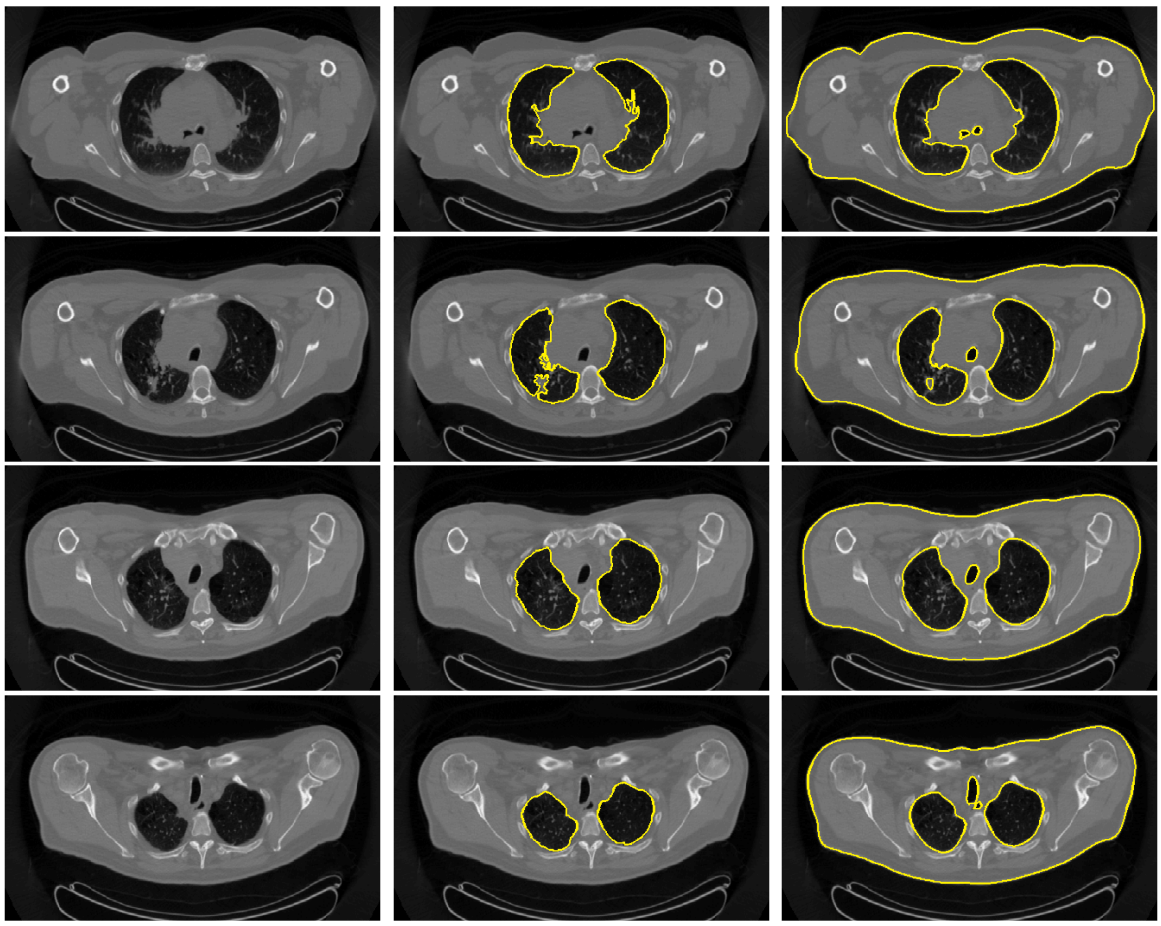

Figure 4.21. Comparison with the ground truth established by our expert for four thorax CT images. Column 1: original images (images courtesy of J.-M. Rocchisani, Avicenne-Medicine Nucleaire Hospital, Bobigny, France). Column 2: ground truth images on thorax CT. Column 3: C_LGR results.

we have based on the original papers of these models [79, 80] for the blood vessel X-ray images. In Figure 4.23, the red lines are the initial contours and the yellow lines are the final contours. The CPU time and the number of iteration of these results are shown in Table 4.5. It is easy to see that our C_LGR method not only is faster but also has less number of iteration than the LGIF models. Moreover, we can see that, the CPU time of the LCV model is faster than our model, but the number of iteration is more than our model.

Finally, an interested point of the C_LGR model is that it can apply to segment lesion region in PET image as show in Figure 4.24 and Figure 4.25. The lesion region in PET image has smooth boundary and the intensity of the image is very smooth and fuzzy. This can be seen clearly in Figure 4.25 where we cannot distinguish object and background by

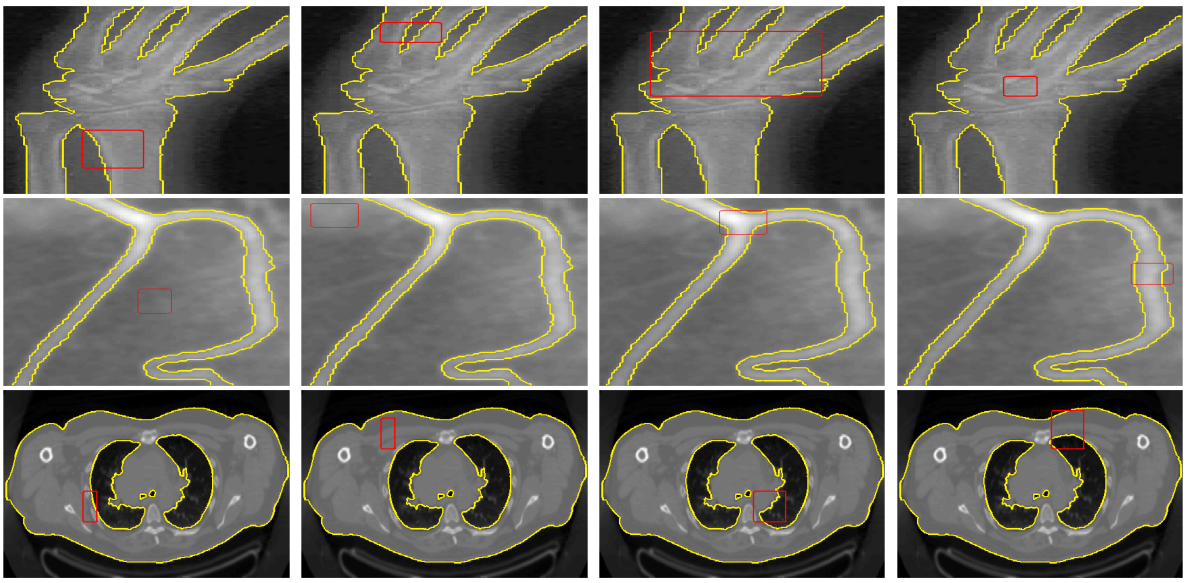

Figure 4.22. Results of our C_LGR method on blood and hand vessel X-ray and thorax CT images with the different positions of initial contour. Red line: initial contour. Yellow line: final contour.

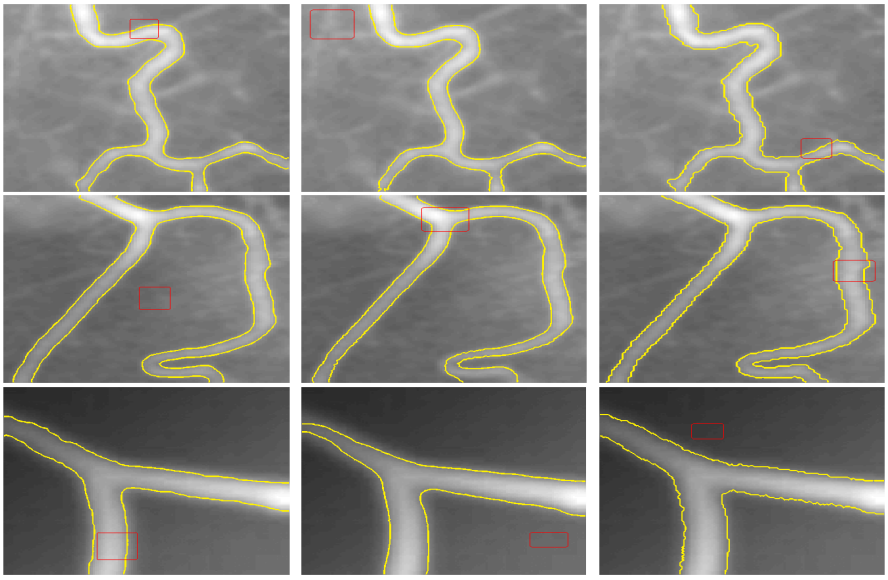

Figure 4.23. Accurate results of the LGIF (column 1), the LCV (column 2) and our C_LGR methods (column 3) on blood vessel X-ray images (source `http://www.unc.edu/~liwa/`). Red line: initial contour. Yellow line: final contour.

eyes. Therefore, the combination between the global and local components in the energy function of C_LGR helps in obtaining good result when segmenting PET image.

Table 4.6. Parameters μ, λ_2 and σ of the C_LGR model in Section 4.4.5

Figure	4.19			4.20	4.24				4.25
	row 1	row 2	row 3	all	e	f	g	h	b
μ	1	1	1	1	1	1	1	1	1
λ_2	1	0.1	0.1	0.1	0.01	0.1	0.1	0.01	0.1
σ	3	15	11	7	13	5	31	3	3

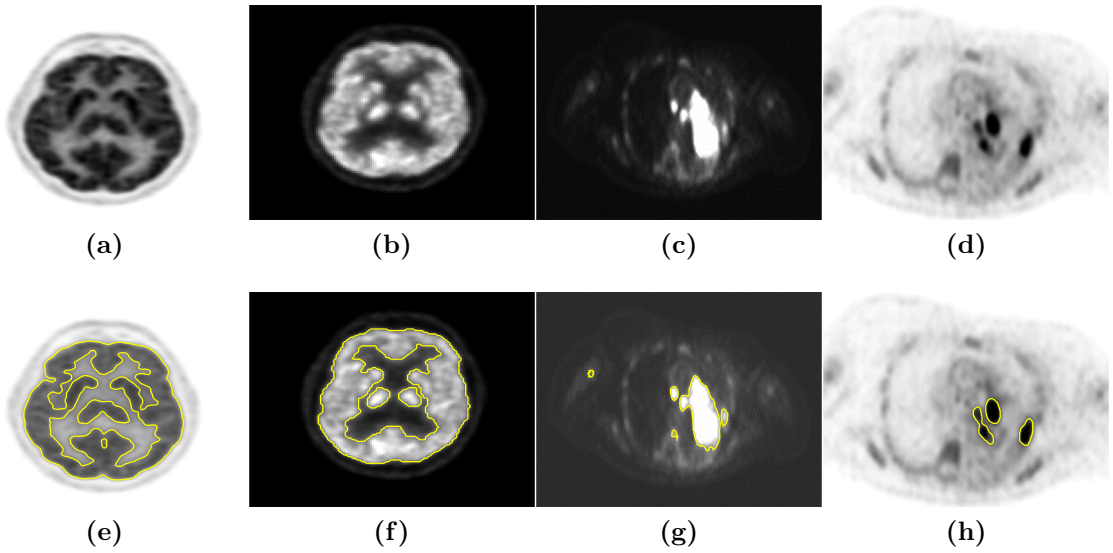

Figure 4.24. Results of C_LGR for PET images (images courtesy of J.-M. Rocchisani, Avicenne-Medicine Nucleaire Hospital, Bobigny, France).

4.4.6 Conclusion

The list of the main contribution of this paper is as follows:

1. We have developed a novel local and global region-based convex energy functional C_LGR with respect to the bounded level set function f used to determine the active contour to efficiently deal with the Intensity In-homogeneity and make the model independent with respect to initial contour, hence providing reliable results.

2. The combination of local intensity image information with the global intensity information allows improving the robustness to noises and weak object boundaries compared to the C_LR.

3. The C_LGR parameters λ, λ_2, μ and σ have been studied and recommendations has been provided as to the values that will provide high accuracy of boundary extraction

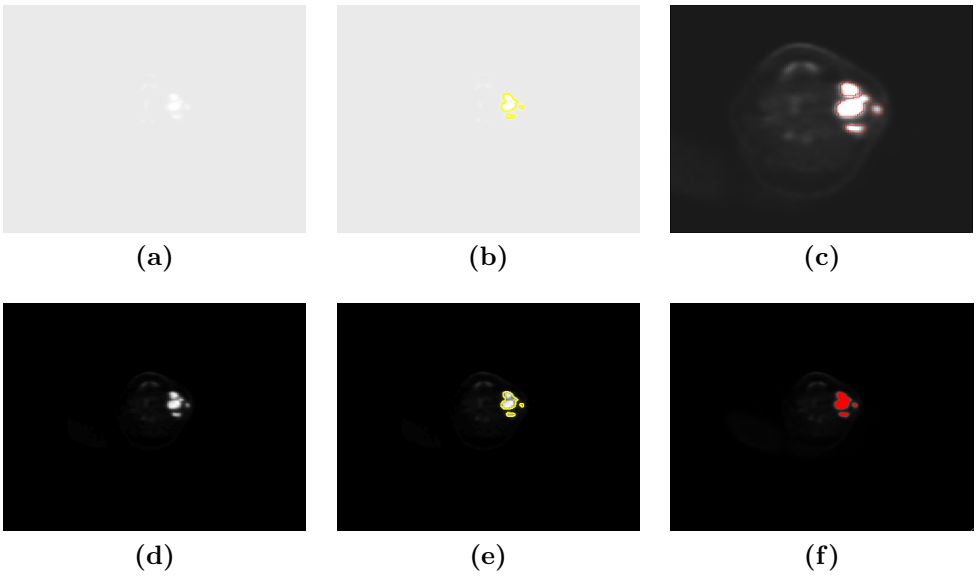

Figure 4.25. Result of the C_LGR model on a neck PET image: (a) Original image (images courtesy of J.-M. Rocchisani, Avicenne-Medicine Nucleaire Hospital, Bobigny, France), (b) Result of (a), (c) Ground truth in zoom, (d) Hight contrast of (a), (e) Hight contrast of (b), (f) Hot-spot by threshold 40% max.

to non-homogeneous regions with/or without noise.

The advantages of our paper versus the other convex methods and active contours [35, 41, 79, 80] are as follows:

a) Higher accuracy of extraction of multiple non-homogeneous regions;

b) The obtained results are invariant with respect to the position of the initial curve which is guaranteed by the convexity of the model;

c) Computationally fast numerical implementation.

d) From the application field point of view, the C_LGR is successfully tested on medical images such as the X-Ray, CT, MR and PET images, as well as synthetic and natural images such as those used for skin lesion detetion.

4.5 Third Proposed Convex Model: A Convex Local and Global Fuzzy Gaussian Distribution Energy Minimization of an Active Contour Model (C_LGFGD)

The two previously proposed convex models have proven their ability of dealing with IIH and the robustness to noises as well as weak boundaries. However, a trade-off is required for the performance of segmentation when dealing with simultaneous IIH and noises. In this case, the performance of the model is reduced compared with the case when image is only affected with IIH.

In order to improve the performance when dealing with simultaneous presence of IIH and noises, we propose in this section, another convex region-based AC model which results from the hybridization of a fuzzy clustering with the region-based AC model defined in the Bayesian formulation.

In this fuzzy region-base AC model, fuzzy c-means clustering and region-based AC are combined and defined in the Bayesian approach and provide the local and global region information to attract the curve towards object boundaries. A length regularization term imposes smoothness constraints on the geometry of the curve, providing accurate and stable result in case of noises. The combination of the FCM and the AC model in the Bayesian with full statistics can effectively improve the segmentation results especially in case of simultaneous noises and IIH.

The Fuzzy clustering such as fuzzy c-means can account for uncertainty in medical images (due to noises, limited resolution) by assigning a pixel to different classes (e.g. adjacent tissues) with different memberships.

The Bayesian formulation is adopted in this work to fully account for statistical distribution of the pixel intensity used in a region-based AC. As explained in the state-of-the-art (Chapter 2), Brox and Cremer [43] have shown that, in the Bayesian approach, local region statistics can model the piecewise smooth approximation of intensity within a region, for the region-based approach of the Mu,ford-Shah model. By assuming piecewise smooth variation of the intensity for IIH, Bayesian is a good framework to describe IIH and regions. Here, regions are described by the statistical distribution of the pixel intensity. In the present method, intensity is assumed to be the realization of an independent random variable described by the Gaussian probability density function (pdf) with varying means and standard deviation.

To effectively deal with the intensity in-homogeneity and the robustness to noise and to weak edges, the region-based approach is defined with the local and global information distributions. The local information is taken into account to tackle the intensity in-homogeneity, while the global information is used to handle the objects whose boundaries

are not well defined by the gradient.

Furthermore, in order to obtain accurate and stable result in case of noises, we need to regularize the evolving curve by choosing appropriate length regularized term to obtain the minimal distance while smoothing the curve. Unlike the two previous convex models (C_LR and C_LGR) where the smoothness regularization constraint is the total variation of the level set function restricted in [0,1], we adopt the total variation of the membership function which is also a restricted function in [0, 1]. So, the membership function can be considered as the pseudo level-set function. Hence, the regularization term is similar to the one in the convex Chan-Vese model [35]. By this way, this regularization function is convex with respect to this bounded level set function.

Hereafter, we will refer to our model as C_LGFGD (convex local and global fuzzy Gaussian distribution).

We will first describe the related works and then present our proposed convex model along with the pseudo level set formulation, the convexity of the energy functional and the numerical implementation as well as an illustration of the method through example for a better understanding of the proposed method, and the computational complexity. Like the previously proposed methods, we will report the study of the sensitivity of the parameters of the method followed by the experimental results and comparison.

4.5.1 Related works

In the state-of-the-art, we have described existing on the problem of IIH. Here, we only present some existing works related on the fuzzy approach combined with AC model as well as works on the Bayesian approach. These works also inspired our proposed model.

Some interesting works combined the fuzzy clustering with the ACM to enhance robustness to noises, weak boundaries and initial condition [28, 47]. In [47], Krinidis *et al.* hybridize the region-base active contour model with the fuzzy c-means and obtain an effective ACM based on fuzzy energy, called FEBAC, to segment objects whose boundaries are very smooth and discontinuous. The fuzzy clustering methods provide robust data clustering, while the region-based active contours are robust to noise, weak/blur edges and initialization. However, this model cannot segment images with intensity in-homogeneity by assuming that each region is homogeneous, as the Chan-Vese model does. In [28], fuzzy clustering and level set methods are combined to improve the segmentation accuracy of the brain tissues and robustness to noise. In this method, fuzzy clustering is first performed, and the resulting fuzzy membership degree is used to generate the speed (in direction and norm) of the Geometric/Geodesic Active contour [29] to guide the evolving curve, instead of the edge detector function, avoiding hence the use of gradient information of the image data.

In the Bayesian approach, Wang *et al.* [83] proposed the local-Gaussian-distribution-fitting (LGDF) energy model where statistical characteristics of local intensities are used for more accuracy. This model is effective in dealing with IIH but not convex.

The main and common weakness of these methods is that they depend on the initialization or the energy functional are not convex. Hence, the results are not always the same with respect to the initialization.

4.5.2 Description of the C_LGFGD model

Let us first recall some assumption in this model before presenting the model in details.

Assumption

In this model, intensity is assumed to be distributed by the Gaussian pdf with varying means and standard deviation. In the Bayesian approach, our defined active contour is derived from the energy functional including data terms and a regularization term to account for the smoothness geometric constraints on the curve. Data terms are described by the intensity mainly because the objective is to deal with the variation of intensity due to IIH, which results from a local change of intensity. So, IIH can be handled by taking into account local region information. To characterize the local region information, a neighborhood for each pixel is used such as a Gaussian kernel window, and the region is modelled as a piecewise-smooth approximation of intensity within the local window.

Model description

We search for a final segmentation as a smooth contour of minimal length which minimizes the fidelity in terms of local (and global) intensity differences between the original image intensity and the associated piecewise-smooth (piecewise-constant, respectively) approximation of the original image.

The proposed ACM is based on the minimization of a fuzzy and statistical energy function, which finds the minimal length of curve, while creating a partition of image data into two clusters which minimize the global and local differences in the distributions (varying means and standard deviations) as follows:

$$F(M) = \mu|C| + \lambda F_G(M_G) + (1-\lambda)F_L(M_L) \tag{4.80}$$

where $M = (C, c_1, c_2, \epsilon_1^2, \epsilon_2^2, f_1, f_2, \sigma_1^2, \sigma_2^2, u)$, $M_G = (c_1, c_2, \epsilon_1^2, \epsilon_2^2, u)$ and $M_L = (f_1, f_2, \sigma_1^2, \sigma_2^2, u)$, μ is a positive constant, $|C|$ is the length of the contour C, $0 < \lambda < 1$ is a constant to control the influence of the global term F_G and the local term F_L, c_1 (c_2) and ϵ_1 (ϵ_2) are respectively the global mean and standard deviation of the Gaussian intensity inside the contour C (outside the contour, respectively), while f_1 (f_2) and σ_1 (σ_2) are respectively the

local mean and standard deviation of the Gaussian intensity inside the contour C (outside the contour, respectively).

The first term is the smoothness-regularization term. The last two terms are the local and global energy functionals derived from the fuzzy c-means clustering where c is the number of classes. Here, for dealing with IIH, we only consider two classes ($c = 2$): the first class is the region inside the contour C and the second one is the region outside the contour C.

Let us first describe the data terms. The global and local terms are defined from the fuzzy clustering.

The global data term is defined as an objective function (in terms of global intensity differences) to minimize with respect to the membership function $u_i(y)$ ($i = 1, 2$) and the centroids defined by the pdf (mean c_i and standard deviation ϵ_i):

$$F_G(M_G) = -\int_\Omega \log p(I(y), \epsilon_1)[u(y)]^m dy - \int_\Omega \log p(I(y), \epsilon_2)[1 - u(y)]^m dy \tag{4.81}$$

where $p(I(y), \epsilon_i)$, $i = 1, 2$, is the Gaussian distribution of intensity at pixel location y:

$$p(I(y), \epsilon_i) = \frac{1}{\sqrt{2\pi}\epsilon_i} \exp\left(- \frac{\big(c_i - I(y)\big)^2}{2\epsilon_i^2} \right) \tag{4.82}$$

while $m > 1$ is a weighting exponent, which determines the degree of fuzziness of the resulting clustering, $u_i(y)$ is the membership value of pixel location y for class i such that $\sum_{i=1}^{c} u_i(y) = 1$. Then, in our case ($c = 2$), let us denote the membership value of pixel location inside the contour (class 1) by $u_1(y) = u(y) \in [0, 1]$. Therefore, the membership value of pixel location outside the contour (class 2) is $u_2(y) = (1 - u(y)) \in [0, 1]$.

As to the local data term, it is defined by the following objective function (in terms of local intensity differences) to minimize with respect to the membership function $u_i(y)$ ($i = 1, 2$) (i.e. $u(y)$ and $(1-u(y))$ respectively) and the centroids defined by the pdf (mean f_i and standard deviation σ_i):

$$\begin{aligned} F_L(M_L) = &-\int_\Omega \left[\int_\Omega K_\sigma(x - y) \log p_x(I(y), \sigma_1)[u(y)]^m dx \right] dy \\ &-\int_\Omega \left[\int_\Omega K_\sigma(x - y) \log p_x(I(y), \sigma_2)[1 - u(y)]^m dx \right] dy \end{aligned} \tag{4.83}$$

where x is a pixel, K_σ is a Gaussian kernel with a standard deviation σ, $p_x(I(y), \sigma_i)$, $i = 1, 2$, is the Gaussian distribution with standard deviation σ_i of intensity within the local window centered at y:

$$p_x(I(y), \sigma_i) = \frac{1}{\sqrt{2\pi}\sigma_i} \exp\left(- \frac{\big(f_i(x) - I(y)\big)^2}{2\sigma_i^2} \right) \tag{4.84}$$

Regularization term

The regularisation term is the length term that allows for obtaining the minimal distance while smoothing the curve. We adopt the total variation of the membership function which is also a restricted function in [0, 1]. Here, like the bounded level set function in the convex Chan-Vese model [35], the fuzzy membership function can be considered as the pseudo level-set function since it is a bounded function in [0, 1]. Inspired from the regularization term in the Convex Chan-Vese model, we use the total variation of the membership function as regularization term for our model (see Section 4.5.3).

4.5.3 Pseudo level set formulation

In this section, we formulate the fuzzy energy function by using a pseudo level set formulation based on the membership values of u as defined in [47]. The curve C in Ω is represented by the pseudo zero level set of u such that $C = \{x \in \Omega : u(x) = 0.5\}$, $inside(C) = \{x \in \Omega : u(x) > 0.5\}$, $outside(C) = \{x \in \Omega : u(x) < 0.5\}$.

Now, we change the contour length $|C|$ in (4.80) by the total variation of u as explained above, $TV(u) = \int_\Omega |\nabla u| dx$. This length term can be also interpreted as follows: when the energy function (4.80) is minimized, the membership values u of all the pixels inside located inside the contour C are approximately similar. Likewise, the pixels located outside the contour have similar membership values. In the other hand, the membership values u of the pixels inside the contour C are different from the membership values for the pixels located outside the contour. Thus, $|\nabla u|$ is really different from 0 on the contour C, while it approximates 0 at other image pixels. Thus, the total variation of u allows to obtain the length of the contour C. Besides, $TV(u)$ also ensures to regularize the contour. So, the energy function (4.80) is transformed as follows:

$$F(M) = \mu \int_\Omega |\nabla u| dx + \lambda F_G(M_G) + (1 - \lambda) F_L(M_L) \tag{4.85}$$

4.5.4 Convexity of the proposed energy functional

As for the C_LR and the C_LGR models, the first term in Equation (4.85) is convex with respect to u. The convexity of F_G and F_L with respect to u is obtained by their positive twice derivatives with respect to u. Then, because μ, λ and λ_2 are positive, energy functional (4.85) is convex with respect to u.

The convexity of F with respect to the other variables is also proved as their twice derivatives with respect to these variable are positive.

The convexity with respect to each of variables allows us to find a global solution. So, the minimizer of (4.85) can be found by minimizing separately each of variables when the others are fixed.

4.5.5 Numerical implementation

The energy function could be minimized by the gradient descent method derived from the Euler-Lagrange equation which converges relatively slowly and need some conditions for the numerical stability issues. However, for the C_LGFGD model, we apply the fast numerical scheme which is proposed by Song *et al.* [46] and developed by Krinidis *et al.* [47]. Instead of solving the Euler-Lagrange equation, this method calculates the energy directly and verifies if the energy decreases when the intensity membership on the image changes.

Before presenting the algorithm to solve our model, we compute each variable fixing the others. For the sake of simplicity, without losing the generality, Equation (4.85) has been considered without the length term ($\mu = 0$). There are two following steps:

Step 1: For fixed u, the minimization of the energy in Equation (4.85) with respect to $c_1, c_2, \epsilon_1^2, \epsilon_2^2, f_1, f_2, \sigma_1^2, \sigma_2^2$ gives by calculus variation [63, 64]:

$$c_i = \frac{\int_\Omega I(y)[a_i(y)]^m dy}{\int_\Omega [a_i(y)]^m dy} \tag{4.86}$$

$$\epsilon_i^2 = \frac{\int_\Omega (c_i - I(y))^2 [a_i(y)]^m dy}{\int_\Omega [a_i(y)]^m dy} \tag{4.87}$$

$$f_i(x) = \frac{\int_\Omega K_\sigma(x-y) I(y)[a_i(y)]^m dy}{\int_\Omega K_\sigma(x-y)[a_i(y)]^m dy} \tag{4.88}$$

$$\sigma_i^2(x) = \frac{\int_\Omega K_\sigma(x-y)(f_i(x) - I(y))^2 [a_i(y)]^m dy}{\int_\Omega K_\sigma(x-y)[a_i(y)]^m dy} \tag{4.89}$$

where $i = 1, 2$, $a_1(\cdot) = u(\cdot)$, $a_2(\cdot) = 1 - u(\cdot)$.

Step 2: For fixed $c_1, c_2, \epsilon_1^2, \epsilon_2^2, f_1, f_2, \sigma_1^2, \sigma_2^2$, the minimization of the energy F with respect to u, by calculus of variation, is computed as follows:

$$u(y) = \frac{1}{1 + \left[\dfrac{\lambda \log p_1(I(y), \epsilon_1) + (1-\lambda)\int_\Omega K_\sigma(x-y) \log p_{1,x}(I(y), \sigma_1) dx}{\lambda \log p_2(I(y), \epsilon_2) + (1-\lambda)\int_\Omega K_\sigma(x-y) \log p_{2,x}(I(y), \sigma_2) dx}\right]^{\frac{1}{m-1}}} \tag{4.90}$$

Now, given a point y_0 in Ω, the intensity of point y_0 is $I(y_0)$, and the corresponding membership value of $I(y_0)$ is u_{y_0}. Assume that the membership value of $I(y_0)$ changes to the new value u_{ny_0}. Denote by ΔF the difference between the new and old energies, also referred to as the rate of change of F. ΔF is calculated at the new and old degree of membership of $I(y_0)$. Suppose that the changes in value of ϵ_1, ϵ_2, σ_1 and σ_2 at a point are very small. Then ΔF is calculated as follows:

$$\Delta F = \lambda \Delta F_G + (1-\lambda)\Delta F_L \tag{4.91}$$

The changes in value of the global fuzzy energy ΔF_G and the local fuzzy energy ΔF_L are calculated as follows (see Appendix C):

$$\begin{aligned}\Delta F_G = &- \log \frac{1}{\sqrt{2\pi}\epsilon_1}\Delta u_m + \frac{s_1 \Delta u_m}{s_1 + \Delta u_m}\frac{(I(y_0)-c_1)^2}{2\epsilon_1^2} \\ &- \log \frac{1}{\sqrt{2\pi}\epsilon_2}\Delta v_m + \frac{s_2 \Delta v_m}{s_2 + \Delta v_m}\frac{(I(y_0)-c_2)^2}{2\epsilon_2^2} \qquad (4.92)\\ \Delta F_L = &- K_\sigma * \left(\log \frac{1}{\sqrt{2\pi}\sigma_1}\right)(y_0)\Delta u_m - K_\sigma * \left(\log \frac{1}{\sqrt{2\pi}\sigma_2}\right)(y_0)\Delta v_m \\ &+ \sum_{x\in\Omega} \frac{s_3(x)K_\sigma(x-y_0)\Delta u_m}{s_3(x) + K_\sigma(x-y_0)\Delta u_m}\frac{(I(y_0)-f_1(x))^2}{2\sigma_1^2(x)} \\ &+ \sum_{x\in\Omega} \frac{s_4(x)K_\sigma(x-y_0)\Delta v_m}{s_4(x) + K_\sigma(x-y_0)\Delta v_m}\frac{(I(y_0)-f_2(x))^2}{2\sigma_2^2(x)} \qquad (4.93)\end{aligned}$$

where $s_1 = \sum_{y\in\Omega}[u(y)]^m$, $s_2 = \sum_{y\in\Omega}[1-u(y)]^m$, $s_3 = K_\sigma * [u]^m$, $s_4 = K_\sigma * [1-u]^m$, $\Delta u_m = [u_{ny_0}]^m - [u_{y_0}]^m$, $\Delta v_m = [1-u_{ny_0}]^m - [1-u_{y_0}]^m$.

If $\mu \neq 0$, then Equation (4.91) leads to:

$$\Delta F = \mu \Delta l + \lambda \Delta F_G + (1-\lambda)\Delta F_L, \qquad (4.94)$$

where Δl is the rate of change of the contour length.

Utilizing the change of the fuzzy energy function given by Equation (4.94) along with Equations (4.92) and (4.93), we designed the algorithm given below to evolve an active contour from its initial contour towards the boundaries of image objects:

1) Initial partition: setup $u > 0.5$ for the interior of the contour, and $u < 0.5$ for the exterior.

2) For each iteration, the following sub-steps are performed:

   (i) Compute $c_1, c_2, \epsilon_1, \epsilon_2, f_1, f_2, \sigma_1, \sigma_2$ by fixing u and using (4.86)-(4.89).

   (ii) For each pixel $y_0 \in \Omega$, we are given u_{y_0} as the membership value of $I(y_0)$ in the previous iteration. The new membership value u_{ny_0} is calculated using (4.90) where the fixed $c_1, c_2, \epsilon_1, \epsilon_2, f_1, f_2, \sigma_1, \sigma_2$ are calculated in the previous step. Then, we use (4.92)-(4.94) to calculate the difference between the new and old energy ΔF at the pixel y_0. If $\Delta F < 0$, then we change u_{y_0} with u_{ny_0}; otherwise, we keep the old value u_{y_0}.

   (iii) Repeat Step (ii) for all the pixels $y_0 \in \Omega$ to obtain all new membership value u_{ny_0}. Then, we compute the total energy F of the image.

Repeat Step 2 until the rate of change of F is slower than a threshold.

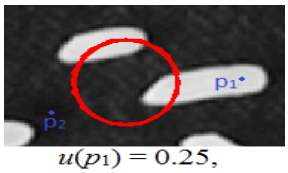

$u(p_1) = 0.25$, $u(p_2) = 0.25$

(a) Initial contour

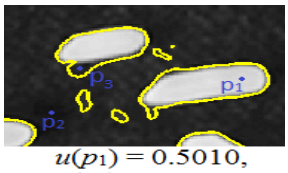

$u(p_1) = 0.5010$, $u(p_2) = 0.4964$

(b) 2^{nd} iteration

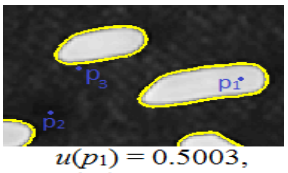

$u(p_1) = 0.5003$, $u(p_2) = 0.4989$

(c) 5^{th} iteration

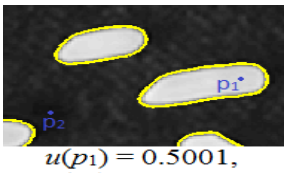

$u(p_1) = 0.5001$, $u(p_2) = 0.4999$

(d) 25^{th} iteration

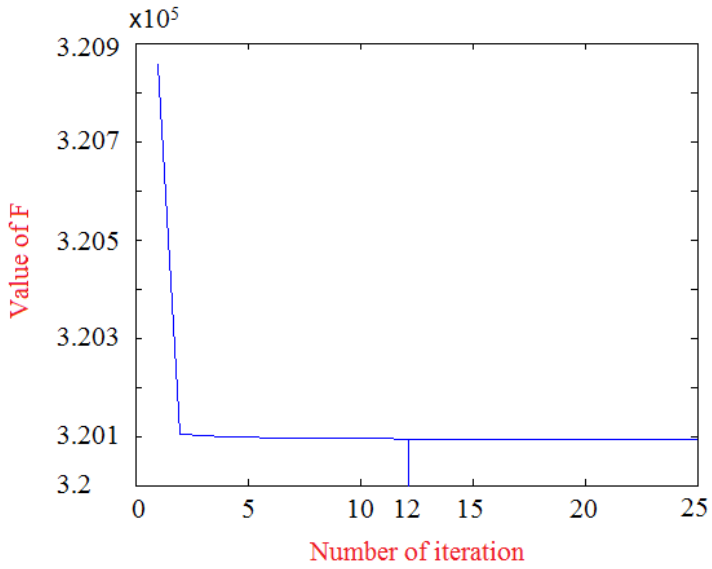

(e) Evolution of F

Figure 4.26. Illustration for the C_LGFGD method on a real image of rices.

3) We use the following criterion: if $u(x) > 0.5$, then x is in the object. Otherwise, x is in the background.

4.5.6 Illustration for the C_LGFGD method

In this section, we illustrate the C_LGFGD method on a real image of rices. We present the evolution of the contour in Figures 4.26a - 4.26d where the initial contour is in red (dark gray) and the evolving contours are in yellow (light gray) as well; the evolution of the energy function F (Figure 4.26e). Figure 4.26e shows that our energy function converges to the minimum at the 12^{nd} iteration. However, we see that the contours at the 5^{th} (Figure 4.26c) and 25^{th} (Figure 4.26d) iterations are visually similar. This can be explained with more details on the values of u at two points p_1 and p_2 reported in each figure as follows: at the 5^{th} iteration, $u(p_1) = 0.5003$, $u(p_2) = 0.4989$. Since $u(p_1) > 0.5$, pixel p_1 is clustered in the object. Since $u(p_2) < 0.5$, pixel p_2 is a clustered in the background. However,

Table 4.7. Values of $f_1, f_2, \sigma_1, \sigma_2$ and u for the pixel p_3 reported in Figure 4.26b-4.26c.

	f_1	f_2	σ_1	σ_2	u
2^{nd} iteration	63.5085	44.5250	2537.4	922.3	0.5003
5^{th} iteration	51.1039	51.2402	1564.9	1579.1	0.4986

Table 4.8. Computational complexity of the C_LGFGD model.

	original image	enlarged version		
		by 2	by 4	by 8
size	65×68	130×136	260×272	510×544
CPU time (s)	1.44	5.52	23.05	92.13

the value of our energy function is not minimized at this iteration. Therefore, the values of u must be changed. But, this change does not affect the fact that p_1 and p_2 are the pixels of the object and background, respectively, as it can be seen in Figures 4.26c- 4.26d. Moreover, Table 4.7 shows the evolution of the pixel p_3, reported in Figures 4.26b-4.26c, through the values of f_1, f_2, σ_1, σ_2, and u. At the 2^{nd} iteration, as $u(p_3) = 0.5003 > 0.5$, pixel p_3 is clustered in the object. At this iteration, we have at this iteration: $f_1 > f_2$, $\sigma_1 < \sigma_2$. However, at the 5^{th} iteration, as $u(p_3) = 0.4986 < 0.5$, pixel p_3 is clustered in the background, we also observe in Table 4.7 the changes in value of f_1, f_2, σ_1 and σ_2: $f_1 < f_2$ and $\sigma_1 > \sigma_2$.

4.5.7 Computational complexity

The computational complexity of the C_LGFGD method is in the order of $O(N_{xyG})$, where $N_{xyG} = N_x.N_y.N_{G_x}.N_{G_y}$, N_x and N_y are the column and row numbers of the considered image, respectively; N_{G_x} and N_{G_y} are the column and row numbers of the Gaussian kernel K_σ, respectively. To validate the above complexity, we test the C_LGFGD method on an image with size 65×68 (Figure 4.27a) and its zoom-in image with double size for each dimension 130×136 (Figure 4.27b), using the same Gaussian kernel sizes ($\sigma = 8$). As it can be observed in Figures 4.27a - 4.27b, the initial contours are at the same positions and the corresponding results in respective Figures 4.27c - 4.27d. The CPU times to obtain results in Figures 4.27c - 4.27d are 1.44 second and 5.52 second, respectively. We can see that, since the size of Figure 4.27b is four times the size of Figure 4.27a, the CPU time to obtain Figure 4.27d is approximately four times the CPU time to obtain Figure 4.27c. Moreover, Table 4.8 shows the validation providing results with enlargement by 4 and 8. All obtained results confirm the computational complexity determined above.

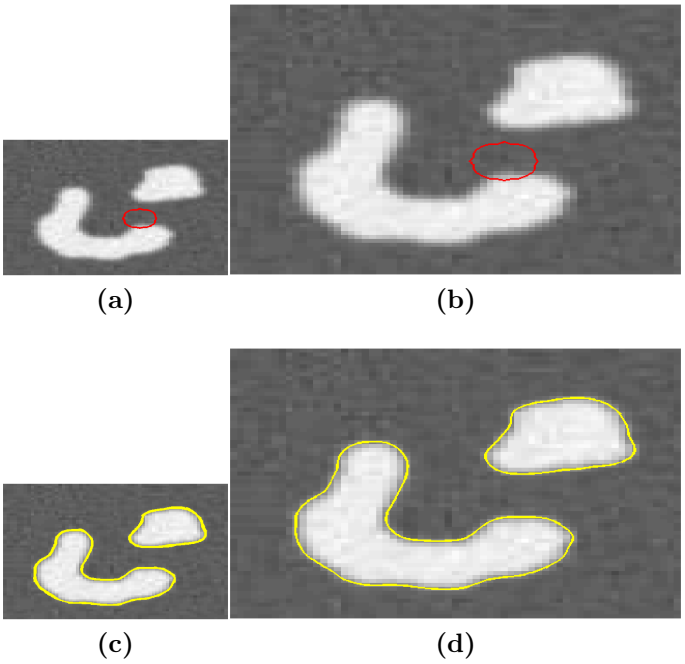

Figure 4.27. (a) and (b) Images with sizes 65×68 and 130×136, resepectively. (c) and (d) Segmentation results applying the C_LGFGD on (a) and (b), respectively.

4.5.8 Sensibility of the parameters

The C_LGFGD model is developed to handle intensity in-homogeneity by employing the local intensity feature. To determine this feature, we use the Gaussian kernel with standard deviation σ. For our practical application, a Gaussian window with size $(4\sigma+1)\times(4\sigma+1)$ is applied. Therefore, the parameters chosen by the user to run the C_LGFGD algorithm are σ and λ (in Equation (4.85)). In addition, we will also study the sensibility of the weighting exponent m, which determines the degree of fuzziness of the resulting clustering in Equations (4.81) and (4.83). For the purpose of simplicity and without losing generality, we assume $\mu = 1$.

4.5.8.1 Parameter σ

In the C_LGFGD method the intensity of a pixel is approximated by the average of the intensities in the neighborhood inside and outside the evolving contour with a weight determined by the Gaussian kernel K_σ. Figure 4.28 shows how the graph of the Gaussian changes when σ varies. One may observe that if σ is small (blue line), $K_\sigma(x-y)$ is large for a pixel x close to y and its value is small for the pixel x far from y. This case is sensitive to the local image information such as noise. On the contrary, if σ is large (red line), the values of $K_\sigma(x-y)$ at x and y are almost the same. Therefore if the size of

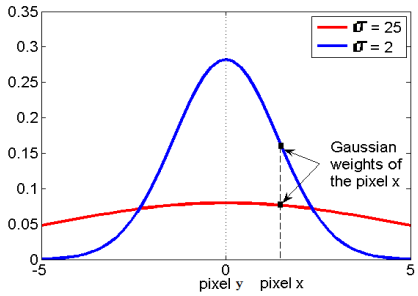

Figure 4.28. Graph of Gaussian kernel.

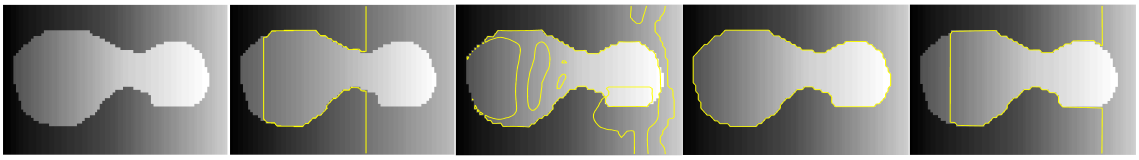

(a) **(b)** **(c)** $\sigma = 2$ **(d)** $\sigma = 7$ **(e)** $\sigma = 18$

Figure 4.29. Test on a nonhomogeneous image with different values of σ: (a) Original image, (b) Result of FEBAC, (c)-(e) Results of C_LGFGD.

the Gaussian window is large enough to contain the whole considered image, the local information approaches the global information.

Figure 4.29 shows how the accuracy of extraction varies with respect to σ. If σ is small (Figure 4.29c) the used window for the kernel is small. Thus a lot of local information is missed and artifacts are captured. If σ is large (Figure 4.29e, the local information and global information ae nearly the same and the result is then similar to the one of the FEBAC [47] (Figure 4.29b) which uses only global information. Note that $\lambda = 0.01$ and $m = 2$ for all tests of the C_LGFGD model in this figure.

4.5.8.2 Parameter λ

The parameter λ (in Equation (4.85)) controls the sensibility of the local and the global terms. If λ is close to 1, the sensibility of the local term is weaker compared with the global term. On the contrary, if λ is close to 0, the sensibility of the local term is stronger compared with the global term. Therefore, if one works with images containing non-homogeneous regions, the value of λ should be close to 0. Figure 4.30 validates the above reasoning applying multiple values of λ. Note that we use $\sigma = 9$ and $m = 2$ for all the results in Figure 4.30. One may observe that the most accurate results are obtained for λ closer to 0.

As stated above when segmenting intensity in-homogeneity, we should chose λ closed to

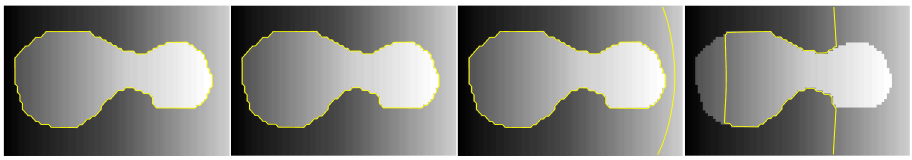

(a) $\lambda = 0.0001$ **(b)** $\lambda = 0.1$ **(c)** $\lambda = 0.2$ **(d)** $\lambda = 0.9$

Figure 4.30. Test on a nonhomogeneous images with different values of λ.

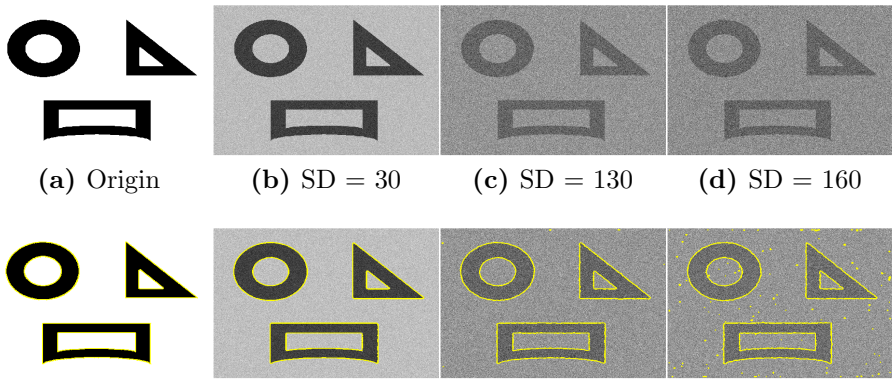

(a) Origin **(b)** SD = 30 **(c)** SD = 130 **(d)** SD = 160

(e) Result of (a) **(f)** Result of (b) **(g)** Result of (c) **(h)** Result of (d)

Figure 4.31. Test on a synthetic image and its noisy versions with varying standard deviation (SD).

0. This implies that the global information term is weakly weighted. On the other hand, as we known, models using only the global information effectively deal with noise. So, in case of noisy image with intensity in-homogeneity, if λ is selected close to 0 to handle IIH, then sigma should be large to deal with the noise because the obtained result is similar with the models using only global information as we stated in Section 4.5.8.2. In this case, the run time is more expensive according to the computational complexity developed in Section 4.5.7.

On the contrary, if we select λ closed to 1 and small value of σ, the global term is more dominant than the local term. Therefore, the model is robust to noise. The advantage to select small value of sigma in this case is that the run time is low. We have tested the robustness of the method to noise with respect to sigma on a synthetic image (see Figure 4.31). For all the results in Figure 4.31 we have used the same set of parameters $\lambda = 0.9$, $\sigma = 1$ and $m = 2$. One may observe in Figure 4.31 that the C_LGFGD model gives accurate result for Gaussian noise with very higher standard deviation 130 (see Figure 4.31g). For image noise with standard deviation higher than 130, example 160 (Figure 4.31d), this is evident that the active contour detects false positive pixels.

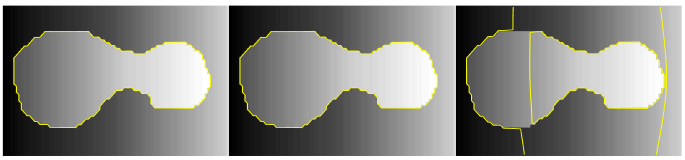

(a) $m = 1.5$ **(b)** $m = 4$ **(c)** $m = 9$

Figure 4.32. Test on a nonhomogeneous images with different values of m.

Table 4.9. The used parameters of the C_LGFGD model in Section 4.5. Rx = row x.

Figure	μ	m	σ	λ
4.33	1	2	8	0.01
4.34 (R1)	1	2	17	0.1
4.34 (R2)	1	2	23	0.01
4.34 (R3)	1	2	15	0.1
4.35 (R1)	1	2	15	0.01
4.35 (R2)	1	2	15	0.1
4.36 (R1)	1	2	20	0.1
4.36 (R2)	1	2	20	0.1
4.37 (R1)	1	2	19	0.1
4.37 (R2)	1	2	25	0.01
4.37 (R3)	1	2	25	0.01
4.38 (R1-R4)	1	2	20	0.1

4.5.8.3 Parameter m

In what concern m in Equations (4.81) and (4.83), we have determined that the accuracy of boundary detection decreases when m increases from 1 to infinity. The above reasoning holds because u and $1 - u$ are in $(0, 1)$. Consequently, if m is large enough, u^m and $(1 - u)^m$ approach 0, and the local and global terms are close to 0 as well. Then, we are left with the regularization term and receive a trivial solution $u =$ constant (the gradient $\nabla u = 0$ and the energy function is 0). To validate the theoretical derivation, experiments are performed using the original images from Figure 4.29. The obtained results are shown in Figure 4.32. We observe that the results are not accurate for large values of m, when $\sigma = 9$ and $\lambda = 0.01$.

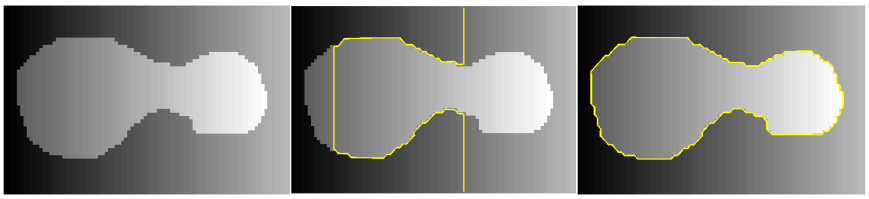

(a) (b) (c)

Figure 4.33. Experiment on a non-homogeneous synthetic image: (a) Original image; (b) Result of the FEBAC model; (c) Result of the C_LGFGD model.

4.5.9 Experimental results and comparison

We present results of the C_LGFGD model on a variety of synthetic and medical images, namely PET, CT, X-Ray and MR images. A comparative evaluation has been performed to demonstrate the advantages of our C_LGFGD method over similar contemporary methods such as the LGIF [79], the LCV [80] and the FEBAC [47]. The code of the LGIF model is obtained by incorporating the global term in the code of the LBF [77] model, which is obtained from the home page of the author [77]. The code of the LCV model is provided by emails with the author of [80]. The code of the FEBAC model is implemented based on the algorithm published in [47] and discussions with authors by email. To provide a fair comparison, all the methods used same initial contour. The used parameters are shown in Table 4.9.

We use the MATLAB r2008b to implement our algorithm on a computer with Intel Core 2 Duo CPU 2.93GHz and 4GB RAM. The images used for the experiments vary in size between 65×68 and 452×348.

Performance to deal with IIH

First, we demonstrate that the C_LGFGD model can detect object with intensity inhomogeneity by testing the model on a synthetic non-homogeneous image and comparing with the FEBAC model as presented in Figure 4.33. Figure 4.33a shows an image where the intensities of object and background are non-homogeneous. One can see in Figures 4.33b that the final contour of the result obtained from the FEBAC model is not accurate. This can be explained by the fact the fact that this model utilizes only the global intensities. On the contrary, by taking into account the local intensities, the final contour of the C_LGFGD accurately stops at the boundary of object (Figure 4.33c).

Figure 4.34 compares the segmentation capabilities of the LGIF, the LCV and the newly proposed C_LGFGD method. Three X-ray images of blood vessels are used for the purpose of comparison. All images are non-homogeneous. In this experiment, the results provided from the LGIF (3^{rd} column) and the C_LGFGD (4^{th} column) models are similar and good.

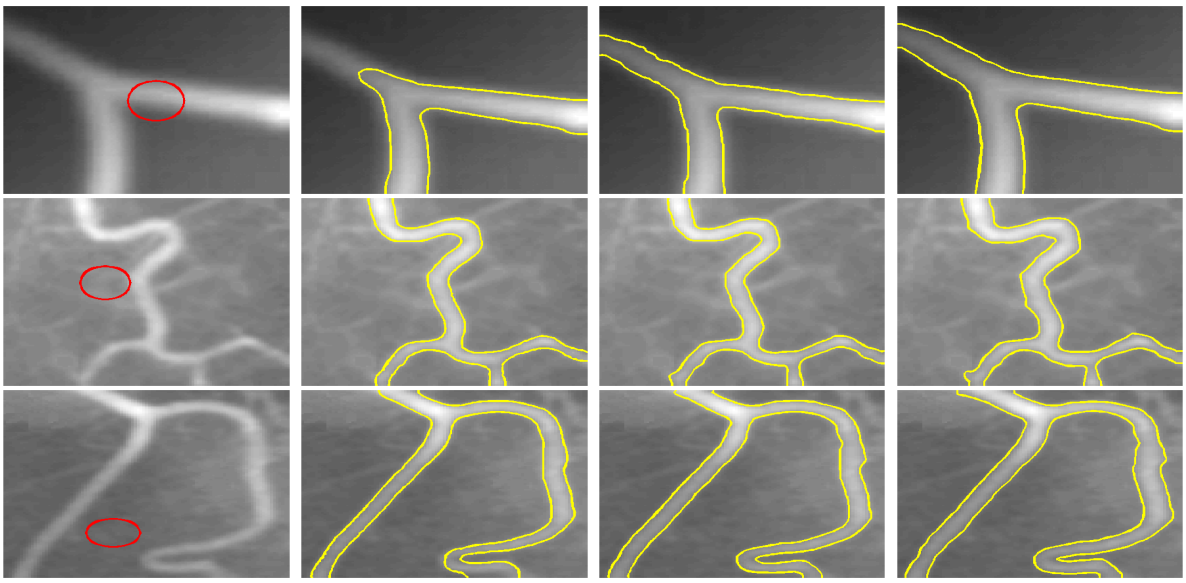

Figure 4.34. Results obtained on three blood vessel X-ray images (source `http://www.unc.edu/~liwa/`). From left to right columns: Original images with initial contours, results of the LCV, the LGIF and the C_LGFGD models, respectively.

For the LCV model (2^{rd} column), the result of the top image is not accurate, while the result of the middle image is similar to the results of the LGIF and the C_LGFGD models. The bottom image is sufficiently well segmented except the right corner part where the contour is missed. Note that we can find the better results of the LCV model for these X-Ray images in [80]. For a same image, different results of the LCV model are obtained because the energy function of this model is not convex and the positions of the initial contour in Figure 4.34 are not suitable to obtain the accurate results. The reason why the LGIF, the LCV (depending on the initialization) and the C_LGFGD models provide good results on these non-homogeneous images is that these models utilize the local information in the energy function. We can find in Figure 4.39 that the results of the C_LGFGD model for some other positions of the initial contour are the same, due to the convexity of the associated energy functional.

Moreover, we compare the C_LGFGD model with the LCV and the LGIF models using two heart MR images. The results are illustrated in Figure 4.35 where one may observe that the proposed C_LGFGD model detects the object boundary in a more accurate fashion than the LCV and the LGIF did. On the top images, the results of the LCV and the LGIF models are good enough, but some contours are not correctly detected. On the bottom row, the image is corrupted with non-homogeneous intensity, the result of LGIF model is definitely incorrect, while the LCV contour cannot be stopped at the exact contour. This is not the case for the C_LGFGD model which stops the final contours at the boundaries

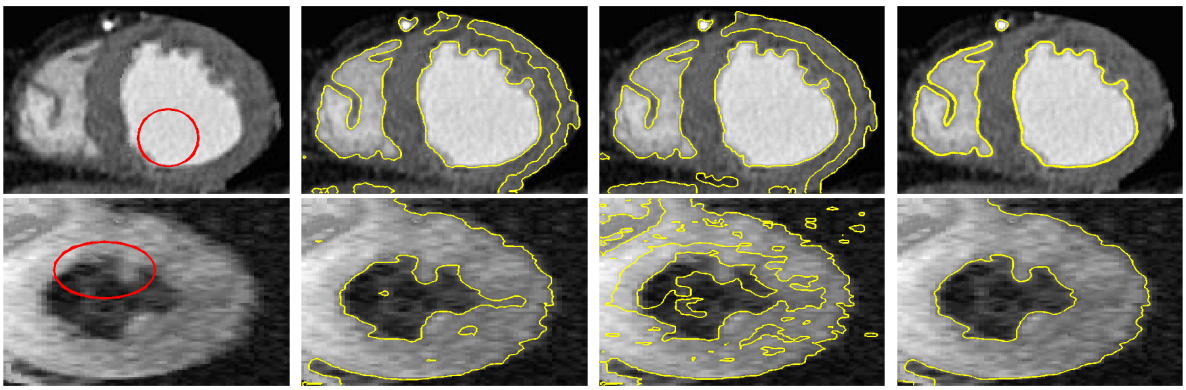

Figure 4.35. Results obtained on two heart MR images (source `http://www4.comp.polyu.edu.hk/~cslzhang/RD/RD.htm`). Column 1: Original images and initial contours. Column 2: Results of the LCV model. Column 3: Results of the LGIF model. Column 4: Results of the C_LGFGD model.

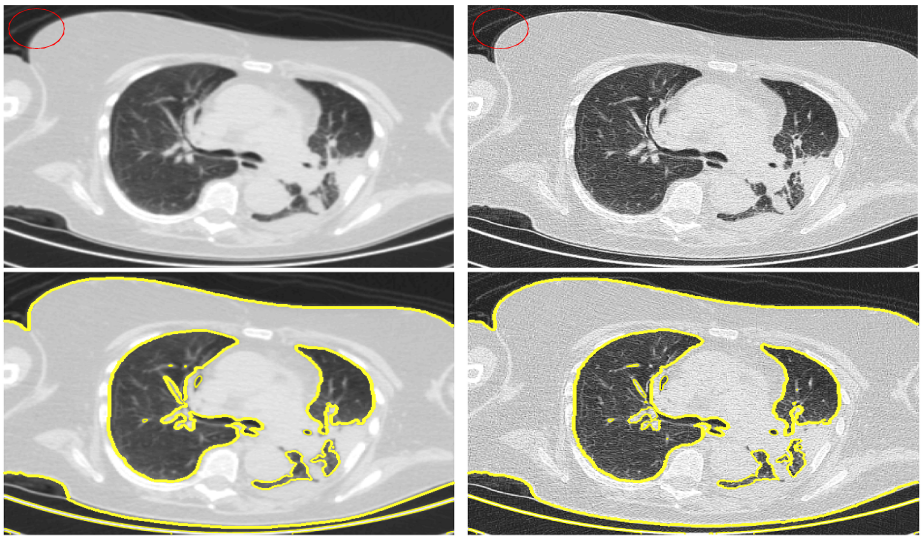

Figure 4.36. Results on a thorax CT image and its noisy version. Top row: Original images with initial contour (images courtesy of J.-M. Rocchisani, Avicenne-Medicine Nucleaire Hospital, Bobigny, France). Bottom row: The corresponding segmentation results.

of objects.

Robustness to noise

Now, we present in Figure 4.36 the experiments on a noisy slice of CT image of 3mm thickness (at top left), which contains the thorax at the level of the pulmonary arteries. This image is acquired with standard reconstruction filter and exhibits low noise. Another CT image (at top right) is of 2mm thickness, acquired at the same position with optimized

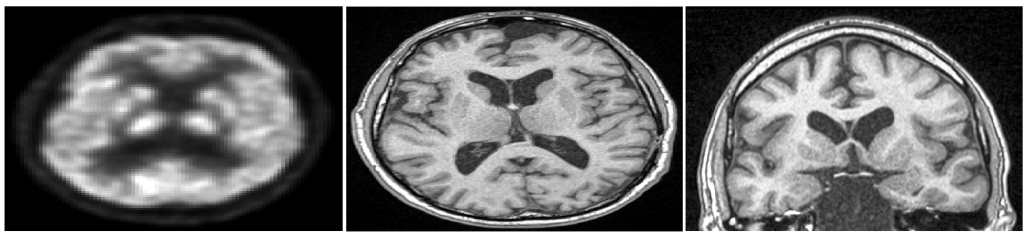

(a) Brain PET **(b)** Brain MR **(c)** Brain MR

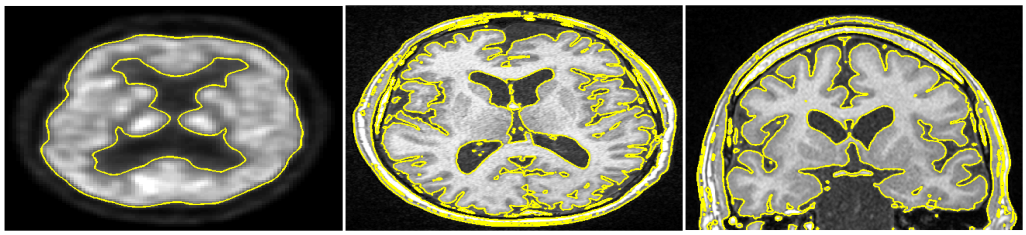

(d) Result of (a) **(e)** Result of (b) **(f)** Result of (c)

Figure 4.37. Results of the C_LGFGD method for some medical images (images courtesy of J.-M. Rocchisani, Avicenne-Medicine Nucleaire Hospital, Bobigny, France).

reconstruction filter, and different values of the parameters for tomography re-construction. This is hence a noisy image. The original images and the initial contours are shown in the top row, while the segmented images are shown in the bottom. It is not difficult to see that the results are very similar.

Accuracy

Figure 4.37 depicts multiple images with clinical importance. We present segmentation of a brain PET image (Figure 4.37a) and two brain MR images (Figures 4.37b and 4.37c) to underline the flexibility of our C_LGFGD method. The obtained results (Figures 4.37d-4.37f) are evaluated by our medical expert, as accurate in detecting the boundary. One may notice on the brain MR image that sulci and gyri are well delineated.

Next, we present validation results with real expert-segmented thorax CT images and heart MR image. As can be seen in Figure 4.38, the interior boundaries of the thorax are accurately extracted, compared with the contour segmented by our expert. Moreover, to quantitatively evaluate the accuracy of our results, we use Dice Similarity Coefficient (DSC) [88], which is defined as:

$$DSC = \frac{2N(S_1 \cap S_2)}{N(S_1) + N(S_2)} \tag{4.95}$$

where S_1 and S_2 represent the obtained segmentation and the ground truth, respectively, $N(\cdot)$ indicates the numbers of pixels in the enclosed set. The closer the DSC value is to

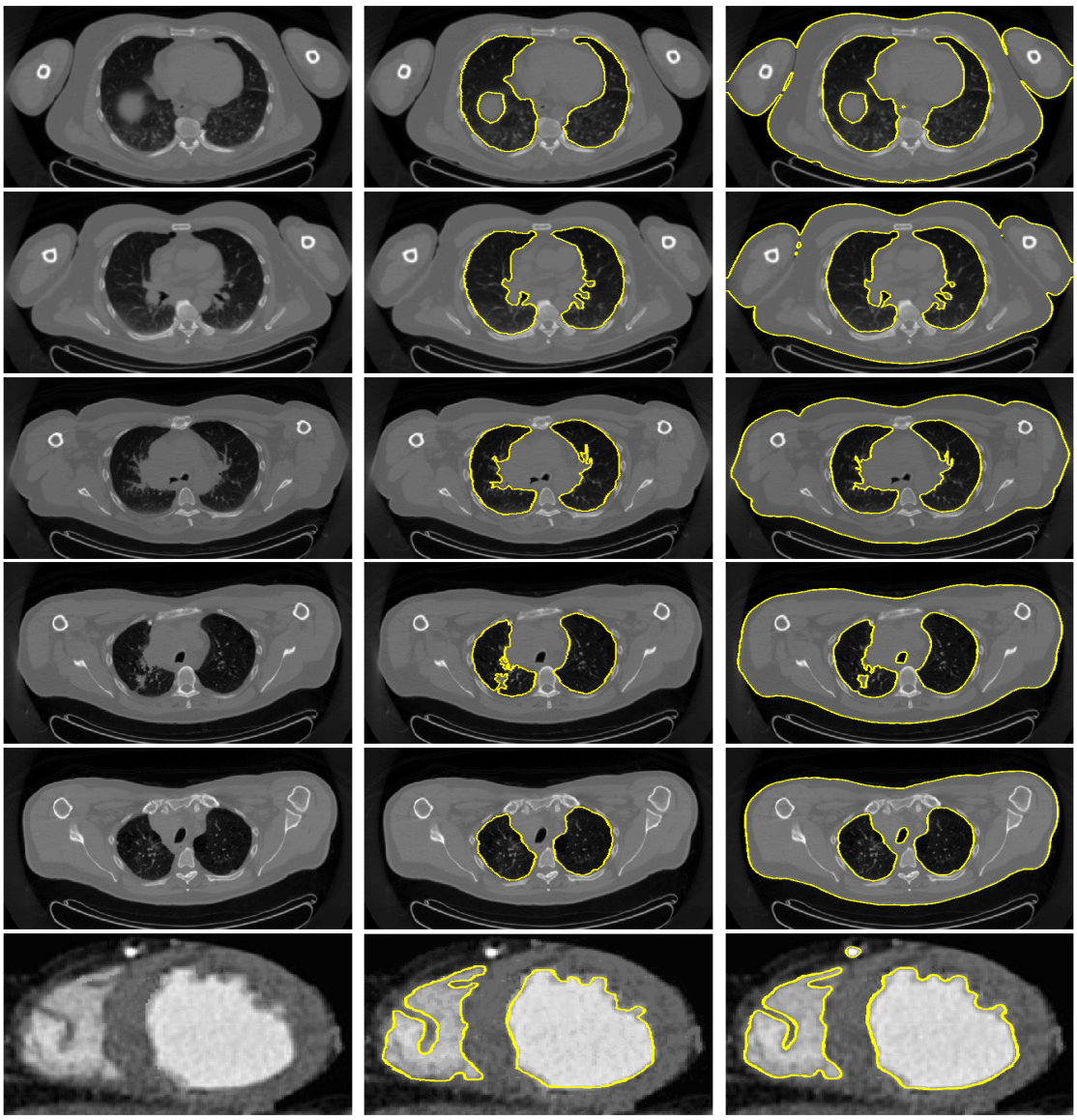

Figure 4.38. Comparison with ground truth established by our expert on thorax CT images and heart MR image (images courtesy of J.-M. Rocchisani, Avicenne-Medicine Nucleaire Hospital, Bobigny, France). Column 1: Original image. Column 2: Ground truth image. Column 3: Result of the C_LGFGD method.

1, the better the segmentation is. Table 4.10 shows the *DSC* values of the C_LGFGD method. From this table, our results are very close to the ground truth established by expert, since the DSC values C_LGFGD are very close to 1.

Table 4.10. DSC values for third column of Figure 4.38

		Row 1	Row 2	Row 3	Row 4	Row 5	Row 6
DSC	left part	0.98	0.97	0.97	0.96	0.98	0.94
	right part	0.96	0.98	0.97	0.98	0.99	0.98

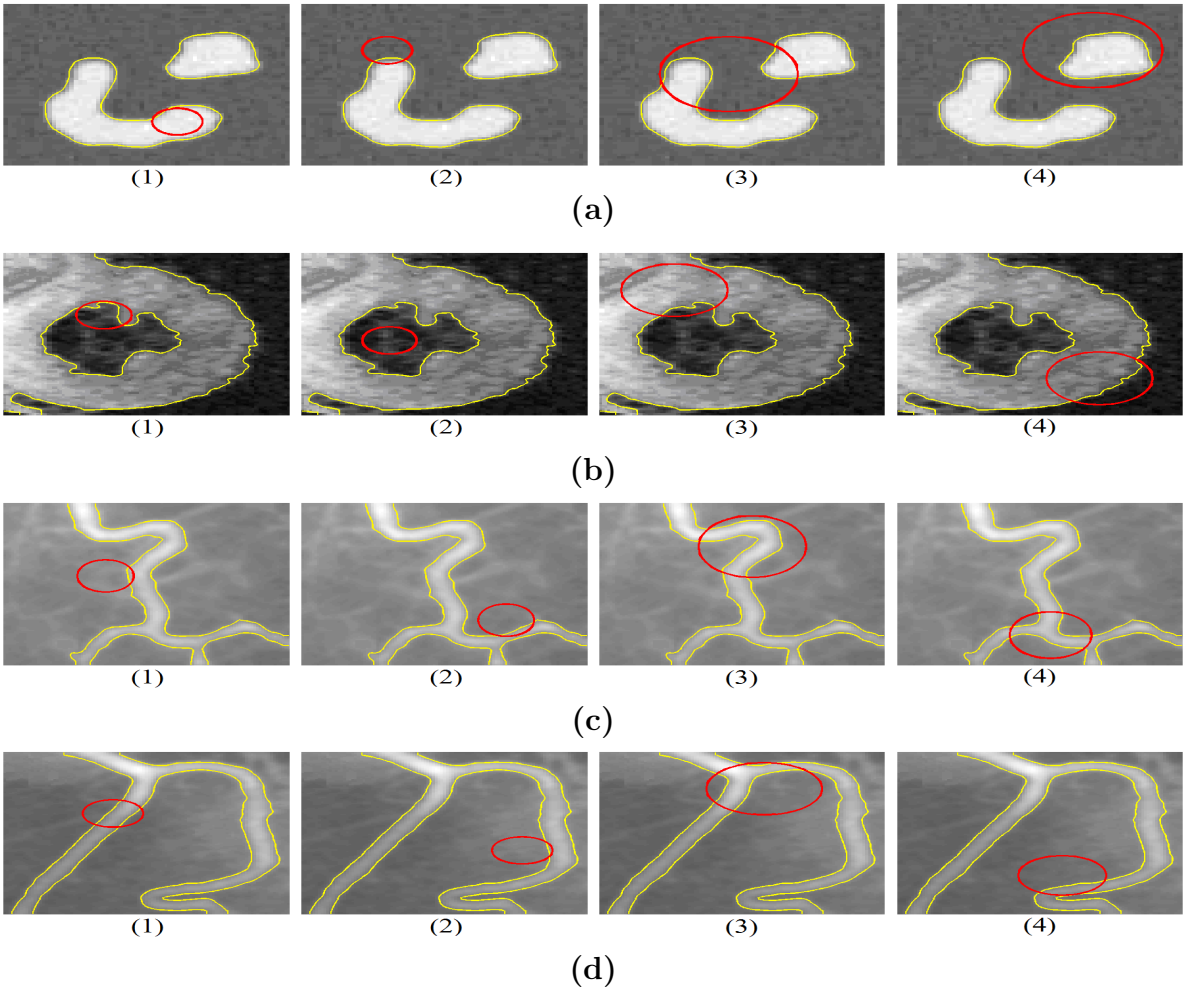

Figure 4.39. Results of the C_LGFGD model with the different initial contours.

Independence with respect to the initial contour

To validate the convexity of our model, we performed experiments using one synthetic images, one heart MR images and two X-Ray blood vessel images. In every experiment, we placed the initial contour on a different position with a varying contour size. In every instance, the accuracy of segmentation is the same, which validates the independence of

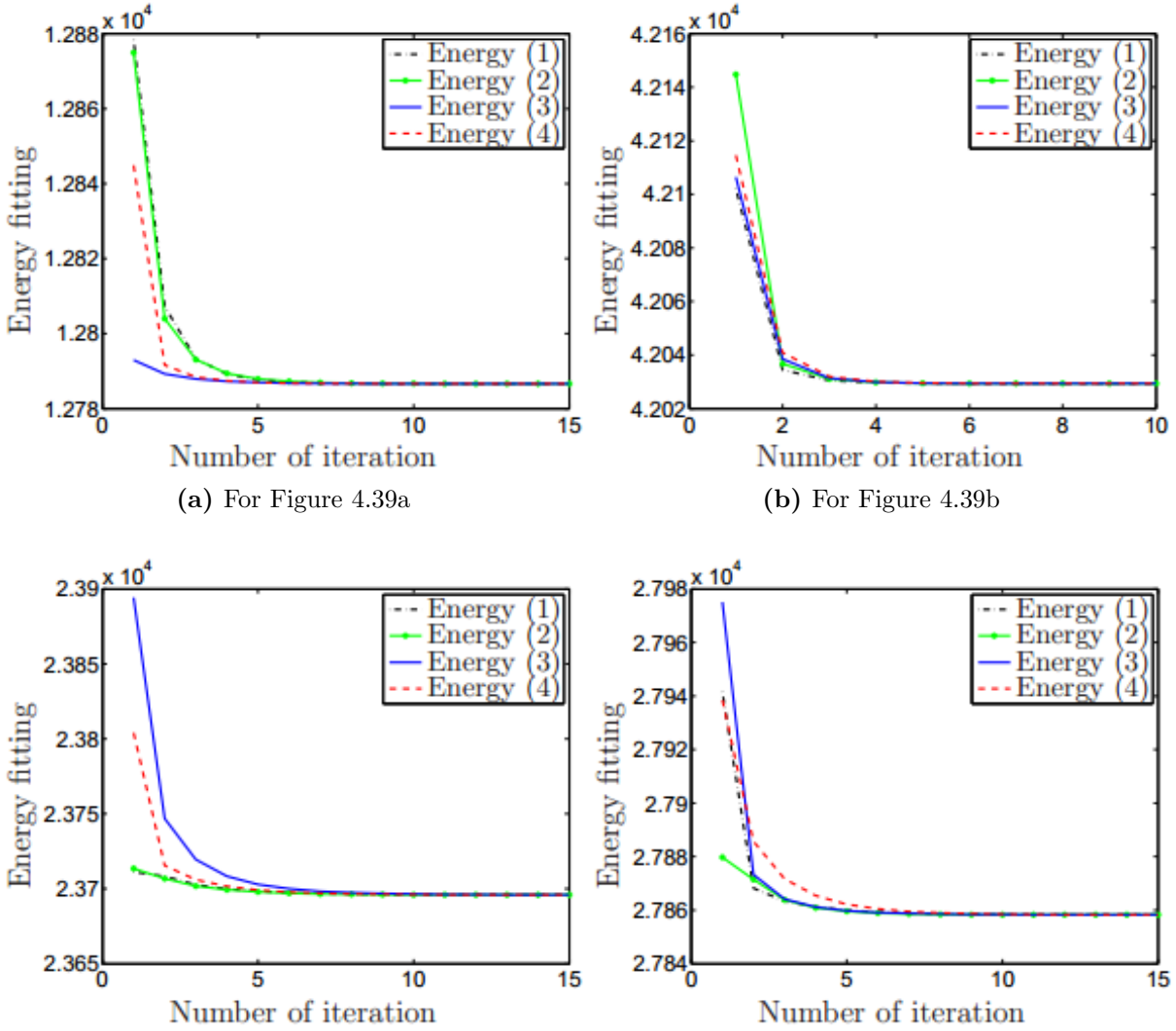

(a) For Figure 4.39a **(b)** For Figure 4.39b

(c) For Figure 4.39c **(d)** For Figure 4.39d

Figure 4.40. Corresponding energy with the positions of the initial contours in Figure 4.39.

the C_LGFGD model with respect to the initial contour (see Figure 4.39). Moreover, we show in Figure 4.40 the corresponding energy F versus iterations for each image. We can see that the energy fittings in all of cases for each image converge to one value after some iterations, this is the minimized value of the energy function.

4.5.10 Conclusion

This section presents the C_LGFGD model which is a novel convex and fuzzy energies-based active contour model. By taking into account the local information with a distribution of different means and variances, the proposed C_LGFGD, is capable to efficiently segment non-homogeneous regions. On the other hand, the fuzzy energy function is convex, which makes the model invariant with respect to the initial position of the contour while giving the same accuracy and repeatability. Furthermore, to minimize the energy function, we calculates directly and verifies if the energy decreases when the intensity membership of the intensity changes. By this way, it avoids the issues of the numerical stability constrains as in the PDE method.

The list of the main contribution of the C_LGFGD model consists of:

1. We have proposed a region-based AC model in the Bayesian approach that unifies local and global to cope with IIH while providing accuracy and robustness to noise;

2. The Bayesian approach with complete statistical characteristics of local intensities is combined with the Fuzzy clustering to deal with IIH while improving robustness to noise;

3. We have proved that the energy functional is convex with respect to membership function u which is the variable to determine the contour;

4. The fuzziness of the model is proven and its calculation complexity was experimentally validated;

5. The C_LGFGD parameters σ, λ, m have been studied and recommendations have been derived about the values that will provide high accuracy of boundary extraction and robustness to non-homogeneous regions with heavy noise.

The advantages of C_LGFGD versus the other convex methods and level set active contours are as follows:

a) ability of segmenting non-homogeneous regions while being independent of the initial contour,

b) 100% of accuracy repeatability with respect to the initial position of the contour,

c) better accuracy performance in case of noise or weak boundaries, compared to the C_LR and the C_LGR models,

d) from the application field point of view, the C_LGFGD can be used for medical images such as the X-Ray, CT, and MR images, as well as synthetic images.

4.6 Comparison of the Proposed Models

In this section, we present a comparison of the proposed convex models, namely the C_LR, C_LGR and C_LGFGD, for

- dealing with IIH

- robustness to noise.

- accuracy

- computation time

We also compared the performance of these convex models with the non-convex model, namely the R_LGR, for the same criteria. The main difference of this model with the three other ones is that this model is not convex. So the model depends on the initial contour.

First, let us recall briefly the proposed models

The R_LGR model

This model is defined by:

$$E(\phi) = \int_{\Omega} \big(I(x) - c_1\big)^2 H(\phi(x))dx + \int_{\Omega} \big(I(x) - c_2\big)^2 (1 - H(\phi(x)))dx + \frac{\lambda}{2} \int_{\Omega} \big(I(x) - I_L(x,\phi)\big)^2 dx \tag{4.96}$$

where ϕ is the level set function to determine the evolution contour with

$$I_L(x,\phi) = f_1(x)H(\phi(x)) + f_2(x)(1 - H(\phi(x))) \tag{4.97}$$

$$f_1(x) = \frac{\int_\Omega K_\sigma(x-y)I(y)H(\phi(y))dy}{\int_\Omega K_\sigma(x-y)H(\phi(y))dy} \tag{4.98}$$

$$f_2(x) = \frac{\int_\Omega K_\sigma(x-y)I(y)(1-H(\phi(y)))dy}{\int_\Omega K_\sigma(x-y)(1-H(\phi(y)))dy} \tag{4.99}$$

In Equations (4.97)-(4.99), K_σ and H are the constant window and the Heaviside function, respectively.

The C_LR model

The C_LR model is the first proposed convex model which is formulated as follows:

$$\min_{\substack{u_1,u_2\\0\le f\le 1}} \left\{ E(u_1,u_2,f) = \mu TV_g(f) + \int_\Omega f(x)e_{in}(x,u_1)dx + \int_\Omega (1-f(x))e_{out}(x,u_2)dx \right\} \tag{4.100}$$

where u is a bounded function in $[0,1]$ which is used to determine the evolving contour and

$$TV_g(f) = \int_\Omega g(x)|\nabla f(x)|dx \tag{4.101}$$

$$e_{in}(x,u_1) = \frac{\int_\Omega K_\sigma(x-y)(I(x)-u_1(y))^2dy}{\int_\Omega K_\sigma(x-y)dy} \tag{4.102}$$

$$e_{out}(x,u_2) = \frac{\int_\Omega K_\sigma(x-y)(I(x)-u_2(y))^2dy}{\int_\Omega K_\sigma(x-y)dy} \tag{4.103}$$

In Equations (4.101)-(4.103), $g = \frac{1}{1+|\nabla I|^2}$ (I is a given image) and K_σ are the edge function and the Gaussian kernel with standard deviation σ.

The C_LGR model

The C_LGR model is the second proposed convex model which is formulated as follows:

$$\min_{\substack{u_1,u_2,c_1,c_2\\0\le f\le 1}} \left\{ E(u_1,u_2,c_1,c_2,f) = \mu \int_\Omega g(x)|\nabla f(x)|dx + \lambda E_L(u_1,u_2,f) + \lambda_2 E_G(c_1,c_2,f) \right\} \tag{4.104}$$

where u is a bounded function in $[0,1]$ which is used to determine the active contour, E_L and E_G are the local and global terms, respectively:

$$E_L = \int_\Omega f(x)e_{in}(x,u_1)dx + \int_\Omega (1-f(x))e_{out}(x,u_2)dx \tag{4.105}$$

$$E_G = \int_\Omega f(x)(I(x)-c_1)^2dx + \int_\Omega (1-f(x))(I(x)-c_2)^2dx \tag{4.106}$$

e_{in} and e_{out} in Equation (4.105) are determined by Equations (4.102) and (4.103) in the C_LR model.

The C_LGFGD model

The energy function of the C_LGFGD model is as follows:

$$F(M) = \mu \int_{\Omega} |\nabla u| dx + \lambda F_G(M_G) + (1-\lambda) F_L(M_L) \tag{4.107}$$

where $M = (c_1, c_2, \epsilon_1^2, \epsilon_2^2, f_1, f_2, \sigma_1^2, \sigma_2^2, u)$, $M_G = (c_1, c_2, \epsilon_1^2, \epsilon_2^2, u)$ and $M_L = (f_1, f_2, \sigma_1^2, \sigma_2^2, u)$. F_1 and F_2 are the global and local terms:

$$F_G(M_G) = -\int_{\Omega} \log p(I(y), \epsilon_1)[u(y)]^m dy - \int_{\Omega} \log p(I(y), \epsilon_2)[1-u(y)]^m dy \tag{4.108}$$

$$\begin{aligned} F_L(M_L) = &-\int_{\Omega} \left[\int_{\Omega} K_\sigma(x-y) \log p_x(I(y), \sigma_1)[u(y)]^m dx \right] dy \\ &-\int_{\Omega} \left[\int_{\Omega} K_\sigma(x-y) \log p_x(I(y), \sigma_2)[1-u(y)]^m dx \right] dy \end{aligned} \tag{4.109}$$

In F_G and F_L, K_σ is the Gaussian kernel with standard deviation σ while p and p_x are Gaussian distributions:

$$p(I(y), \epsilon_i) = \frac{1}{\sqrt{2\pi}\epsilon_i} \exp\left(-\frac{\big(c_i - I(y)\big)^2}{2\epsilon_i^2} \right) \tag{4.110}$$

$$p_x(I(y), \sigma_i) = \frac{1}{\sqrt{2\pi}\sigma_i} \exp\left(-\frac{\big(f_i(x) - I(y)\big)^2}{2\sigma_i^2} \right) \tag{4.111}$$

We will now present the results of the comparison.

4.6.1 Field of Application and Ability of the models in dealing with intensity in-homogeneity

On the application point of view, Table 4.11 shows the ability of the proposed methods for image types such as synthetic, X-ray, MR, CT, PET, Ultrasound and Skin lesion. The synthesis obtained in this table is produced from the experiments on each method in Chapter 3 and Chapter 4 as well as in Appendix E - Sensibility of the parameters (for images with intensity in-homogeneity). In this case, we can see that the C_LGR model is the best because of the wide range of images modalities that passed successfully IIH test. The second position in the ranking is the C_LGFGD which can be applied to all of these modalities except the PET images. The C_LR and the R_LGR models can deal with the following types of images: non-homogeneous synthetic, X-ray, MR and skin lesion/ultrasound. However, from the obtained results, we estimate that the quality of the C_LR is better than the quality of the R_LGR. Note that for the ultrasound images, except the R_LGR model, we will develop the other models for this modality.

4.6.2 CPU time

To compare the CPU time, we test the proposed models on a non-homogeneous synthetic image, a X-ray image and a MR image. The experiments are performed on a computer with core I7 2.8Ghz and 6Gb RAM. The accurate results of proposed models are shown in Figures 4.41- 4.43 and the CPU time of each method is shown in Table 4.12. One may observe that the obtained C_LGR results are the smallest for all cases while the obtained C_LGFGD results are the largest for all cases. The CPU time of C_LGFGD is larger than the R_LGR's because in our program, we have to calculate an iteration for each pixel. This is a drawback in our program. In the future, we will develop faster program. The smallest CPU times of the C_LGR and the C_LR prove that the fast algorithm proposed by Chambolle [45] is more effective compared with the PDE method (to solve the R_LGR model or the C_LGFGD).

4.6.3 Accuracy by DSC value

Based on the ground truths provided by our experts, we compare the accuracy of the proposed models for MR and CT images by calculating their DSC values [88]. We also make the comparison on a synthetic image. The results on the accuracy of the proposed model are presented in Figures 4.44- 4.46, while the DSC values and the corresponding parameters are reported in Table 4.13.

Note that, we will compare all of the proposed methods on synthetic and MR images while for CT image, we will only compare the C_LGR and the C_LGFGD models because one can see from Table 4.11 that there are only the C_LGR and the C_LGFGD models can apply successfully for segmenting CT images.

From Table 4.13 we can see that the C_LGR and the C_LGFGD give the most accurate results. The results of R_LGR and C_LR are not better than the C_LGR and the C_LGFGD, but they are also very good and the difference between them is very small.

Comparing between the DSC values of the CC_LGR and the C_LGFGD, one can see that the obtained result by the C_LGFGD is better than the C_LGR. Accounting for the CPU time, if we select the C_LGFGD model to segment images, the obtained results are very good but the CPU time is slow. Another effective selection is the C_LGR model which not only gives very good result but also is very fast.

4.6.4 Robustness to noise

In this section, for the purpose of comparison, we will use a homogeneous synthetic image and a synthetic image with intensity in-homogeneity. To obtain noisy versions, we add Gaussian noise with varying standard deviation.

In what concern the homogeneous synthetic image, for the C_LR model which uses only the local information, we have to select large value of σ to change the local information to the global information. For the R_LGR, the C_LGR and the C_LGFGD models which combine the local and global information, we can select small value of σ and small coefficient of the local term to have dominant global term as explained in Sections 3.4, 4.4.4 and 4.5.8.2 which study the sensibility of the parameters of each model. The results of the proposed models for the homogeneous synthetic image are shown in Figures 4.47- 4.50. The maximum of the standard deviation, that the proposed models can deal with, is shown in Table 4.14. The parameters for each model are also presented in Table 4.14. From Figures 4.47- 4.50 and Table 4.14, we found that the performance of R_LGR is the best for its ability to deal with noise standard deviation $\sigma = 160$. The second in the rankings is the C_LGFGD for dealing with standard deviation 140. The highest standard deviation of noise that the C_LGR and the C_LR model can deal with, are 40 and 15, respectively.

In the case of the intensity in-homogeneity, we will still select large value of σ for the C_LR model. For the other proposed models, the selection is more difficult. We have to select large coefficient of the local term compared with the coefficient of the global term to deal with intensity in-homogeneity. Then, σ is selected so that it is not either small nor large to deal with noise because if it is large, the local information becomes the global information and the models fail to tackle intensity in-homogeneity. The results of the proposed models for image with intensity in-homogeneity are shown in Figures 4.51-4.54. The corresponding parameters are shown in Table 4.15. Once again, we see that the R_LGR is the best with maximum of standard deviation equal to 70, the second in the ranking is the C_LGFGD with maximum of standard deviation equal to 50, the C_LGR and the C_LR are the next with maximum of standard deviation equal to 30 and 20.

4.6.5 Comparison of the C_LGR and the C_LGFGD Robustness to noise

Especially, we focus to the C_LGR and the C_LGFGD models because of their best performances in dealing with IIH and noise. In Figure 4.55, we compare the two models on a heart MR image affected strongly by IIH. The purpose of these comparisons is to decide which model has the best performance to deal with image affected by both IIH and noise. One may observe that the two models give the accurate results for the original images. However, when we add Gaussian noise with different standard deviations, the C_LGFGD model not only can tackle with higher standard deviation but also gives better results for each standard deviation than the C_LGR model . So, we can conclude that the C_LGR and the C_LGFGD models give results of high accuracy when dealing with IIH without noise. However, in the case of images affected by both IIH and noise, the C_LGFGD model gives better result than the C_LGR model.

4.6.6 Conclusion

In this Chapter, we have synthesized the proposed methods in this thesis, namely the R_LGR, C_LR, C_LGR and C_LGFGD by comparisons on the CPU time, the DSC value, ability for images to deal with intensity in-homogeneity and/or for dealing with noise. The common advantage of the proposed models are to deal with intensity in-homogeneity. Besides, each method has its advantage compared to the others:

- The R_LGR model is best for dealing with noise;

- The C_LR and the C_LGR are the best for the CPU time, the CC_LGR is also the best for its ability to deal with intensity in-homogeneity, the accuracy of the C_LGR when comparing with the ground truth is also very good;

- The C_LGFGD model gives the most accurate results compared with ground truth by calculating the DSC value. In particular, the results of the C_LGFGD model when segmenting images proved that this model is the best to handle both IIH and noise. However, the computation of this method is not as good as the C_LGR;

- The C_LGR is the best in its category of filed of applications, computation time.

So, depending on the objectives, we can recommend a suitable method to segment image. The best parameters for the models can be seen in Table 4.16.

4.7 Conclusion

We have presented in this chapter three novel convex region-based active contour models, namely C_LR, C_LGR and C_LGFGD to effectively segment images with intensity in-homogeneity while being independent of the initial contour. By defining convex energy functions for these models, they are independent of the initial contour. Moreover, the convexity of the energy function allows us to locate the initial contour at everywhere in the image.The proposed models use local intensities with or without combining with global intensities in the energy function to deal with intensity in-homogeneity in images. With the global information in addition to the local information, the resulting model improves the robustness to noise and weak contour. For each model, we have studied the sensibility of the model parameters and provided recommendations about the values that will allow for high accuracy of boundary extraction in case of IIH and robustness to non-homogeneous regions with heavy noise (except for the first convex method). Furthermore, these models are implemented using fats algorithms, hence suitable to treat large volume of image data such as in medical applications.

Table 4.11. The potential Applications of the proposed region-based active contour models. +: good enough, ++: good, //: fail, *: to develop.

Model	Synthetic	X-ray	MR	CT	PET	Ultrasound	Skin lesion
R_LGR	++	+	+	//	//	+	*
C_LR	++	++	+	//	//	*	++
C_LGR	++	++	++	++	+	*	++
C_LGFGD	++	++	++	++	//	*	+

The results, analyses and comparisons on synthetic and medical images with other active contour methods show the performance of the proposed methods.

A synthesis of the three proposed convex models allow us conclude that the C_LGR and the C_LGFGD have better performance. However, based on the Gaussian distribution of intensity for all the modalities considered in our experiences, the C_LGR and the C_LGFGD can handle IIH on different medical modalities such as the X-ray, MR and CT images. However, the C_LGR outperforms C_LGFGD because this latter cannot correctly segment PET image. On the other hand, the advantage of the PET over the C_LGR is its great ability to deal with IIH while being robust to severe noise.

Table 4.12. CPU time and parameters for Figures 4.41-4.43 (computer with core I7 2.8Ghz, ram 6G)

Figure	Model	CPU time	σ	μ	λ	λ_2
Figure 4.41 88×53	R_LGR	0.52	9	x	1000	x
	C_LR	0.11	5	1	x	x
	C_LGR	0.09	5	1	1	0.01
	C_LGFGD	3.08	7	1	0.01	x
Figure 4.42 103×131	R_LGR	5.4	35	x	10	x
	C_LR	0.73	22	1	x	x
	C_LGR	0.39	7	1	1	0.1
	C_LGFGD	104.44	15	1	0.01	x
Figure 4.43 112×129	R_LGR	0.41	7	x	10	x
	C_LR	0.38	13	0.1	x	x
	C_LGR	0.29	11	0.1	1	0.1
	C_LGFGD	58.71	15	1	0.01	x

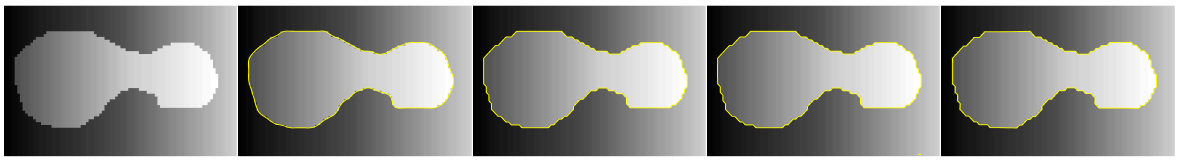

(a) Original image **(b)** R_LGR **(c)** C_LR **(d)** C_LGR **(e)** C_LGFGD

Figure 4.41. Result of the R_LGR, the C_LR, the C_LGR and the C_LGFGD models on a nonhomogeneous image.

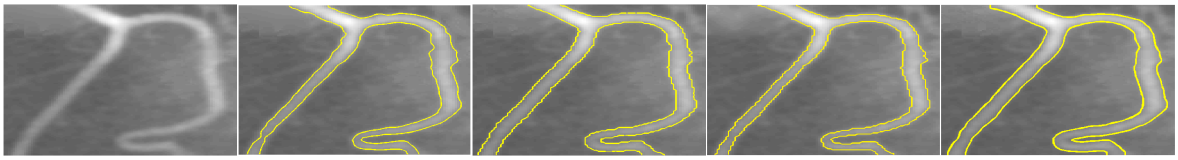

(a) Original image **(b)** R_LGR **(c)** C_LR **(d)** C_LGR **(e)** C_LGFGD

Figure 4.42. Result of the R_LGR, the C_LR, the C_LGR and the C_LGFGD models on a X-ray image (source `http://www.unc.edu/~liwa/`).

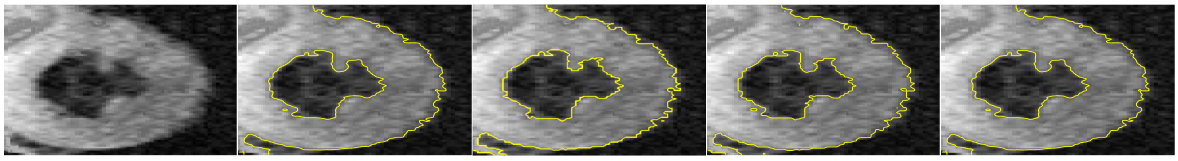

(a) Original image **(b)** R_LGR **(c)** C_LR **(d)** C_LGR **(e)** C_LGFGD

Figure 4.43. Result of the R_LGR, the C_LR, the C_LGR and the C_LGFGD models on a heart MR image (source `http://www4.comp.polyu.edu.hk/~cslzhang/RD/RD.htm`).

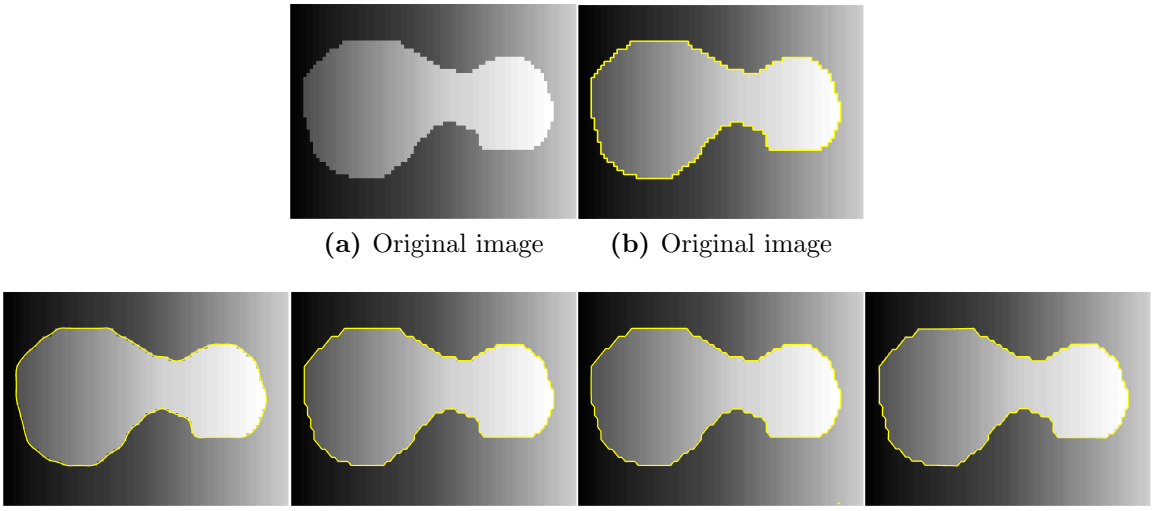

(a) Original image **(b)** Original image

(c) R_LGR **(d)** C_LR **(e)** C_LGR **(f)** C_LGFGD

Figure 4.44. Accurate results of the R_LGR, the C_LR, the C_LGR and the C_LGFGD models on a nonhomogeneous image.

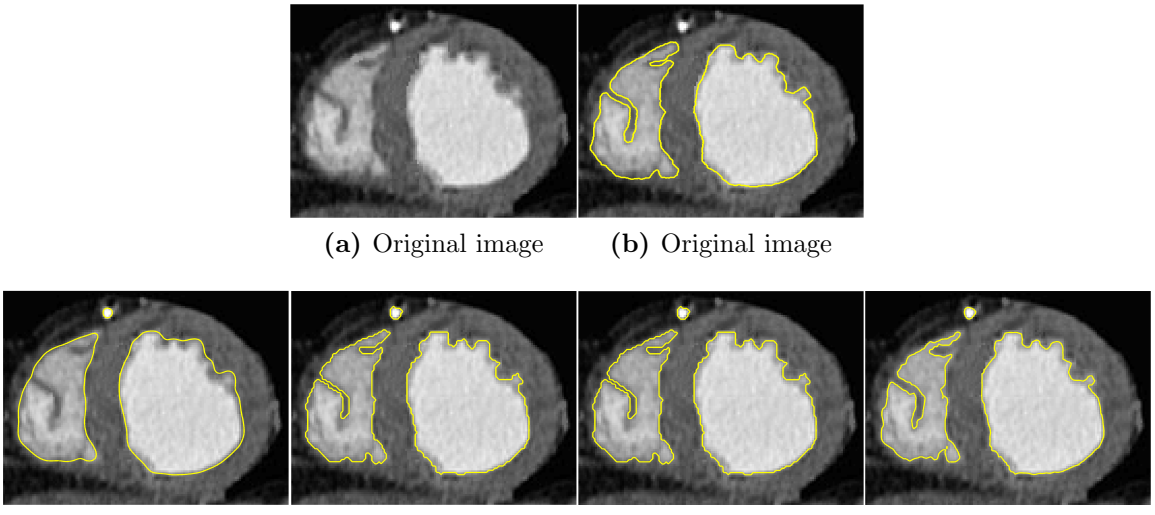

(a) Original image **(b)** Original image

(c) R_LGR **(d)** C_LR **(e)** C_LGR **(f)** C_LGFGD

Figure 4.45. Accurate results of the R_LGR, the C_LR, the C_LGR and the C_LGFGD models on a heart MR image (source `http://www4.comp.polyu.edu.hk/~cslzhang/RD/RD.htm`).

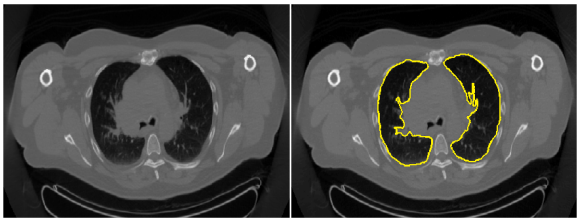

(a) Original image **(b)** Original image

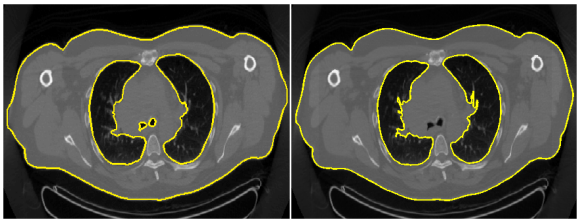

(c) C_LGR **(d)** C_LGFGD

Figure 4.46. Accurate results of the C_LGR and the C_LGFGD models on a thorax CT image (images courtesy of J.-M. Rocchisani, Avicenne-Medicine Nucleaire Hospital, Bobigny, France).

Table 4.13. DSC values and parameters for Figures 4.44-4.46

Figure	Model	DSC (%)	σ	μ	λ	λ_2
Figure 4.44 (synthetic)	R_LGR	98.51	9	x	1000	x
	C_LR	98.45	5	1	x	x
	C_LGR	98.54	5	1	1	0.01
	C_LGFGD	98.54	7	1	0.01	x
Figure 4.45 (MR)	R_LGR	93.44	35	x	10	x
	C_LR	93.19	22	1	x	x
	C_LGR	95.44	7	1	1	0.1
	C_LGFGD	96.29	15	1	0.01	x
Figure 4.46 (CT)	R_LGR	x	x	x	x	x
	C_LR	x	x	x	x	x
	C_LGR	95.24	11	0.1	1	0.1
	C_LGFGD	97.14	20	1	0.01	x

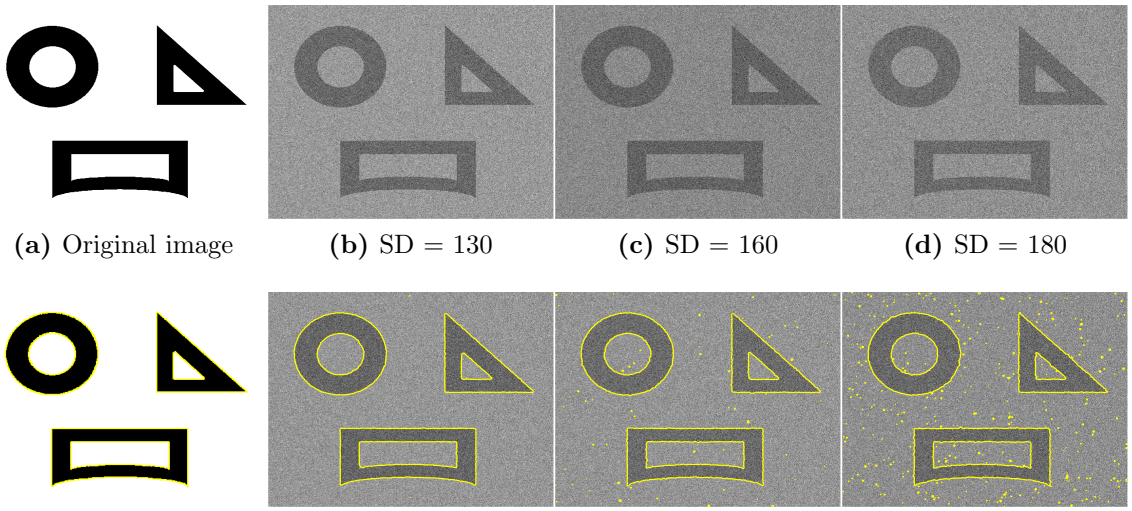

(a) Original image **(b)** SD = 130 **(c)** SD = 160 **(d)** SD = 180

(e) Result of (a) **(f)** Result of (b) **(g)** Result of (c) **(h)** Result of (d)

Figure 4.47. Results of the R_LGR on a synthetic homogeneous image and its noisy version with varying standard deviation (SD).

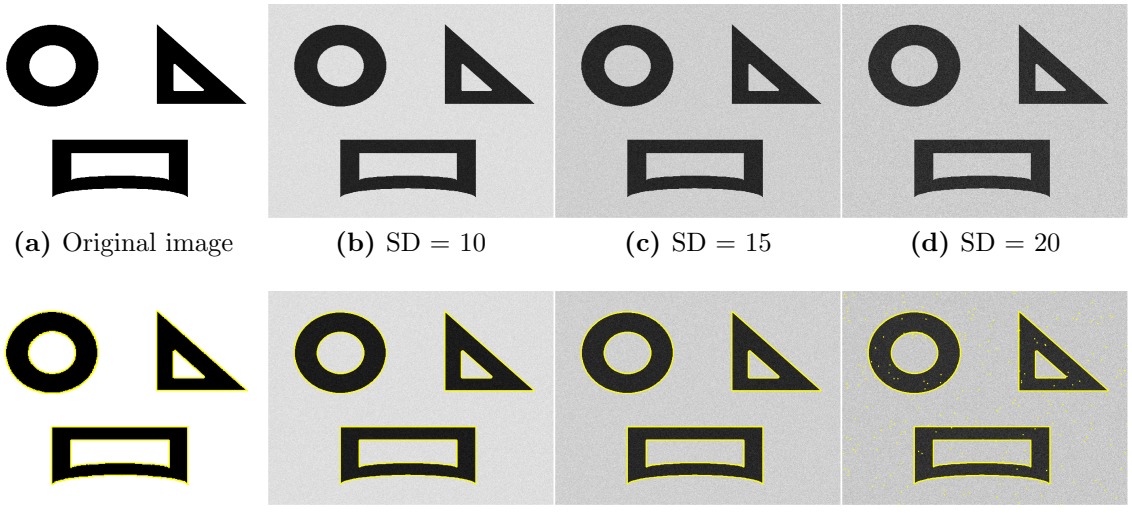

(a) Original image **(b)** SD = 10 **(c)** SD = 15 **(d)** SD = 20

(e) Result of (a) **(f)** Result of (b) **(g)** Result of (c) **(h)** Result of (d)

Figure 4.48. Results of the C_LR on a synthetic homogeneous image and its noisy version with varying standard deviation (SD).

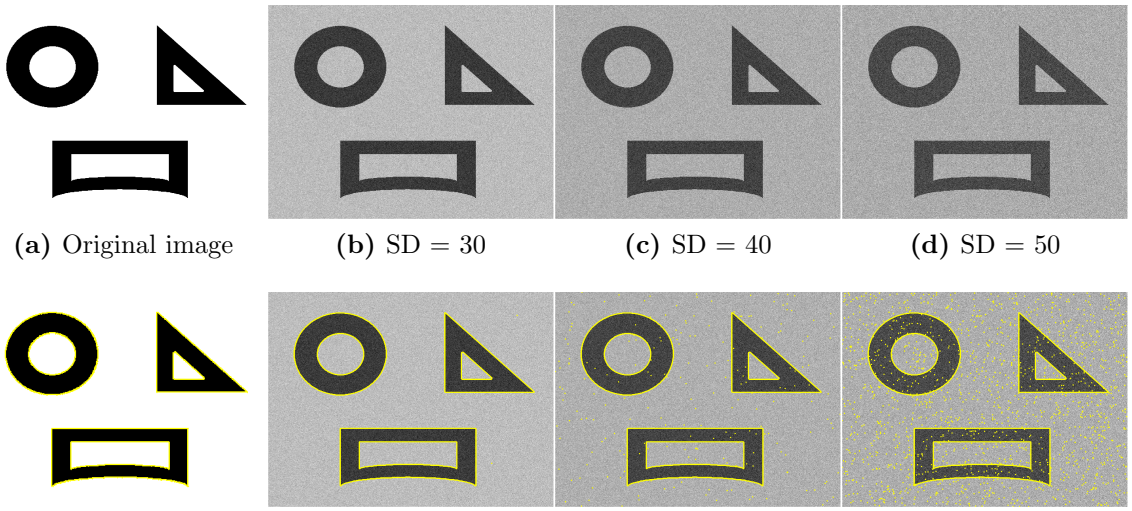

(a) Original image **(b)** SD = 30 **(c)** SD = 40 **(d)** SD = 50

(e) Result of (a) **(f)** Result of (b) **(g)** Result of (c) **(h)** Result of (d)

Figure 4.49. Results of the C_LGR on a synthetic homogeneous image and its noisy version with varying standard deviation (SD).

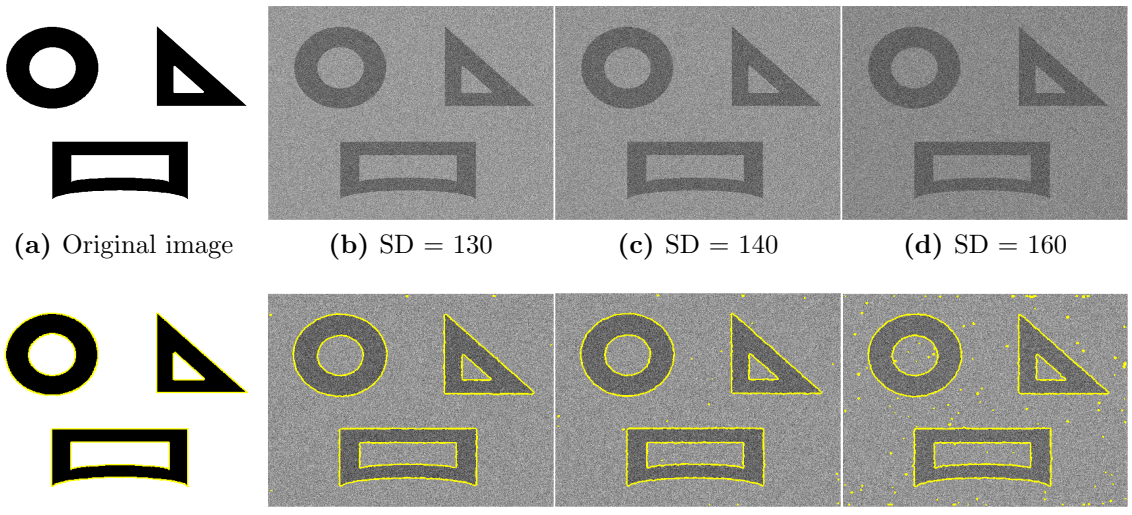

(a) Original image **(b)** SD = 130 **(c)** SD = 140 **(d)** SD = 160

(e) Result of (a) **(f)** Result of (b) **(g)** Result of (c) **(h)** Result of (d)

Figure 4.50. Results of the C_LGFGD on a synthetic homogeneous image and its noisy version with varying standard deviation (SD).

Table 4.14. Maximum of the standard deviations (that the proposed models can deal with) and parameters for Figures 4.47-4.50.

Model	Standard deviation	σ	μ	λ	λ_2
R_LGR	160	3	x	100	x
C_LR	15	25	1	x	x
C_LGR	40	1	1	0.01	1
C_LGFGD	140	1	1	0.99	x

Table 4.15. Maximum of the standard deviations (that the proposed models can deal with) and parameters for Figures 4.51-4.54.

Model	Standard deviation	σ	μ	λ	λ_2
R_LGR	70	3	x	10	x
C_LR	20	25	1	x	x
C_LGR	30	1	1	1	1
C_LGFGD	50	1	1	0.5	x

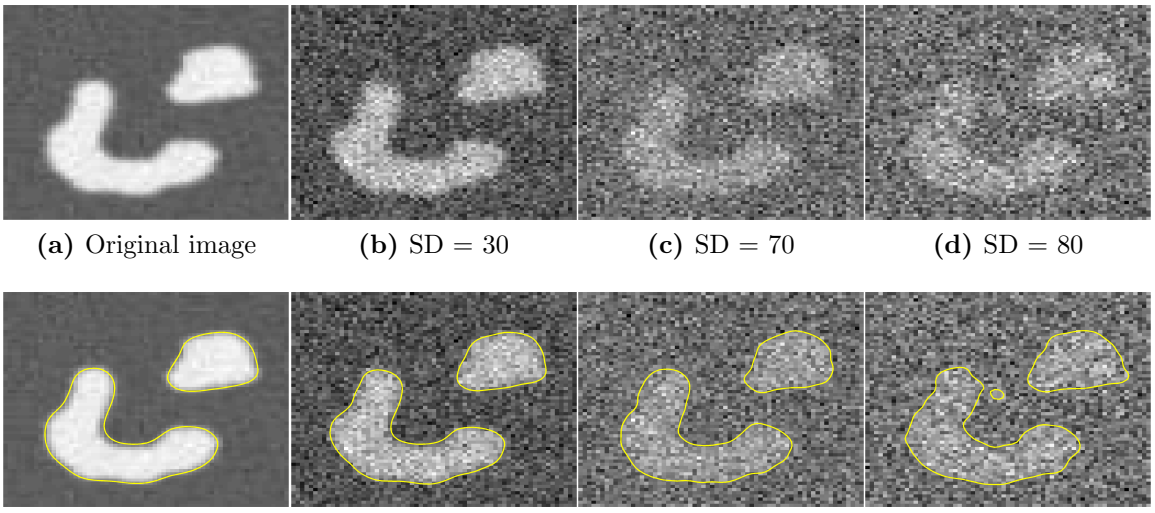

(a) Original image **(b)** SD = 30 **(c)** SD = 70 **(d)** SD = 80

(e) Result of (a) **(f)** Result of (b) **(g)** Result of (c) **(h)** Result of (d)

Figure 4.51. Results of the R_LGR on a synthetic nonhomogeneous image and its noisy version with varying standard deviation (SD).

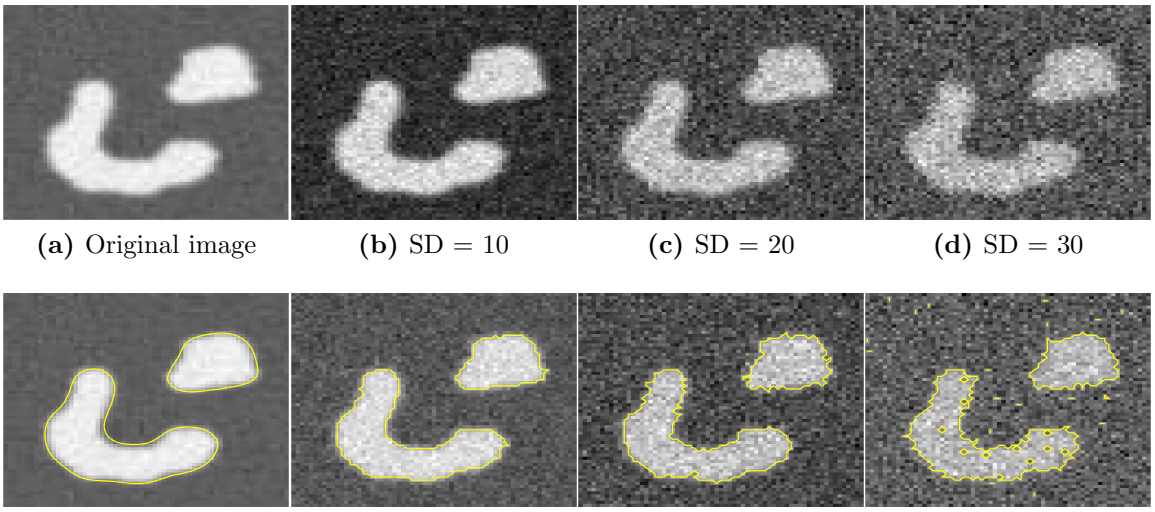

(a) Original image **(b)** SD = 10 **(c)** SD = 20 **(d)** SD = 30

(e) Result of (a) **(f)** Result of (b) **(g)** Result of (c) **(h)** Result of (d)

Figure 4.52. Results of the C_LR on a synthetic nonhomogeneous image and its noisy version with varying standard deviation (SD).

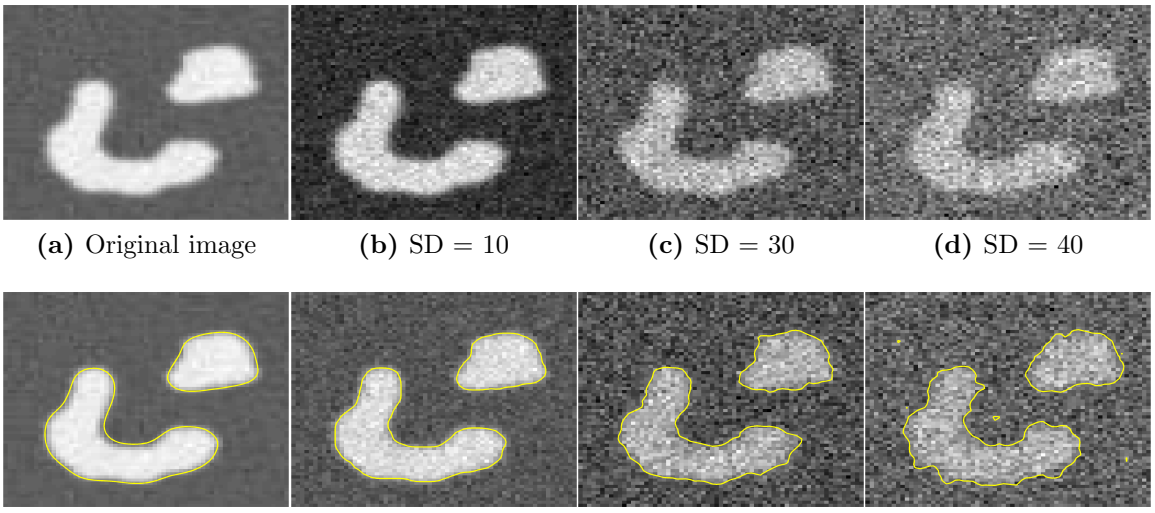

(a) Original image **(b)** SD = 10 **(c)** SD = 30 **(d)** SD = 40

(e) Result of (a) **(f)** Result of (b) **(g)** Result of (c) **(h)** Result of (d)

Figure 4.53. Results of the C_LGR on a synthetic nonhomogeneous image and its noisy version with varying standard deviation (SD).

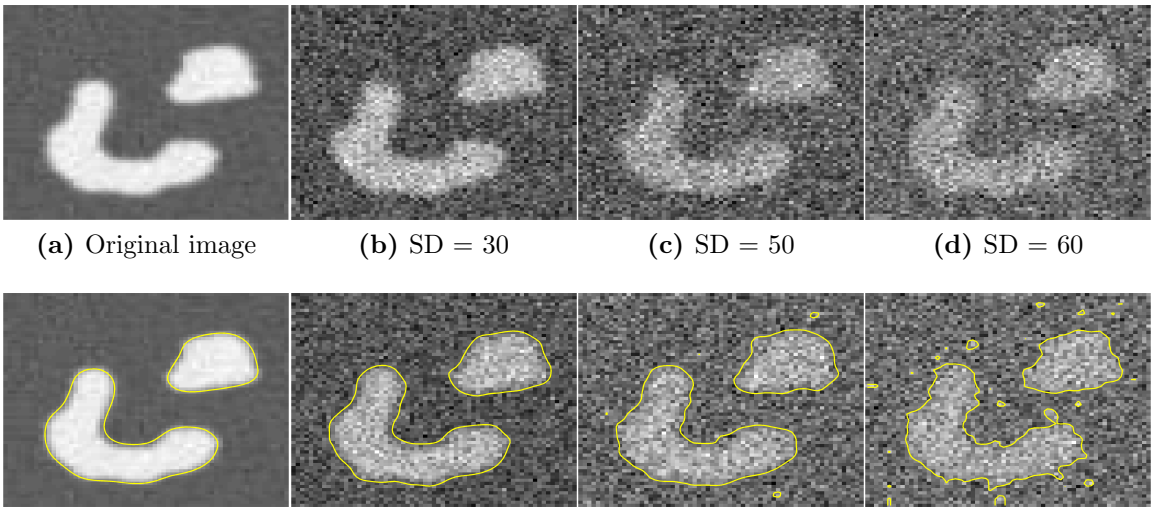

(a) Original image **(b)** SD = 30 **(c)** SD = 50 **(d)** SD = 60

(e) Result of (a) **(f)** Result of (b) **(g)** Result of (c) **(h)** Result of (d)

Figure 4.54. Results of the C_LGFGD on a synthetic nonhomogeneous image and its noisy version with varying standard deviation (SD).

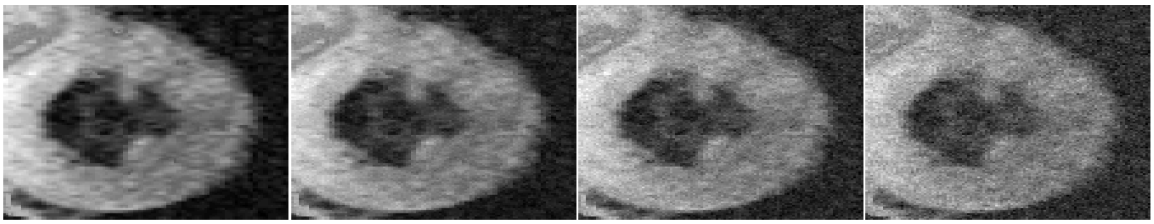

(a) Original image **(b)** SD = 5 **(c)** SD = 10 **(d)** SD = 15

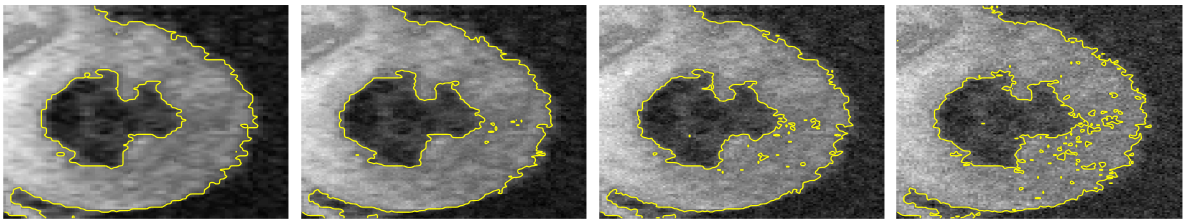

(e) Results of the C_LGR model

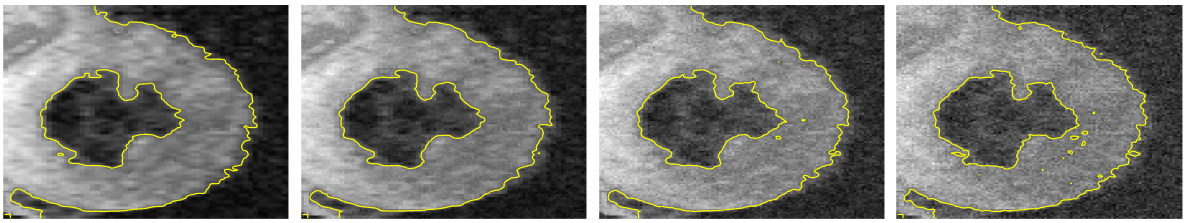

(f) Results of the C_LGFGD model

Figure 4.55. Results of the C_LGR and the C_LGFGD on a hear MR image (source `http://www4.comp.polyu.edu.hk/~cslzhang/RD/RD.htm`) affected strongly IIH and its noisy version with varying standard deviation (SD).

Table 4.16. Suitable values of parameters for segmentating images when fixing $\mu = 1$ and $\lambda_2 = 1$. (* : subjective evaluation without ground truth from experts).

Model	Type of image	Parameter	Value
R_LGR	Synthetic	σ	- Homogeneous object and weak IIH of the background: $7 \leq \sigma$ - Weak IIH: $5 \leq \sigma \leq 15$ - Strong IIH of the object and weak IIH of the background: $29 \leq \sigma \leq 41$ - Strong IIH: $40 \leq \sigma \leq 114$
		λ	$1000 \leq \lambda$
	X-ray*	σ	$9 \leq \sigma \leq 15$
		λ	$9 \leq \lambda$
	MR	σ	- Weak IIH of the object: $26 \leq \sigma \leq 30$ - Strong IIH of the object: $59 \leq \sigma$
		λ	$60 \leq \lambda$
	Ultrasound*	σ	$5 \leq \sigma \leq 9$
		λ	$9 \leq \lambda$
C_LR	Synthetic	σ	- Homogeneous object and weak IIH of the background: $7 \leq \sigma$ - Weak IIH: $5 \leq \sigma \leq 10$ - Strong IIH of the object and weak IIH of the background: $9 \leq \sigma \leq 17$ - Strong IIH: $17 \leq \sigma \leq 25$
	X-ray*	σ	$5 \leq \sigma \leq 20$
	MR	σ	- Weak IIH of the object: $7 \leq \sigma \leq 20$ - Strong IIH of the object: $7 \leq \sigma$
C_LGR		σ	- Homogeneous object and weak IIH of the background: $7 \leq \sigma$ - Weak IIH: $5 \leq \sigma \leq 10$ - Strong IIH of the object and weak IIH of the background: $9 \leq \sigma \leq 17$ - Strong IIH: $17 \leq \sigma \leq 21$
		λ	- Homogeneous object and weak IIH background: $1000 \leq \lambda$ - Weak IIH: $1000 \leq \lambda$ - Strong IIH of the object and weak IIH of the background: $100 \leq \lambda$ - Strong IIH: $10000 \leq \lambda$
	X-ray*	σ	$11 \leq \sigma \leq 20$
		λ	$10 \leq \lambda \leq 20$
	MR	σ	- Weak IIH of the object: $7 \leq \sigma \leq 20$ - Strong IIH of the object: $13 \leq \sigma$
		λ	$1000 \leq \lambda$
	CT	σ	$12 \leq \sigma$
		λ	$10 \leq \lambda$
C_LGFGD	Synthetic	σ	- Homogeneous object and weak IIH of the background: $8 \leq \sigma$ - Weak IIH: $7 \leq \sigma \leq 10$ - Strong IIH: $26 \leq \sigma \leq 30$
		λ	- Homogeneous object and weak IIH of the background: $0< \lambda < 1$ - Weak IIH: $0 < \lambda \leq 0.01$ - Strong IIH: $\lambda \leq 0.1$
	X-ray*	σ	$15 \leq \sigma \leq 27$
		λ	$0.001 \leq \lambda \leq 0.1$
	MR	σ	- Weak IIH of the object: $10 \leq \sigma \leq 13$ - Strong IIH of the object: $16 \leq \sigma$
		λ	- Weak IIH of the object: $0 < \lambda \leq 0.01$ - Strong IIH of the object: $0 < \lambda \leq 0.1$
	CT	σ	$19 \leq \sigma \leq 22$
		λ	$0 < \sigma \leq 0.01$

CHAPTER 5

Application

Contents

5.1 Introduction

In medical imaging, segmentation is necessary for detection of pathological regions such as tumors or lesions [9, 27, 11]. With the newest imaging technologies and computer vision, segmentation can help improving the diagnostics, monitoring and staging of patients. Despite the recent acquisition technologies and performances of reconstruction algorithms, the quality of medical images can be affected by inherent noise or artifacts involving PET (Positron Emission Tomography), MR (Magnetic Resonance) images as well as low dose CT (Computed Tomography) images [89], making it difficult to distinguish the organ structure. This in turn makes the segmentation more difficult [90]. An important obstacle for the effective segmentation is the intensity in-homogeneity, which is due to a typical phenomenon known as shading artifact in medical images. It behaves as a relative variation of the intensity in the object of interest.

This chapter presents applications

1. of the C_LR model for dot extraction from skin lesion images;
2. of the C_LGFGD model for extracting boundaries of lesion regions from skin lesion images;
3. of the C_LGR model for 3D CT images.

5.2 Dot Extraction from Skin Lesion Images

A computer automated interpretation of classic melanoma dots and globules could augment the clinical visual diagnosis of melanoma, increase the probability of biopsy for suspicious skin lesions, lead to earlier pathological diagnosis of melanomas, reduce the biopsy rates of benign lesions, and assist in the screening of melanomas by lesser-experienced operators. The computer automated interpretation of skin lesions could identify the classic melanoma features of dots and globules of dark tissue superimposed over lighter colored tissue.

The method developed hereafter is designed for accurate boundary extraction of dots typical of melanoma. The finding of dots is used to produce a numerical measurement of the probability of the lesion being malignant. This probability is used to influence the clinical dermatologist's opinion: If the clinical visual opinion is a low probability and biopsy would not be done or postponed, a high computer generated probability score could change the clinical opinion and result in a biopsy being performed earlier, potentially leading to an earlier diagnosis, treatment, and improved patient outcome.

This study uses skin lesion images [91] that have been biopsied and pathologically diagnosed as melanoma and images which are benign. For every image a boundary extraction ground truth and clinical diagnosis of dots has been made.

Skin lesion dots are features which play significant role for melanoma diagnosis. In the clinical practice there are multiple procedures and rules, used by dermatologists, which involve dots to classify a skin lesion as melanoma.

The ABCD rule (Asymmetry of the lesion, Boundary abrupt, Colors number, Dermoscopic Structures) [92] uses dots in the D component. At least three dots are necessary to be observed in order to increase the likelihood of melanoma. The 7-points rule [93] applies two criterions. The first one checks for atypical pigment network, blue-whitish veil, and atypical vascular pattern. The second one is searching for irregular dots, irregular streaks, irregular pigmentation, and regression structures.

The Menzies method [94] uses a set of negative features and a set of positive ones. The negative category consists of: symmetry of pattern, presence of a single color. The positive one contains: peripheral black dots, multiple brown dots, multiple blue/gray dots, blue-white veil, radial streaming, scar-like depigmentation, multiple colors, and broadened network. Hence, the dots are the part of the second set and a lesion is classified as melanoma if none of the negative features is present and at least one of the positive features is found in the skin lesion.

From the above rules, finding more than two dots in skin lesions increases the probability of a melanoma diagnosis. Vertergaard *et al.* [95] found the sensitivity for melanoma detection using the naked eye was 74% and dermoscopy, a non-invasive in vivo observation using optical magnification, was 90%. This illustrates that automatic methods of melanoma identification have the potential of increasing melanoma detection.

The automatic extraction of lesion's boundary and features is a subject of interest among the image processing and analysis society. In [96] a level set approach is applied to extract the lesion's boundary from noisy images. In [97] a gradient vector flow has been employed to tackle this problem. The lesion boundary, the boundary of the different lesion's colored regions and the number of colors present in the lesion are extracted in [98] by applying an active contour based on the geometric heat differential equation. But this model was unsuccessful to determine the lesion's dots from an image.

In [99] the authors present an approach capable of defining pigment networks by using graphs. To do so the method "removes other round structures such as globules, dots, and oil bubbles, based on their size and color" [99].

To the best of our knowledge there is no method in the literature capable of automatic skin lesion dots extraction from images. One of the reasons is that dots can be difficult to observe and missed by the clinician. It is also difficult to automatically extract the boundary of lesion's dots due to their size, location, ill-defined boundaries, background color, and the fact that they are surrounded by other skin artifacts considered as noise: other lesions structures, oil bubbles, other injuries.

This section utilizes the C_LR model presented in Section 4.3.1 for automatic dots

extraction from skin lesion images. Let us recall here the C_LR model:

$$\min_{\substack{u_1,u_2\\0\leq f\leq 1}} \left\{ E(u_1,u_2,f) = \mu TV_g(f) + \int_\Omega f(x)e_{in}(x,u_1)dx + \int_\Omega (1-f(x))e_{out}(x,u_2)dx \right\} \quad (5.1)$$

where $\Omega \subset \mathbb{R}^+$ is a bounded image domain, $I : \Omega \to \mathbb{R}+$ is a given image on this domain, x is a pixel in Ω, u_1 (u_2) is the smooth function that approximates local intensity inside (outside, respectively) the contour, μ denotes a positive constant, f is a bounded level set function in $[0,1]$, g is an edge detector function so that its value vanishes at object boundaries. The energy function (5.1) contains three terms: the first one is the regularization term, the second and third terms are the data fidelity ones. The regularization term $TV_g(f)$ is defined as:

$$TV_g(f) = \int_\Omega g(x)|\nabla f(x)|dx. \quad (5.2)$$

where $g(x) = \frac{1}{1+|\nabla I(x)|^2}$.

The second and third term are the data fidelity terms. Here e_{in} (e_{out}) represents the local differences in intensity between the average intensity u_1 (u_2, respectively) and the image I. Theses data fidelity terms are computed within the local Gaussian K_σ:

$$e_{in}(x,u_1) = \frac{\int_\Omega K_\sigma(x-y)(I(x)-u_1(y))^2dy}{\int_\Omega K_\sigma(x-y)dy} \quad (5.3)$$

$$e_{out}(x,u_2) = \frac{\int_\Omega K_\sigma(x-y)(I(x)-u_2(y))^2dy}{\int_\Omega K_\sigma(x-y)dy} \quad (5.4)$$

where x and y are pixels, and $K_\sigma(u) = \frac{1}{\sqrt{2\pi}\sigma}\exp\big(-\frac{|u|^2}{2\sigma^2}\big)$, where σ is the standard deviation.

In this section, we test the C_LR model on a set of skin lesion images with ground truth about existence of dots provided by clinician. A second clinician defined the dots manually as a ground truth for comparison. For verification purposes the ground truth definition of dots was performed twice along with the automated results obtained by our method C_LR.

Recall that our goal is to detect the dots in these images. Since the dots are small distinct objects, we selected large values of μ (see Section 4.3.4) to detect as many objects as possible at the finest level. To demonstrate the efficiency of the C_LR model, we compare our results with the ground truth of our expert, as well as with the results of smaller value of μ.

In addition, comparisons with the convex model of Chan *et al.* [35] (convex Chan-Vese) and the LBF model [77] are shown to emphasize that C_LR performed more accurately and consistently.

We use MATLAB r2008b to implement our algorithm on a computer with Intel Core 2 Duo CPU 2.93GHz and 4GB RAM. The images used for the experiments are in the

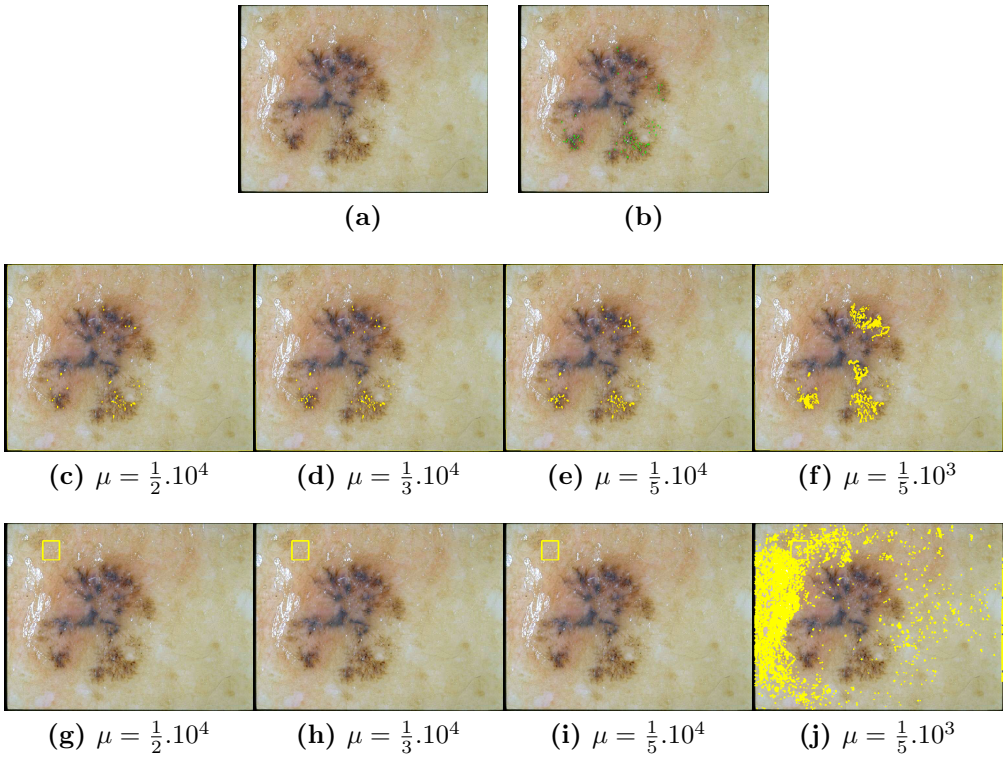

Figure 5.1. Test on a skin lesion image with different values of μ. (a) Original image. (b) Ground truth marked with green dots. (c) (d) (e) (f) Results by the C_LR model. (g) (h) (i) (j) Results of the convex Chan-Vese model [35].

size 768 512. The parameter σ is chosen 3 for all experiments. The other parameters in Algorithm 4.1 (Section 4.3.3) are selected as follows: $\theta = 0.1$, $\tau = 0.1$ and $\alpha_{thres} = \frac{1}{2}$. The tested images are from Dr. Nikolay Metodiev Sirakov and Dr. Richard Selvaggi (Texas A&M University Commerce in USA).

Figure 5.1 shows a comparison between C_LR and the convex Chan-Vese model [35]. Both models used the same parameters as described in Section 4.3.4. An observation of the results obtained in Figure 5.1 tells that when μ increases, the number of extracted non-dots regions (False Positive - FP) increases as well. The most accurate result confirmed by our physician was obtained for $\mu = \frac{1}{3}.10^4$ (Figure 5.1d). To decrease the subjectivity, the image has been considered three times on different dates. With $\mu = \frac{1}{3}.10^4$, the dots have been successfully extracted, while the convex Chan-Vese model [35] did not find any dot. Comparing the results obtained by C_LR with the ground truth, we can see that the C_LR model cannot detect all dots at the right part of the lesion regions (False Negative - FN). The reason is that the intensities of the dots in these regions are very similar with the neighboring pixels. However, the multiple dots extracted (51 true detected dots on

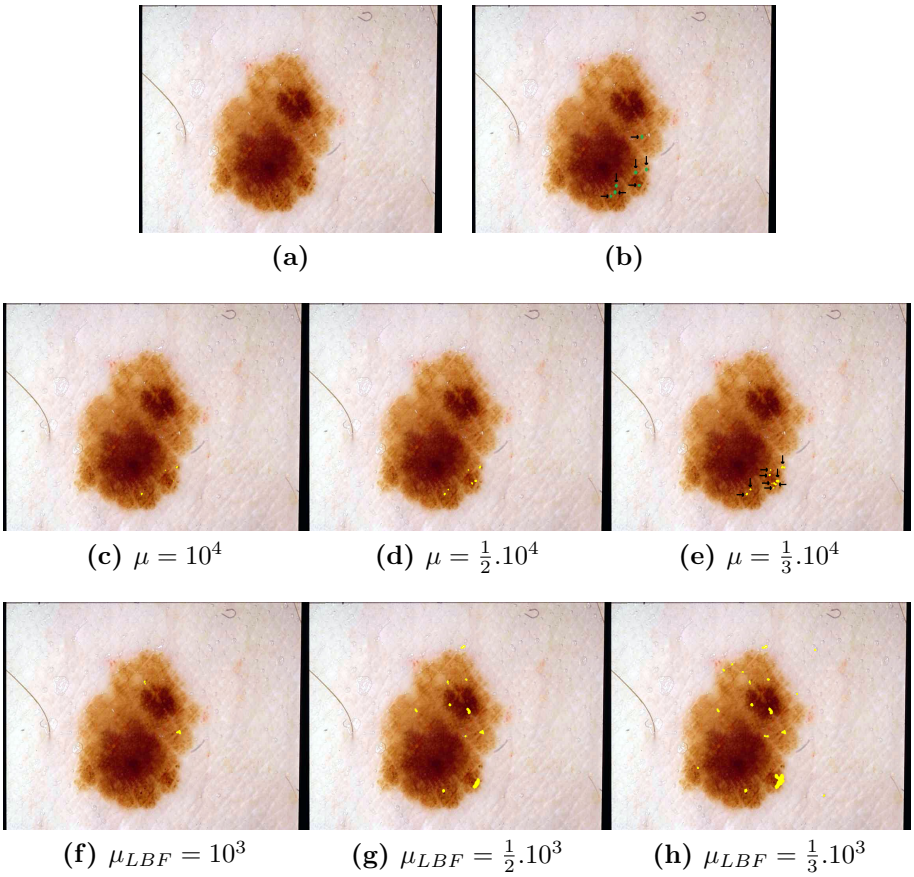

(a) **(b)**

(c) $\mu = 10^4$ **(d)** $\mu = \frac{1}{2}.10^4$ **(e)** $\mu = \frac{1}{3}.10^4$

(f) $\mu_{LBF} = 10^3$ **(g)** $\mu_{LBF} = \frac{1}{2}.10^3$ **(h)** $\mu_{LBF} = \frac{1}{3}.10^3$

Figure 5.2. Test on a skin lesion image with different values of μ. (a) Original image. (b) Ground truth in green. (c) (d) (e) Results of the C_LR model. (f) (g) (h) Results of the LBF model [77].

69 ground truth dots) are sufficient for a dermatologist to increase the probability for melanoma using any of the clinical methods described in [92, 93, 94].

Figure 5.2 depicts a comparison between the C_LR and the LBF models [77], which utilizes local information as well. Both models used the same set of parameters with the exception that λ for the LBF, μ_{LBF}, is 10 times larger than μ for C_LR. The reason is that for larger values, LBF misses almost all dots (large FN). Studying Figure 5.2 one may observe that the number of false positive (FP-non dot regions) extracted by LBF is significantly larger than the FP extracted by the C_LR. In the same time the LBF is detecting less true positive (TP-real dots) than the C_LR does.

Figure 5.3 depicts an image with a few dots but sufficient to increase the likelihood of melanoma. We have used again a very large value of $\mu = \frac{1}{4}.10^5$ (Figure 5.3c) and extracted 5 out of 7 dots in the image. But their influence on the likelihood for melanoma is significant, because more than three dots are sufficient. Note that the detection of these

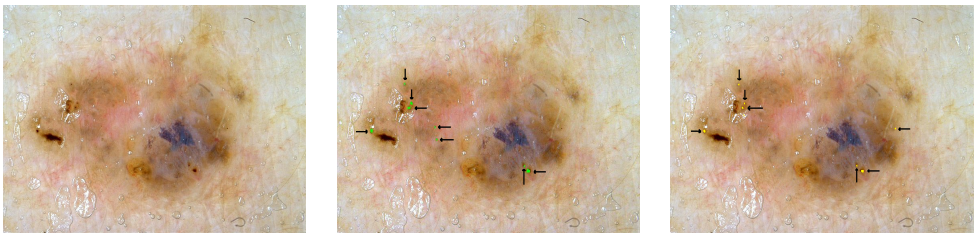

(a) **(b)** **(c)** $\mu = \frac{1}{4}.10^5$

Figure 5.3. Test on a skin lesion image. (a) Original image. (b) Ground truth: green dots pointed by arrows. (c) Result of the C_LR model: yellow dots pointed by arrows.

dots is very difficult for dermatologist, too.

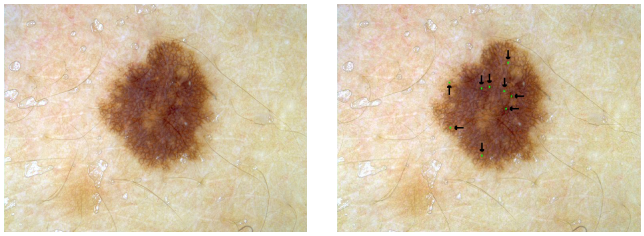

(a) **(b)**

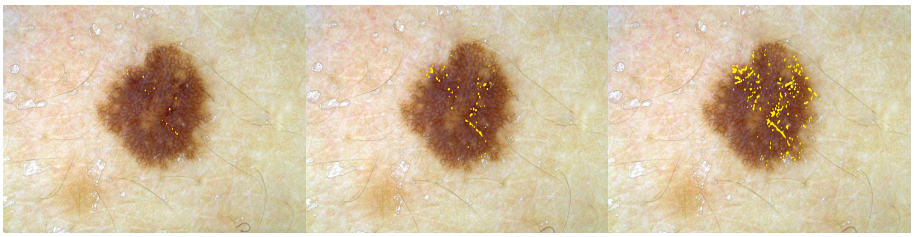

(c) $\mu = \frac{1}{25}.10^5$ **(d)** $\mu = \frac{1}{5}.10^4$ **(e)** $\mu = 10^3$

Figure 5.4. Test on a skin lesion image with different values of μ. (a) Original image. (b) Ground truth in green. (c) (d) (e) Results of the C_LR model.

Another experiment is shown in Figure 5.4. In this figure, we show the original image (Figure 5.4a), the ground truth (Figure 5.4b), and our results with a number of μ values (Figure 5.4c-5.4e). The most accurate results was obtained with $\mu = \frac{1}{25}.10^5$. In this experiment, one may observe the limitations of the C_LR method as in the two experiments described above (Figures 5.1 and 5.3), where dots with low contrast are not detected.

In Figure 5.5, we show another experiment on a skin lesion image which has a large number of dots. In this figure, the two most accurate and expert confirmed results are shown in Figure 5.5c-5.5d. Figure 5.5b shows some of the dots missed by the C_LR (FN) and painted in red by our medical expert. The rules for melanoma diagnosis [92, 93, 94, 95]

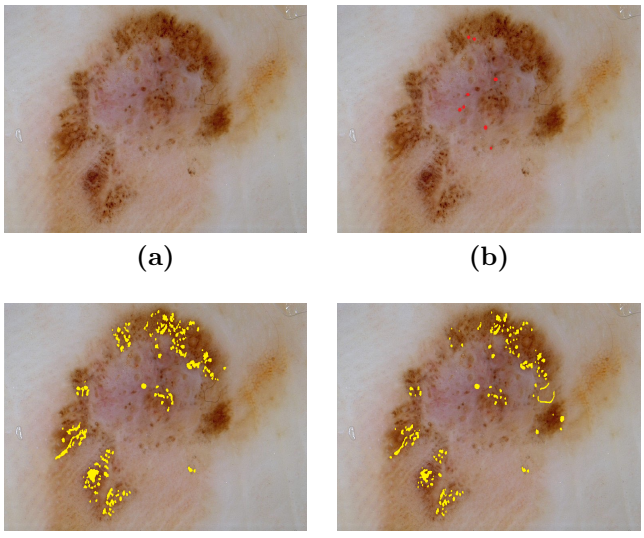

(a) **(b)**

(c) $\mu = \frac{1}{5}.10^4$ **(d)** $\mu = \frac{1}{3}.10^4$

Figure 5.5. Test on a skin lesion image with different values of μ. (a) Original image. (b) In red are shown dots that the C_LR model has missed. (c) (d) Results of the C_LR model.

state that the missed dots do not affect the diagnostic conclusion in this particular case. The result with $\mu = \frac{1}{5}.10^4$ (Figure 5.5c) concurs well by estimation of our physician. Another useful result for a dermatologist is obtained with $\mu = \frac{1}{3}.10^4$ (Figure 5.5d).

Figure 5.6 and Figure 5.7 show another accurate results obtained by the C_LR method on skin lesion images along with the ground truths of our physician. One may observe that the C_LR model gives results very close to the ground truth, but may detect some FP points outside of the lesion regions (black circle (Figure 5.6f)). Although they are skin dots, the dermatologist considers them as artifacts. To overcome this problem, the method given in [98] may be applied to remove the outliers.

Further, six lesion images without dots are shown in Figure 5.8. We tested our C_LR method on these images with a large amount of μ values from 1 to 10^6. The obtained results show that the C_LR method did not detect any dots in the skin lesion regions. These results were confirmed by our physician and the ground truth information. The results demonstrate once again that the C_LR model is suitable to segment the dots in skin lesion images.

Finally, we know that a robust and meaningful evaluation metric is key to objectively compare the results obtained using different algorithms. In this challenge we will evaluate the C_LR performance by finding the precision and recall measures of the method under evaluation. In order to produce such measurements, the following notions will be defined:

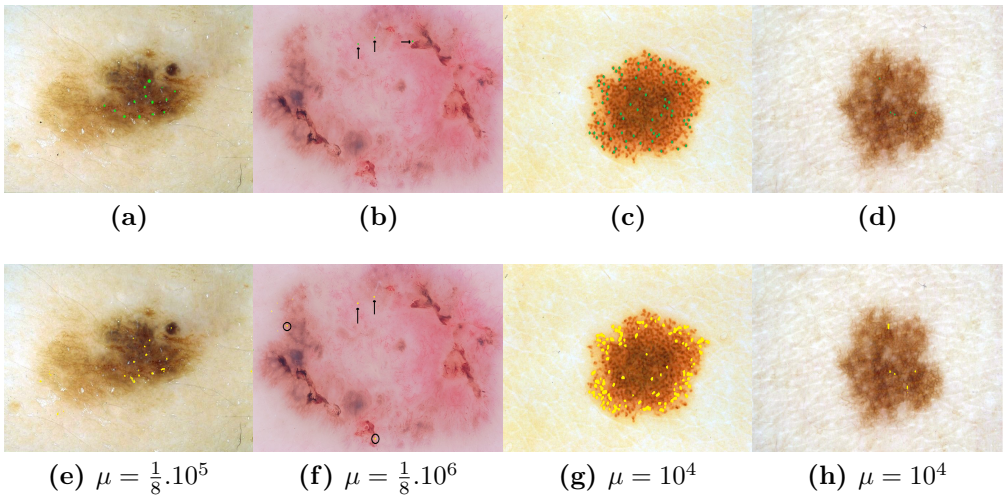

(a) **(b)** **(c)** **(d)**

(e) $\mu = \frac{1}{8}.10^5$ **(f)** $\mu = \frac{1}{8}.10^6$ **(g)** $\mu = 10^4$ **(h)** $\mu = 10^4$

Figure 5.6. Test on four skin lesion images. First row: Ground truths in green. Second row: Results of the C_LR model in yellow.

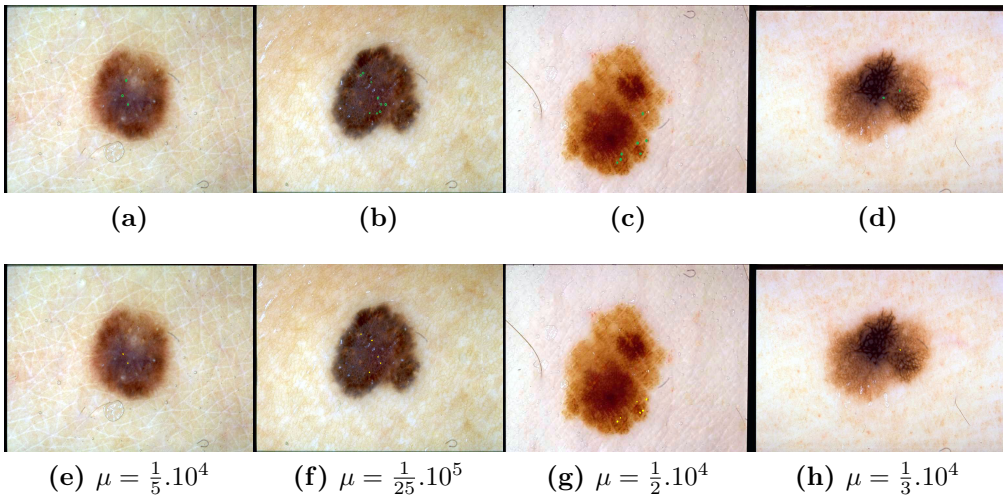

(a) **(b)** **(c)** **(d)**

(e) $\mu = \frac{1}{5}.10^4$ **(f)** $\mu = \frac{1}{25}.10^5$ **(g)** $\mu = \frac{1}{2}.10^4$ **(h)** $\mu = \frac{1}{3}.10^4$

Figure 5.7. Test on four skin lesion images. First row: Ground truths in green. Second row: Results of the C_LR model in yellow.

+ True positive (TP): Any location provided by the algorithm that is within an embolus, or a distance lower than ϵ - a given small value - from the embolus. If there are several detection locations assigned for the same embolus, only the detection with the highest confidence score will be taken into account.

+ False positive (FP): Any location that is outside or at a distance greater than ϵ of

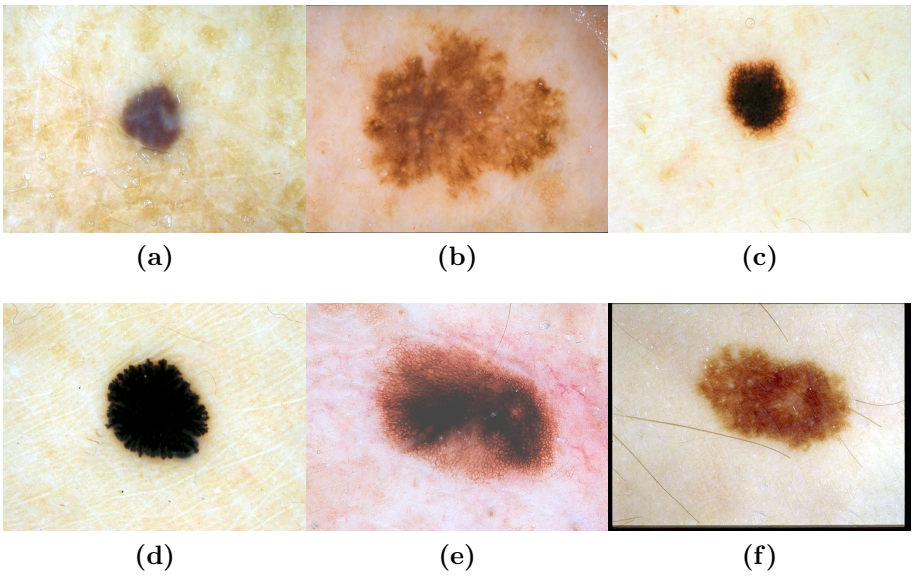

(a) **(b)** **(c)**

(d) **(e)** **(f)**

Figure 5.8. Six images without dots.

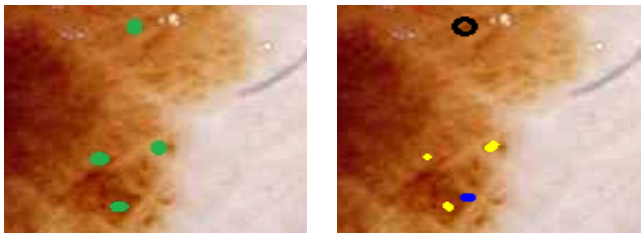

(a) Gound true dots (green)

(b) RCAC detected dots (yellow and blue)

Figure 5.9. Illustration for TP (yellow), FP (blue) and FN (black circle).

any embolus.

+ False negative (FN): any embolus without any detection inside or closer than ϵ to it.

Figure 5.9 provides an illustration for TP, FP and FN on a portion of skin lesion region. In this figure, Figure 5.9a presents the ground true dots marked by our experts while Figure 5.9b shows the dots (in yellow and blue) detected by the C_LR method. Compared with the ground true dots, we observe that there are three C_LR detected dots in yellow which are true dots (TP = 3); there is one C_LR detected dot in blue which is not true dot (FP = 1); there is one C_LR missed dot (FN = 1) which is marked by the black circle.

The formulas to calculate precision and recall are as follows:

$$\text{precision} = \frac{TP}{TP + FP} \tag{5.5}$$

$$\text{recall} = \frac{TP}{TP + FN} \tag{5.6}$$

Note that in some lesion images no dots are present (Figure 5.8). In these cases if the automated method does not detect any dot, then the result is 100% correct. But Equations (5.5) and 5.6 will give precision = recall = 0 (numerically, these equations will yield 0 if FP is different than 0), which does not represents the performance of the method. Also, one has to take into account the fact that at least three dots are necessary to be detected in order to increase the likelihood of melanoma. Thus, for lesion images where no dots are present we suggest the following measurement for precision and recall:

- FP = 0 then precision = recall = 100%;
- FP = 1 then precision = recall = 70%;
- FP = 2 then precision = recall = 40%;
- FP > 2 then precision = recall = 0.

Other border cases appear if two or one dot is given as a ground truth. If 1 is given as a ground truth and if the method detects no dot then FN = 1, which implies that TP = 0. Therefore Equations (5.5) and 5.6 will give a result zero, which shows a very big error. On the other hand, this result does not affect the diagnosis. Thus, we suggest precision = recall = 50%.

Similar reasoning applies if 2 dots are given as a ground truth and FN = 2. Follows that TP = 0 and Equations (5.5) and 5.6 will give a result 0. Thus we suggest for this case precision = recall = 30%.

If two dots are given as a ground truth and FN = 1, follows that the TP = 1 and Equation (5.6) will give a recall of 50% while the value of Equation (5.5) will depend on the FP detected by C_LR.

For each of the above border cases three additional cases could be added with respect to the number of FP (1, 2, more than 2). To generalize such amount of particular cases a new statistical approach is necessary. Since this is a complex study which may involve intervals of confidence. Such a study is a subject of development in the future.

On the other hand, for the images with ground truth of more than 3 dots, if the precision is close to 1 (is close to 100%), there are only a few FP dots detected. If the recall is close to 1 (is close to 100%), there are only a few true dots which are missed (FN). The precision and recall for the images in this paper are reported in Table 5.1.

Table 5.1. The precision and recall of the C_LR

Fig.	Precision (%)	Recall (%)
5.3c	86	75
5.6e	69	69
5.6f	67	50
5.6g	58	73
5.6h	50	75
5.7e	100	67
5.7f	100	56
5.7g	83	71
5.7h	100	50
5.8(all)	100	100

In addition to the results shown in Figures 5.1 to 5.8 (19 images), experiments were performed with 15 new skin lesion images. For each of these images a ground truth about existence of dots is determined by a clinician and a second one independently marked the dots manually for the comparison purposes with the C_LR performance. Thus, for each of the additional 15 skin lesion images, the precision and recall have been calculated using Equations (5.5) and (5.6) and the border cases introduced above. Further, for the total of 34 results obtained by the C_LR, from 34 skin lesion images, average, min, max and standard deviation were calculated for precision and recall. The results are presented in Table 5.2.

Table 5.2. The precision and recall of the C_LR

	Precision (%)	Recall (%)
average	74	73.7
min	11	13
max	100	100
standard deviation	30.3	27

Out of the 34 images, 9 are defined by ground truth without dots, 6 lesions contain 1 or 2 dots. The remaining 19 images contain 3 or more dots.

The min precision and recall calculated in Table 5.2 corresponds to a benign lesion image where the ground truth determined 9 dots, the C_LR defined TP = 1, FN = 8, FP

= 7. The max of 100% comes from benign and malignant lesion image with less than 3 dots. One cancer lesion with a few dots provided 100% precision and 50% recall. Other 4 cancer images with multiple dots showed precision in the eighties and recall above the average.

There are multiples images where more than twenty dots are present. The precision and recall for these images is below the average. But even if the precision and recall are below the average the obtained dots are well above three. Therefore they are sufficient to increase the probability of melanoma.

We have proved the C_LR model capable of detecting dots in skin lesion images. The results of the C_LR compared with the ground truths are promising. Using large value of μ, the parameter controls the length of the contour such that the C_LR model gives results on extracting the dots as many as possible and sufficiently for a dermatologist to reach a decision about the likelihood of melanoma. Note that presences of more than two dots, in a lesion, are sufficient for a doctor to diagnose an increase of the likelihood of melanoma [92, 93, 94], which will require biopsy.

However, a limitation of the C_LR model is its difficulty to extract dots having low contrast with the surrounding skin. The lowest recalls on the sample space of 34 images are obtained from high number of FN. They come from missed dark dots on dark lesion, as shown in Figures 5.6f and 5.6h (see also Table 5.1). Note that these dots are at risk for being missed by the clinician, too. In the future, we will work to find ways to adapt the C_LR model so that the dots with low contrast can be detected as well.

Conclusion

We have applied the Convex local region-based to detect small objects such as dots in lesion skill images. Due to the regularization term which combines gradient information on image data with the total variation of the level set function, the detection of dots is enhanced while maintaining smoothness of the curve. This results in accurate and reliable detection of dots. This confirm the potential applicability of the method as computerized tool for the detection and diagnosis of skin lesion. We can extend the method in the Bayesian framework to benefit from the fully statistical distribution. For example, if the standard deviation is taken into consideration, the detection may be improved with low contrast

5.3 Lesion Region Extraction from Skin Lesion Images

This section will complete for the previous section to lesion region extraction but utilizing the C_LGFGD model. As the C_LGFGD is designed with full local statistics, it is able to

detect regions of different textures such as lesion region. We have applied the C_LGFGD model to skin lesion images to extract their boundaries. To perform a statistical evaluation of C_LGFGD, set of experiments were performed with 24 skin lesion images (which are from Dr. Nikolay Metodiev Sirakov and Dr. Richard Selvaggi (Texas A&M University Commerce in USA)). Figure 5.11 shows four of them. Except the lesion, these images are often populated with other injuries, oil bubbles and hair which make the automatic lesion boundary extraction very difficult task. A ground truth is provided for every image from the collection. Three dermatologists were involved in the production of each ground truth boundary. To assess the accuracy of C_LGFGD, we calculate the DSC, the recall and the precision values for each automatic extraction with respect to the ground truth for every image.

Different from estimating dot extraction that the precision and recall are calculated based on number of dots, to estimate region extraction, the precision and recall are calculated based on number of pixels of the regions:

$$\text{recall} = \frac{N(S_1 \cap S_2)}{N(S_2)} \times 100\% = \frac{TP}{TP + FN} \tag{5.7}$$

$$\text{precision} = \frac{N(S_1 \cap S_2)}{N(S_1)} \times 100\% = \frac{TP}{TP + FP} \tag{5.8}$$

where S_1 and S_2 represent the active contour segmentation and the ground truth, respectively, $N(\cdot)$ indicates the numbers of pixels in the enclosed set. Now, denote by $TP = N(S_1 \cap S_2)$ - true positive, $FN = N(S_2 \backslash S_1)$ - false negative, $FP = N(S_1 \backslash S_2)$ - false positive and $TN = N(\Omega \backslash S_2)$ - true negative. One may observe in Figure 5.10 an illustration for the above notions. From the above expressions we conclude that for:

+) *high recall and high precision:* the pixels in these kind of result are mostly in the ground truth such that TP is large, while FN and FP are small,

+) *high recall and low precision:* most of the pixels in the result are also pixels in the ground truth but there are also pixels which are not in the ground truth. Thus TP and FP are large while FN is small,

+) *low recall and high precision:* there are only a few FP, but the FN are relatively large with respect to TP,

+) *low recall and low precision:* both FP and FN are relatively large with respect to the TP.

For the skin lesion images shown on Fig. 5.11, we have calculated the recall, the precision and the DSC, and posted the values on Table 5.3. The same attributes were determined for the collection of 24 skin lesion images and the calculated values are given on Table 5.4.

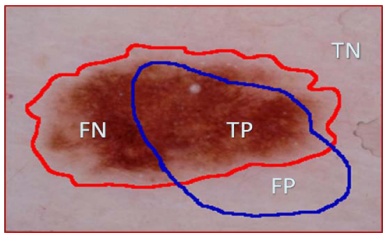

Figure 5.10. An illustration for TP, FP, FN and TN. S_2 is the region inside the red line, S_1 is the region inside the blue line.

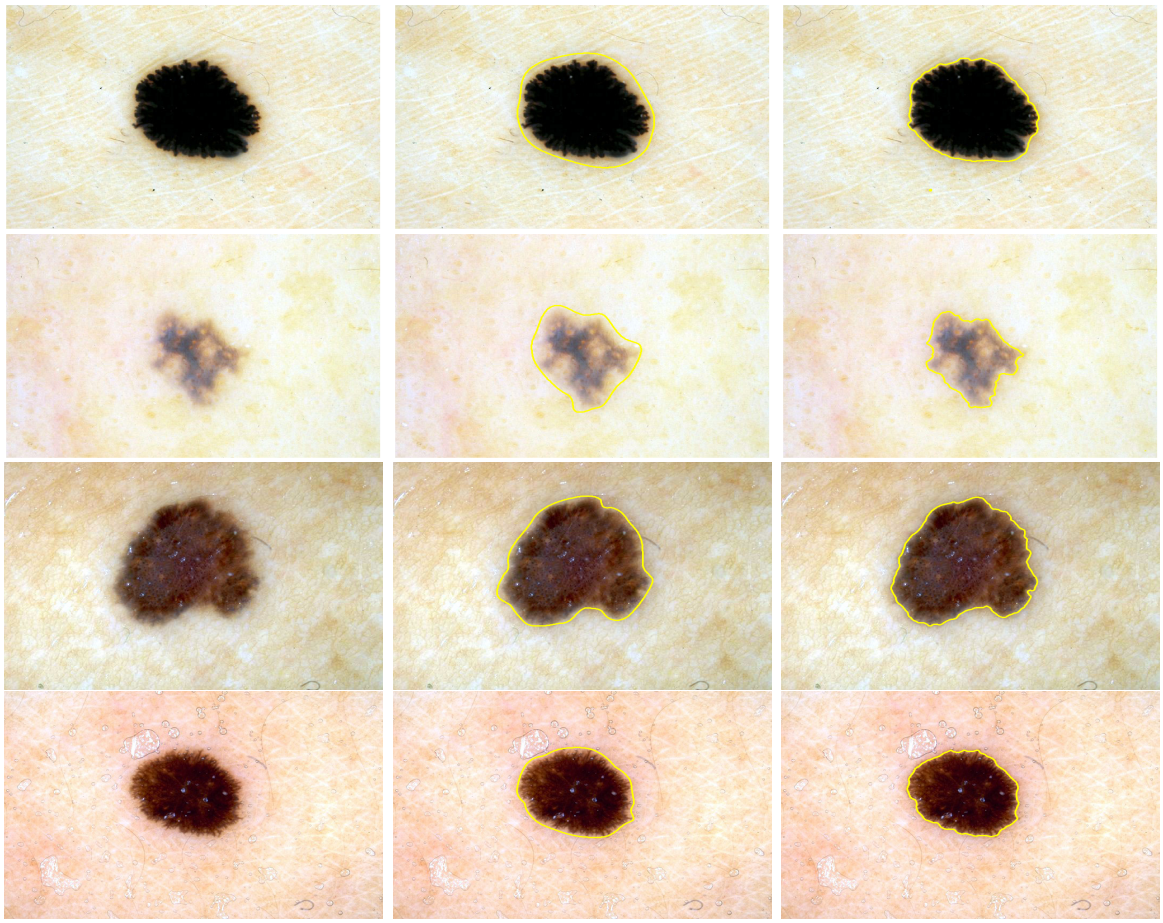

Figure 5.11. First to third columns: original skin lesion image, gound truth and C_LGFGD result.

One may tell from there that the minimal precision is 95.73%, the max is 100% and the average is 99.72%. Follows that most of the pixels in the results belong to the ground truth and the number of the FP pixels detected by the active contour is very small. This fact is confirmed in Figure 5.11. This is the reason for the relative large minimal DSC values

Table 5.3. Recall, precision and DSC values for the third column of Figure 5.11

	Row 1	Row 2	Row 3	Row 4
recall (%)	81.35	74.55	91.89	90.77
precision (%)	99.97	99.99	99.98	100
DSC (%)	91.50	85.42	95.77	95.16

Table 5.4. Min, max, average, standard deviation of the recall, precision and DSC values of 24 skin lesion images.

	min	max	average	standard deviation
recall (%)	24.26	91.89	71.77	16.38
precision (%)	95.73	100	99.72	0.90
DSC (%)	39.05	95.77	82.23	12.83

in Table 5.4. The large minimal DSC suggests also a large difference between the FP and FN. Since FP is small, FN is relatively large. The latter conclusion is confirmed also by the relatively low recall average of 71.77%.

Another contribution of the present study is the calculation of the confidence intervals into which fall the mean of the recall and the accuracy of image segmentation by the C_LGFGD. There are different approaches in the literature used to calculate the interval of confidence for the mean of a large population using the mean and the standard deviation of a sample space. The application of a particular formula depends on the size of the sample space and the nature of the performed experiments: binomial or non-binomial trial.

The extraction of boundaries by the C_LGFGD and the comparison with ground truth boundaries constitutes a non-binomial trail. Also the number of the sample is 24, which is considered as small. Therefore we assume a $t-$distribution and apply the following formula to calculate intervals of confidence:

$$\bar{X} \pm t_{\frac{\alpha}{2},n-1} \frac{S}{\sqrt{n}} \tag{5.9}$$

In Equation (5.9), $\bar{X}$ is the mean of the sample space, $t_{\frac{\alpha}{2},n-1}$ is determined from a table on the base of $\frac{\alpha}{2}$ which is a parameter that depends on the confidence percentile required. $(n-1)$ is a degree of freedom. Further S is the standard deviation of the sample data, while n gives the number of the elements in the sample.

Applying Equation (5.9), we have calculated that with 95% of confidence we may state that the mean of the precision of boundary detection with the C_LGFGD of a large population of skin lesion images will belong to the interval $[99.4, 100]$. With 95% of confidence

we may state that the mean of the DSC for a large set of images will belong to the interval $[76.82, 87.64]$, and the mean of the recall for a large set of images will belong to $[64.86, 78.68]$.

Conclusion

We have evaluated the performance of the proposed C_LGFGD model for the extraction of lesion region in skin images. The statistical quality measures indicate promising performance of the method. As the C_LGFGD is designed with full local statistics, it is able to detect regions of different textures such as lesion region and the background of different mean or variance, since the curve is guided by the difference in distribution. In the future, we can improve the method with respect to the computation time. Note that, in the previous section, sometime we need extract the lesion region before applying the C_LR model to detect dots in the lesion region. Therefore, the C_LGFGD model can be utilized as the first step when detecting dots from skin lesion images.

5.4 3D Medical Images

Volume segmentation of medical images is an important part for diagnosis and analysis of anatomical data. The 3D medical images obtained from the MRI, the CT or PET technologies, offer high benefices for diagnosis, radiotherapy planning, surgical planning and simulation. However, segmentation of 3D volume still faces challenges due to many issues: large variability in organs and tissues, complex structures and variability in textures of many adjacent tissues.

This is necessary to provide segmentation method suitable for medical images. Hereafter, we will present some results of the C_LGR model for 3D medical images. They are considered as beginning results for our perspectives for one or more applications such as detection of lung, airways or lung nodule for cancer detection.

In this section, we adapt our algorithm for 2D images to segment 3D thorax and heart CT images. The 3D images are obtained from our experts and from the databases [100]. Each image 3D is obtained from 154 to 260 slices. The thickness of slices varies between 1.5mm and 1.9mm. Note that, the slices of a 3D image have the same thickness, while the thickness of two slices in two different 3D images may be different. The 2D dimension of each slice vary between 250×350 and 340×460. As the thickness of slices, the slices of a 3D image have the same dimension, while the dimension of two slices in two different 3D images can be different. Table 5.5 shows the information of the 3D CT images that we present in this paper.

From our experts, we have two 3D thorax CT images. The obtained results are quite good as proven by our expert. We present a result of the C_LGR in Figure 5.12. We can

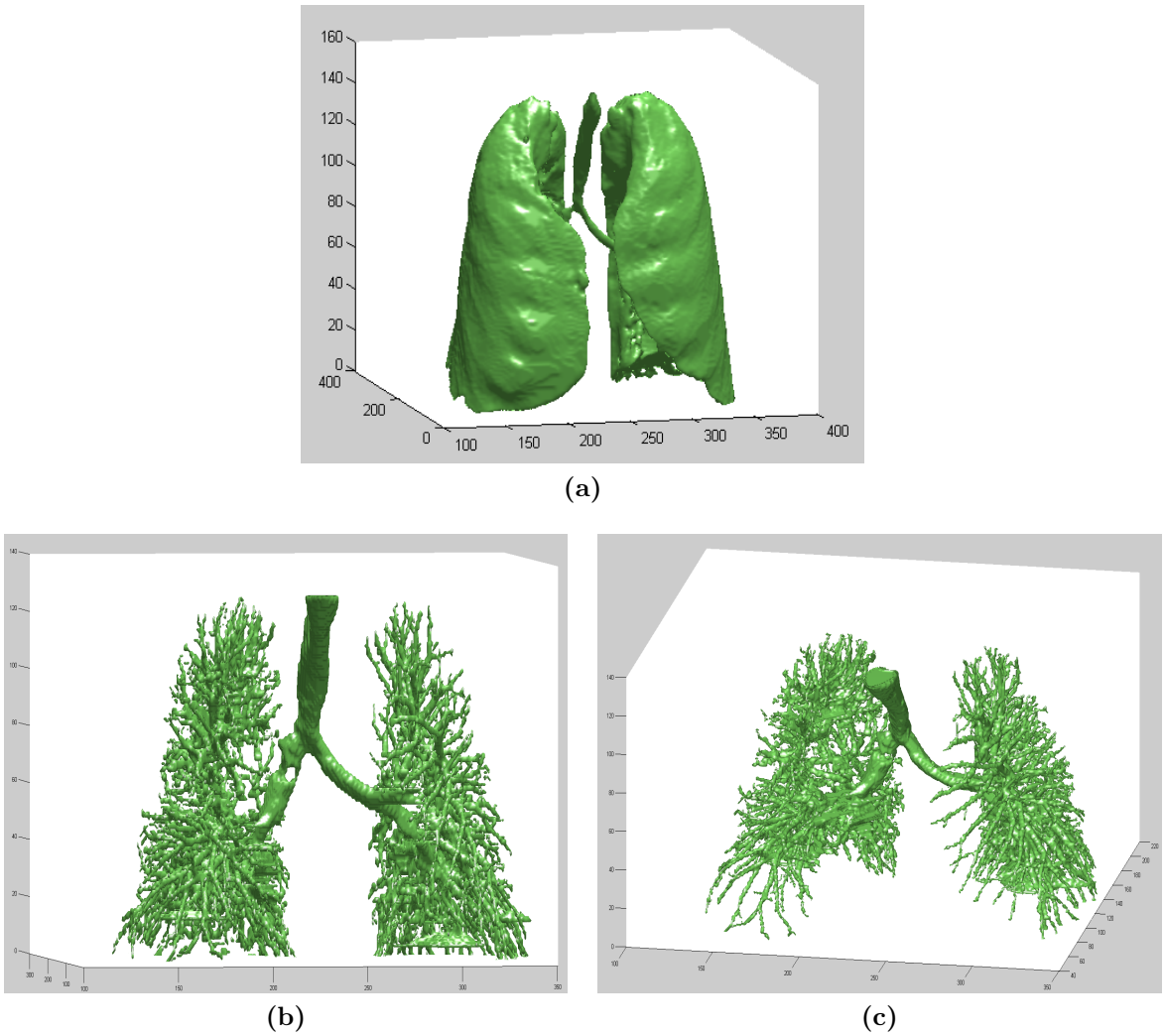

(a)

(b) **(c)**

Figure 5.12. Experiment on a thorax 3D CT image. (a) Surface of a thorax. (b) and (c) The inside of (a) with two different observations.

see the surface of the lung segmented by the C_LGR model in Figure 5.12a. Moreover, we show in Figures 5.12b-5.12c the inside of the lung with two different observations. One can see the bronchi as well as the bronchial tree of the lung in the images. Further, in Figure 5.13, we present a zoom-in a sub-part of the top left-lung presented in Figure 5.12b and Figure 5.12c to see more clearly the bronchiole of the lung.

From the database [100], we obtain heart 3D images. The obtained results are very promising. Hereafter, we report four segmentation results in Figure 5.14. From these results and our experts, we can determine the ventricles, the atrium, the vena cava, the pulmonary trunk, the coronary arteries and the aorta of the heart. However, these parts are not distinguished by the different color in our results, because there are only two regions

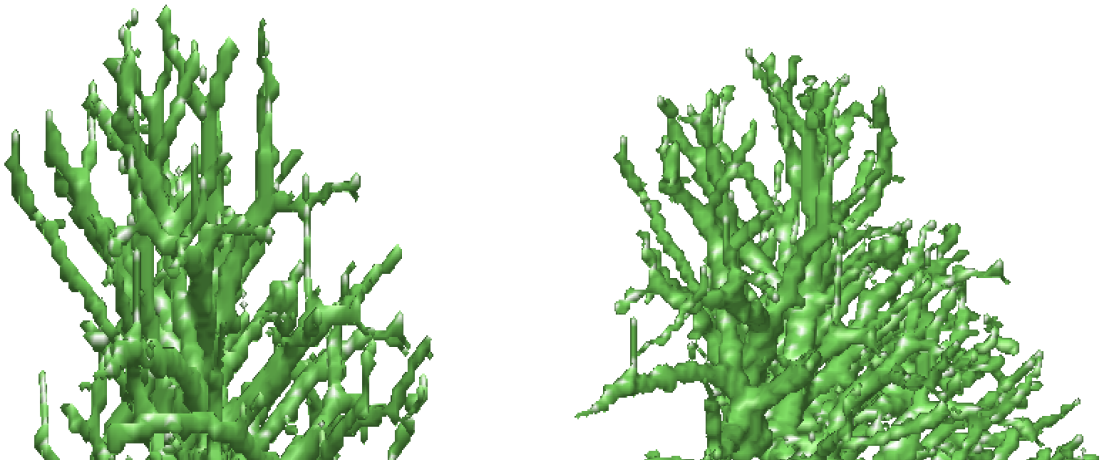

(a) (b)

Figure 5.13. Zoom-in of Figure 5.12b (a) and Figure 5.12c (b).

(object and background) in our C_LGFGD model. This is considered as a limitation of the C_LGFGD model, as well as most of other models assuming two regions in an image. In Figure 5.15, we mark the heart anatomy in different colors (for Figure 5.14a). Our perspective for this section is to be able to automatically mark the human anatomy in a 3D image.

Table 5.5. Information of 3D images in this section 5.4.

Figure	Number of slices	Thickness of a slice	Dimension of a slice	Resolution (mm^3)
5.12a	130	1.5mm	257×459	$1.17 \times 1.17 \times 1.5$
5.14a	321	1.5mm	333×308	$0.40 \times 0.40 \times 1.5$
5.14b	286	1.5mm	361×388	$0.37 \times 0.37 \times 1.5$
5.14c	209	1.5mm	357×408	$0.40 \times 0.40 \times 1.5$
5.14d	255	1.5mm	368×335	$0.40 \times 0.40 \times 1.5$

5.5 Conclusion

In this chapter, we have just presented three applications for medical and skin lesion images: the first one is the application of the C_LR model for dot extraction from skin lesion images (Section 5.2); the second one is the application of the C_LGFGD for extraction

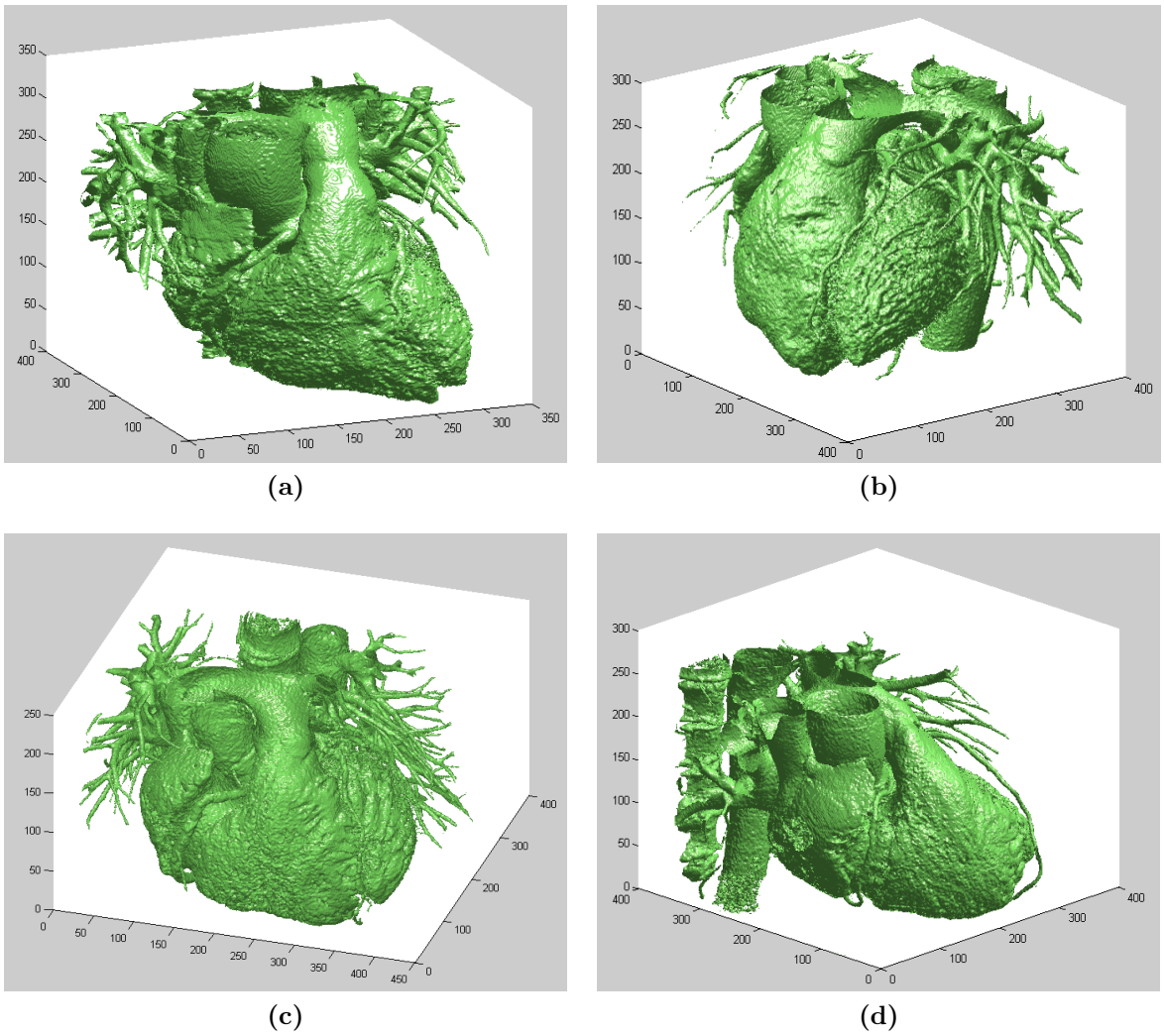

Figure 5.14. Experiment on four heart 3D CT images.

of boundaries of lesion regions from skin lesion images (Section 5.3) and the third one is the application of the C_LGR for the anatomy extraction in 3D medical images (Section 5.4). The results and analyses for skin images show that the C_LR model can be efficiently applied for dot extraction, while the initial results for 3D medical images of the C_LGR model are very promising. As to the C_LGFGD, this method provides promising results to boundary extraction of skin legion. These results of the C_LGR are encouraging to continue to develop the this model on a specific application or for anatomy atlas.

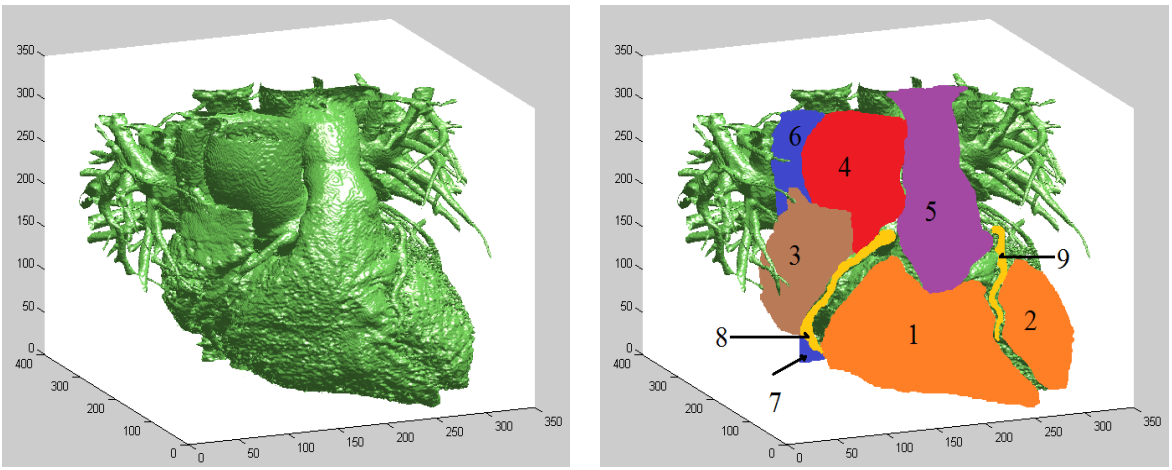

(a) Figure 5.14a **(b)**

Figure 5.15. Heart Anatomy of Figure 5.14a. (a) Figure 5.14a. (b) Marked image: 1. Right ventrice, 2. Left ventrice, 3. Right atrium, 4. Aorta, 5. Pulmonary trunk, 6. Superior vena cava, 7. Inferior vana cava, 8. Right coronary artery, 9. Left coronary artery.

CHAPTER 6

Conclusion and Perspectives

Contents

This chapter provides a summary of the work presented and the conclusions drawn from this work. It lists the contributions to knowledge already achieved in this research and provides directions for future work.

6.1 Summary and Conclusion

In this thesis, one of major artifacts in medical images, namely intensity in-homogeneity has been addressed by the novel proposed region-based active contour models to provide accurate segmentation. For this purpose, we exploit the local intensity information to design appropriate energy function. The local property is determined by a local window and the local intensities are approximated on this window by assuming a piecewise-smooth approximation of the image. Furthermore, image intensity is modelled by the Gaussian distribution. In the three proposed convex models, regions are characterized by local and/or global intensity means. In the last model, we consider the full Gaussian distribution with the means and the standards deviations of local and global intensities.

In the other hand, the global region-based provides accurate results and robustness to noises, weak edges and boundary gaps as well as varying initialization. Hence, the combination of the global information with the local information allows for the benefice

from the two approaches. It is also interesting to adaptively control the weight between these two terms.

The associated energy functionals of these models also include a regularization term. This term is important to maintain the evolving curve smooth. We have adopted the regularization term of the convex Chan-Vese model [33], and that of the Bresson *et al.*'s model [41]. The regularization term of Bresson *et al.*' model is a hybridized GAC model with he total variation of a bounded level set function. This allows more accurate segmentation while maintaining smoothness of he contours.

Another problem of the image segmentation is the dependence of the initial contour. This issue has been tackled with different solutions in this thesis. For this purpose and to deal with IIH, we proposed firstly in Chapter 3 a non-convex model that uses the traditional level set function ϕ and takes into account the local and global information in the energy function. The experimental results show that this model not only can efficiently deal with intensity in-homogeneity but also is very robust to noise and to the initial contour. This model can apply for non-homogeneous synthetic, MR, X-ray and ultrasound images. However, because the energy function of this model is not convex with respect to the level set function ϕ which is used to determine the contour, the dependence of the initial contour is not completely solved.

In Chapter 4, three novel convex models were proposed to solve the dependence of the initial contour. In these models, the intensity local information is taken into account in their energy functionals to tackle IIH in images.

1. The first proposed convex model, namely C_LR, utilizes the bounded level set function instead of the conventional level set, as well as the regularization term to impose smoothness constraints using the total variation of the bounded level set function with the edge detector as in the Bresson's *et al.* model [41]. As a consequence, the energy function of the proposed models in this chapter is convex with respect to the bounded level set function. This allow us to locate the initial contour everywhere in an image and the results are the same providing reliability to the results. In the energy function, the C_LR model only uses the local information. So, it can deal with intensity in-homogeneity. As application, this model can be efficiently used for non-homogeneous synthetic, MR, X-ray as well as to identify dots from skin lesion images.

2. The second proposed convex model, namely C_LGR, is an extended version of the C_LR model by combining with the global information inspired from the convex Chan-Vese model [33]. Therefore, the energy function of this model is also convex. Moreover, the combination with global information allows this model to overcome problems of noise or smooth boundary which often affect adversely medical images. This model is successfully tested for non-homogeneous synthetic, MR, X-ray, CT and PET images.

The ability for segmenting 3D images as presented in Chapter 5 can allow this model to accurately identify and extract tumors in the lung such as nodules.

3. The third proposed model, namely C_LGFGD, also combine local information and global information to benefit from the advantages as the C_LGR model: dealing with IIH and robustness to noise or smooth boundary. Unlike the above two models, the C_LGFGD combines the Fuzzy c-means clustering and the statistical region-based approach defined in the Bayesian framework to take advantage of the robustness of the two approaches and the accuracy from the statistical approach. We suppose that intensity of each pixel is distributed by the Gaussian pdf with varying variance and mean. This is not the case of the C_LR and the C_LGR models: only mean varies. This implies that results of the C_LGFGD model are more accurate than results of the C_LG and the C_LGFGD models. On the other hand, the C_LGFGD model utilizes the fuzzy membership function which is also a restricted function and considered as a pseudo level set function to cluster image while imposing smoothness from the total variation of the membership function. This allows the convexity of the energy function implied that the final contour is independent from the initial position of the contour. This model gives more accurate segmentation for non-homogeneous synthetic, MR, X-ray and CT images. Besides, the C_LGFGD model succeeds to extract lesion regions in skin lesion images with high confidence as presented in Chapter 5. It is also used to help the C_LR model in the case of erasing artifact outlier the lesion regions which may be understood mistakenly as dots. It means that there are two step to extract dots: the first one is to use the C_LGFGD model to extract a lesion region, then the C_LR is utilized in the second step to identify dots in the lesion region

We have proposed fast schemes for the implementation to solve the models in Chapter 4, we used algorithms based on dual problems for the C_LR and the C_LGR. By this way, the energy function is minimized in a cheaper computational way. For the model C_LGFGD, we directly calculate the energy function which allows to avoid conditions about stability as PDE method.

Moreover, for each method, sensibility studies of the model parameters have been investigated, resulting in recommendation for the appropriate values of these parameters to obtain good segmentation.

6.2 Perspectives

The aim of our research is to propose models which are suitable to automatic segmentation (convex model) and for dealing with intensity in-homogeneity. So, in the future, we will

develop the C_LR, the C_LGR and the C_LGFGD models presented in this thesis for their potential applications.

Apart from some promising results, the three proposed convex methods have still some limitations which need to be improved. They are listed below:

1. The C_LR model does not work for dots with low contrast.

2. The three convex models cannot distinguish multiple regions be cause we assume that there are only two regions (object and background) in images. Especially in segmenting 3D medical image, this does not allow to distinguish automatically different parts of body at the same time.

3. The CPU time of the C_LGFGD model is slow calculating for each pixel in each iteration step.

4. Another disadvantage is that the C_LGFGD model cannot work for PET image. One of the reasons is that we use the Gaussian distribution to describe global and local intensities in the energy function, while the PET images are often corrupted by the Poisson distribution.

So, in the future, we envisage to deal with the above inconvenience in their application as follows:

1. We will adapt our models using a prior information, e.g. *a priori* of dots, to overcome the drawback of low contrast of dots.

2. Second, we will extend the C_LGR method to automatically discriminate multiple regions.

3. Next, to overcome the problem about CPU time, we will find algorithms more rapid and suitable to solve the C_LGFGD model.

4. We plan to use suitable distribution which makes the C_LGFGD model more effective to apply for PET images. Another interesting aim for this model is to combine with the belief function theory as the works published in [103] end extend our models to deal with partial volume effect.

5. Lasly, the non-convex R_LGR model gives very good result for segmentation of ultrasound image. This is interesting to have ground truth of this modality and to adapt this model to convex model.

APPENDIX A

Appendix: Euler-Lagrange Equation

In calculus of variations, the Euler Lagrange equation is a differential equation whose solutions are the functions so that at this solution functional, another given functional is stationary. This equation was developed by Swiss mathematician Leonhard Euler and Italian mathematician Joseph Louis Lagrange in the 1750s.

Because a differentiable functional is stationary at its local maxima and minima, the Euler Lagrange equation is useful for solving optimization problems where we need find a function to minimize or to maximize another function.

A.1 Euler - Lagrange Equation for the Case of One Variable and One Function

Theorem A.1. [101, 102] *Let $J : C^2[a, b] \to \mathbb{R}$ be a functional of the form:*

$$J(y) = \int_a^b F(x, y, y')dx \tag{A.1}$$

where F has continuous derivatives of second order with respect to x, y and y', and $a < b$. Let

$$S = \{y \in C^2[a, b] : y(a) = y_a, y(b) = y_b\}, \tag{A.2}$$

where y_a and y_b are two given real numbers. If $y \in S$ is an extremal for J, then y satisfies the following Euler - Lagrange equation:

$$\frac{\partial F}{\partial y} - \frac{d}{dx}\frac{\partial F}{\partial y'} = 0 \tag{A.3}$$

Remark A.1. *The left side of Equation* (A.3) *is obtained by calculating the derivative of* J *with respect to* y*. It means that:*

$$\frac{\partial J}{\partial y} = \frac{\partial F}{\partial y} - \frac{d}{dx}\frac{\partial F}{\partial y'}. \tag{A.4}$$

A.2 Euler - Lagrange Equation for the Case of Two Variables and One Function

Theorem A.2. [101, 102] *The Euler - Lagrange equation for the functional*

$$J(y) = \int_{\Omega} F(x_1, x_2, y, y_1, y_2)dx \tag{A.5}$$

where $(x_1, x_2) \in \Omega \subset \mathbb{R}^2$*,* $y = y(x_1, x_2), y_1 = \frac{\partial y}{\partial x_1}, y_2 = \frac{\partial y}{\partial x_2}$*,* $dx = dx_1 dx_2$*, is as follows:*

$$\frac{\partial F}{\partial y} - \frac{\partial}{\partial x_1}\frac{\partial F}{\partial y_1} - \frac{\partial}{\partial x_2}\frac{\partial F}{\partial y_2} = 0 \tag{A.6}$$

Remark A.2. *The left side of Equation* (A.6) *is obtained by calculating the derivative of* J *with respect to* y*. It means that:*

$$\frac{\partial J}{\partial y} = \frac{\partial F}{\partial y} - \frac{\partial}{\partial x_1}\frac{\partial F}{\partial y_1} - \frac{\partial}{\partial x_2}\frac{\partial F}{\partial y_2}. \tag{A.7}$$

A.3 Application: Euler - Lagrange Equation of the Chan-Vese Model

Recall the energy function of the Chan-Vese model:

$$\begin{aligned} E_{CV}(c_1, c_2, \phi) = &\int_{\Omega} (I(x) - c_1)^2 H(\phi(x))dx \\ &+ \int_{\Omega} (I(x) - c_2)^2 (1 - H(\phi(x)))dx + \mu \int_{\Omega} |\nabla H(\phi(x))|dx \end{aligned} \tag{A.8}$$

We will find ϕ for fixed c_1 and c_2 by using the Euler - Lagrange equation and the steepest descent method. Note that

1. to use the Euler - Lagrange equation to find ϕ, the Heaviside function H has to been approximated by a smooth version:

$$H_\epsilon(z) = \frac{1}{2}\left[1 + \frac{2}{\pi}\arctan\left(\frac{z}{\epsilon}\right)\right], \quad z \in \mathbb{R} \tag{A.9}$$

where ϵ is small positive

2. $|\nabla H_\epsilon(\phi)| = \delta_\epsilon(\phi)|\nabla\phi| = \delta_\epsilon(\phi)\sqrt{\left(\frac{\partial\phi}{\partial x_1}\right)^2 + \left(\frac{\partial\phi}{\partial x_2}\right)^2}$, where

$$\delta_\epsilon(z) = H'_\epsilon(z) = \frac{1}{2}\frac{\epsilon}{\epsilon^2 + z^2} \tag{A.10}$$

Then, Equation A.8 is rewritten as follows:

$$E_{CV}(c_1, c_2, \phi) = \int_\Omega G(x_1, x_2, \phi, \phi_1, \phi_2)dx \tag{A.11}$$

where $(x_1, x_2) = x$, $\phi_1 = \frac{\partial\phi}{\partial x_1}$, $\phi_2 = \frac{\partial\phi}{\partial x_2}$, and

$$\begin{aligned} G(x_1, x_2, \phi, \phi_1, \phi_2) =& (I(x) - c_1)^2 H_\epsilon(\phi(x)) + (I(x) - c_2)^2(1 - H_\epsilon(\phi(x))) \\ &+ \mu\delta_\epsilon(\phi(x))\sqrt{\phi_1^2 + \phi_2^2} \end{aligned} \tag{A.12}$$

Then, the Euler - Lagrange equation for (A.11) has the following form:

$$\frac{\partial G}{\partial\phi} - \frac{\partial}{\partial x_1}\frac{\partial G}{\partial\phi_1} - \frac{\partial}{\partial x_2}\frac{\partial G}{\partial\phi_2} = 0 \tag{A.13}$$

We calculate each term in the above equation.

For the first term in the left side of Equation (A.13):

$$\frac{\partial G}{\partial\phi} = (I - c_1)^2\delta_\epsilon(\phi) - (I - c_2)^2\delta_\epsilon(\phi) + \mu\delta'_\epsilon(\phi)\sqrt{\phi_1^2 + \phi_2^2} \tag{A.14}$$

In what concern the second term in the left side of Equation (A.13):

$$\begin{aligned} \frac{\partial}{\partial x_1}\frac{\partial G}{\partial\phi_1} &= \frac{\partial}{\partial x_1}\left(\mu\delta_\epsilon(\phi)\frac{\phi_1}{\sqrt{\phi_1^2 + \phi_2^2}}\right) \\ &= \mu\frac{\partial\delta_\epsilon(\phi)}{\partial x_1}\frac{\phi_1}{\sqrt{\phi_1^2 + \phi_2^2}} + \mu\delta_\epsilon(\phi)\frac{\partial}{\partial x_1}\frac{\phi_1}{\sqrt{\phi_1^2 + \phi_2^2}} \\ &= \mu\delta'_\epsilon(\phi)\frac{\partial\phi}{\partial x_1}\frac{\phi_1}{\sqrt{\phi_1^2 + \phi_2^2}} + \mu\delta_\epsilon(\phi)\frac{\phi_{11}\phi_2^2 - \phi_1\phi_2\phi_{12}}{\sqrt{(\phi_1^2 + \phi_2^2)^3}} \\ &= \mu\delta'_\epsilon(\phi)\frac{\phi_1^2}{\sqrt{\phi_1^2 + \phi_2^2}} + \mu\delta_\epsilon(\phi)\frac{\phi_{11}\phi_2^2 - \phi_1\phi_2\phi_{12}}{\sqrt{(\phi_1^2 + \phi_2^2)^3}} \end{aligned} \tag{A.15}$$

where $\phi_{ij} = \frac{\partial^2\phi}{\partial x_i\partial x_j}$, $i, j = 1, 2$.

Analogously for the third term in the left side of Equation (A.13), we have:

$$\frac{\partial}{\partial x_2}\frac{\partial G}{\partial\phi_2} = \mu\delta'_\epsilon(\phi)\frac{\phi_2^2}{\sqrt{\phi_1^2 + \phi_2^2}} + \mu\delta_\epsilon(\phi)\frac{\phi_{22}\phi_1^2 - \phi_1\phi_2\phi_{12}}{\sqrt{(\phi_1^2 + \phi_2^2)^3}} \tag{A.16}$$

So, Equation (A.13) becomes:

$$\begin{aligned}
&(I-c_1)^2\delta_\epsilon(\phi) - (I-c_2)^2\delta_\epsilon(\phi) + \mu\delta'_\epsilon(\phi)\sqrt{\phi_1^2+\phi_2^2} \\
&- \mu\delta'_\epsilon(\phi)\frac{\phi_1^2}{\sqrt{\phi_1^2+\phi_2^2}} - \mu\delta_\epsilon(\phi)\frac{\phi_{11}\phi_2^2 - \phi_1\phi_2\phi_{12}}{\sqrt{(\phi_1^2+\phi_2^2)^3}} \\
&- \mu\delta'_\epsilon(\phi)\frac{\phi_2^2}{\sqrt{\phi_1^2+\phi_2^2}} - \mu\delta_\epsilon(\phi)\frac{\phi_{22}\phi_1^2 - \phi_1\phi_2\phi_{12}}{\sqrt{(\phi_1^2+\phi_2^2)^3}} = 0
\end{aligned} \tag{A.17}$$

Note that

$$\begin{aligned}
\mu\delta'_\epsilon(\phi)\frac{\phi_1^2}{\sqrt{\phi_1^2+\phi_2^2}} + \mu\delta'_\epsilon(\phi)\frac{\phi_2^2}{\sqrt{\phi_1^2+\phi_2^2}} &= \mu\delta'_\epsilon(\phi)\frac{\phi_1^2+\phi_2^2}{\sqrt{\phi_1^2+\phi_2^2}} \\
&= \mu\delta'_\epsilon(\phi)\sqrt{\phi_1^2+\phi_2^2}
\end{aligned} \tag{A.18}$$

and

$$\mu\delta_\epsilon(\phi)\frac{\phi_{11}\phi_2^2 - \phi_1\phi_2\phi_{12}}{\sqrt{(\phi_1^2+\phi_2^2)^3}} + \mu\delta_\epsilon(\phi)\frac{\phi_{22}\phi_1^2 - \phi_1\phi_2\phi_{12}}{\sqrt{(\phi_1^2+\phi_2^2)^3}} = \mu\delta_\epsilon(\phi)\nabla\cdot\left(\frac{\nabla\phi}{|\nabla\phi|}\right) \tag{A.19}$$

where $\nabla\cdot$ is the divergence operator.

Therefore, the Euler - Lagrange equation of the Chan - Vese model is as follows:

$$(I-c_1)^2\delta_\epsilon(\phi) - (I-c_2)^2\delta_\epsilon(\phi) - \mu\delta_\epsilon(\phi)\nabla\cdot\left(\frac{\nabla\phi}{|\nabla\phi|}\right) = 0 \tag{A.20}$$

or

$$\delta_\epsilon(\phi)\left[(I-c_1)^2 - (I-c_2)^2 - \mu\nabla\cdot\left(\frac{\nabla\phi}{|\nabla\phi|}\right)\right] = 0 \tag{A.21}$$

By Remark A.2, we also have:

$$\frac{\partial E_{CV}}{\partial\phi} = \delta_\epsilon(\phi)\left[(I-c_1)^2 - (I-c_2)^2 - \mu\nabla\cdot\left(\frac{\nabla\phi}{|\nabla\phi|}\right)\right] \tag{A.22}$$

Then, by steepest descent method, we have the following evolution equation of ϕ for fixed c_1 and c_2:

$$\begin{aligned}
\frac{\partial\phi}{\partial t} &= -\frac{\partial E_{CV}}{\partial\phi} \\
&= \delta_\epsilon(\phi)\left[\mu\nabla\cdot\left(\frac{\nabla\phi}{|\nabla\phi|}\right) - (I-c_1)^2 + (I-c_2)^2\right]
\end{aligned} \tag{A.23}$$

The above Equation (A.23) is exactly the evolution equation (2.44) of the Chan-Vese model that we presented in Chapter 2.

Remark A.3. *By the same way, we will obtain the others evolution equations presented in this thesis:*

1. *Equation* (2.60) *for the model of Zhu*
2. *Equation* (2.67) *for the LBF model*
3. *Equation* (2.71) *for the LIF model*
4. *Equations* (4.9)-(4.10) *for the convex Chan-Vese model*

APPENDIX B

Appendix: Proof the Formulas in Chapter 3

B.1 Proof of Theorem 3.1

Let us recall Theorem 3.1

Theorem 3.1. *Let c_1 and c_2 be constants, $\phi \in L^2(\Omega)$−the space of functions so that the square of these functions are integrable on Ω. Consider the following functions:*

$$E_\epsilon^G(\phi) = \int_\Omega \big(I(x) - c_1\big)^2 H_\epsilon(\phi(x))dx + \int_\Omega \big(I(x) - c_2\big)^2 (1 - H_\epsilon(\phi(x)))dx \tag{B.1}$$

The derivative of E_ϵ^G with respect to ϕ is as follows:

$$\frac{\partial E_\epsilon^G}{\partial \phi} = \delta_\epsilon(\phi)\Big[\big(I - c_1\big)^2 - \big(I - c_2\big)^2\Big] \tag{B.2}$$

Proof. Let $\phi, \psi \in L^2(\Omega)$, we have:

$$< \frac{\partial E_\epsilon^G}{\partial \phi}, \psi >= \lim_{s\to 0} \frac{E_\epsilon^G(\phi + s\psi) - E_\epsilon^G(\phi)}{s} \tag{B.3}$$

where $s \in \mathbb{R}\backslash\{0\}$ and $< \cdot, \cdot >$ is the scalar product in $L^2(\Omega)$: $< A, B >= \int_\Omega A(x)B(x)dx$ with $A, B \in L^2(\Omega)$.

We have

$$\begin{aligned}
&\frac{E_\epsilon^G(\phi + s\psi) - E_\epsilon^G(\phi)}{s} \\
&= \frac{1}{s}\Bigg[\int_\Omega \big(I(x) - c_1\big)^2 H_\epsilon(\phi(x) + s\psi(x))dx + \int_\Omega \big(I(x) - c_2\big)^2 (1 - H_\epsilon(\phi(x) + s\psi(x)))dx \\
&\qquad - \int_\Omega \big(I(x) - c_1\big)^2 H_\epsilon(\phi(x))dx - \int_\Omega \big(I(x) - c_2\big)^2 (1 - H_\epsilon(\phi(x)))dx\Bigg] \\
&= \int_\Omega \big(I(x) - c_1\big)^2 \frac{H_\epsilon(\phi(x) + s\psi(x)) - H_\epsilon(\phi(x))}{s}dx \\
&\quad - \int_\Omega \big(I(x) - c_2\big)^2 \frac{H_\epsilon(\phi(x) + s\psi(x)) - H_\epsilon(\phi(x))}{s}dx
\end{aligned} \tag{B.4}$$

Note that the derivative of H_ϵ is δ_ϵ (see Equation (2.44)) which leads to:

$$\lim_{s\to 0} \frac{H_\epsilon(\phi(x) + s\psi(x)) - H_\epsilon(\phi(x))}{s} = \delta_\epsilon(\phi(x))\psi(x) \tag{B.5}$$

Therefore, we obtain:

$$\begin{aligned}
< \frac{\partial E_\epsilon^G}{\partial \phi}, \psi > &= \lim_{s\to 0} \frac{E_\epsilon^G(\phi + s\psi) - E_\epsilon^G(\phi)}{s} \\
&= \int_\Omega \big(I(x) - c_1\big)^2 \delta_\epsilon(\phi(x))\psi(x)dx - \int_\Omega \big(I(x) - c_2\big)^2 \delta_\epsilon(\phi(x))\psi(x)dx \\
&= \int_\Omega \Big[\delta_\epsilon(\phi(x))\Big[\big(I(x) - c_1\big)^2 - \big(I(x) - c_2\big)^2\Big]\Big]\psi(x)dx
\end{aligned} \tag{B.6}$$

which states the following equation:

$$\frac{\partial E_\epsilon^G}{\partial \phi} = \delta_\epsilon(\phi)\Big[\big(I - c_1\big)^2 - \big(I - c_2\big)^2\Big] \tag{B.7}$$

□

B.2 Proof of Theorem 3.2

Let us recall Theorem 3.2

Theorem 3.2. *Let f_1 and f_2 be given functions determined on Ω, $\phi \in L^2(\Omega)$−the space of functions so that the square of these functions are integrable on Ω. Consider the*

following functions:

$$E_\epsilon^L(\phi) = \frac{\mu}{2}\int_\Omega \big(I(x) - f_1(x)H_\epsilon(\phi(x)) - f_2(x)(1 - H_\epsilon(\phi(x)))\big)^2 dx \tag{B.8}$$

The derivative of E_ϵ^L with respect to ϕ is as follows:

$$\frac{\partial E_\epsilon^L}{\partial \phi} = -\delta_\epsilon(\phi)\Big[\mu\big(I - f_1H_\epsilon(\phi) - f_2(1 - H_\epsilon(\phi))\big)\big(f_1 - f_2\big)\Big] \tag{B.9}$$

Proof. Let $\phi, \psi \in L^2(\Omega)$, we have:

$$< \frac{\partial E_\epsilon^L}{\partial \phi}, \psi >= \lim_{s\to 0}\frac{E_\epsilon^L(\phi + s\psi) - E_\epsilon^L(\phi)}{s} \tag{B.10}$$

where $s \in \mathbb{R}\backslash\{0\}$ and $< \cdot, \cdot >$ is the scalar product in $L^2(\Omega)$: $< A, B >= \int_\Omega A(x)B(x)dx$ with $A, B \in L^2(\Omega)$.

In the following integrals, we write the type $\int_\Omega A dx$ to replace $\int_\Omega A(x)dx$. We have

$$\begin{aligned}
&\frac{E_\epsilon^L(\phi + s\psi) - E_\epsilon^L(\phi)}{s} \\
&= \frac{\mu}{2s}\Bigg[\int_\Omega \big(I - f_1H_\epsilon(\phi + s\psi) - f_2(1 - H_\epsilon(\phi + s\psi))\big)^2 dx \\
&\qquad - \int_\Omega \big(I - f_1H_\epsilon(\phi) - f_2(1 - H_\epsilon(\phi))\big)^2 dx\Bigg] \\
&= \frac{\mu}{2}\int_\Omega \Bigg[\bigg(-f_1\frac{H_\epsilon(\phi + s\psi) - H_\epsilon(\phi)}{s} + f_2\frac{H_\epsilon(\phi + s\psi) - H_\epsilon(\phi)}{s}\bigg)\cdot\bigg(\\
&\qquad 2I - f_1\big(H_\epsilon(\phi + s\psi) - H_\epsilon(\phi)\big) - f_2\big(2 - H_\epsilon(\phi + s\psi) - H_\epsilon(\phi)\big)\bigg)\Bigg] dx
\end{aligned} \tag{B.11}$$

Note that the derivative of H_ϵ is δ_ϵ (see Equation (2.44)) which leads to:

$$\lim_{s\to 0}\frac{H_\epsilon(\phi + s\psi) - H_\epsilon(\phi)}{s} = \delta_\epsilon(\phi)\psi \tag{B.12}$$

Then, the limitation of two sides in Equation (B.11) when $s \to 0$ allows us to obtain

$$\begin{aligned}
&\lim_{s\to 0}\frac{E_\epsilon^L(\phi + s\psi) - E_\epsilon^L(\phi)}{s} \\
&= \frac{\mu}{2}\int_\Omega \left[\Big(- f_1\delta_\epsilon(\phi)\psi + f_2\delta_\epsilon(\phi)\psi\Big).\Big(2I - 2f_1H_\epsilon(\phi) - 2f_2(1 - H_\epsilon(\phi))\Big)\right]dx \\
&= \int_\Omega \left[- \delta_\epsilon(\phi)\Big[\mu\big(I - f_1H_\epsilon(\phi) - f_2(1 - H_\epsilon(\phi))\big)\big(f_1 - f_2\big)\Big]\right]\psi dx \qquad \text{(B.13)}
\end{aligned}$$

which states to obtain the derivative of E_ϵ^L with respect to ϕ:

$$\frac{\partial E_\epsilon^L}{\partial \phi} = -\delta_\epsilon(\phi)\Big[\mu\big(I - f_1H_\epsilon(\phi) - f_2(1 - H_\epsilon(\phi))\big)\big(f_1 - f_2\big)\Big] \qquad \text{(B.14)}$$

□

B.3 Proof of Equation (3.23)

Equation (3.23) is as follows

$$\frac{\partial \mathcal{L}}{\partial \phi} = -\delta_\epsilon(\phi)\nabla\cdot\left(\frac{\nabla\phi}{|\nabla\phi|}\right)$$

where $\delta_\epsilon(z) = H'_\epsilon(z)$, $z \in \mathbb{R}$, and $\mathcal{L}(\phi) = \int_\Omega |\nabla H_\epsilon(\phi(x))|dx$.

First, we formulate the following proposition:

Proposition B.1. *Let $\Omega \subset \mathbb{R}^2$ be a bounded domain. Let $F : L^2(\Omega) \to L^2(\Omega)$ be a continuous function and N denote the exterior normal to the boundary $\partial\Omega$. Then, we have:*

$$\min_{\phi\in L^2(\Omega)}\int_\Omega F(\phi(x))dx = \min_{\substack{\phi\in L^2(\Omega)\\ \frac{\partial\phi}{\partial N}=0}}\int_\Omega F(\phi(x))dx \qquad \text{(B.15)}$$

Proof. In this proof, to reduce symbols, we replace $F(\phi(x))$ and $\int_\Omega F(\phi(x))dx$ by $F(\phi)$ and $\int_\Omega F(\phi)$, respectively.

Obviously, the set $\{\phi \in L^2(\Omega) : \frac{\partial\phi}{\partial N} = 0\}$ is a subset of the set $\{\phi \in L^2(\Omega)\}$. Thus, we have the following inequality:

$$\min_{\substack{\phi\in L^2(\Omega)\\ \frac{\partial\phi}{\partial N}}}\int_\Omega F(\phi) \geq \min_{\phi\in L^2(\Omega)}\int_\Omega F(\phi) \qquad \text{(B.16)}$$

Now, let ϵ be small positive, we approximate continuously $\phi \in L^2(\Omega)$ by a continuous function $\phi_\epsilon \in L^2(\Omega)$ such that $|\phi - \phi_\epsilon| \leq \epsilon$. Figure B.1 illustrates this approximation: Ω_ϵ

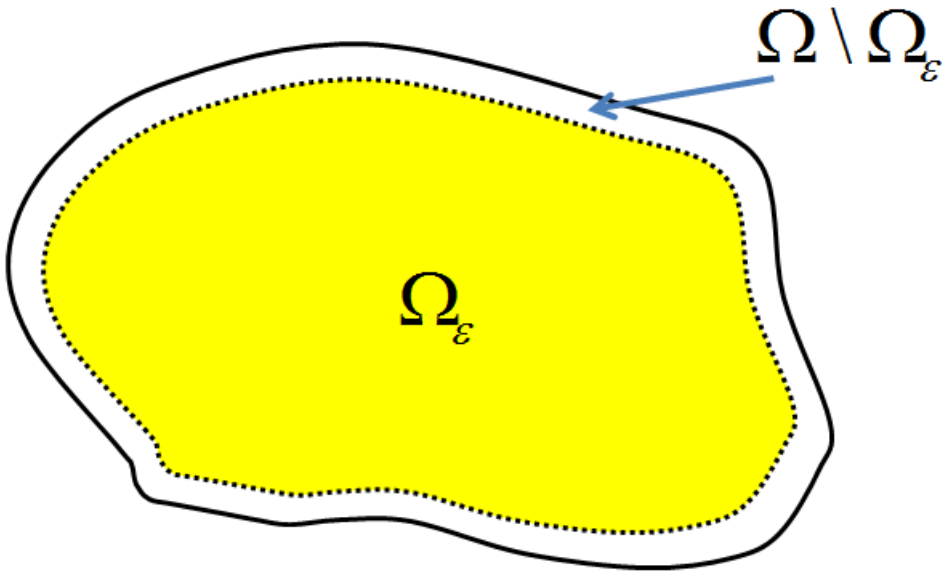

Figure B.1. Illustration for Ω and Ω_ϵ.

is a sub-region of Ω such that $\Omega_\epsilon \to \Omega$ when $\epsilon \to 0$. We chose $\phi_\epsilon = \phi$ on Ω_ϵ. On $\Omega \backslash \Omega_\epsilon$, ϕ_ϵ is chosen such that ϕ_ϵ is continuous on $\Omega = \Omega \cup \Omega_\epsilon$ and $\frac{\partial \phi_\epsilon}{\partial N} = 0$.

Then, because of the continuity of F, therefore $\forall \phi$, there exists a sub-sequence $\phi_{\epsilon_n} \subset \phi_\epsilon$, where $n = 1, 2, 3, ...$ such that:

$$F(\phi) - F(\phi_{\epsilon_n}) \geq -\frac{1}{n}, \quad n = 1, 2, 3, ... \tag{B.17}$$

Inequality (B.17) states the following inequality:

$$\begin{aligned} F(\phi) &= F(\phi_{\epsilon_n}) + F(\phi) - F(\phi_{\epsilon_n}) \\ &\geq F(\phi_{\epsilon_n}) - \frac{1}{n} \end{aligned} \tag{B.18}$$

which implies that

$$\int_\Omega F(\phi) \geq \int_\Omega F(\phi_{\epsilon_n}) - \frac{1}{n}|\Omega| \tag{B.19}$$

where $|\Omega|$ is the area of Ω. Obviously, we have $\int_\Omega F(\phi_{\epsilon_n}) \geq \min\{\int_\Omega F(\phi_{\epsilon_n}) : \phi_{\epsilon_n} \in L^2(\Omega) : \frac{\partial \phi_{\epsilon_n}}{\partial N} = 0\}$. This combines with above inequality, we obtain:

$$\begin{aligned} \int_\Omega F(\phi) &\geq \min_{\substack{\phi_{\epsilon_n} \in L^2(\Omega) \\ \frac{\partial \phi_{\epsilon_n}}{\partial N} = 0}} \int_\Omega F(\phi_{\epsilon_n}) - \frac{1}{n}|\Omega| \\ &= \min_{\substack{\phi \in L^2(\Omega) \\ \frac{\partial \phi}{\partial N} = 0}} \int_\Omega F(\phi) - \frac{1}{n}|\Omega| \end{aligned} \tag{B.20}$$

Inequality (B.20) holds for $\forall \phi \in L^2(\Omega)$. Thus, we have:

$$\min_{\phi \in L^2(\Omega)} \int_\Omega F(\phi) \geq \min_{\substack{\phi \in L^2(\Omega) \\ \frac{\partial \phi}{\partial N} = 0}} \int_\Omega F(\phi) - \frac{1}{n}|\Omega| \tag{B.21}$$

Note that Ω is a bounded domain in $\mathbb{R}^2$. So, we have that $|\Omega| < \infty$ which implies that $\lim_{n \to \infty} \frac{1}{n}|\Omega| = 0$. Now, we limit two side of Inequality (B.21) when $n \to \infty$ to obtain:

$$\min_{\phi \in L^2(\Omega)} \int_\Omega F(\phi) \geq \min_{\substack{\phi \in L^2(\Omega) \\ \frac{\partial \phi}{\partial N} = 0}} \int_\Omega F(\phi) \tag{B.22}$$

From Inequality (B.16) and Inequality (B.22), we obtain:

$$\min_{\phi \in L^2(\Omega)} \int_\Omega F(\phi) = \min_{\substack{\phi \in L^2(\Omega) \\ \frac{\partial \phi}{\partial N} = 0}} \int_\Omega F(\phi) \tag{B.23}$$

□

Now, we describe the evolution equation of $\mathcal{L}(\phi)$ when minimizing with respect to $\phi \in L^2(\Omega)$, where N is the exterior nomal to the boundary $\partial\Omega$. By Proposition B.1, we can consider $\frac{\partial \phi}{\partial N} = 0$

Let $\phi, \psi \in L^2(\Omega) : \frac{\partial \phi}{\partial N} = \frac{\partial \psi}{\partial N} = 0$, we have:

$$< \frac{\partial \mathcal{L}}{\partial \phi}, \psi >= \lim_{s \to 0} \frac{\mathcal{L}(\phi + s\psi) - \mathcal{L}(\phi)}{s} \tag{B.24}$$

where $s \in \mathbb{R} \backslash \{0\}$ and $< \cdot, \cdot >$ is the scalar product in $L^2(\Omega)$: $< A, B >= \int_\Omega A(x)B(x)dx$ with $A, B \in L^2(\Omega)$.

Recall the formula of $\mathcal{L}(\phi)$:

$$\mathcal{L}(\phi) = \int_\Omega |\nabla H_\epsilon(\phi(x))|dx = \int_\Omega \delta_\epsilon(\phi(x))|\nabla \phi(x)|dx \tag{B.25}$$

where $\delta_\epsilon(z) = H'_\epsilon(z)$, $z \in \mathbb{R}$. Then, we develop:

$$\begin{aligned} \frac{\mathcal{L}(\phi + s\psi) - \mathcal{L}(\phi)}{s} &= \int_\Omega \frac{\delta_\epsilon(\phi + s\psi)|\nabla(\phi + s\psi)| - \delta_\epsilon(\phi)|\nabla\phi|}{s} \\ &= \int_\Omega \frac{\delta_\epsilon(\phi + s\psi)|\nabla(\phi + s\psi)| - \delta_\epsilon(\phi + s\psi)|\nabla\phi|}{s} \\ &\quad + \int_\Omega \frac{\delta_\epsilon(\phi + s\psi)|\nabla\phi| - \delta_\epsilon(\phi)|\nabla\phi|}{s} \end{aligned} \tag{B.26}$$

Consider

$$\mathcal{L}_1 = \int_\Omega \frac{\delta_\epsilon(\phi + s\psi)|\nabla(\phi + s\psi)| - \delta_\epsilon(\phi + s\psi)|\nabla\phi|}{s}, \tag{B.27}$$

$$\mathcal{L}_2 = \int_\Omega \frac{\delta_\epsilon(\phi + s\psi)|\nabla\phi| - \delta_\epsilon(\phi)|\nabla\phi|}{s} \tag{B.28}$$

We have:

$$\begin{aligned}
\mathcal{L}_1 &= \int_\Omega \frac{\delta_\epsilon(\phi + s\psi)}{s}\big(|\nabla(\phi + s\psi)| - |\nabla\phi|\big) \\
&= \int_\Omega \frac{\delta_\epsilon(\phi + s\psi)}{s}\frac{\big(\nabla\phi + s\nabla\psi\big)^2 - \big(\nabla\phi\big)^2}{|\nabla(\phi + s\psi)| + |\nabla\phi|} \\
&= \int_\Omega \frac{\delta_\epsilon(\phi + s\psi)}{|\nabla(\phi + s\psi)| + |\nabla\phi|}\frac{2s\nabla\phi\nabla\psi + s^2\big(\nabla\psi\big)^2}{s} \\
&= \int_\Omega \frac{\delta_\epsilon(\phi + s\psi)}{|\nabla(\phi + s\psi)| + |\nabla\phi|}\big(2\nabla\phi\nabla\psi + s\big(\nabla\psi\big)^2\big)
\end{aligned} \tag{B.29}$$

which follows that:

$$\begin{aligned}
\lim_{s\to 0}\mathcal{L}_1 &= \int_\Omega \frac{\delta_\epsilon(\phi)}{2|\nabla\phi|}2\nabla\phi\nabla\psi \\
&= \int_\Omega \delta_\epsilon(\phi)\frac{\nabla\phi}{|\nabla\phi|}\nabla\psi
\end{aligned} \tag{B.30}$$

Using the Green formula, we obtain:

$$\int_\Omega \delta_\epsilon(\phi)\frac{\nabla\phi}{|\nabla\phi|}\nabla\psi = \int_{\partial\Omega} \delta_\epsilon(\phi)\frac{\nabla\phi}{|\nabla\phi|}\nabla\psi\cdot N - \int_\Omega \nabla\cdot\left(\delta_\epsilon(\phi)\frac{\nabla\phi}{|\nabla\phi|}\right)\psi \tag{B.31}$$

Note that $\nabla\psi\cdot N = \frac{\partial\psi}{\partial N} = 0$ which implies

$$\int_{\partial\Omega} \delta_\epsilon(\phi)\frac{\nabla\phi}{|\nabla\phi|}\nabla\psi\cdot N = \int_{\partial\Omega} \delta_\epsilon(\phi)\frac{\nabla\phi}{|\nabla\phi|}\frac{\partial\psi}{\partial N} = 0 \tag{B.32}$$

So, we have:

$$\begin{aligned}
\lim_{s\to 0}\mathcal{L}_1 &= -\int_\Omega \nabla\cdot\left(\delta_\epsilon(\phi)\frac{\nabla\phi}{|\nabla\phi|}\right)\psi \\
&= -\int_\Omega \nabla(\delta_\epsilon(\phi))\frac{\nabla\phi}{|\nabla\phi|}\psi - \int_\Omega \delta_\epsilon(\phi)\nabla\cdot\left(\frac{\nabla\phi}{|\nabla\phi|}\right)\psi \\
&= -\int_\Omega \delta'_\epsilon(\phi)\nabla\phi\frac{\nabla\phi}{|\nabla\phi|}\psi - \int_\Omega \delta_\epsilon(\phi)\nabla\cdot\left(\frac{\nabla\phi}{|\nabla\phi|}\right)\psi \\
&= -\int_\Omega \delta'_\epsilon(\phi)|\nabla\phi|\psi - \int_\Omega \delta_\epsilon(\phi)\nabla\cdot\left(\frac{\nabla\phi}{|\nabla\phi|}\right)\psi
\end{aligned} \tag{B.33}$$

On the other hand,

$$\mathcal{L}_2 = \int_\Omega \frac{\delta_\epsilon(\phi+s\psi)-\delta_\epsilon(\phi)}{s}|\nabla\phi| \tag{B.34}$$

which follows that:

$$\lim_{s\to 0}\mathcal{L}_2 = \int_\Omega \delta'_\epsilon(\phi)\psi|\nabla\phi| \tag{B.35}$$

Replace Equations (B.33) and (B.35) in Equation (B.24) we have

$$\begin{aligned}
<\frac{\partial\mathcal{L}}{\partial\phi},\psi> &= \lim_{s\to 0}\frac{\mathcal{L}(\phi+s\psi)-\mathcal{L}(\phi)}{s} \\
&= \lim_{s\to 0}\mathcal{L}_1 + \lim_{s\to 0}\mathcal{L}_2 \\
&= -\int_\Omega \delta'_\epsilon(\phi)|\nabla\phi|\psi - \int_\Omega \delta_\epsilon(\phi)\nabla\cdot\left(\frac{\nabla\phi}{|\nabla\phi|}\right)\psi + \int_\Omega \delta'_\epsilon(\phi)\psi|\nabla\phi| \\
&= -\int_\Omega \delta_\epsilon(\phi)\nabla\cdot\left(\frac{\nabla\phi}{|\nabla\phi|}\right)\psi
\end{aligned} \tag{B.36}$$

which states that

$$\frac{\partial\mathcal{L}}{\partial\phi} = -\delta_\epsilon(\phi)\nabla\cdot\left(\frac{\nabla\phi}{|\nabla\phi|}\right) \tag{B.37}$$

APPENDIX C

Appendix: Proof the Formulas in Chapter 4

C.1 Proof of Formula (4.26)

Let us recall Formula (4.26) as follows:

$$\Delta F = \frac{s_1 \Delta u_m}{s_1 + \Delta u_m}\big(I_0 - c_1\big)^2 + \frac{s_2 \Delta v_m}{s_2 + \Delta v_m}\big(I_0 - c_2\big)^2$$

First, we have two global intensity values c_1 and c_2 as follows:

$$c_1 = \frac{\int_\Omega [u(x)]^m I(x) dx}{\int_\Omega [u(x)]^m dx} = \frac{\sum_{x\in\Omega} [u(x)]^m I(x)}{\sum_{x\in\Omega} [u(x)]^m} \tag{C.1}$$

$$c_2 = \frac{\int_\Omega [1-u(x)]^m I(x) dx}{\int_\Omega [1-u(x)]^m dx} = \frac{\sum_{x\in\Omega} [1-u(x)]^m I(x)}{\sum_{x\in\Omega} [1-u(x)]^m} \tag{C.2}$$

Now, consider a given point $x_0 \in \Omega$, the intensity value of point x_0 is I_0, and the corresponding degree of membership for this point is u_{x_0}. Suppose that we change the degree of membership of point x_0 to the new value u_{nx_0}. Consequently, the values of c_1 and c_2 will be changed to the new ones $\widetilde{c_1}$ and $\widetilde{c_2}$ respectively.

The new value $\widetilde{c_1}$ is expressed as follows:

$$\begin{aligned}\widetilde{c_1} &= \frac{\sum_{x\in\Omega} I_0(x)[\widetilde{u}(x)]^m}{\sum_{x\in\Omega}[\widetilde{u}(x)]^m} \\ &= \frac{\sum_{x\in\Omega} I_0(x)[u(x)]^m + I_0(u^m_{nx_0} - u^m_{x_0})}{\sum_{x\in\Omega}[u(x)]^m + (u^m_{nx_0} - u^m_{x_0})} \\ &= \frac{\sum_{x\in\Omega} I_0(x)[u(x)]^m + I_0\Delta u_m}{s_1 + \Delta u_m}\end{aligned} \tag{C.3}$$

where $s_1 = \sum_{x\in\Omega}[u(x)]^m$ and $\Delta u_m = u^m_{nx_0} - u^m_{x_0}$. From (C.1), we have $\sum_{x\in\Omega} I_0(x)[u(x)]^m = c_1 s_1$, so

$$\begin{aligned}\widetilde{c_1} &= \frac{c_1 s_1 + I_0\Delta u_m}{s_1 + \Delta u_m} \\ &= \frac{c_1(s_1 + \Delta u_m) + (-c_1 + I_0)\Delta u_m}{s_1 + \Delta u_m} \\ &= c_1 + \frac{-c_1 + I_0}{s_1 + \Delta u_m}\Delta u_m\end{aligned} \tag{C.4}$$

In the similar calculation, we can get the new value $\widetilde{c_2}$ as follows:

$$\widetilde{c_2} = c_2 + \frac{-c_2 + I_0}{s_2 + \Delta v_m}\Delta v_m \tag{C.5}$$

where $s_2 = \sum_{x\in\Omega}[1 - u(x)]^m$, and $\Delta v_m = (1 - u_{nx_0})^m - (1 - u_{x_0})^m$.

We will calculate the energy value $\widetilde{F}$ for the case $\mu = 0$:

$$\begin{aligned}\widetilde{F} &= \int_\Omega [\widetilde{u}(x)]^m \big(I(x) - \widetilde{c_1}\big)^2 dx + \int_\Omega [1 - \widetilde{u}(x)]^m \big(I(x) - \widetilde{c_2}\big)^2 dx \\ &= \underbrace{\sum_{x\in\Omega}[\widetilde{u}(x)]^m \big(I(x) - \widetilde{c_1}\big)^2}_{\widetilde{F_1}} + \underbrace{\sum_{x\in\Omega}[1 - \widetilde{u}(x)]^m \big(I(x) - \widetilde{c_2}\big)^2}_{\widetilde{F_2}}\end{aligned} \tag{C.6}$$

We will separately examine $\widetilde{F_1}$ and $\widetilde{F_2}$ to formulate the result.

So,

$$\begin{aligned}\widetilde{F_1} &= \sum_{x\in\Omega}[\widetilde{u}(x)]^m \big(I(x) - \widetilde{c_1}\big)^2 \\ &= \sum_{x\in\Omega}[u(x)]^m \big(I(x) - \widetilde{c_1}\big)^2 + \big([u_{nx_0}]^m - [u_{x_0}]^m\big)\big(I(x_0) - \widetilde{c_1}\big)^2 \\ &= \underbrace{\sum_{x\in\Omega}[u(x)]^m \big(I(x) - \widetilde{c_1}\big)^2}_{\widetilde{F_{11}}} + \underbrace{\Delta u_m \big(I_0 - \widetilde{c_1}\big)^2}_{\widetilde{F_{12}}}\end{aligned} \tag{C.7}$$

We have

$$\begin{aligned}\widetilde{F_{11}} &= \sum_{x\in\Omega}[u(x)]^m\big(I(x)-\widetilde{c_1}\big)^2\\ &= \sum_{x\in\Omega}[u(x)]^m\big(I(x)-c_1-\frac{-c_1+I_0}{s_1+\Delta u_m}\Delta u_m\big)^2\\ &= \sum_{x\in\Omega}[u(x)]^m(I(x)-c_1)^2-2\frac{-c_1+I_0}{s_1+\Delta u_m}\Delta u_m\sum_{x\in\Omega}[u(x)]^m(I(x)-c_1)\\ &\quad+\big(\frac{-c_1+I_0}{s_1+\Delta u_m}\Delta u_m\big)^2\underbrace{\sum_{x\in\Omega}[u(x)]^m}_{s_1}\end{aligned}\tag{C.8}$$

We note that $\sum_{x\in\Omega}[u(x)]^m(I(x)-c_1)=0$ according to (C.1). Therefore,

$$\widetilde{F_{11}}=\sum_{x\in\Omega}[u(x)]^m(I(x)-c_1)^2+\big(\frac{-c_1+I_0}{s_1+\Delta u_m}\Delta u_m\big)^2 s_1\tag{C.9}$$

Besides

$$\begin{aligned}\widetilde{F_{12}} &= \Delta u_m\big(I_0-\widetilde{c_1}\big)^2\\ &= \Delta u_m\big(I_0-c_1-\frac{-c_1+I_0}{s_1+\Delta u_m}\big)^2\\ &= \Delta u_m\big((I_0-c_1)\frac{s_1}{s_1+\Delta u_m}\big)^2\end{aligned}\tag{C.10}$$

So

$$\begin{aligned}\widetilde{F_1} &= \widetilde{F_{G1}}+\widetilde{F_{12}}\\ &= \sum_{x\in\Omega}[u(x)]^m(I(x)-c_1)^2\\ &\quad+\big(\frac{-c_1+I_0}{s_1+\Delta u_m}\Delta u_m\big)^2 s_1+\Delta u_m\big((I_0-c_1)\frac{s_1}{s_1+\Delta u_m}\big)^2\\ &= F_1+\big(\frac{I_0-c_1}{s_1+\Delta u_m}\big)^2 s_1\Delta u_m\big(\Delta u_m+s_1\big)\\ &= F_G+\frac{s_1\Delta u_m}{s_1+\Delta u_m}(I_0-c_1)^2\end{aligned}\tag{C.11}$$

In a similar way for $\widetilde{F_2}$, we obtain:

$$\widetilde{F_2}=F_2+\frac{s_2\Delta v_m}{s_2+\Delta v_m}(I_0-c_2)^2\tag{C.12}$$

where $\Delta v_m=[1-u_{nx_0}]^m-[1-u_{x_0}]^m$, $s_2=\sum_{x\in\Omega}[1-u(x)]^m$.

Combining (C.11) and (C.12), the new energy value $\widetilde{F}$ is given by:

$$\widetilde{F} = F + \frac{s_1 \Delta u_m}{s_1 + \Delta u_m}(I_0 - c_1)^2 + \frac{s_2 \Delta v_m}{s_2 + \Delta v_m}(I_0 - c_2)^2 \tag{C.13}$$

which implies that

$$\Delta F = \widetilde{F} - F = \frac{s_1 \Delta u_m}{s_1 + \Delta u_m}(I_0 - c_1)^2 + \frac{s_2 \Delta v_m}{s_2 + \Delta v_m}(I_0 - c_2)^2 \tag{C.14}$$

Now, if $\mu \neq 0$, we complete the change of the contour length $\mu \Delta l$ into (C.14) and we obtain:

$$\Delta F = \mu \Delta l + \frac{s_1 \Delta u_m}{s_1 + \Delta u_m}(I_0 - c_1)^2 + \frac{s_2 \Delta v_m}{s_2 + \Delta v_m}(I_0 - c_2)^2 \tag{C.15}$$

Formula (C.15) is exactly Formula (4.26). Therefore, we have the necessary proof. □

C.2 Proof of Formula (4.92)

Let us recall Formula (4.92) as follows:

$$\begin{aligned} \Delta F_G = &- \log \frac{1}{\sqrt{2\pi}\epsilon_1} \Delta u_m + \frac{s_1 \Delta u_m}{s_1 + \Delta u_m} \frac{(I_0 - c_1)^2}{2\epsilon_1^2} \\ &- \log \frac{1}{\sqrt{2\pi}\epsilon_2} \Delta v_m + \frac{s_2 \Delta v_m}{s_2 + \Delta v_m} \frac{(I_0 - c_2)^2}{2\epsilon_2^2} \end{aligned} \tag{C.16}$$

First, we have two global intensity values c_1 and c_2 as follows:

$$c_1 = \frac{\int_\Omega I(x)[u(x)]^m dx}{\int_\Omega [u(x)]^m dx} = \frac{\sum_{x \in \Omega} I(x)[u(x)]^m}{\sum_{x \in \Omega}[u(x)]^m} \tag{C.17}$$

$$c_2 = \frac{\int_\Omega I(x)[1 - u(x)]^m dx}{\int_\Omega [1 - u(x)]^m dx} = \frac{\sum_{x \in \Omega} I(x)[1 - u(x)]^m}{\sum_{x \in \Omega}[1 - u(x)]^m} \tag{C.18}$$

Now, consider a given point $x_0 \in \Omega$, the intensity value of point x_0 is I_0, and the corresponding degree of membership for this point is u_{x_0}. Suppose that we change the degree of membership of point x_0 to the new value u_{nx_0}. Consequently, the values of c_1 and c_2 will be changed to the new ones $\widetilde{c_1}$ and $\widetilde{c_2}$ respectively. We assume that the values of ϵ_1 and ϵ_2 are changed but remain small.

The new value $\widetilde{c_1}$ is expressed as follows:

$$\begin{aligned} \widetilde{c_1} &= \frac{\sum_{x \in \Omega} I(x)[\widetilde{u}(x)]^m}{\sum_{x \in \Omega}[\widetilde{u}(x)]^m} \\ &= \frac{\sum_{x \in \Omega} I(x)[u(x)]^m + I_0(u_{nx_0}^m - u_{x_0}^m)}{\sum_{x \in \Omega}[u(x)]^m + (u_{nx_0}^m - u_{x_0}^m)} \\ &= \frac{\sum_{x \in \Omega} I(x)[u(x)]^m + I_0 \Delta u_m}{s_1 + \Delta u_m} \end{aligned} \tag{C.19}$$

where $s_1 = \sum_{x\in\Omega}[u(x)]^m$ and $\Delta u_m = u^m_{nx_0} - u^m_{x_0}$. From (C.17), we have $\sum_{x\in\Omega} I(x)[u(x)]^m = c_1 s_1$, so

$$\begin{aligned}\widetilde{c_1} &= \frac{c_1 s_1 + I_0 \Delta u_m}{s_1 + \Delta u_m} \\ &= c_1 + \frac{-c_1 + I_0}{s_1 + \Delta u_m}\Delta u_m \end{aligned} \tag{C.20}$$

In the similar calculation, we can get the new value $\widetilde{c_2}$ as follows:

$$\widetilde{c_2} = c_2 + \frac{-c_2 + I_0}{s_2 + \Delta v_m}\Delta v_m \tag{C.21}$$

where $s_2 = \sum_{x\in\Omega}[1 - u(x)]^m$, and $\Delta v_m = (1 - u_{nx_0})^m - (1 - u_{x_0})^m$.

Now, we note that, with $i = 1, 2$:

$$\begin{aligned}\log p(I(x), \epsilon_i) &= \log\left(\frac{1}{\sqrt{2\pi}\epsilon_i}\exp\left(-\frac{(c_i - I(x))^2}{2\epsilon_i^2}\right)\right) \\ &= \log\frac{1}{\sqrt{2\pi}\epsilon_i} - \frac{(c_i - I(x))^2}{2\epsilon_i^2}\end{aligned} \tag{C.22}$$

Then, we can rewrite the formulation of F_G as follows:

$$F_G = F_{G1} + F_{G2} \tag{C.23}$$

where

$$F_{G1} = \int_\Omega \left(-\log\frac{1}{\sqrt{2\pi}\epsilon_1} + \frac{(c_1 - I(x))^2}{2\epsilon_1^2}\right)[u(x)]^m dx \tag{C.24}$$

$$F_{G2} = \int_\Omega \left(-\log\frac{1}{\sqrt{2\pi}\epsilon_2} + \frac{(c_2 - I(x))^2}{2\epsilon_2^2}\right)[1 - u(x)]^m dx \tag{C.25}$$

The new value $\widetilde{F_{G1}}$ can be calculated as follows:

$$\begin{aligned}
\widetilde{F_{G1}} &= \int_{\Omega} \Big(-\log \frac{1}{\sqrt{2\pi}\epsilon_1} + \frac{(\widetilde{c}_1 - I(x))^2}{2\epsilon_1^2} \Big) [\widetilde{u}(x)]^m dx \\
&= \sum_{x\in\Omega} \big(-\log \frac{1}{\sqrt{2\pi}\epsilon_1} \big) [\widetilde{u}(x)]^m + \sum_{x\in\Omega} \big(\frac{(\widetilde{c}_1 - I(x))^2}{2\epsilon_1^2} \big) [\widetilde{u}(x)]^m \\
&= \sum_{x\in\Omega} \big(-\log \frac{1}{\sqrt{2\pi}\epsilon_1} \big) [u(x)]^m - \log \frac{1}{\sqrt{2\pi}\epsilon_1} \Delta u_m \\
&\quad + \frac{1}{2\epsilon_1^2} \sum_{x\in\Omega} (c_1 + \frac{-c_1 + I_0}{s_1 + \Delta u_m} \Delta u_m - I(x))^2 [\widetilde{u}(x)]^m \\
&= \sum_{x\in\Omega} \big(-\log \frac{1}{\sqrt{2\pi}\epsilon_1} \big) [u(x)]^m - \log \frac{1}{\sqrt{2\pi}\epsilon_1} \Delta u_m \\
&\quad + \frac{1}{2\epsilon_1^2} \underbrace{\sum_{x\in\Omega} (c_1 + \frac{-c_1 + I_0}{s_1 + \Delta u_m} \Delta u_m - I(x))^2 [u(x)]^m}_{\widetilde{F_{G12}}} \\
&\quad + \frac{1}{2\epsilon_1^2} \underbrace{(c_1 + \frac{-c_1 + I_0}{s_1 + \Delta u_m} \Delta u_m - I_0)^2 \Delta u_m}_{\widetilde{F_{G13}}}
\end{aligned} \tag{C.26}$$

We have

$$\begin{aligned}
\widetilde{F_{G12}} &= \sum_{x\in\Omega} (c_1 + \frac{-c_1 + I_0}{s_1 + \Delta u_m} \Delta u_m - I(x))^2 [u(x)]^m \\
&= \sum_{x\in\Omega} (c_1 - I(x))^2 [u(x)]^m + \sum_{x\in\Omega} \left(\frac{-c_1 + I_0}{s_1 + \Delta u_m} \Delta u_m \right)^2 [u(x)]^m \\
&\quad + \sum_{x\in\Omega} 2 \frac{-c_1 + I_0}{s_1 + \Delta u_m} \Delta u_m (c_1 - I(x)) [u(x)]^m \\
&= \sum_{x\in\Omega} (c_1 - I(x))^2 [u(x)]^m + \sum_{x\in\Omega} \left(\frac{-c_1 + I_0}{s_1 + \Delta u_m} \Delta u_m \right)^2 [u(x)]^m \\
&\quad + 2 \frac{-c_1 + I_0}{s_1 + \Delta u_m} \Delta u_m \sum_{x\in\Omega} (c_1 - I(x)) [u(x)]^m
\end{aligned} \tag{C.27}$$

We note that $\sum_{x\in\Omega} (c_1 - I(x))[u(x)]^m = 0$ according to Formula (C.17) in this file.

Therefore,

$$\begin{aligned}\widetilde{F_{G12}} =& \sum_{x\in\Omega}(c_1 - I(x))^2[u(x)]^m + \sum_{x\in\Omega}\left(\frac{-c_1+I_0}{s_1+\Delta u_m}\Delta u_m\right)^2[u(x)]^m \\ =& \sum_{x\in\Omega}(c_1 - I(x))^2[u(x)]^m + \left(\frac{-c_1+I_0}{s_1+\Delta u_m}\Delta u_m\right)^2\sum_{x\in\Omega}[u(x)]^m \\ =& \sum_{x\in\Omega}(c_1 - I(x))^2[u(x)]^m + \left(\frac{-c_1+I_0}{s_1+\Delta u_m}\Delta u_m\right)^2 s_1 \end{aligned} \tag{C.28}$$

Besides,

$$\begin{aligned}\widetilde{F_{G13}} =& \big(c_1 + \frac{-c_1+I_0}{s_1+\Delta u_m}\Delta u_m - I_0\big)^2\Delta u_m \\ =& \big(\frac{s_1}{s_1+\Delta u_m}(c_1 - I_0)\big)^2\Delta u_m \end{aligned} \tag{C.29}$$

So

$$\begin{aligned}\widetilde{F_{G1}} =& \sum_{x\in\Omega}\big(-\log\frac{1}{\sqrt{2\pi}\epsilon_1}\big)[u(x)]^m - \log\frac{1}{\sqrt{2\pi}\epsilon_1}\Delta u_m \\ &+ \widetilde{F_{G2}} + \widetilde{F_{G3}} \\ =& \sum_{x\in\Omega}\big(-\log\frac{1}{\sqrt{2\pi}\epsilon_1}\big)[u(x)]^m - \log\frac{1}{\sqrt{2\pi}\epsilon_1}\Delta u_m \\ &+ \sum_{x\in\Omega}(c_1 - I(x))^2[u(x)]^m + \left(\frac{-c_1+I_0}{s_1+\Delta u_m}\Delta u_m\right)^2 s_1 \\ &+ \big(\frac{s_1}{s_1+\Delta u_m}(c_1 - I_0)\big)^2\Delta u_m \\ =& \sum_{x\in\Omega}\big(-\log\frac{1}{\sqrt{2\pi}\epsilon_1}\big)[u(x)]^m + \sum_{x\in\Omega}(c_1 - I(x))^2[u(x)]^m \\ &- \log\frac{1}{\sqrt{2\pi}\epsilon_1}\Delta u_m \\ &+ \left(\frac{-c_1+I_0}{s_1+\Delta u_m}\Delta u_m\right)^2 s_1 + \big(\frac{s_1}{s_1+\Delta u_m}(c_1 - I_0)\big)^2\Delta u_m \\ =& \sum_{x\in\Omega}\big(-\log\frac{1}{\sqrt{2\pi}\epsilon_1}\big)[u(x)]^m + \sum_{x\in\Omega}(c_1 - I(x))^2[u(x)]^m \\ &- \log\frac{1}{\sqrt{2\pi}\epsilon_1}\Delta u_m + \frac{s_1\Delta u_m}{s_1+\Delta u_m}\frac{(I_0-c_1)^2}{2\epsilon_1^2} \\ =& F_{G1} - \log\frac{1}{\sqrt{2\pi}\epsilon_1}\Delta u_m + \frac{s_1\Delta u_m}{s_1+\Delta u_m}\frac{(I_0-c_1)^2}{2\epsilon_1^2} \end{aligned} \tag{C.30}$$

By the similar calculation, we have:

$$\widetilde{F_{G2}} = F_{G2} - \log \frac{1}{\sqrt{2\pi}\epsilon_2}\Delta v_m + \frac{s_2 \Delta v_m}{s_2 + \Delta v_m}\frac{(I_0 - c_2)^2}{2\epsilon_2^2} \tag{C.31}$$

So

$$\begin{aligned}
\widetilde{F_G} =& \widetilde{F_{G1}} + \widetilde{F_{G2}} \\
=& F_{G1} + F_{G2} - \log \frac{1}{\sqrt{2\pi}\epsilon_1}\Delta u_m + \frac{s_1 \Delta u_m}{s_1 + \Delta u_m}\frac{(I_0 - c_1)^2}{2\epsilon_1^2} \\
& - \log \frac{1}{\sqrt{2\pi}\epsilon_2}\Delta v_m + \frac{s_2 \Delta v_m}{s_2 + \Delta v_m}\frac{(I_0 - c_2)^2}{2\epsilon_2^2} \\
=& F_G - \log \frac{1}{\sqrt{2\pi}\epsilon_1}\Delta u_m + \frac{s_1 \Delta u_m}{s_1 + \Delta u_m}\frac{(I_0 - c_1)^2}{2\epsilon_1^2} \\
& - \log \frac{1}{\sqrt{2\pi}\epsilon_2}\Delta v_m + \frac{s_2 \Delta v_m}{s_2 + \Delta v_m}\frac{(I_0 - c_2)^2}{2\epsilon_2^2}
\end{aligned} \tag{C.32}$$

From (C.32), we have the necessary proof. □

C.3 Proof of Formula (4.93)

Let us recall Formula (4.93) as follows:

$$\begin{aligned}
\Delta F_L =& - K_\sigma * \left(\log \frac{1}{\sqrt{2\pi}\sigma_1}\right)(y_0)\Delta u_m - K_\sigma * \left(\log \frac{1}{\sqrt{2\pi}\sigma_2}\right)(y_0)\Delta v_m \\
& + \sum_{x\in\Omega} \frac{s_3(x) K_\sigma(x - y_0)\Delta u_m}{s_3(x) + K_\sigma(x - y_0)\Delta u_m}\frac{(I(y_0) - f_1(x))^2}{2\sigma_1^2(x)} \\
& + \sum_{x\in\Omega} \frac{s_4(x) K_\sigma(x - y_0)\Delta v_m}{s_4(x) + K_\sigma(x - y_0)\Delta v_m}\frac{(I(y_0) - f_2(x))^2}{2\sigma_2^2(x)}
\end{aligned}$$

First, we have two local intensity functions that approximate the intensity means of the local regions around the point x as follows:

$$\begin{aligned}
f_1(x) &= \frac{\int_\Omega K_\sigma(x - y) I(y)[u(y)]^m dy}{\int_\Omega K_\sigma(x - y)[u(y)]^m dy} \\
&= \frac{\sum_{y\in\Omega} K_\sigma(x - y) I(y)[u(y)]^m}{\sum_{y\in\Omega} K_\sigma(x - y)[u(y)]^m} = \frac{[K_\sigma * (Iu^m)](x)}{[K_\sigma * u^m](x)}
\end{aligned} \tag{C.33}$$

$$\begin{aligned}
f_2(x) &= \frac{\int_\Omega K_\sigma(x - y) I(y)(1 - [u(y)])^m dy}{\int_\Omega K_\sigma(x - y)(1 - [u(y)])^m dy} \\
&= \frac{\sum_{y\in\Omega} K_\sigma(x - y) I(y)[1 - u(y)]^m}{\sum_{y\in\Omega} K_\sigma(x - y)[1 - u(y)]^m} = \frac{[K_\sigma * (I(1 - u)^m)](x)}{[K_\sigma * (1 - u)^m](x)}
\end{aligned} \tag{C.34}$$

Consider a given point $y_0 \in \Omega$. The intensity value of point y_0 is I_0, and the corresponding degree of membership for this point is u_{y_0}. Suppose that we change the degree of membership of point y_0 to the new value u_{ny_0}. Therefore, the values of $f_1(x)$ and $f_2(x)$ will be changed to the new ones $\widetilde{f}_1(x)$ and $\widetilde{f}_2(x)$ respectively. We assume the values of σ_1 and σ_2 are changed but remain small.

The value of $\widetilde{f}_1(x)$ is expressed as follows:

$$\begin{aligned}\widetilde{f}_1(x) &= \frac{\sum_{y\in\Omega} K_\sigma(x-y)I(y)[\widetilde{u}(y)]^m}{\sum_{y\in\Omega} K_\sigma(x-y)[\widetilde{u}(y)]^m} \\ &= \frac{\sum_{y\in\Omega} K_\sigma(x-y)I(y)[u(y)]^m + K_\sigma(x-y_0)(u_{ny_0}^m I_0 - u_{y_0}^m I_0)}{\sum_{y\in\Omega} K_\sigma(x-y)[u(y)]^m + K_\sigma(x-y_0)(u_{ny_0}^m - u_{y_0}^m)} \\ &= \frac{[K_\sigma * (Iu^m)](x) + K_\sigma(x-y_0)\Delta u_m I_0}{[K_\sigma * u^m](x) + K_\sigma(x-y_0)\Delta u_m}\end{aligned} \tag{C.35}$$

where $\Delta u_m = u_{ny_0}^m - u_{y_0}^m$.

From (C.33), and let $s_3(x) = [K_\sigma * u^m](x)$, we have:

$$[K_\sigma * (Iu^m)](x) = [K_\sigma * u^m](x) f_1(x) = s_3(x) f_1(x) \tag{C.36}$$

Inserting (C.36) into (C.35), we obtain:

$$\begin{aligned}\widetilde{f}_1(x) &= \frac{s_3(x)f(x) + K_\sigma(x-y_0)\Delta u_m I_0}{s_3(x) + K_\sigma(x-y_0)\Delta u_m} \\ &= f_1(x) + \frac{K_\sigma(x-y_0)\Delta u_m}{s_3(x) + K_\sigma(x-y_0)\Delta u_m}(I_0 - f_1(x))\end{aligned} \tag{C.37}$$

A similar calculation gives the new value $\widetilde{f}_2(x)$ as follows:

$$\widetilde{f}_2(x) = f_2(x) + \frac{K_\sigma(x-y_0)\Delta v_m}{s_4(x) + K_\sigma(x-y_0)\Delta v_m}(I_0 - f_2(x)) \tag{C.38}$$

where $s_4(x) = [K_\sigma * (1-u)^m](x)$, and $\Delta v_m = (1-u_{ny_0})^m - (1-u_{y_0})^m$.

Now, we note that, with $i = 1, 2$:

$$\begin{aligned}\log p_x(I(y), \sigma_i) &= \log\left(\frac{1}{\sqrt{2\pi}\sigma_i(x)} \exp\left(-\frac{(f_i(x) - I(y))^2}{2\sigma_i^2(x)}\right)\right) \\ &= \log\frac{1}{\sqrt{2\pi}\sigma_i(x)} - \frac{(f_i(x) - I(y))^2}{2\sigma_i^2(x)}\end{aligned} \tag{C.39}$$

Then, we can rewrite the formulation of F_L as follows:

$$F_L = F_{L1} + F_{L2} \tag{C.40}$$

where

$$F_{L1} = \int_{\Omega}\int_{\Omega} K_\sigma(x-y)\left[-\log\frac{1}{\sqrt{2\pi}\sigma_1(x)} + \frac{(f_1(x)-I(y))^2}{2\sigma_1^2(x)}\right][u(y)]^m dydx \tag{C.41}$$

$$F_{L2} = \int_{\Omega}\int_{\Omega} K_\sigma(x-y)\left[-\log\frac{1}{\sqrt{2\pi}\sigma_2(x)} + \frac{(f_2(x)-I(y))^2}{2\sigma_2^2(x)}\right][1-u(y)]^m dydx \tag{C.42}$$

The new value $\widetilde{F_{L1}}$ can be calculated as follows:

$$\begin{aligned}
\widetilde{F_{L1}} &= \int_{\Omega}\int_{\Omega} K_\sigma(x-y)\left[-\log\frac{1}{\sqrt{2\pi}\sigma_1(x)} + \frac{(\widetilde{f}_1(x)-I(y))^2}{2\sigma_1^2(x)}\right][\widetilde{u}(y)]^m dydx \\
&= \int_{\Omega}\int_{\Omega} K_\sigma(x-y)\left[-\log\frac{1}{\sqrt{2\pi}\sigma_1(x)}\right][\widetilde{u}(y)]^m dydx \\
&+ \int_{\Omega}\int_{\Omega} K_\sigma(x-y)\frac{(\widetilde{f}_1(x)-I(y))^2}{2\sigma_1^2(x)}[\widetilde{u}(y)]^m dydx \\
&= \sum_{x\in\Omega}\sum_{y\in\Omega} K_\sigma(x-y)\left[-\log\frac{1}{\sqrt{2\pi}\sigma_1(x)}\right][\widetilde{u}(y)]^m \\
&+ \sum_{x\in\Omega}\sum_{y\in\Omega} K_\sigma(x-y)\frac{(\widetilde{f}_1(x)-I(y))^2}{2\sigma_1^2(x)}[\widetilde{u}(y)]^m \\
&= \sum_{x\in\Omega}\sum_{y\in\Omega} K_\sigma(x-y)\left[-\log\frac{1}{\sqrt{2\pi}\sigma_1(x)}\right][u(y)]^m + \sum_{x\in\Omega} K_\sigma(x-y_0)\left[-\log\frac{1}{\sqrt{2\pi}\sigma_1(x)}\right]\Delta u_m \\
&+ \sum_{x\in\Omega}\sum_{y\in\Omega} K_\sigma(x-y)\frac{(\widetilde{f}_1(x)-I(y))^2}{2\sigma_1^2(x)}[u(y)]^m \\
&\qquad + \sum_{x\in\Omega} K_\sigma(x-y_0)\frac{(\widetilde{f}_1(x)-I_0)^2}{2\sigma_1^2(x)}\Delta u_m \\
&= \sum_{x\in\Omega}\sum_{y\in\Omega} K_\sigma(x-y)\left[-\log\frac{1}{\sqrt{2\pi}\sigma_1(x)}\right][u(y)]^m + \left[K_\sigma * \left(-\log\frac{1}{\sqrt{2\pi}\sigma_1}\right)\right](y_0)\Delta u_m \\
&+ \underbrace{\sum_{x\in\Omega}\sum_{y\in\Omega} K_\sigma(x-y)\frac{(\widetilde{f}_1(x)-I(y))^2}{2\sigma_1^2(x)}[u(y)]^m}_{\widetilde{F}_{L12}} \\
&\qquad + \underbrace{\sum_{x\in\Omega} K_\sigma(x-y_0)\frac{(\widetilde{f}_1(x)-I_0)^2}{2\sigma_1^2(x)}\Delta u_m}_{\widetilde{F}_{213}}
\end{aligned} \tag{C.43}$$

We have

$$
\begin{aligned}
\widetilde{F}_{L12} &= \sum_{x\in\Omega}\sum_{y\in\Omega} K_\sigma(x-y)\frac{(\widetilde{f}_1(x)-I(y))^2}{2\sigma_1^2(x)}[u(y)]^m \\
&= \sum_{x\in\Omega}\sum_{y\in\Omega} K_\sigma(x-y)\frac{\left[f_1(x)-I(y)+\frac{K_\sigma(x-y_0)\Delta u_m}{s_3(x)+K_\sigma(x-y_0)\Delta u_m}(I_0-f_1(x))\right]^2}{2\sigma_1^2(x)}[u(y)]^m \\
&= \sum_{x\in\Omega}\sum_{y\in\Omega} K_\sigma(x-y)\frac{(f_1(x)-I(y))^2}{2\sigma_1^2(x)}[u(y)]^m \\
&+ 2\sum_{x\in\Omega}\sum_{y\in\Omega} \frac{K_\sigma(x-y)}{2\sigma_1^2(x)}(f_1(x)-I(y))\frac{K_\sigma(x-y_0)\Delta u_m}{s_3(x)+K_\sigma(x-y_0)\Delta u_m}(I_0-f_1(x))[u(y)]^m \\
&+ \sum_{x\in\Omega}\sum_{y\in\Omega} \frac{K_\sigma(x-y)}{2\sigma_1^2(x)}\left[\frac{K_\sigma(x-y_0)\Delta u_m}{s_3(x)+K_\sigma(x-y_0)\Delta u_m}\right]^2(I_0-f_1(x))^2[u(y)]^m \\
&= \sum_{x\in\Omega}\sum_{y\in\Omega} K_\sigma(x-y)\frac{(f_1(x)-I(y))^2}{2\sigma_1^2(x)}[u(y)]^m \\
&+ 2\sum_{x\in\Omega}\left[\frac{K_\sigma(x-y_0)\Delta u_m}{s_3(x)+K_\sigma(x-y_0)\Delta u_m}\frac{(I_0-f_1(x))}{2\sigma_1^2(x)}\underbrace{\sum_{y\in\Omega}K_\sigma(x-y)(f_1(x)-I(y))[u(y)]^m}_{tg_{local}}\right] \\
&+ \sum_{x\in\Omega}\left[\Big[\frac{K_\sigma(x-y_0)\Delta u_m}{s_3(x)+K_\sigma(x-y_0)\Delta u_m}\Big]^2\frac{(I_0-f_1(x))^2}{2\sigma_1^2(x)}\sum_{y\in\Omega}K_\sigma(x-y)[u(y)]^m\right] \qquad \text{(C.44)}
\end{aligned}
$$

We note that $tg_{local} = \sum\limits_{y\in\Omega} K_\sigma(x-y)\frac{(f_1(x)-I(y))}{2\sigma_1^2(x)}[u(y)]^m = 0$ according to Formula (C.36).

Therefore,

$$
\begin{aligned}
\widetilde{F_{L12}} &= \sum_{x\in\Omega}\sum_{y\in\Omega} K_\sigma(x-y)\frac{(f_1(x)-I(y))^2}{2\sigma_1^2(x)}[u(y)]^m \\
&+ \sum_{x\in\Omega}\left[\Big[\frac{K_\sigma(x-y_0)\Delta u_m}{s_3(x)+K_\sigma(x-y_0)\Delta u_m}\Big]^2\frac{(I_0-f_1(x))^2}{2\sigma_1^2(x)}\sum_{y\in\Omega}K_\sigma(x-y)[u(y)]^m\right] \\
&= \sum_{x\in\Omega}\sum_{y\in\Omega} K_\sigma(x-y)\frac{(f_1(x)-I(y))^2}{2\sigma_1^2(x)}[u(y)]^m \\
&+ \sum_{x\in\Omega}\Big[\frac{K_\sigma(x-y_0)\Delta u_m}{s_3(x)+K_\sigma(x-y_0)\Delta u_m}\Big]^2\frac{(I_0-f_1(x))^2}{2\sigma_1^2(x)}s_3(x) \qquad \text{(C.45)}
\end{aligned}
$$

Next,

$$\begin{aligned}
\widetilde{F_{L13}} &= \sum_{x\in\Omega} K_\sigma(x-y_0)\frac{(\widetilde{f}_1(x)-I_0)^2}{2\sigma_1^2(x)}\Delta u_m \\
&= \sum_{x\in\Omega} K_\sigma(x-y_0)\frac{\left[f_1(x)-I_0+\frac{K_\sigma(x-y_0)\Delta u_m}{s_3(x)+K_\sigma(x-y_0)\Delta u_m}(I_0-f_1(x))\right]^2}{2\sigma_1^2(x)}\Delta u_m \\
&= \sum_{x\in\Omega} \frac{K_\sigma(x-y_0)}{2\sigma_1^2(x)}\left[\left(f_1(x)-I_0\right)\left(1-\frac{K_\sigma(x-y_0)\Delta u_m}{s_3(x)+K_\sigma(x-y_0)\Delta u_m}\right)\right]^2\Delta u_m \\
&= \sum_{x\in\Omega} \frac{K_\sigma(x-y_0)}{2\sigma_1^2(x)}\left(f_1(x)-I_0\right)^2\frac{s_3^2(x)\Delta u_m}{\left(s_3(x)+K_\sigma(x-y_0)\Delta u_m\right)^2}
\end{aligned} \tag{C.46}$$

Then, inserting (C.45) and (C.46) into (C.43), we have:

$$\begin{aligned}
\widetilde{F_{L1}} &= \sum_{x\in\Omega}\sum_{y\in\Omega} K_\sigma(x-y)\left[-\log\frac{1}{\sqrt{2\pi}\sigma_1(x)}\right][u(y)]^m + \left[K_\sigma * \left(-\log\frac{1}{\sqrt{2\pi}\sigma_1}\right)\right](y_0)\Delta u_m \\
&+ \sum_{x\in\Omega}\sum_{y\in\Omega} K_\sigma(x-y)\frac{(f_1(x)-I(y))^2}{2\sigma_1^2(x)}[u(y)]^m \\
&+ \sum_{x\in\Omega}\left[\frac{K_\sigma(x-y_0)\Delta u_m}{s_3(x)+K_\sigma(x-y_0)\Delta u_m}\right]^2\frac{(I_0-f_1(x))^2}{2\sigma_1^2(x)}s_3(x) \\
&+ \sum_{x\in\Omega}\frac{K_\sigma(x-y_0)}{2\sigma_1^2(x)}\left(f_1(x)-I_0\right)^2\frac{s_3^2(x)\Delta u_m}{\left(s_3(x)+K_\sigma(x-y_0)\Delta u_m\right)^2} \\
&= \sum_{x\in\Omega}\sum_{y\in\Omega} K_\sigma(x-y)\left[-\log\frac{1}{\sqrt{2\pi}\sigma_1(x)}+\frac{(f_1(x)-I(y))^2}{2\sigma_1^2(x)}\right][u(y)]^m \\
&+ \sum_{x\in\Omega}\frac{s_3(x)K_\sigma(x-y_0)\Delta u_m}{\left(s_3(x)+K_\sigma(x-y_0)\Delta u_m\right)^2}(s_3(x)+K_\sigma(x-y_0)\Delta u_m)\frac{(f_1(x)-I_0)^2}{2\sigma_1^2(x)} \\
&+ \left[K_\sigma * \left(-\log\frac{1}{\sqrt{2\pi}\sigma_1}\right)\right](y_0)\Delta u_m \\
&= F_{L1} + \left[K_\sigma * \left(-\log\frac{1}{\sqrt{2\pi}\sigma_1}\right)\right](y_0)\Delta u_m \\
&+ \sum_{x\in\Omega}\frac{s_3(x)K_\sigma(x-y_0)\Delta u_m}{s_3(x)+K_\sigma(x-y_0)\Delta u_m}\frac{(f_1(x)-I_0)^2}{2\sigma_1^2(x)}
\end{aligned} \tag{C.47}$$

By the similar calculation, we have:

$$\widetilde{F_{L2}} = F_{L2} + \left[K_\sigma * \left(-\log \frac{1}{\sqrt{2\pi}\sigma_2}\right)\right](y_0)\Delta v_m + \sum_{x\in\Omega} \frac{s_4(x)K_\sigma(x-y_0)\Delta v_m}{s_4(x)+K_\sigma(x-y_0)\Delta v_m}\frac{(f_2(x)-I_0)^2}{2\sigma_2^2(x)} \tag{C.48}$$

Then, we obtain:

$$\begin{aligned}
\widetilde{F_L} &= \widetilde{F_{L1}} + \widetilde{F_{L2}} \\
&= F_{L1} + F_{L2} \\
&+ \left[K_\sigma * \left(-\log \frac{1}{\sqrt{2\pi}\sigma_1}\right)\right](y_0)\Delta u_m + \left[K_\sigma * \left(-\log \frac{1}{\sqrt{2\pi}\sigma_2}\right)\right](y_0)\Delta v_m \\
&+ \sum_{x\in\Omega} \frac{s_3(x)K_\sigma(x-y_0)\Delta u_m}{s_3(x)+K_\sigma(x-y_0)\Delta u_m}\frac{(f_1(x)-I_0)^2}{2\sigma_1^2(x)} \\
&+ \sum_{x\in\Omega} \frac{s_4(x)K_\sigma(x-y_0)\Delta v_m}{s_4(x)+K_\sigma(x-y_0)\Delta v_m}\frac{(f_2(x)-I_0)^2}{2\sigma_2^2(x)} \qquad \text{(C.49)} \\
&= F_L - \left(K_\sigma * \log \frac{1}{\sqrt{2\pi}\sigma_1}\right)(y_0)\Delta u_m - \left(K_\sigma * \log \frac{1}{\sqrt{2\pi}\sigma_2}\right)(y_0)\Delta v_m \\
&+ \sum_{x\in\Omega} \frac{s_3(x)K_\sigma(x-y_0)\Delta u_m}{s_3(x)+K_\sigma(x-y_0)\Delta u_m}\frac{(f_1(x)-I_0)^2}{2\sigma_1^2(x)} \\
&+ \sum_{x\in\Omega} \frac{s_4(x)K_\sigma(x-y_0)\Delta v_m}{s_4(x)+K_\sigma(x-y_0)\Delta v_m}\frac{(f_2(x)-I_0)^2}{2\sigma_2^2(x)} \qquad \text{(C.50)}
\end{aligned}$$

From (C.50), we obtain the formula of ΔF_L as presented in (4.93). □

APPENDIX D

Appendix: Convexity of the Energy Functional of the C_LR Model

Recall the energy function of the C_LR model:

$$\min_{\substack{u_1,u_2\\0\le f\le 1}} \left\{ E(u_1,u_2,f) = \mu TV_g(f) + \int_\Omega f(x)e_{in}(x,u_1)dx + \int_\Omega (1-f(x))e_{out}(x,u_2)dx \right\} \quad \text{(D.1)}$$

where μ is a positive constant and $TV_g(f) = \int_\Omega g(x)|\nabla f(x)|dx$

Convexity with respect to f

For fixed u_1 and u_2, Equation (D.1) is equivalent to the following problem:

$$\min_{0\le f\le 1} \left\{ E(f) = \mu TV_g(f) + \int_\Omega f(x)e_r^{CLR}(x,u_1,u_2)dx \right\} \quad \text{(D.2)}$$

where $e_r^{CLR}(x,u_1,u_2) = e_{in}(x,u_1) - e_{out}(x,u_2)$, $x \in \Omega$.

Energy functional (D.2) can be rewritten as follows:

$$E(f) = \int_\Omega (G(f))(x)dx \quad \text{(D.3)}$$

where

$$(G(f))(x) = \mu g(x)|\nabla f(x)| + f(x)e_r^{CLR}(x,u_1,u_2) \quad \text{(D.4)}$$

As the Euclidean norm $|y|$, $y = (y_1, y_2) \in \mathbb{R}^2$, is convex with respect to y. Therefore, $|\nabla f(x)|$ is also convex with respect to f. Besides, because μ and g are positive, and because $f(x)e_r^{CLR}(x, u_1, u_2)$ is an affine function with respect to f, then $G(f)$ is convex with respect to f. Consequently, $E(f)$ is convex with respect to f.

Convexity with respect to u_1 and to u_2

In the energy functional from (D.2), only the data fidelity terms depend on u_1 and u_2. Each term depends on either u_1 or u_2 and is twice differentiable with positive value with respect to u_1 or to u_2.

In conclusion, the energy functional is convex with respect to each variable f, u_1 and u_2.

APPENDIX E

Appendix: Sensibility of the Parameters of the Proposed Models

This Appendix shows results of the proposed models in this thesis such as R_LGR, C_LR, C_LGR and C_LGFGD on non-homogeneous, MRI, CT and PET images when the parameters in their energy functions vary. We limit this Appendix for the parameters influenced to deal with intensity in-homogeneity: size of the local window and the coefficient of the local term.

E.1 The R_LGR Model

Recall the energy function of the R_LGR model:

$$E(\phi) = \int_{\Omega} \big(I(x) - I_G(x,\phi)\big)^2 dx + \frac{\lambda}{2} \int_{\Omega} \big(I(x) - I_L(x,\phi)\big)^2 dx \tag{E.1}$$

Parameters:

·) σ: the size of the local window,

·) λ: controls the influence of the local term compared with the global term.

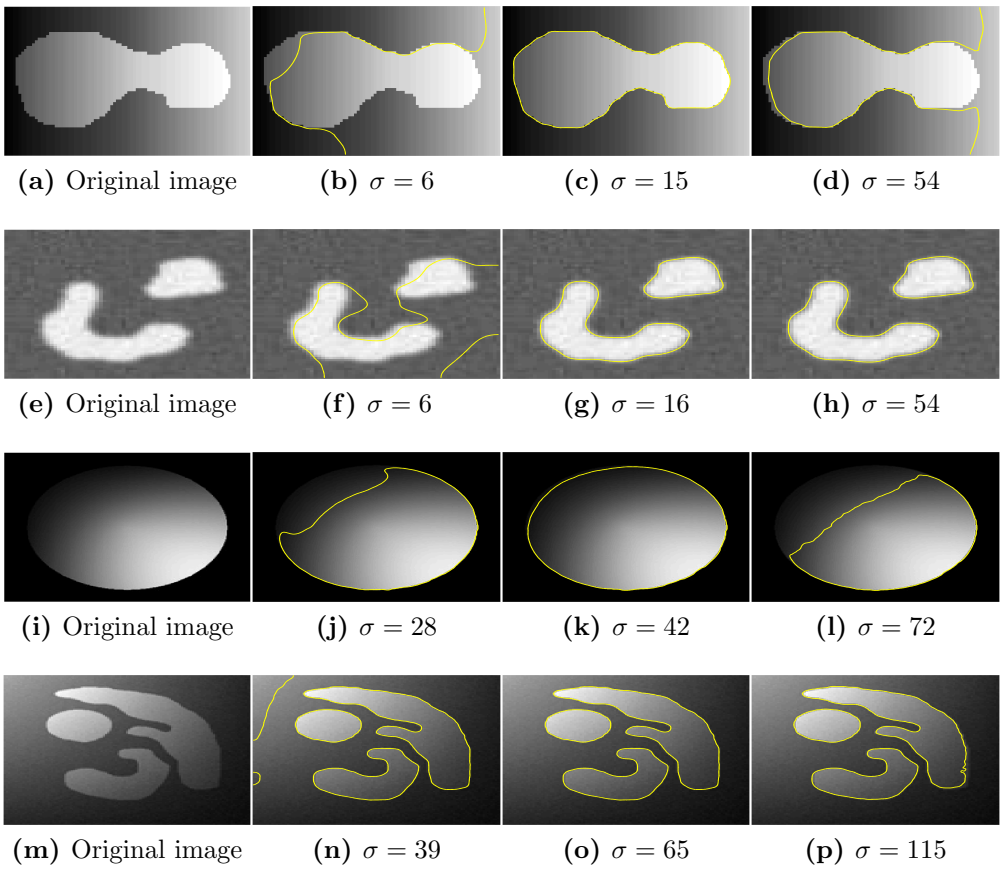

(a) Original image **(b)** $\sigma = 6$ **(c)** $\sigma = 15$ **(d)** $\sigma = 54$

(e) Original image **(f)** $\sigma = 6$ **(g)** $\sigma = 16$ **(h)** $\sigma = 54$

(i) Original image **(j)** $\sigma = 28$ **(k)** $\sigma = 42$ **(l)** $\sigma = 72$

(m) Original image **(n)** $\sigma = 39$ **(o)** $\sigma = 65$ **(p)** $\sigma = 115$

Figure E.1. Results of the R_LGR model on non-homogeneous synthetic images with different values of σ ($\lambda = 1000$ for all tests).

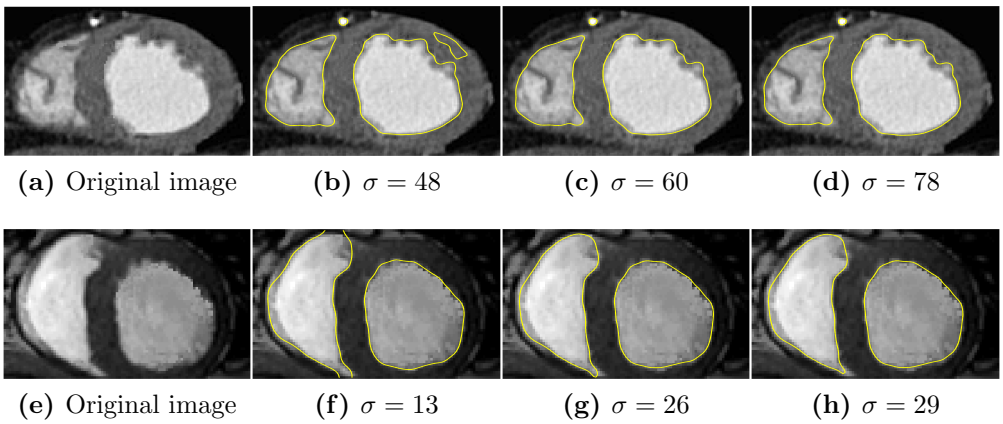

(a) Original image **(b)** $\sigma = 48$ **(c)** $\sigma = 60$ **(d)** $\sigma = 78$

(e) Original image **(f)** $\sigma = 13$ **(g)** $\sigma = 26$ **(h)** $\sigma = 29$

Figure E.2. Results of the R_LGR model on MR images with different values of σ ($\lambda = 100$ for all tests).

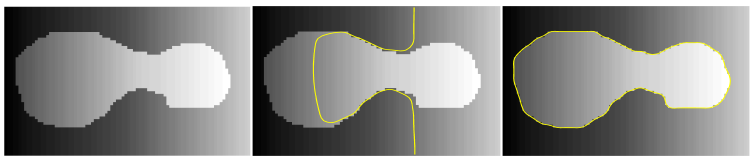

(a) Original image **(b)** $\lambda = 100$ **(c)** $\lambda = 1000$

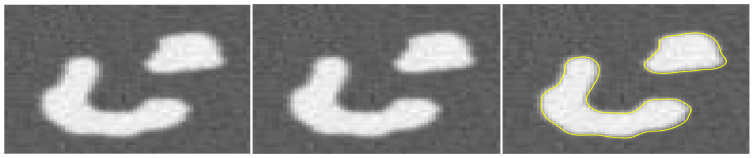

(d) Original image **(e)** $\lambda = 100$ **(f)** $\lambda = 1000$

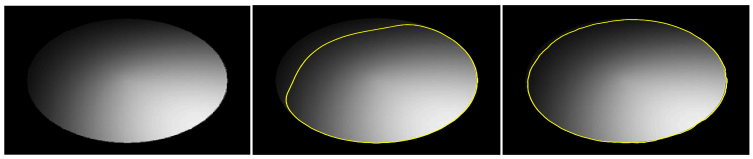

(g) Original image **(h)** $\lambda = 100$ **(i)** $\lambda = 1000$

(j) Original image **(k)** $\lambda = 100$ **(l)** $\lambda = 1000$

Figure E.3. Results of the R_LGR model on non-homogeneous synthetic images with different values of λ. Row 1: $\sigma = 9$, Row 2: $\sigma = 8$, Row 3: $\sigma = 31$, Row 4: $\sigma = 40$.

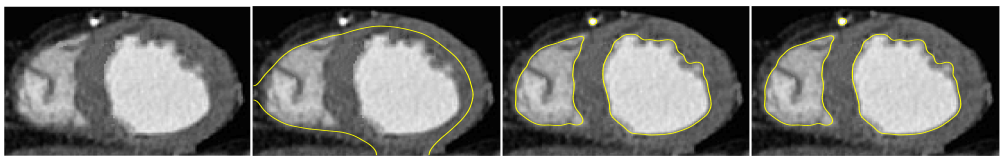

(a) Original image **(b)** $\lambda = 1$ **(c)** $\lambda = 40$ **(d)** $\lambda = 50$

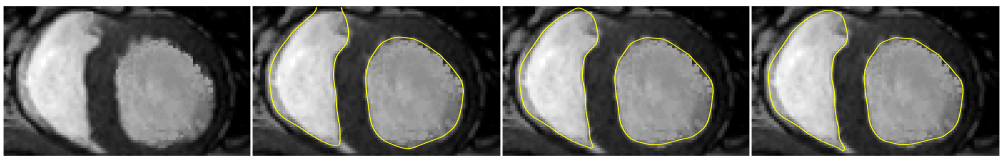

(e) Original image **(f)** $\lambda = 20$ **(g)** $\lambda = 60$ **(h)** $\lambda = 80$

Figure E.4. Results of the R_LGR model on MR images with different values of λ. Row 1: $\sigma = 60$, Row 2: $\sigma = 27$.

E.2 The C_LR Model

Recall the energy function of the CLGRAC model:

$$\min_{\substack{u_1,u_2\\0\leq f\leq 1}} \left\{ E(u_1,u_2,f) = \mu TV_g(f) + \int_\Omega f(x)e_{in}(x,u_1)dx + \int_\Omega (1-f(x))e_{out}(x,u_2)dx \right\} \quad \text{(E.2)}$$

Parameters:

·) σ: the size of the local window.

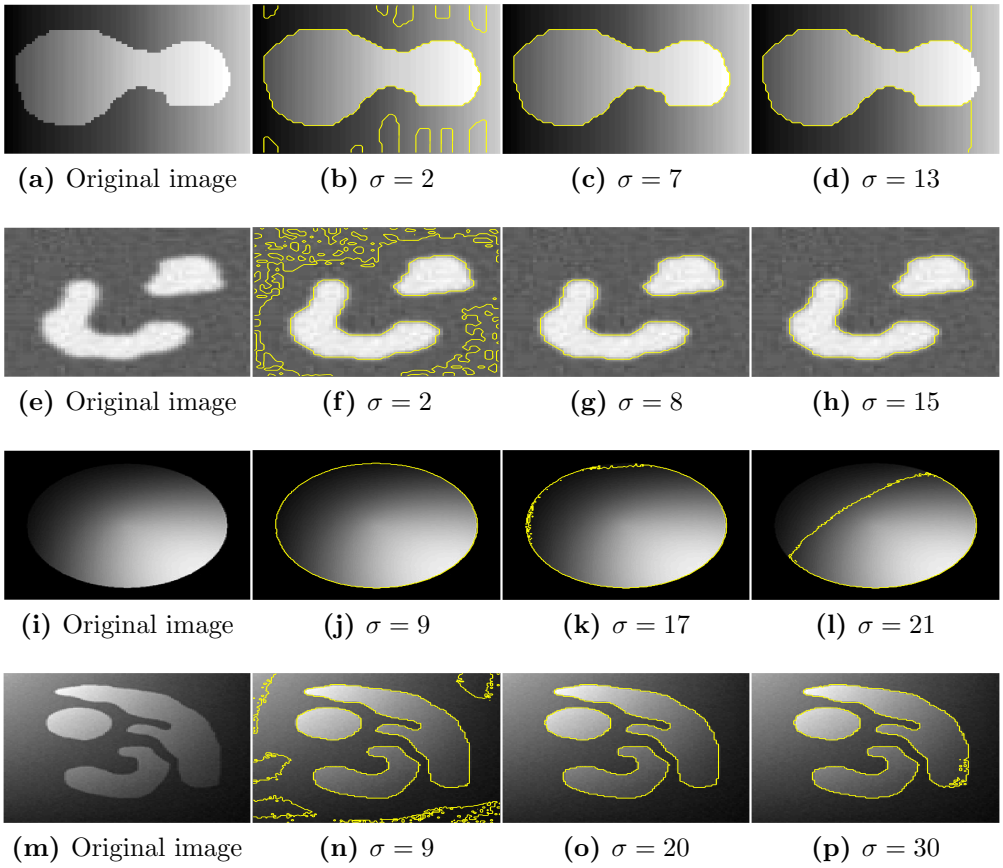

(a) Original image **(b)** $\sigma = 2$ **(c)** $\sigma = 7$ **(d)** $\sigma = 13$

(e) Original image **(f)** $\sigma = 2$ **(g)** $\sigma = 8$ **(h)** $\sigma = 15$

(i) Original image **(j)** $\sigma = 9$ **(k)** $\sigma = 17$ **(l)** $\sigma = 21$

(m) Original image **(n)** $\sigma = 9$ **(o)** $\sigma = 20$ **(p)** $\sigma = 30$

Figure E.5. Results of the C_LR model on non-homogeneous synthetic images with different values of σ ($\mu = 1$ for all tests).

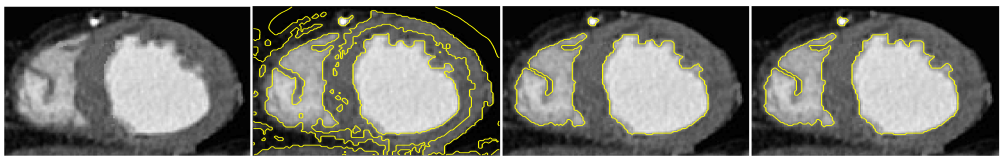

(a) Original image **(b)** $\sigma = 2$ **(c)** $\sigma = 15$ **(d)** $\sigma = 20$

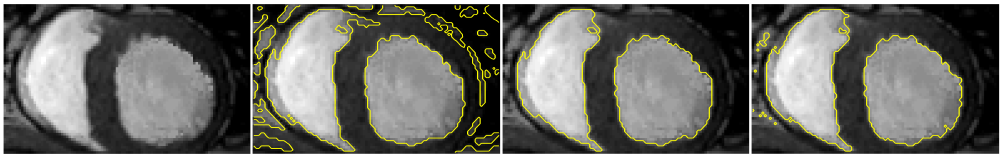

(e) Original image **(f)** $\sigma = 2$ **(g)** $\sigma = 11$ **(h)** $\sigma = 25$

Figure E.6. Results of the C_LR model on MR images with different values of σ. Row 1: $\mu = 10$, Row 2: $\mu = 1$.

E.3 The C_LGR Model

Recall the energy function of the C_LGR model:

$$\min_{\substack{u_1,u_2,c_1,c_2 \\ 0\le f\le 1}} E(u_1,u_2,c_1,c_2,f) = \mu \int_\Omega g(x)|\nabla f(x)|dx + \lambda E_L(u_1,u_2,f) + \lambda_2 E_G(c_1,c_2,f) \quad \text{(E.3)}$$

Parameters:

·) σ: the size of the local window,

·) λ: controls the influence of the local term F_L compared with the global term F_G (fixed $\lambda_2 = 1$).

E.4 The C_LGFGD Model

Recall the energy function of the C_LGFGD model:

$$F(M) = \mu \int_\Omega |\nabla u|dx + \lambda F_G(M_G) + (1-\lambda)F_L(M_L) \quad \text{(E.4)}$$

Parameters:

·) σ: the size of the local window,

·) λ: controls the influence of the local term F_L compared with the global term F_G.

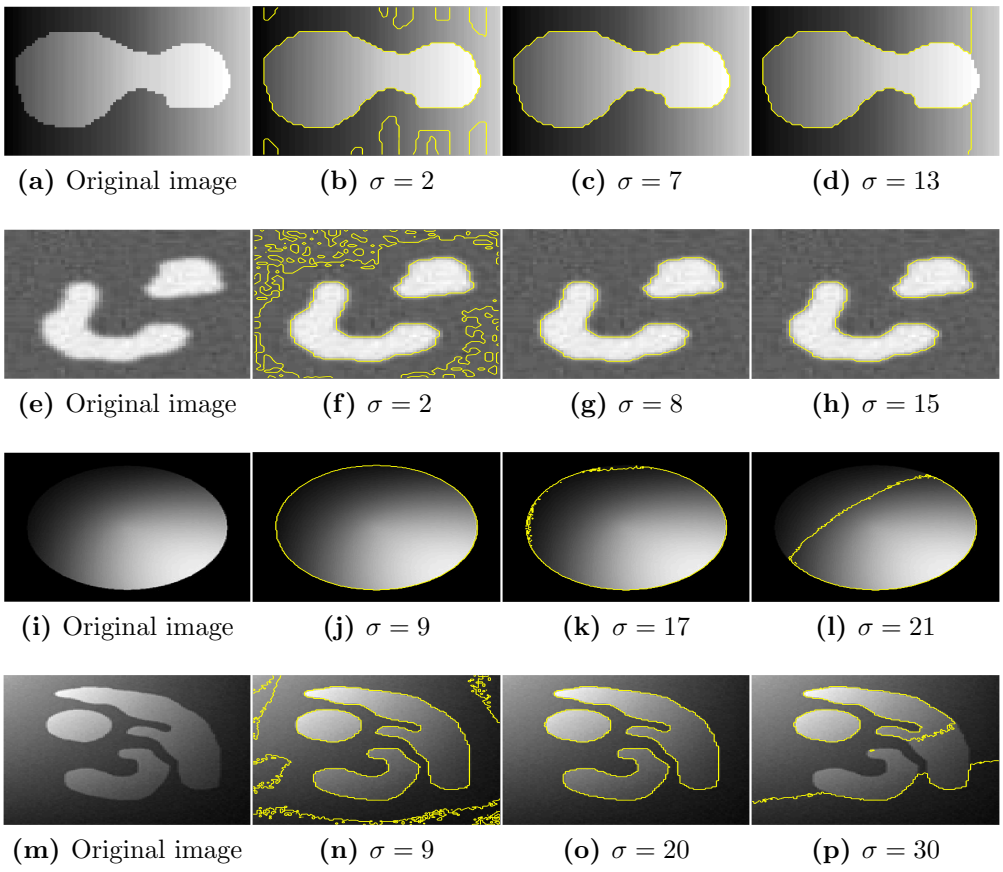

(a) Original image **(b)** $\sigma = 2$ **(c)** $\sigma = 7$ **(d)** $\sigma = 13$

(e) Original image **(f)** $\sigma = 2$ **(g)** $\sigma = 8$ **(h)** $\sigma = 15$

(i) Original image **(j)** $\sigma = 9$ **(k)** $\sigma = 17$ **(l)** $\sigma = 21$

(m) Original image **(n)** $\sigma = 9$ **(o)** $\sigma = 20$ **(p)** $\sigma = 30$

Figure E.7. Results of the C_LGR model on non-homogeneous synthetic images with different values of σ ($\mu = 1$ and $\lambda = 10000$ for all tests).

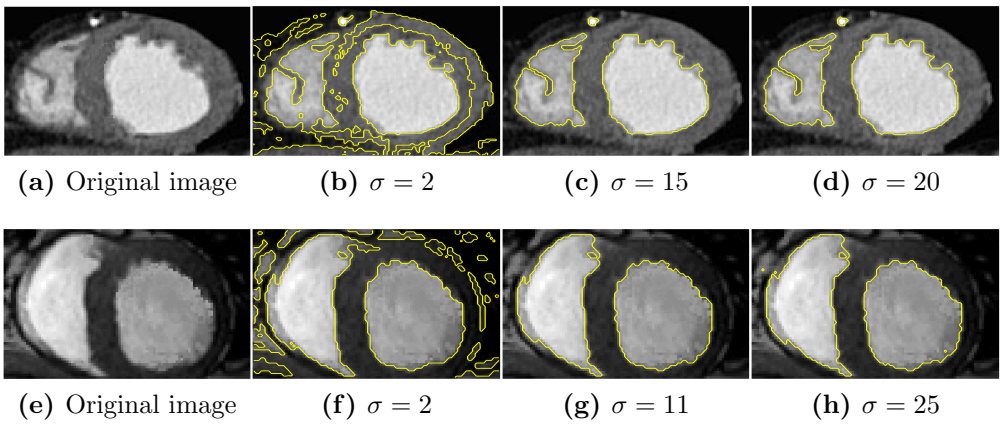

(a) Original image **(b)** $\sigma = 2$ **(c)** $\sigma = 15$ **(d)** $\sigma = 20$

(e) Original image **(f)** $\sigma = 2$ **(g)** $\sigma = 11$ **(h)** $\sigma = 25$

Figure E.8. Results of the C_LGR model on MR images with different values of σ. Row 1: $\mu = 10$, $\lambda = 1000$. Row 2: $\mu = 1$, $\lambda = 1000$.

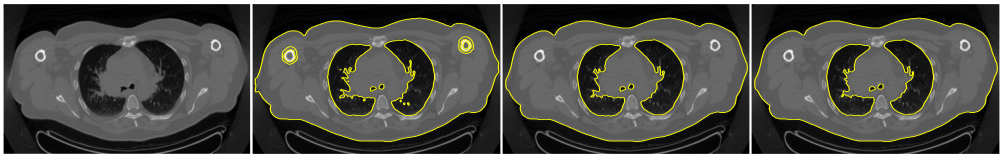

(a) Original image **(b)** $\sigma = 2$ **(c)** $\sigma = 11$ **(d)** $\sigma = 22$

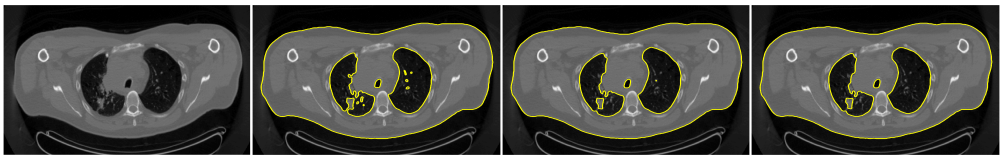

(e) Original image **(f)** $\sigma = 2$ **(g)** $\sigma = 12$ **(h)** $\sigma = 22$

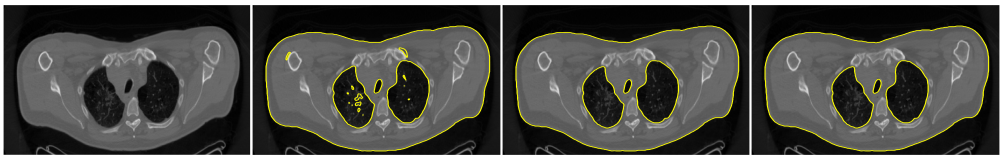

(i) Original image **(j)** $\sigma = 2$ **(k)** $\sigma = 12$ **(l)** $\sigma = 22$

Figure E.9. Results of the C_LGR model on CT images with different values of σ ($\mu = 1$ and $\lambda = 10$ for all test).

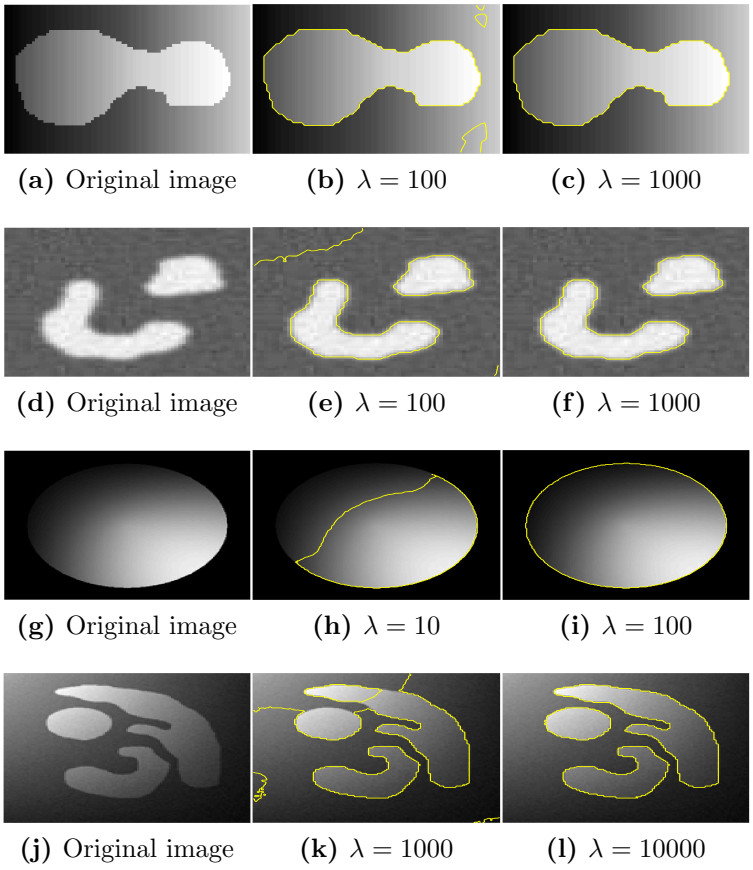

(a) Original image **(b)** $\lambda = 100$ **(c)** $\lambda = 1000$

(d) Original image **(e)** $\lambda = 100$ **(f)** $\lambda = 1000$

(g) Original image **(h)** $\lambda = 10$ **(i)** $\lambda = 100$

(j) Original image **(k)** $\lambda = 1000$ **(l)** $\lambda = 10000$

Figure E.10. Results of the C_LGR model on non-homogeneous synthetic images with different values of λ. Row 1: $\sigma = 5, \mu = 1$. Row 2: $\sigma = 7, \mu = 1$. Row 3: $\sigma = 9, \mu = 1$. Row 4: $\sigma = 17, \mu = 1$.

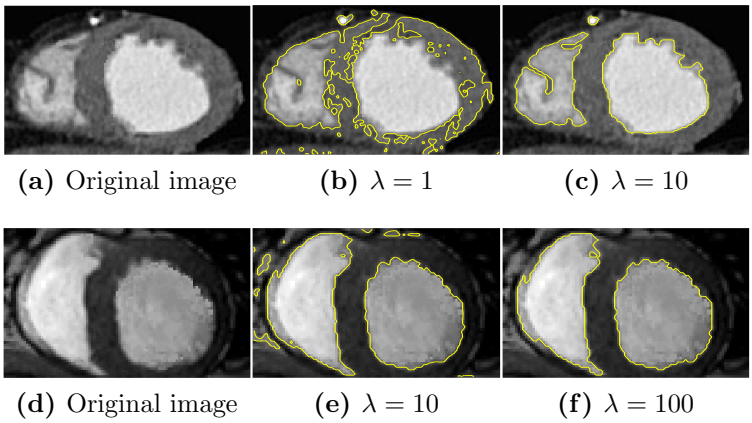

(a) Original image **(b)** $\lambda = 1$ **(c)** $\lambda = 10$

(d) Original image **(e)** $\lambda = 10$ **(f)** $\lambda = 100$

Figure E.11. Results of the C_LGR model on MR images with different values of λ. Row 1: $\sigma = 13, \mu = 10$. Row 2: $\sigma = 8, \mu = 1$.

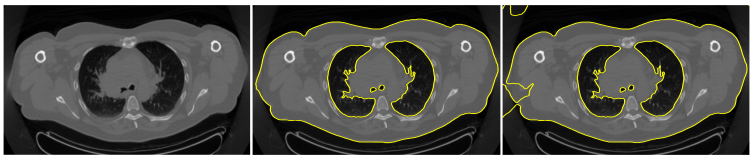

(a) Original image **(b)** $\lambda = 100$ **(c)** $\lambda = 1000$

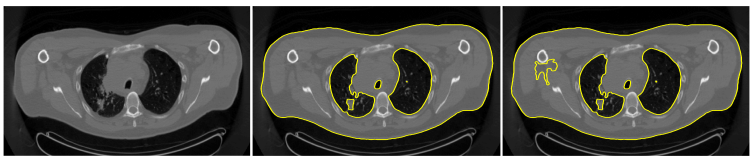

(d) Original image **(e)** $\lambda = 10$ **(f)** $\lambda = 100$

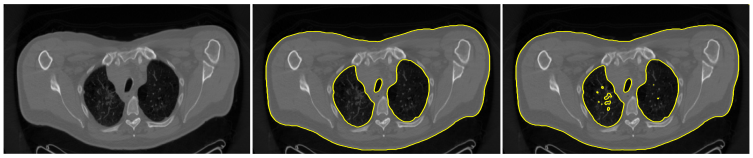

(g) Original image **(h)** $\lambda = 1$ **(i)** $\lambda = 10$

Figure E.12. Results of the C_LGR model on CT images with different values of λ. $\sigma = 12$ and $\mu = 1$ for all test.

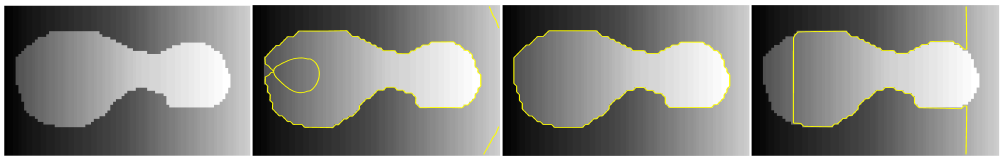

(a) Original image **(b)** $\sigma = 6$ **(c)** $\sigma = 10$ **(d)** $\sigma = 17$

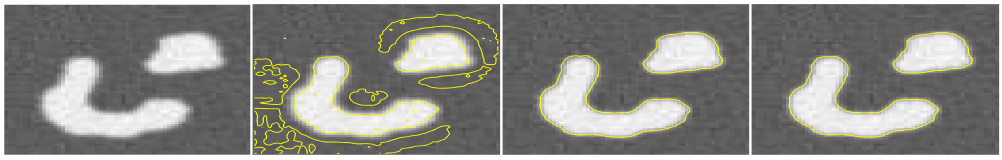

(e) Original image **(f)** $\sigma = 2$ **(g)** $\sigma = 10$ **(h)** $\sigma = 15$

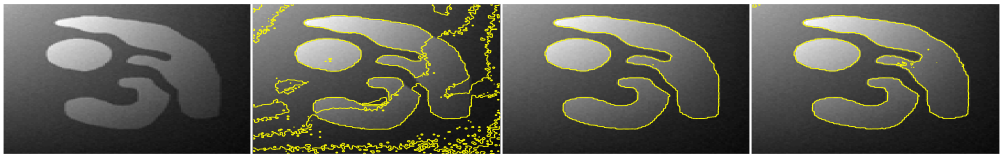

(i) Original image **(j)** $\sigma = 9$ **(k)** $\sigma = 28$ **(l)** $\sigma = 32$

Figure E.13. Results of the C_LGFGD model on non-homogeneous synthetic images with different values of σ. $m = 2$ and $\lambda = 0.01$ for all test.

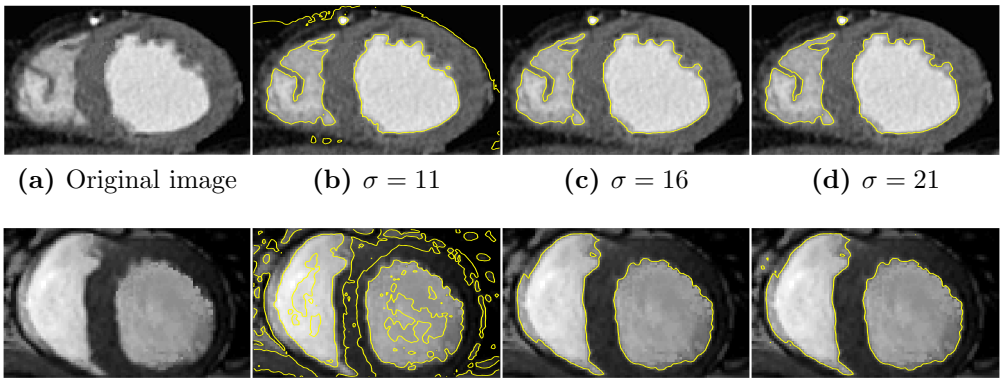

(a) Original image **(b)** $\sigma = 11$ **(c)** $\sigma = 16$ **(d)** $\sigma = 21$

(e) Original image **(f)** $\sigma = 2$ **(g)** $\sigma = 12$ **(h)** $\sigma = 16$

Figure E.14. Results of the C_LGFGD model on MR images with different values of σ. $m = 2$ and $\lambda = 0.0001$ for all test.

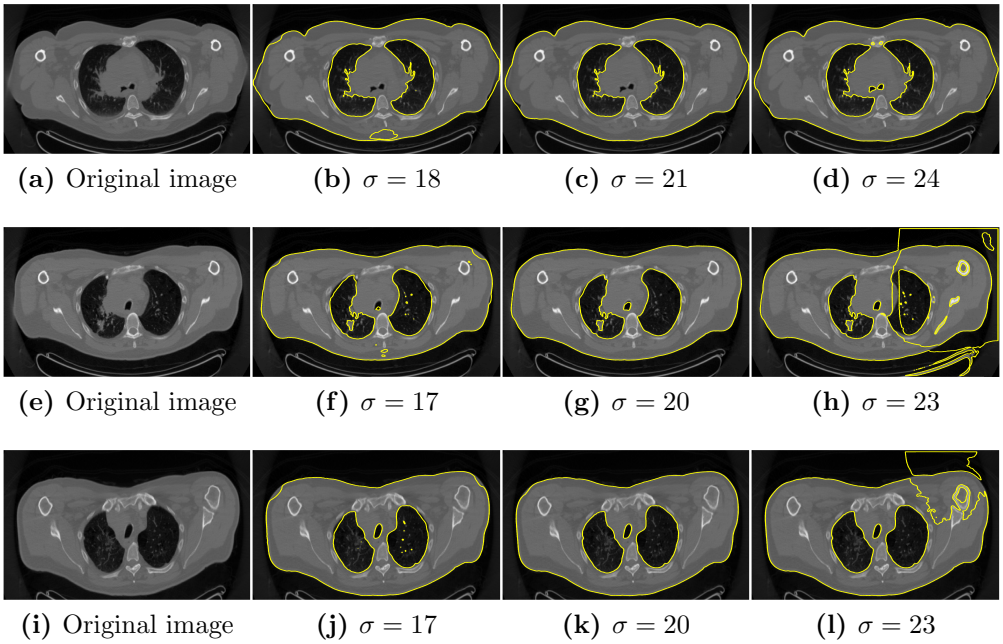

(a) Original image **(b)** $\sigma = 18$ **(c)** $\sigma = 21$ **(d)** $\sigma = 24$

(e) Original image **(f)** $\sigma = 17$ **(g)** $\sigma = 20$ **(h)** $\sigma = 23$

(i) Original image **(j)** $\sigma = 17$ **(k)** $\sigma = 20$ **(l)** $\sigma = 23$

Figure E.15. Results of the C_LGFGD model on CT images with different values of σ. $m = 2$ and $\lambda = 0.0001$ for all test.

(a) Original image **(b)** $\lambda = 0.1$ **(c)** $\lambda = 0.2$

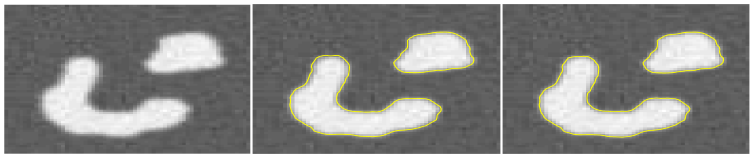

(d) Original image **(e)** $\lambda = 0.1$ **(f)** $\lambda = 0.9$

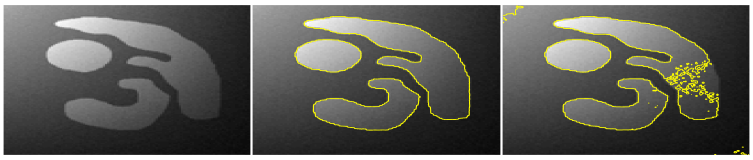

(g) Original image **(h)** $\lambda = 0.1$ **(i)** $\lambda = 0.2$

Figure E.16. Results of the C_LGFGD model on non-homogeneous synthetic images with different values of λ. Row 1: $\sigma = 9$ and $m = 2$, Row 2: $\sigma = 9$ and $m = 2$. Row 3: $\sigma = 27$ and $m = 2$.

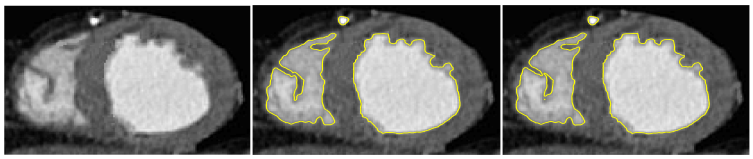

(a) Original image **(b)** $\lambda = 0.1$ **(c)** $\lambda = 0.2$

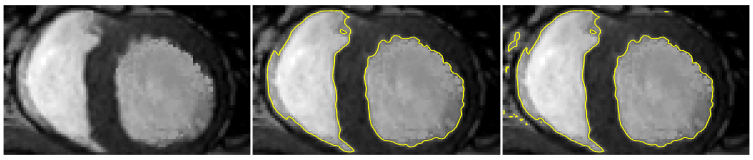

(d) Original image **(e)** $\lambda = 0.01$ **(f)** $\lambda = 0.1$

Figure E.17. Results of the C_LGFGD model on MR images with different values of λ. Row 1: $\sigma = 17$ and $m = 2$. Row 2: $\sigma = 11$ and $m = 2$

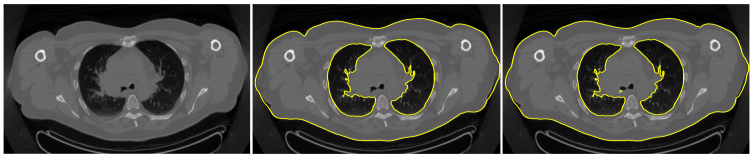

(a) Original image **(b)** $\lambda = 0.01$ **(c)** $\lambda = 0.1$

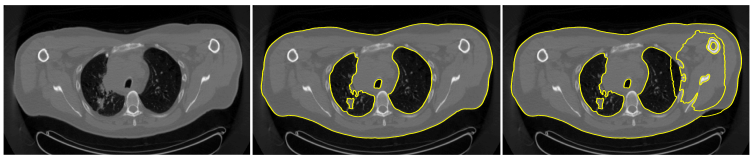

(d) Original image **(e)** $\lambda = 0.01$ **(f)** $\lambda = 0.1$

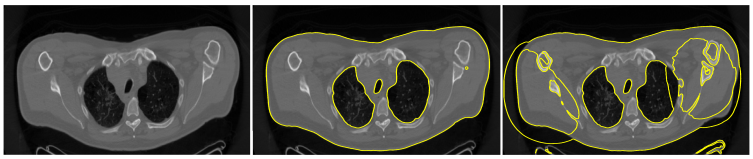

(g) Original image **(h)** $\lambda = 0.1$ **(i)** $\lambda = 0.3$

Figure E.18. Results of the C_LGFGD model on CT images with different values of λ. $\sigma = 21$ and $m = 2$ for all test.

Bibliography

[1] Q.T. Thieu, M. Luong, J. M. Rocchisani, N. M. Sirakov, E. Viennet, *Segmentation by a Local and Global Fuzzy Gaussian Distribution Energy Minimization of an Active Contour Model.* R.P. Barneva et al. (Eds.): IWCIA 2012, LNCS 7655, pp. 298-312. Springer, Heidelberg 2012

[2] Q. T. Thieu, M. Luong, J. M. Rocchisani, N. Linh-Trung, E. Viennet, *Novel Active Contour Model for Image Segmentation Based on Local Fuzzy Gaussian Distribution Fitting.* International Conference on Signal, Image Processing and Applications ICSIA, Hong Kong 2012

[3] Q. T. Thieu, M. Luong, J. M. Rocchisani, E. Viennet, D. Tran, *Novel Convex Active Contour Model Using Local and Global Information.* IEEE International Conference on Digital Image Computing: Techniques and Applications (DICTA), Noosa, Queensland, pp. 346-351, Digital Object Identifier: 10.1109/DICTA.2011.65, 6-8 December, Australia, 2011

[4] Q. T. Thieu, M. Luong, J. M. Rocchisani, E. Viennet, *A Convex Active Contour Region-based Model for Image Segmentation.* Proceeding CAIP'11, Proceedings of the 14th international conference on Computer analysis of images and patterns - Part I, LNCS 2011, Springer-Verlag Berlin, Heidelberg 2011, Volume 6854/2011, pp. 135143, 2011. (DOI: http://dx.doi.org/10.1007/978-3-642-23672-3_17)

[5] Q. T. Thieu, M. Luong, J. M. Rocchisani, D. Tran, E. Viennet, *An Efficient Local and Global Model for Image Segmentation.* In 2011 International Conference on Advanced Technologies for Communications, pp. 260 263, ISBN: 978-1-4577-1206-7, Digital Object Identifier: 10.1109/ATC.2011.6027480, Da Nang, August 2-4, Vietnam, 2011

[6] T. Brox, J. Malik, *Object segmentation by long term analysis of point trajectories.* European Conference on Computer Vision (ECCV), Springer, LNCS, Sept. 2010

[7] J. B. Stephanie, *Modeles de contours actifs bases regions pour la segmentation d'images et de videos.* Thesis, 2003

[8] P. Taylor, *Invited review: computer aids for decision-making in diagnostic radiology - a literature review.* British Journal of Radiology, Vol. 68, 945-957, 1995

[9] V.S. Khoo, D.P. Dearnaley, D.J. Finnigan, A. Padhani, S.F. Tanner, M.O. Leach, *Magnetic resonance imaging (MRI): considerations and applications in radiotheraphy treatment planning.* Radiother. Oncol., 42, 1-15, 1997

[10] S.M. Larie and S.S. Abukmeil, *Brain abnormality in schizophrenia: a systematic and quantitative review of volumetric magnetic resonance imaging studies.* J. Psych., 172:110-120, 1998

[11] A.P. Zijdenbos, B.M. Dawant, *Brain segmentation and white matter lesion detection in MR images.* Critical Reviews in Biomedical Eng., 22, 401-465, 1994

[12] A.J. Worth, N. Makris, V.S. Caviness, and D.N. Kennedy. Neuroanatomical segmentation in MRI: technological objectives. Int. J. Patt. Rec. Art. Intel., 11:1161-1187, 1997

[13] N. Ayache, P. Cinquin, I. Cohen, L. Cohen, F. Leitner, and O. Monga. *Segmentation of complex three dimensional medical objects: a challenge and a requirement for computer-assisted surgery planning and performance.* In R.H. Taylor, S. Lavallee, G.C. Burdea, and R. Mosges, editors, Compute integrated surgery: technology and clinical applications, pages 59-74. MIT Press, 1996

[14] W.E.L. Grimson, G.J. Ettinger, T. Kapur, M.E. Leventon, W.M.Wells, et al. *Utilizing segmented MRI data in image-guided surgery.* Int. J. Patt. Rec. Art. Intel., 11:1367-1397, 1997. review. Brit. J. Radiol.., 68:945-957, 1995

[15] J. M. Fitzpatrick; M. Sonka, *Handbook of Medical Imaging, Volume 2. Medical Image Processing and Analysis.* 2000

[16] P. Sprawls, *Physical principles of medical imaging.* Aspen Publishers, 1993

[17] G. Dougherty, *Digital image processing for medical applications.* Cambridge University Press, 2009

[18] J. Jan, *Medical image processing, reconstruction and restoration: Concepts and methods.* Taylor and Francis Group, 2006

[19] F. Barrett, N. Keat, *Artifacts in CT: Recognition and Avoidance.* RadioGraphics, 24, 1679-1691, November 2004

[20] J. G. Sled, G. B. Pike, *Understanding intensity non-uniformity in MRI.* Medical Image Computing and Computer-Assisted Interventation MICCAI'98 , Lecture Notes in Computer Science Volume 1496, pp 614-622, 1998

[21] J. G. Sled, G. B. Pike, *Standing-wave and RF penetration artifacts caused by elliptic geometry: an electrodynamic analysis of MRI.* IEEE Transactions on Medical Imaging, Volume: 17 , Issue: 4 , Page(s): 653-662, 1998

[22] J. Hsieh, *Computed Tomography: Principles, Design, Artifacts, and Recent Advances.* ISBN-10: 0470563532, Wiley-Blackwell, 2009

[23] D. L. Pham, C. Xu, J. L. Prince, *A Survey of Current Methods in Medical Image Segmentation.* Annual Review of Biomedical Engineering, Vol. 2, pp. 315-338, 2000

[24] I. Bankman, *Handbook of Medical Image Processing and Analysis.* Academic Press series in biomedical engineering, Academic Press, ISBN: 008055914X, 9780080559148, 2008

[25] M. Kass, A. Witkin, D. Terzopoulos, *Snakes : Active contour models.* International Journal of Computer Vision, 1 :321-332, 1988

[26] R. Boscolo, M. Brown, M. McNitt-Gray, *Medical Image Segmentation with Knowledge-guided Robust Active Contours.* Radiographics, 22(2): 437-448, 2002

[27] C. Xu, D.L. Pham, J.L. Prince, *Medical Image Segmentation Using Deformable Models.* SPIE Handbook on Medical Imaging: Med. Ima. Anal., 29-174, 2000

[28] Z. Chen, T. Qui, S. Ruan, *Fuzzy adaptive level set algorithm for brain tissue segmentation.* Proceedings of International Conference Signal Processing, Beijing, China, 1047-1050, 2008

[29] V. Caselles, F. Catte, T. Coll, F. Dibos, *A geometric model for active contours.* Numerische Mathematik, 66 :1-31, 1993

[30] V. Caselles, R. Kimmel, and G. Sapiro, *Geodesic active contours.* International Conference of Computer Vision, Boston, June 1995

[31] V. Caselles, R. Kimmel, and G. Sapiro, *Geodesic active contours.* International Journal of Computer Vision, Vol. 22, pp. 61-79, 1997

[32] D. Mumford and J. Shah, *Optimal Approximations of Piecewise Smooth Functions and Associated Variational Problems.* Communications on Pure and Applied Mathematics, 42:577-685, 1989

[33] T. Chan and L. Vese, *Active Contours Without Edges.* IEEE Transactions on Image Processing, 10(2):266-277, 2001

[34] L. A. Vese and T. F. Chan, *A Multiphase Level Set Framework for Image Segmentation Using the Mumford and Shah Model.* International Journal of Computer Vision, Vol. 50, No. 3, pp. 271-293, 2002

[35] T. Chan, S. Esedoglu, M. Nikolova, *Algorithms for Finding Global Minimizers of Image Segmentation and Denoising Models.* J. App. Math., 66: 1632-1648, 2004

[36] D. Cremers, M. Rousson, R. Deriche, *A review of statistical approaches to level set segmentation: integrating color, texture, motion and shape.* In International Journal of Computer Vision, volume 72, 2007

[37] P. K. Sahoo, S. Soltani, and A. K. C. Wong, *A survey of thresholding techniques.* Comput. Vis. Graph. Im. Proc., 1988

[38] D. L. Pham, J.L Prince. *An adaptive fuzzy C-means algorithm for image segmentation in the presence of intensity inhomogeneities.* Pattern Recognit. Lett. 20(1), 57-68, 1998

[39] W. M. Wells, III, W. E. L. Grimson, R. Kikins, and F. A. Jolezs, *Adaptive segmentation of MRI data.* IEEE Trans. Med. Imag., vol. 15, no. 8, pp. 429-442, Aug. 1996

[40] J.-F. Mangin, *Entropy minimization for automatic correction of intensity nonuniformity.* Presented at the IEEE Workshop Math. Methods Biomed. Image Anal. , Hilton Head Island, SC, 2000

[41] X. Bresson, S. Esedoglu, P. Vandergheyns, J. Thiran, S. Osher, *Fast Global Minimization of the Active Contour/Snake Model.* Journal of Mathematical Imaging and Vision, 28(2): 151-167, 2007

[42] J. Wojak, E. D. Angelini, I. Bloch, *Segmentation multimodale de tumeurs pulmonaires et de ganglions lymphatiques par une mthode variationnelle.* RFIA, Caen, France, pp. 199-205, 2010

[43] T. Brox, D. Cremers, *On local region models and a statistical interpretation of the piecewise smooth Mumford-Shah functional.* International Journal of Computer Vision, 84(2): 184-193, Jun. 2009

[44] B. Mory, R. Ardon, *Fuzzy region competition : A convex two-phase segmentation framework.* In : Scale Space and Variational Methods in Computer Vision, pages 214-226, 2007

[45] A. Chambolle, *An Algorithm for Total Variation Minimization and Applications.* Journal of Mathematical Imaging and Vision, Vol. 20 Issue 1-2, pp. 89-97, January-March 2004

[46] B. Song, T. Chan, *A fast algorithm for level set based optimization.* UCLA CAM Report 02-68, 2002

[47] S. Krinidis, V. Chatzis, *Fuzzy energy-based active contour.* IEEE Transactions on Image Processing, 18(12): 2747-2755, 2009

[48] M. E. Leventon, W. E. L. Grimson, and O. Faugeras, *Statistical shape influence in geodesic active contours.* In Proc. 2000 IEEE Computer Society Conference on Computer Vision and Pattern Recognition, volume 1, pages 316-323, Hilton Head, SC, June 2000

[49] T. Brox, M. Rousson, R. Deriche, and J.Weickert, *Unsupervised segmentation incorporating color, texture, and motion.* In N. Petkov and M. A.Westenberg, editors, Computer Analysis of Images and Patterns, volume 2756 of Lecture Notes in Computer Science, pages 353-360, Springer, Berlin, 2003

[50] L. D. Cohen, *On active contour models and balloons.* Computer Vision, Graphics and Image Processing : Image Understanding, vol. 53, pp. 211-218, 1991

[51] L. Cohen, E. Bardinet, N. Ayache, *Surface reconstruction using active contour models.* SPIE Conference on Geometric Methods in Computer Vision, San Diego, CA, 1993

[52] T. McInerney, D. Terzopoulos, *Topologically adaptable snakes.*, ICCV, 840-845, 1995

[53] S. Osher, J. Sethian, *Fronts propagating with curvature-dependent speed : Algorithms based on Hamilton-Jacobi formulation.* Journal of computational physics, vol. 79, pp. 12-49, 1988

[54] L. Alvarez, F. Guichard, P. L. Lions, and J. M. Morel, *Axioms and fundamental equations of image processing.* Archive for Rational Mechanics and Analysis, vol. 123, no. 3, pp. 199-257, 1993

[55] G. Sapiro, A. Tannenbaum, *Area and length preserving geometric invariant scale-spaces.* IEEE Transactions on Pattern Analysis and Machine Intelligence, Jan 1995, Volume: 17, Issue: 1 , Page(s): 67-72

[56] C. Epstein and M. Gage, *The curve shortening flow, Wave motion: theory, modelling, and computation* Mathematical Sciences Research Institute, vol. 7, 15-59 Springer, New York, 1987

[57] M. Sussman, P. Smereka, S. Osher, *A Level Set Approach for Computing Solutions to Incompressible Two-Phase Flow.* J. Comp. Phys., vol. 114, pp. 146-159, 1994

[58] D. Peng, B. Merriman, S. Osher, H. Zhao, and M. Kang, *A PDE-Based Fast Local Level Set Method.* J. Comp. Phys.,vol. 155, pp. 410-438, 1999

[59] H. Zhao, T. Chan, B. Merriman, and S. Osher, *A Variational Level Set Approach to Multiphase Motion.* J. Comp. Phys.,vol. 127, pp. 179-195, 1996

[60] S. Osher and R. Fedkiw, *Level Set Methods and Dynamic Implicit Surfaces.* Springer-Verlag, New York, 2002

[61] D. Chopp, *Computing Minimal Surface via Level Set Curvature Flow.* J. Comput. Phys., vol. 106, pp. 77-91, 1993

[62] E. Rudin and A. Tourin, *A Viscosity Solutions Approach to Shape-From-Shading.* SIAM J.Num. Anal., vol. 29, pp. 867-884, 1992.

[63] L. Evans, *Partial Differential Equations.* Providence: American Mathematical Society, 1998

[64] G. Aubert and P. Kornprobst, *Mathematical problems in image processing: Partial Differential Equations and the Calculus of Variations.* Vol. 47, Springer-Verlag, 2001

[65] C. Li, C. Xu, C. Gui, and M. D. Fox, *Level set evolution without re-initialization: A new variational formulation.* Proc. IEEE Conf. Computer Vision and Pattern Recognition, vol. 1, pp. 430-436, 2005

[66] C. Li, C. Xu, C. Gui, and M. D. Fox, *Distance Regularized Level Set Evolution and Its Application to Image Segmentation.* IEEE Trans. Image Processing, vol. 19, no. 12, pp. 154-164, Dec. 2010

[67] X. Xie, *Active Contouring Based on Gradient Vector Interaction and Constrained Level Set Diffusion.* IEEE Trans. Image Processing, vol. 19, no. 1, pp. 154-164, Jan. 2010

[68] S.C. Zhu and A.L. Yuille, *Region competition : Unifying snakes, region growing, and Bayes/MDL for multiband image segmentation.* IEEE Transactions on Pattern Analysis and Machine Intelligence 18, no. 9, 884-900, 1996

[69] A. Tsai, A. Yezzi, A.S. Willsky, *Curve evolution implementation of the Mumford-Shah functional for image segmentation, denoising, interpolation, and magnification.* IEEE Trans. Image Processing, 2001

[70] N. Paragios, *Geodesic active regions and level set methods : contributions and applications in artificial vision.* Ph.D. thesis, Université de Nice-Sophia Antipolis, January 2000

[71] N. Paragios, *Geodesic active regions : A new paradigm to deal with frame partition problems in Computer Vision.* Journal of Visual Communication and Image Representation 13, no. 1/2, 249-268, 2002

[72] M. Rousson and R. Deriche, *A variational framework for active and adaptive segmentation of vector valued images.* Tech. report, INRIA, 2002

[73] M. Rousson, *Cue integration and front evolution in image segmentation.* Ph.D. thesis, Université de Nice-Sophia Antipolis, December 2004

[74] D. Mumford and J.Shah, *Boundary detection by minimizing functionals.* Proc. CVPR'85, pp. 22-26, 1985

[75] E. D. Giorgi, E. Magenes, and U. Mosco, *Convergence Problems for Functionals and Operators.* In International Meeting on Recent Methods on Nonlinear Analysis, 131-188, 1978

[76] G.D. Maso, *An Introduction to* Γ*-convergence.* In Progress in Linear Differential Equations and their Applications, Birkhauser, Boston, 1993.

[77] C. Li, C. Kao, J. Gore, Z. Ding, *Implicit Active Driven by Local Binary Fitting Energy.* Proc. IEEE Conf. Comp. Vi. and Pat. Recog., 1-7, 2007

[78] K. Zhang, H. Song, L. Zhang, *Active Contour Driven by Local Image Fitting Energy.* Journal Pattern Recognition, Vol. 43, Issue 4, 1199-1206, 2010

[79] L. Wang, C. Li, Q. Sun, D. Xia, CY. Kao, *Active contours driven by local and global intensity fitting energy with application to brain MR image segmentation.* Comp. Medi. Imag. and Grap., 33, 520-531, 2009

[80] XF. Wang, DS. Huang, H. Xu, *An efficient local Chan-Vese model for image segmentation.* Pattern Recognition, 43, 603-618, 2010

[81] Q. T. Thieu, M. Luong, J. M. Rocchisani, D. Tran, E. Viennet, *An Efficient Local and Global Model for Image Segmentation.* International conference on Advanced Technologies for Communications (ATC), 2011

[82] W. Guo, Y. Chen. *Using non-parametric kernel to segment and smooth images simultaneous.* Proceedings of International Conference in Image Processing, 217-220, 2006

[83] L. Wang, L. He, A. Mishra, C. Li. *Active Contours Driven by Local Gaussian Distribution Fitting Energy*. Signal Processing, 89(12), 2009,p. 2435-2447

[84] G. Sapiro, *Geometric Partial Differential Equations and Image Analysis*. Cambridge University Press 2001

[85] T. Goldstein, X. Bresson, S. Osher, *Geometric Application of the Split Bregman Method: Segmentation and Surface Reconstruction.* Journal of Scientific Computing, Vol. 45, 272-293, 2010

[86] J. C. Dunn. *A Fuzzy Relative of the ISODATA Process and Its Use in Detecting Compact Well-Separated Clusters*. Journal of Cybernetics 3: 32-57, 1973

[87] J. C. Bezdek. *Pattern Recognition with Fuzzy Objective Function Algoritms*. Plenum Press, New York, 1981

[88] D.W. Shattuck, S.R. Sandor-Leahy, K.A. Schaper, D.A. Rottenberg, R.M. Leahy. *Magnetic Resonance Image Tissue Classfication using a Partial Volume Model*. Neuroimage 13, 856-76, 2001

[89] Y. Wang, G.H. Bock, R.J. Van Klaveren, P. Van Ooyen, W. Tukker, Y. Zhao, M.D. Dorrius, R.V. Proenca, W.J. Post, M. Oudkerk, *Volumetric measurement of pulmonary nodules at low-dose chest CT : effect of reconstruction setting on measurement variability*. Eur Radiol. 2010 May ; 20(5), 1180-1187, 2009

[90] P. Tylski, S. Stute, N. Grotus, K. Doyeux, S. Hapdey, I. Gardin, B. Vanderlinden, I. Buvat, *Comparative Assessment of Methods for Estimating Tumor Volume and Standardized Uptake Value in 18F-FDG PET*. J Nucl Med. 2010 Feb;51(2), 268-76. Epub 2010 Jan 15

[91] G. Argenziano, H.P. Soyer, V. D. Giorgi, et al., *Dermoscopy, an interactive atlas*. Milan, Italy: EDRA Medical Publishing and new media. http://www. dermoscopy.org., 2000

[92] F. Nachbar, W. Stolz, T. Merkle, et al., *The ABCD rule of dermatoscopy: high prospective value in the diagnosis of doubtful melanocytic skin lesions*. Journal of the American Academy of Dermatology 304., pp. 551-559, 1994

[93] G. Argenziano, G. Fabbrocini, P. Carli, V. De Giorgi, E. Sammarco, M. Delfino, *Epiluminescence microscopy for the diagnosis of doubtful melanocytic skin lesions. Comparison of ABCD rule of dermatoscopy and a new 7-point checklist based on pattern analysis*. Arch Dermatol. 13412., pp. 1563-1570, 1998

[94] S. Menzies, C. Ingvar, K. Crotty, W. McCarthy, *Frequency and morphologic characteristics of invasive melanomas lacking specific surface microscopic features.* Arch Dermatol. Vol. 132, No. 10, pp. 1178-1182, 1996

[95] M.E. Vestergaard, P. Macaskill, P.E. Holt, S.W. Menzies, *Dermoscopy compared with naked eye examination for the diagnosis of primary melanoma: a meta-analysis of studies performed in a clinical setting.* Br J Dermotology, 159: pp. 669-676, 2008

[96] M. Silveira, J.S. Marques, *Level set segmentation of dermoscopy images.* 5th IEEE International Symposium on Biomedical Imaging: From Nano to Macro ISBI., pp. 173-176, DOI: 10.1109/ISBI.2008.4540960 2008

[97] H. Zhou, G. Schaefer, M. Emre Celebi, F. Lin, *Gradient vector flow with mean shift for skin lesion segmentation.* Computerized Medical Imaging and Graphics, Vol. 35, Issue 2 , pp. 121-127, March 2011

[98] M. Mete, N.M. Sirakov, 2012, *Dermoscopic Diagnosis Of Melanoma In A 4d Feature Space Constructed By Active Contour Extracted Features.* Computerized Medical Imaging and Graphics 36, pp. 572-579, http://dx.doi.org/10.1016/j.compmedimag.2012.06, 2012

[99] M. Sadeghi, , M. Razmara, , M. Stella Atkins , T. K. Lee, *A novel method for detection of pigment network in dermoscopic images using graphs.* Computerized Medical Imaging and Graphics, Vol. 35, Issue 2 , pp. 137-143, March 2011

[100] `coronary.bigr.nl/stenoses/`

[101] I. M. Gelfand, S. V. Fomin, *Calculus of Variations.* Moscow State University, Revised English Edition, Translated and Edited by R. A. Silverman, 1963 by Prentice-Hall, Inc, Englewood Cliffs, New Jersey, 1963

[102] B. V. Brunt, *The Calculus of Variations.* ISBN 0-387-40247-0, Springer - Verlag New York, 2004

[103] B. Lelandais, I. Gardin, L. Mouchard, P. Vera, S. Ruan, *Segmentation of Biological Target Volumes on Multi-tracer PET Images Based on Information Fusion for Achieving Dose Painting in Radiotherapy.* MICCAI (1), 545-552, 2012

List of Theorems

List of Tables

List of Figures